ornl

NUREG/CR-4219
Volume 2
ORNL/TM-9593/V2

OAK RIDGE
NATIONAL
LABORATORY

MARTIN MARIETTA

Heavy-Section Steel Technology Program Semiannual Progress Report for April–September 1985

C. E. Pugh

Prepared for the U.S. Nuclear Regulatory Commission
Office of Nuclear Regulatory Research
Under Interagency Agreements DOE 40-551-75 and 40-552-75

OPERATED BY
MARTIN MARIETTA ENERGY SYSTEMS, INC.
FOR THE UNITED STATES
DEPARTMENT OF ENERGY

NOTICE

This report was prepared as an account of work sponsored by an agency of the United States Government. Neither the United States Government nor any agency thereof, or any of their employees, makes any warranty, expressed or implied, or assumes any legal liability or responsibility for any third party's use, or the results of such use, of any information, apparatus product or process disclosed in this report, or represents that its use by such third party would not infringe privately owned rights.

Available from

Superintendent of Documents
U.S. Government Printing Office
Post Office Box 37082
Washington, D.C. 20013-7982

and

National Technical Information Service
Springfield, VA 22161

NUREG/CR-4219
Volume 2
ORNL/TM-9593/V2
Dist. Category RF

Engineering Technology Division

HEAVY-SECTION STEEL TECHNOLOGY PROGRAM SEMIANNUAL PROGRESS REPORT FOR APRIL–SEPTEMBER 1985

C. E. Pugh

Manuscript Completed — December 16, 1985
Date Published — January 1986

Prepared for the
U.S. Nuclear Regulatory Commission
Office of Nuclear Regulatory Research
under Interagency Agreements DOE 40-551-75 and 40-552-75

NRC FIN No. B0119

Prepared by the
OAK RIDGE NATIONAL LABORATORY
Oak Ridge, Tennessee 37831
operated by
MARTIN MARIETTA ENERGY SYSTEMS, INC.
for the
U.S. DEPARTMENT OF ENERGY
under Contract No. DE-AC05-840R21400

CONTENTS

LIST OF FIGURES

LIST OF TABLES

PREFACE

The Heavy-Section Steel Technology (HSST) Program, which is sponsored by the Nuclear Regulatory Commission, is an engineering research activity devoted to extending and developing the technology for assessing the margin of safety against fracture of the thick-walled steel pressure vessels used in light-water-cooled nuclear power reactors. The program is being carried out in close cooperation with the nuclear power industry. This report covers HSST work performed in April–September 1985. The work performed by Oak Ridge National Laboratory (ORNL) and by subcontractors is managed by the Engineering Technology Division. Major tasks at ORNL are carried out by the Engineering Technology Division and the Metals and Ceramics Division. Prior progress reports on this program are ORNL-4176, ORNL-4315, ORNL-4377, ORNL-4463, ORNL-4512, ORNL-4590, ORNL-4653, ORNL-4681, ORNL-4764, ORNL-4816, ORNL-4855, ORNL-4918, ORNL-4971, ORNL/TM-4655 (Vol. II), ORNL/TM-4729 (Vol. II), ORNL/TM-4805 (Vol. II), ORNL/TM-4914 (Vol. II), ORNL/TM-5021 (Vol. II), ORNL/TM-5170, ORNL/NUREG/TM-3, ORNL/NUREG/TM-28, ORNL/NUREG/TM-49, ORNL/NUREG/TM-64, ORNL/NUREG/TM-94, ORNL/NUREG/TM-120, ORNL/NUREG/TM-147, ORNL/NUREG/TM-166, ORNL/NUREG/TM-194, ORNL/NUREG/TM-209, ORNL/NUREG/TM-239, NUREG/CR-0476 (ORNL/NUREG/TM-275), NUREG/CR-0656 (ORNL/NUREG/TM-298), NUREG/CR-0818 (ORNL/NUREG/TM-324), NUREG/CR-0980 (ORNL/NUREG/TM-347), NUREG/CR-1197 (ORNL/NUREG/TM-370), NUREG/CR-1305 (ORNL/NUREG/TM-380), NUREG/CR-1477 (ORNL/NUREG/TM-393), NUREG/CR-1627 (ORNL/NUREG/TM-401), NUREG/CR-1806 (ORNL/NUREG/TM-419), NUREG/CR-1941 (ORNL/NUREG/TM-437), NUREG/CR-2141, Vol. 1 (ORNL/TM-7822), NUREG/CR-2141, Vol. 2 (ORNL/TM-7955), NUREG/CR-2141, Vol. 3 (ORNL/TM-8145), NUREG/CR-2141, Vol. 4 (ORNL/TM-8252), NUREG/CR-2751, Vol. 1 (ORNL/TM-8369/V1), NUREG/CR-2751, Vol. 2 (ORNL/TM-8369/V2), NUREG/CR-2751, Vol. 3 (ORNL/TM-8369/V3), NUREG/CR-2751, Vol. 4 (ORNL/TM-8369/V4), NUREG/CR-3334, Vol. 1 (ORNL/TM-8787/V1), NUREG/CR-3334, Vol. 2 (ORNL/TM-8787/V2), NUREG/CR-3334, Vol. 3 (ORNL/TM-8787/V3), NUREG/CR-3744, Vol. 1 (ORNL/TM-9154/V1), NUREG/CR-3744, Vol. 2 (ORNL/TM-9154/V2), and NUREG/CR-4219, Vol. 1 (ORNL/TM-9593/V1).

SUMMARY

1. PROGRAM MANAGEMENT

The total program is arranged into ten tasks: (1) program management, (2) fracture methodology and analysis, (3) material characterization and properties, (4) environmentally assisted crack-growth studies, (5) crack-arrest technology, (6) irradiation effects studies, (7) stainless steel cladding evaluations, (8) intermediate vessel tests and analyses, (9) thermal-shock technology, and (10) pressurized-thermal-shock technology. Progress reports are issued on a semiannual basis, and the chapters of those reports correspond to the ten tasks.

The work performed at Oak Ridge National Laboratory (ORNL) and under existing research and development subcontracts is included in this report. During the report period, 34 program briefings, reviews, or presentations were made, and 12 technical documents were published. Program subcontracts were monitored and coordinated.

2. FRACTURE METHODOLOGY AND ANALYSIS

ORNL developed a dynamic version of the ORMGEN/ADINA/ORVIRT fracture codes and performed qualification analyses with several problems. The code, ADINA/EDF, has been adopted as the reference elastodynamic code at ORNL, replacing SWIDAC. Generally, ADINA/EDF was found to require about one-half of the central processing unit time and input/output operations required by the previously used SWIDAC code. Developments were also made to the ORNL fracture codes ORMGEN and ORVIRT to permit improved finite-element modeling of nozzle-corner crack regions. ORNL is developing a viscoplastic analysis version of the ADINA fracture codes (ADINA/VPF) on the basis of a constitutive model formulated by Perzyna.

ORNL also conducted, as a part of ITV-8A assessments, an examination of the parameters J_D and J_M as measures of toughness controlling the ductile tearing resistance curve.

Integrated fracture-mechanics experimentation and finite-element analyses are being conducted at the Southwest Research Institute (SwRI) to develop improved predictions for crack arrest under upper-shelf toughness conditions. Further, efforts were made to perform viscoplastic material characterization experiments that support use of the Bodner-Partom model. Analytical studies were made of crack-tip fields with the Bodner-Partom model. A two-dimensional finite-element computer code was developed for performing viscoplastic analyses, and generation-phase analyses were performed for Heavy-Section Steel Technology wide-plate crack-arrest test WP-1.3 by SwRI. Cleavage-fibrous transition studies continued at the University of Maryland (UM) with emphasis on low-upper-shelf weldment material. Initial high-loading-rate studies were made.

3. MATERIAL CHARACTERIZATION

Mechanical and fracture properties characterization of the wide-plate crack-arrest material was performed. Testing was performed by ORNL and subcontractors to provide data for the American Society for Testing and Materials (ASTM) round robin on crack arrest. Tests with standard-size specimens, subsize specimens, ASTM split pin, and inverted pin testing were performed. The stainless steel clad plate A 533 grade B class 1 steel, with properties in each region conducive to allowing brittle crack propagation in the base plate while the cladding remained tough, was received from the subcontractor for use in irradiation and clad-beam testing.

4. ENVIRONMENTALLY ASSISTED CRACK-GROWTH TECHNOLOGY

Crack-growth-rate and mechanistic studies of a high-sulfur steel plate are nearing completion at Westinghouse, and results are showing a measurable effect of temperature on crack-growth rate. The environmental enhancement is observed to be directly related to the size and distribution of manganese sulfide inclusions in the steel (a function of steelmaking practice). A series of fatigue crack-growth-rate tests was completed on a heat-affected-zone material with low-sulfur content, and the crack-growth rates were shown to be measurably lower than in the high-sulfur heat-affected-zone materials tested previously. This is consistent with earlier fatigue crack-growth findings, but such differences have not been found in static bolt-load specimen results.

5. CRACK-ARREST TECHNOLOGY

The task to perform wide-plate crack-arrest tests at the National Bureau of Standards (NBS) continued. ORNL designed, machined, and shipped to NBS four additional specimens from HSST plate 13A of A 533 grade B class 1 steel. The third and fourth tests, WP-1.3 and WP-1.4, were performed and included three arrest events that occurred at approximately 52, 77, and 83°C above the RT_{NDT} for this material. ORNL, SwRI, and UM performed posttest dynamic-fracture analyses using the computer codes ADINA/EDF, SWIDAC, and SAMCR. NBS made preparations for the fifth test, WP-1.5, which was performed on October 9.

In other areas, UM continued to administer the ASTM E24.01.06 round robin on crack-arrest testing. Data have been received from 20 of the 27 participating laboratories.

6. IRRADIATION EFFECTS STUDIES

The Fifth Irradiation Series addresses irradiation effects on the initiation toughness of two high-copper welds. Irradiation of 10 of the

12 planned capsules has been completed. These capsules included Charpy V-notch, tensile, drop-weight, 1T compact, 2T compact, and 4T compact specimens. Irradiation of capsules 11 and 12 will start in early FY 1986. The Sixth Series will examine the shift in the crack-arrest toughness of these same two weldments. Final specimen complement and capsule design were completed. Fluence and temperature gradient calculations were performed. The Seventh Series will evaluate irradiation effects on stainless steel cladding. Phase 1 of the study was completed on an irradiated one-wire submerged-arc clad material. Fracture characteristics were examined in terms of microstructure and irradiation effects. Phase 2 will study a commercially produced three-wire cladding representative of that used in the fabrication of early reactor vessels. Irradiation of three capsules was begun at the University of Buffalo reactor. Charpy, tensile, and 0.5T compact specimens are included.

7. CLADDING EVALUATIONS

The topical report on the ORNL clad-beam tests that were performed earlier was issued. Two segments of a boiling-water reactor pressure vessel, which were obtained for flaw and properties characterization, were given nondestructive examinations according to the plan that was reported earlier. Twelve 20% distance-amplitude correction indications were recorded (five code recordable). Code-sizing techniques indicated lengths and depths <25 by 25 mm. Further size analyses and destructive sectioning are planned.

8. INTERMEDIATE VESSEL TESTS AND ANALYSIS

Work continued on preparation of a topical report on the intermediate vessel test ITV-8A, which involved a low-upper-shelf weld.

9. THERMAL-SHOCK TECHNOLOGY

A major effort this period was devoted to the completion and issuance of three topical reports covering HSST thermal-shock experiments TSE-5, -5A, -6, and -7 and the inclusion of three-dimensional flaws in the pressurized-water reactor pressurized-thermal-shock vessel integrity studies. In addition, the ORNL probabilistic fracture-mechanics code OCA-P was adapted to a personal computer. Fracture analyses and experimental definition studies regarding subclad and through-clad flaws were continued.

10. PRESSURIZED-THERMAL-SHOCK TECHNOLOGY

Preparations continued for the second pressurized-thermal-shock experiment, PTSE-2. The Babcock & Wilcox Company, under subcontract, is procuring a 2 1/4 Cr-1 Mo steel plate for use in preparing a plug of material for the flawed region of the PTSE-2 vessel. Heat-treatment studies and a tentative selection of a stress-relieving temperature have been made.

Instrumentation development and preparation are progressing. Preliminary fracture-mechanics analyses were performed to evaluate the suitability of properties of the plug material determined in the heat-treatment studies. Results obtained so far indicate that the unexpectedly high nil-ductility transition temperature and low yield strength will be satisfactory for PTSE-2.

HEAVY-SECTION STEEL TECHNOLOGY PROGRAM SEMIANNUAL PROGRESS REPORT FOR APRIL–SEPTEMBER 1985*

C. E. Pugh

ABSTRACT

The Heavy-Section Steel Technology (HSST) Program is conducted for the Nuclear Regulatory Commission. The studies relate to all areas of the technology of materials fabricated into thick-section primary-coolant containment systems of light-water-cooled nuclear power reactors. The focus is on the behavior and structural integrity of steel pressure vessels containing cracklike flaws. The program is organized into ten tasks: (1) program management, (2) fracture methodology and analysis, (3) material characterization and properties, (4) environmentally assisted crack-growth studies, (5) crack-arrest technology, (6) irradiation effects studies, (7) cladding evaluations, (8) intermediate vessel tests and analysis, (9) thermal-shock technology, and (10) pressurized-thermal-shock technology. During this period, extensions were made to fracture analysis codes, including development of a dynamic fracture version of the ADINA-ORMGEN-ORVIRT analysis codes at Oak Ridge National Laboratory (ORNL). ORMGEN and ORVIRT were further developed for use in analyzing nozzle-corner cracks. Elastodynamic analyses and development work on viscoplastic fracture analysis techniques were performed by ORNL and Southwest Research Institute in support of the wide-plate crack-arrest tests that are being performed by the National Bureau of Standards (NBS) for the HSST Program. Two additional wide-plate crack-arrest tests were performed by NBS. Further results from K_{Ia} tests were received for the American Society for Testing and Materials round robin. Crack-growth rate tests of high-sulfur vessel steels continued. The Fifth HSST Irradiation Series continued for the study of K_{Ic} shifts for welds with different copper contents, and test plans proceeded for the Sixth (on K_{Ia} shift) and Seventh (on stainless steel cladding) Irradiation Series. A report covering the first set of ORNL clad-beam tests was issued. Work continued on the report on the test of ITV-8A, which contained a low-upper-shelf weldment. Detailed exploratory analytical fracture studies were carried out for clad cylinders undergoing thermal-shock loadings, and fracture assessments were completed for the Integrated Pressurized-Thermal-Shock Program. Reports were issued for the last four thermal-shock experiments. Posttest analyses were completed for the first pressurized-thermal-shock

*This report is written in terms of metric units. Conversions from SI to English units for all SI quantities are listed on a foldout page at the end of this report.

test (PTSE-1), and the topical report on the experiment and analyses was issued. Contract work continued for provision of low-upper-shelf energy test material and thermocouple thimbles for use in PTSE-2.

---

1. PROGRAM MANAGEMENT

C. E. Pugh

The Heavy-Section Steel Technology (HSST) Program, a major safety program sponsored by the Nuclear Regulatory Commission (NRC) at Oak Ridge National Laboratory (ORNL), is concerned with the structural integrity of the primary systems [particularly the reactor pressure vessels (RPVs)] of light-water-cooled nuclear power reactors. The structural integrity of these vessels is ensured by (1) designing and fabricating RPVs according to standards set by the code for nuclear pressure vessels, (2) detecting flaws of significant size that occur during fabrication and in service, and (3) developing methods of producing quantitative estimates of conditions under which fracture could occur. The program is concerned mainly with developing pertinent fracture technology, including knowledge of (1) the material used in these thick-walled vessels, (2) the flaw-growth rate, and (3) the combination of flaw size and load that would cause fracture and thus limit the life and/or operating conditions of this type of reactor plant.

The program is coordinated with other government agencies and with the manufacturing and utility sectors of the nuclear power industry in the United States and abroad. The overall objective is a quantification of safety assessments for regulatory agencies, professional code-writing bodies, and the nuclear power industry. Several activities are conducted under subcontract by research facilities in the United States and through an informal cooperative effort on an international basis. Five research and development subcontracts are currently in force.

The program tasks are arranged according to the work breakdown structure shown in Fig. 1.1. Accordingly, the chapters of this progress report correspond to these ten tasks. During this report period, the updated 5-year program plan[1] applicable to FY 1984–1988 was issued as a NUREG report.

Two foreign technical specialists from the Swiss Federal Institute for Reactor Research were at ORNL on temporary assignments to the HSST Program during this period. Robert Wanner will complete a 16-month assignment at the end of October 1985. Stefan Brosi completed in July a 4-month assignment to work on nozzle-cracking analyses. Additionally, Camillo Inversini of the same institute reported to ORNL on September 25 to begin a 1-year assignment in fracture analysis.

During this period, 34 program briefings, reviews, or presentations were made by the HSST staff at technical meetings and at program reviews for NRC staff or visitors. Twelve technical documents, including one technical progress report,[2] nine topical reports,[3-11] and two technical papers,[12-13] were published.

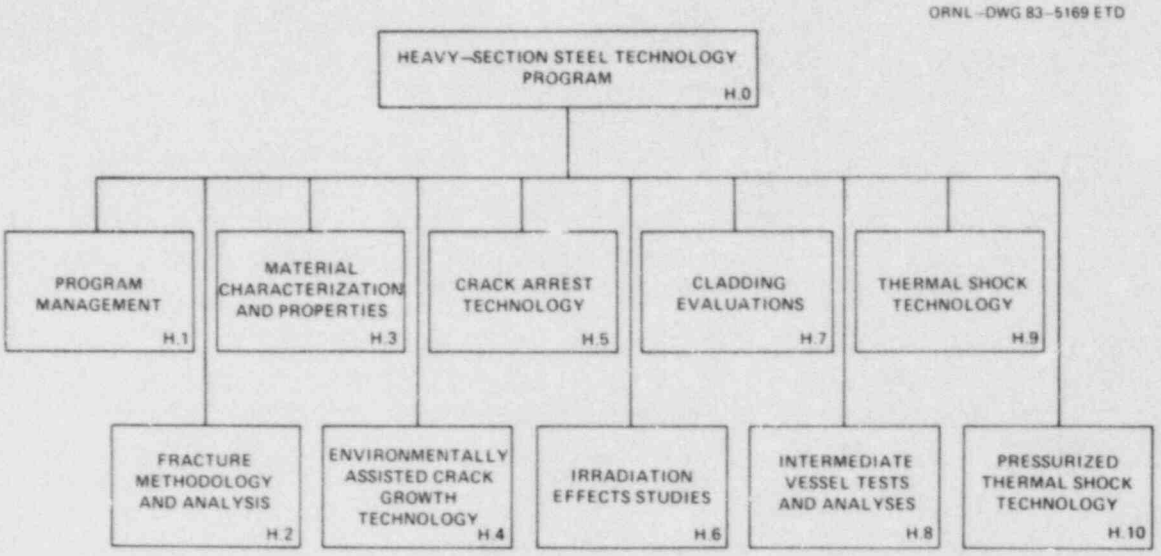

Fig. 1.1. Level-2 work breakdown structures for HSST Program.

References

1. *Heavy-Section Steel Technology Program — Five-Year Plan FY 1984–1988*, NUREG/CR-4275 (ORNL/TM-9654), Martin Marietta Energy Systems, Inc., Oak Ridge Natl. Lab., July 1985.

2. C. E. Pugh, *Heavy-Section Steel Technology Program Semiann. Prog. Rep. October 1984–March 1985*, NUREG/CR-4219, Vol. 1 (ORNL/TM-9593/V1), Martin Marietta Energy Systems, Inc., Oak Ridge Natl. Lab.

3. W. R. Corwin et al., *Effects of Stainless Steel Weld Overlay Cladding on the Structural Integrity of Flawed Steel Plates in Bending, Series 1*, NUREG/CR-4015 (ORNL/TM-9390), Martin Marietta Energy Systems, Inc., Oak Ridge Natl. Lab., April 1985.

4. R. H. Bryan et al., *Pressurized-Thermal-Shock Test of 6-in.-Thick Pressure Vessels. PTSE-1: Investigation of Warm Prestressing and Upper-Shelf Arrest*, NUREG/CR-4106 (ORNL/TM-6135), Martin Marietta Energy Systems, Inc., Oak Ridge Natl. Lab., April 1985.

5. W. J. Stelzman, R. G. Berggren, and T. N. Jones, Jr., *ORNL Characterization of Heavy-Section Steel Technology Program Plates 01, 02, and 03*. NUREG/CR-4092 (ORNL/TM-9491), Martin Marietta Energy Systems, Inc., Oak Ridge Natl. Lab., April 1985.

6. L. F. Miller and R. W. Hobbs, *Data Acquisition and Control of the HSST Series V Irradiation Experiment at the ORR*, NUREG/CR-3872 (ORNL/TM-9253), Martin Marietta Energy Systems, Inc., Oak Ridge Natl. Lab., March 1985.

7. R. D. Cheverton et al., *Pressure Vessel Fracture Studies Pertaining to the PWR Thermal-Shock Issue: Experiments TSE-5, TSE-5A, and TSE-6*, NUREG/CR-4249 (ORNL-6163), Martin Marietta Energy Systems, Inc., Oak Ridge Natl. Lab., June 1985.

8. F. W. Stallmann, F. B. K. Kam, and C. A. Baldwin, *Neutron Exposure Parameters for the Fifth Heavy Section Steel Technology Irradiation Series*, NUREG/CR-4284 (ORNL/TM-9664), Martin Marietta Energy Systems, Inc., Oak Ridge Natl. Lab., July 1985.

9. R. D. Cheverton et al., *Pressure Vessel Fracture Studies Pertaining to the PWR Thermal-Shock Issue: Experiment TSE-7*, NUREG/CR-4304 (ORNL-6177), Martin Marietta Energy Systems, Inc., Oak Ridge Natl. Lab., August 1985.

10. E. C. Rodabaugh, *Comments on the Leak-Before-Break Concept for Nuclear Power Plant Piping Systems*, NUREG/CR-4305 (ORNL/Sub/8222252/3), prepared by E. C. Rodabaugh Associates, Inc., Hilliard, Ohio, for Martin Marietta Energy Systems, Inc., Oak Ridge Natl. Lab., August 1985.

11. R. D. Cheverton and D. G. Ball, *A Parametric Study of PWR Pressure Vessel Integrity During Overcooling Accidents, Considering Both 2-D and 3-D Flaws*, NUREG/CR-4325 (ORNL/TM-9682), Martin Marietta Energy Systems, Inc., Oak Ridge Natl. Lab., August 1985.

12. B. R. Bass et al., "Computational Methods for Fracture Analysis of Heavy-Section Steel Technology (HSST) Pressure Vessel Experiments," *Nucl. Eng. Des.* 86, 93–109 (1985).

13. B. R. Bass, C. E. Pugh, and H. K. Stamm, "Dynamic Analysis of Crack-Run Arrest Experiment in a Nonisothermal Plate," pp. 175–84 in *Proceedings of the 1985 Pressure Vessels and Piping Conference, Pressure Vessel Components Design and Analysis*, ASME, PVP-Vol. 98-2, June 1985.

2. FRACTURE METHODOLOGY AND ANALYSIS

2.1 Computer Program Development for Dynamic Fracture Analysis

B. R. Bass J. K. Walker

During this report period, work continued on the development of Oak Ridge National Laboratory (ORNL) computer programs for linear and nonlinear dynamic analysis of crack run-arrest events. The initial version of the ADINA/EDF (ElastoDynamic Fracture) program for linear thermoelastic analysis was completed, and development of the ADINA/VPF (ViscoPlastic-dynamic Fracture) code for viscoplastic-dynamic analysis was begun. A summary of these program developments is given in the following two sections.

2.1.1 Development of the ADINA/EDF computer program for elastodynamic fracture analysis

The ADINA/EDF code is designed for two-dimensional (2-D) elastodynamic fracture analysis of thermomechanically loaded structures. The code was constructed from the ADINA[1] general purpose finite-element structural analysis program through modifications of existing ADINA subroutines {primarily the truss [one-dimensional (1-D)] element module and the 2-D element module} and through the addition of ten new subroutines. The ADINA/EDF program is capable of performing both application-mode and generation-mode dynamic analyses. In an application-mode analysis, the crack tip is propagated incrementally according to the following relations:

$$\text{if } K_I < K_{ID}(\dot{a},T), \text{ then no propagation ;}$$
$$\text{if } K_I = K_{ID}(\dot{a},T), \text{ then propagation .} \qquad (2.1)$$

Here K_I is the dynamically computed stress-intensity factor, and K_{ID} is the dynamic fracture toughness relation that is taken to be a function of crack velocity $\dot{a}$ and temperature T. The formulation of K_{ID} currently used in ADINA/EDF is given in Ref. 2. In a generation-mode analysis, the crack tip is propagated incrementally according to a prescribed crack position vs time relation, and values of fracture toughness are determined from the dynamically computed K_I.

The crack-growth modeling technique in ADINA/EDF is essentially that used in the SWIDAC code from Southwest Research Institute (SwRI) and described in the paper by Jung et al.[3] In this technique, the finite element immediately ahead of the crack tip is divided into N subelements, where N depends on the mode of analysis, the magnitude of the time step, the dimensions of the element, and the limiting crack velocity. During

propagation, the tip is moved through these subelements along the crack plane in discrete jumps. The position of the crack tip relative to these subelement divisions is determined from restraining forces that are placed on the crack-plane nodes of the element adjacent to the crack tip; these forces are released incrementally as the tip propagates through the element. The restraining forces are postulated to vary linearly with the crack-tip location according to the relation

$$\frac{F_i}{F_{oi}} = (1 - a/\Delta x) \ , \tag{2.2}$$

where F_i is the force at node "i," F_{oi} is the force at node i just prior to node release, and a is the length of the crack in the finite element of length Δx. Prior to node release, the crack-plane nodes are restrained normal to the crack plane by truss (1-D) elements that are assigned an appropriate stiffness. At the time of release for node i, the corresponding nodal force F_{oi} is calculated, and the associated truss element is deactivated. The procedure by which the nodal force F_{oi} is reduced to zero (indicating propagation into the next element) is dependent upon whether an application-mode or a generation-mode analysis is being performed. Additional details concerning this procedure will be described in a forthcoming ORNL report on ADINA/EDF.

In the ADINA/EDF code, the dynamic stress-intensity factor K_I is determined in each time step from a dynamic $\hat{J}$-integral according to the relations

$$\begin{aligned} K_I &= \sqrt{\hat{J}E} \quad \text{(plane stress)} \ , \\ K_I &= \sqrt{\hat{J}E/(1 - \nu^2)} \quad \text{(plane strain)} \ , \end{aligned} \tag{2.3}$$

where E is Young's modulus, ν is Poisson's ratio, and

$$\hat{J} = \int_{\Lambda + \Lambda_s} \left(W \, dx_2 - \sigma_{ij} n_j \frac{\partial u_i}{\partial x_1} \, ds \right) + \iint_A \left(\rho \ddot{u}_i \frac{\partial u_i}{\partial x_1} + \sigma_{ij} \frac{\partial \theta_{ij}}{\partial x_1} \right) dA \ . \tag{2.4}$$

In Eq. (2.4) the first integral is the conventional J-integral evaluated on an arbitrary path $\Lambda + \Lambda_s$ surrounding the crack tip, and the second integral (consisting of inertial and thermal terms) is taken over the area A enclosed by the path $\Lambda + \Lambda_s$ (see Fig. 2.1). The variables in Eq. (2.4)

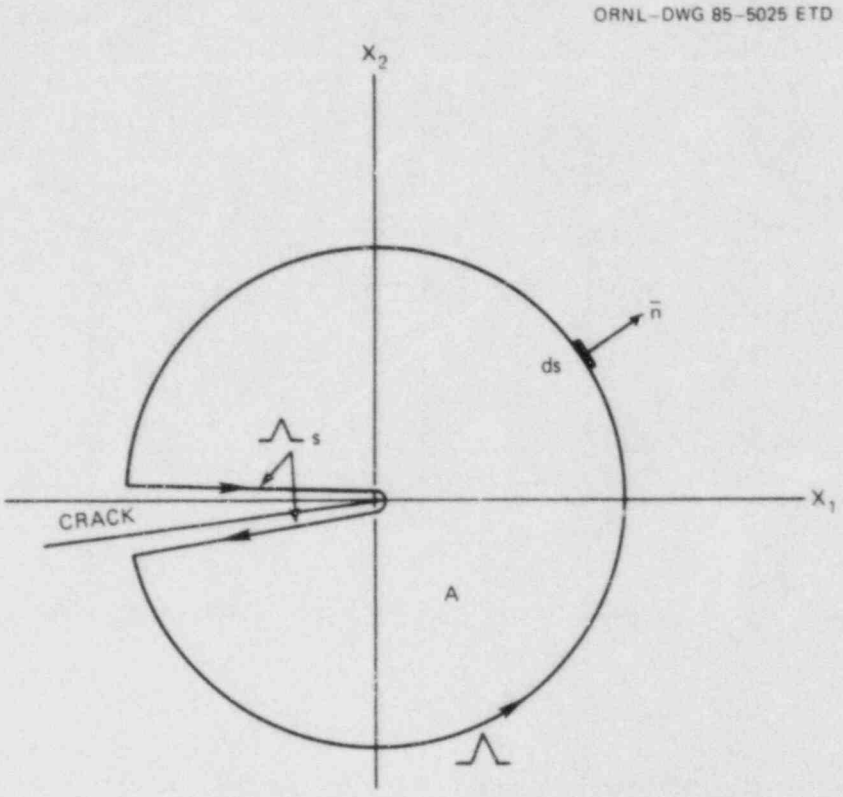

Fig. 2.1. Contour around crack tip for evaluation of $\hat{J}$-integral in ADINA/EDF.

include the spatial coordinates x_i, the arc length s, the elastic strain energy density W, the components of the stress tensor σ_{ij}, the strains of free thermal expansion θ_{ij}, the components of the displacement vector u_i, and the mass density ρ. The line integral in Eq. (2.4) is computed on the contour $\Lambda + \Lambda_s$ taken through nodal points on element boundaries, as illustrated in Fig. 2.2. The integration is performed numerically by using nodal point values of stress σ_{ij}, strain ε_{ij}, and displacement gradient $\partial u_i/\partial x_1$. These nodal-point values are obtained by first mapping element Gauss-point values (available from the finite-element solution) to the nodes, where the contributions from the elements are then averaged according to the smoothing procedures described in Refs. 4 and 5. The area integral in Eq. (2.4) is determined by Gauss quadrature from the conventional finite-element formulation.

For purposes of comparison, the ADINA/EDF program and the ORNL version of the SWIDAC program were applied to a dynamic analysis of the wide-plate configuration depicted in Fig. 2.3 and described in Sect. 5 of this report. The plate contains a crack initially located at $a_o/w = 0.2$ and is subjected to a linear thermal gradient across the plate width defined by $T_{min} = -133.3°C$ and $T_{max} = 233.3°C$. The dynamic analyses were performed with fixed axial displacements at the top of the load-pin holes that were calculated in a static analysis for a 7.952-MN axial load. The

ORNL-DWG 85-5045 ETD

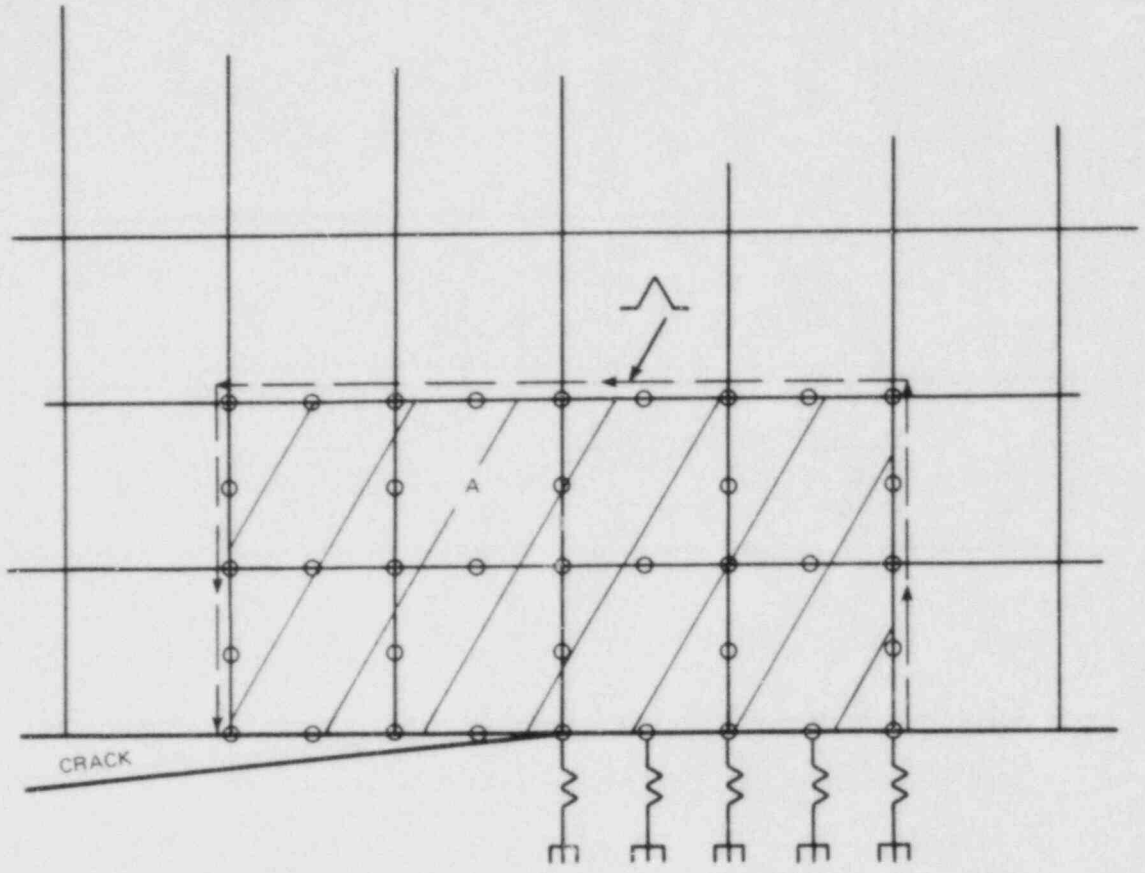

Fig. 2.2. Contour through node points for evaluation of $\hat{J}$-integral.

finite-element model consists of 712 nodes and 208 eight-noded isoparametric elements, with 25 truss elements constraining the ligament on the crack plane. From symmetry considerations, only one-half of the plate is modeled. Figure 2.4 depicts a crack position vs time relation input to the codes in generation-mode analyses performed using a time step Δt = 10 μs (300 steps) and the Newmark time integration scheme. Although the two codes gave the same result for dynamic K_I (see Fig. 2.5), the comparisons in Table 2.1 of central processing unit (CPU) times and I/O (input/output) operations for the analyses indicate that ADINA/EDF requires approximately one-half the computer resources of ORNL-SWIDAC for this problem on the ORNL IBM 3033 mainframe system. As indicated in Table 2.1, this observation is valid also for the application-mode analysis of the same finite-element model. In addition to the benefits of improved computer resource utilization, the ADINA/EDF code has other important features, including restart capability and an efficient out-of-core solver, that will facilitate the solution of larger dynamic problems over longer time intervals.

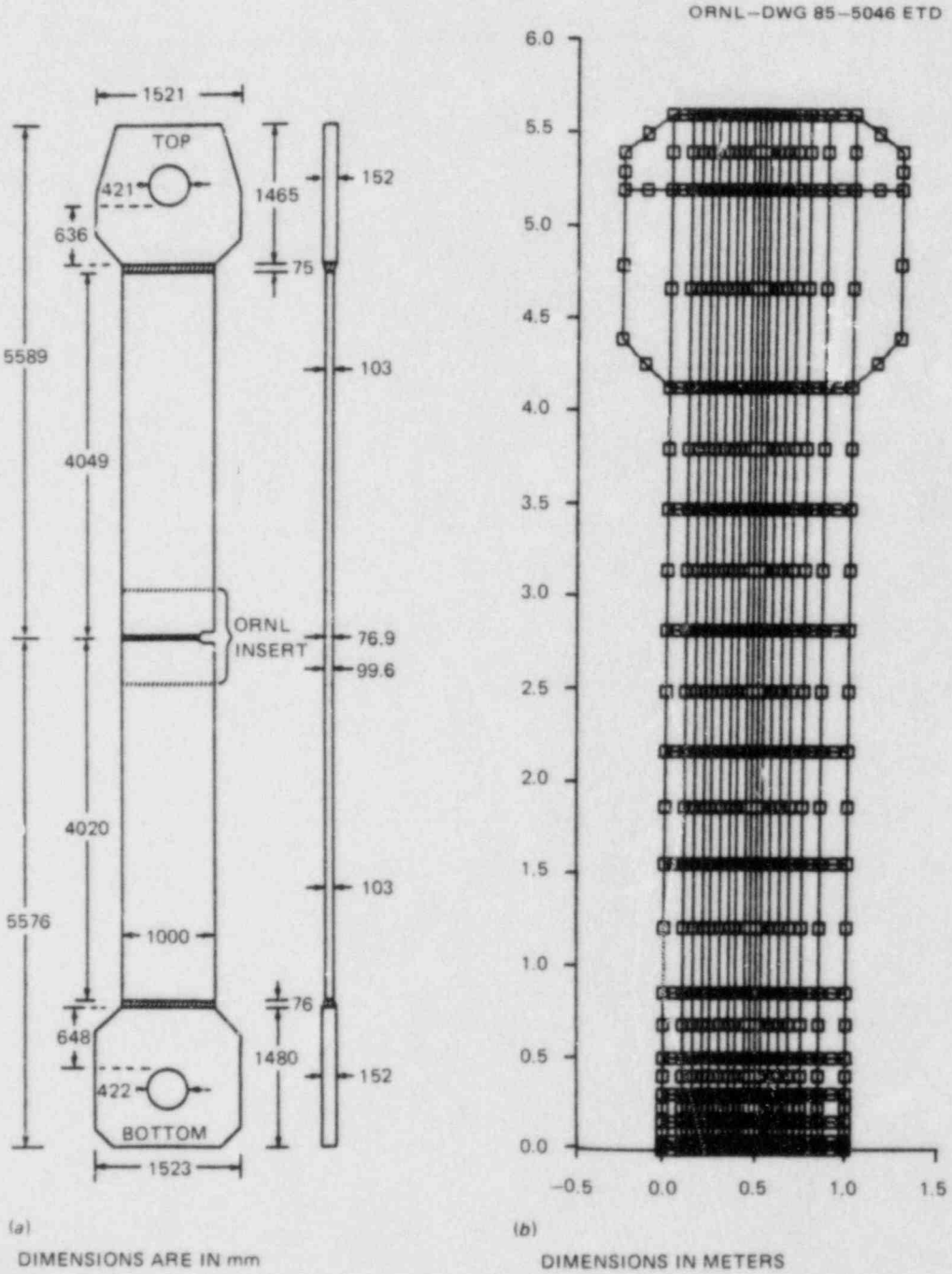

Fig. 2.3. Configuration of wide-plate assembly WP-1.4. (*a*) Geometric dimensions, (*b*) finite-element model for dynamic analysis.

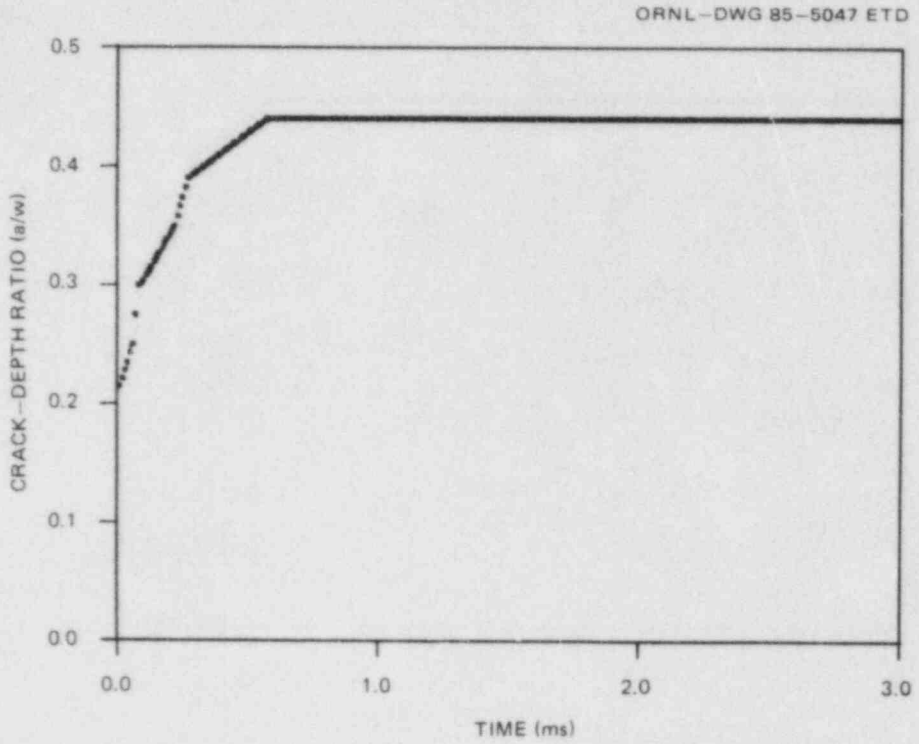

Fig. 2.4. Crack position vs time relation used in generation-mode analysis of wide-plate configuration.

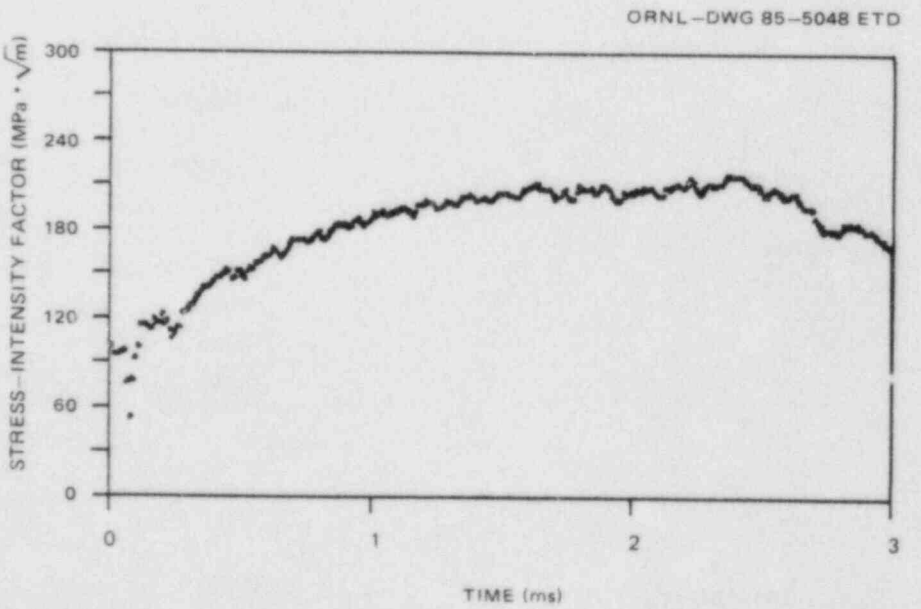

Fig. 2.5. Dynamic stress-intensity factor computed by ADINA/EDF and SWIDAC in generation-mode analysis of wide-plate configuration.

Table 2.1. Comparison of CPU times and I/O operations for ADINA/EDF and SWIDAC wide-plate analyses

Mode	CPU time (min)	I/O (thousands)
Generation		
ADINA/EDF	10	42
SWIDAC	27	74
Application		
ADINA/EDF	10	42
SWIDAC	27	75

2.1.2 ADINA/VPF computer program for viscoplastic-dynamic fracture analysis

The ADINA/VPF program for viscoplastic-dynamic analysis is being constructed from ADINA primarily through the addition of new constitutive model routines. The modular structure of ADINA allows user-supplied constitutive models to be installed in a straightforward manner with relatively few changes to the original code. In addition to the constitutive model, the prototype nonlinear dynamic fracture code also requires a node-release technique for modeling crack propagation and an appropriate fracture criterion.

The first viscoplastic constitutive model selected for installation in ADINA/VPF is similar to that employed in the fracture studies of Brickstad.[6] This model assumes a decomposition of the total strain $\underset{\sim}{\varepsilon}$ into elastic $\underset{\sim}{\varepsilon}_e$ and viscoplastic $\underset{\sim}{\varepsilon}_{vp}$ parts so that the total strain rate can be written[7]

$$\dot{\underset{\sim}{\varepsilon}} = \dot{\underset{\sim}{\varepsilon}}_e + \dot{\underset{\sim}{\varepsilon}}_{vp} \ . \tag{2.5}$$

The total stress rate depends on the elastic strain rate according to

$$\dot{\underset{\sim}{\sigma}} = \underset{\sim}{D}\, \dot{\underset{\sim}{\varepsilon}}_e \ , \tag{2.6}$$

where $\underset{\sim}{D}$ is the elastic matrix. A yield criterion that governs the initiation of viscoplastic flow is introduced in the form

$$F(\underset{\sim}{\sigma}, \underset{\sim}{\varepsilon}_{vp}) - F_o = 0 \ , \tag{2.7}$$

in which F_o is the uniaxial yield stress that may itself be a function of a hardening parameter. Viscoplastic flow occurs only for $F > F_o$. Explicit forms of the viscoplastic strain rate function

$$\dot{\underset{\sim}{\varepsilon}}_{vp} = \underset{\sim}{f} \tag{2.8}$$

for the model are discussed in Refs. 6, 8, and 9. Details concerning implementation of the computational algorithm based on this constitutive model are provided in Ref. 9.

The node-release technique implemented in the ADINA/VPF code is similar to that described in the previous section for ADINA/EDF but modified to incorporate a fracture criterion appropriate for nonlinear analysis. Selection of a suitable fracture criterion is currently under way.

2.2 Development of the ORVIRT.PC Microcomputer Program for Fracture Analysis

J. W. Bryson

During this report period, a new personal computer (PC) stress analysis and fracture mechanics code, ORVIRT.PC (Oak Ridge VIRTual crack extension Personal Computer), was developed. In addition, a report[10] that describes the program and provides user instructions was prepared and is presently in the production process. ORVIRT.PC is a stand-alone, finite-element program that executes on an IBM PC/AT, an IBM PC/XT, or compatible PCs and is capable of performing 2-D linear thermoelastic stress and fracture-mechanics analyses. Special crack-tip elements that allow for an inverse square root variation in the near-tip stress and strain fields may be used at the crack tip.

ORVIRT.PC is based, to a large extent, on the techniques used in the ORMGEN-ADINA-ORVIRT[11-13] fracture analysis system. An enhanced version[13,14] of the deLorenzi virtual-crack-extension development[15] is employed in the code. Although the technique is applicable in principle to the elastoplastic problem, limitations imposed by the microcomputer environment make the inclusion of this aspect impractical at this time.

ORVIRT.PC performs plane-stress or plane-strain analyses. Eight-noded, isoparametric, quadrilateral elements are used everywhere in the modeling, including in the crack-tip region. Either a 2 × 2 or 3 × 3 Gauss integration rule may be employed. These elements were chosen for ORVIRT.PC because they are versatile, perform well, and are tried and tested.

The motivation for developing ORVIRT.PC was to provide an accurate 2-D stand-alone fracture analysis capability for linear thermoelastic applications. The program performs its own stress analysis, and, thus, access to a large structural code such as ADINA[12] is not necessary. ORVIRT.PC employs modified versions of subroutines presented in the finite-element texts by Owen and Fawkes[16] and Hinton and Owen.[17] A very efficient frontal solver described and listed in both of these tests is

used in its entirety in the program. The frontal equation technique was originated by Irons[18] and differs from banded-solver techniques in that equations are assembled and variables eliminated at the same time. The complete structural stiffness matrix is never formed as such because after elimination the reduced equation is immediately written to the hard disk. The frontal technique is, therefore, particularly suitable for microcomputer applications because both core storage requirements and the total number of arithmetic operations are greatly reduced.

The following types of loading may be considered: (1) point loads, (2) distributed edge loads, and (3) thermal loads. Any combination of these loads may be applied simultaneously, or several loading conditions may be applied in succession to the same structural configuration. Distributed edge loads do not have to be constant, but they can vary along the element edge. Thermal loading consists of inputting values of ΔT at node points. As a further simplification, gravity loads and other body force loadings are not included.

The system requirements for executing ORVIRT.PC are

1. IBM PC/AT or PC/XT, 512 kB minimum memory, minimum 10 MB hard disk capacity;
2. math coprocessor;
3. IBM Professional Fortran Compiler, Version 1 or 2; and
4. 132-column printer.

ORVIRT.PC is written in Fortran 77, using 64 bit, double-precision, real words. Typical run times on an IBM PC/AT are 5 min for small problems to 20 min for problems approaching the maximum allowable dimensions of 135 elements and 450 nodes; the program takes ~60% longer to execute on an IBM PC/XT and 80% longer on a COMPAQ-PLUS portable.

Two example problems that demonstrate the high accuracy obtainable with ORVIRT.PC are presented below. Each problem was analyzed by using plane stress with a 3 × 3 Gauss integration rule.

2.2.1 Edge crack in a finite-width sheet subjected to three-point bending

Rooke and Cartwright[19] give $K_I = (1.[illegible])(6M\sqrt{\pi a/b^2})$, where $M = Pl/2$ for three-point bending of a crack configuration in which $l/b = 2$ and $a/b = 0.5$ (see Fig. 2.6). The finite-element mesh, boundary conditions, and applied loading are shown in Fig. 2.7. For $a = 10$ and an applied loading $P/2 = 21.164$, the closed form solution yields $K_I = 100$, and ORVIRT.PC gives $K_I = 99.2$ for 0.8% difference from the known solution.

2.2.2 Center cracked plate with a parabolic temperature distribution

The second example demonstrates application of ORVIRT.PC to a problem with thermal loading. Figure 2.8 shows the finite-element model used for a center cracked plate having $a/b = 0.25$ and $h/b = 3$. The plate, initially stress free at $T_o = 0$, is exposed to a parabolic temperature

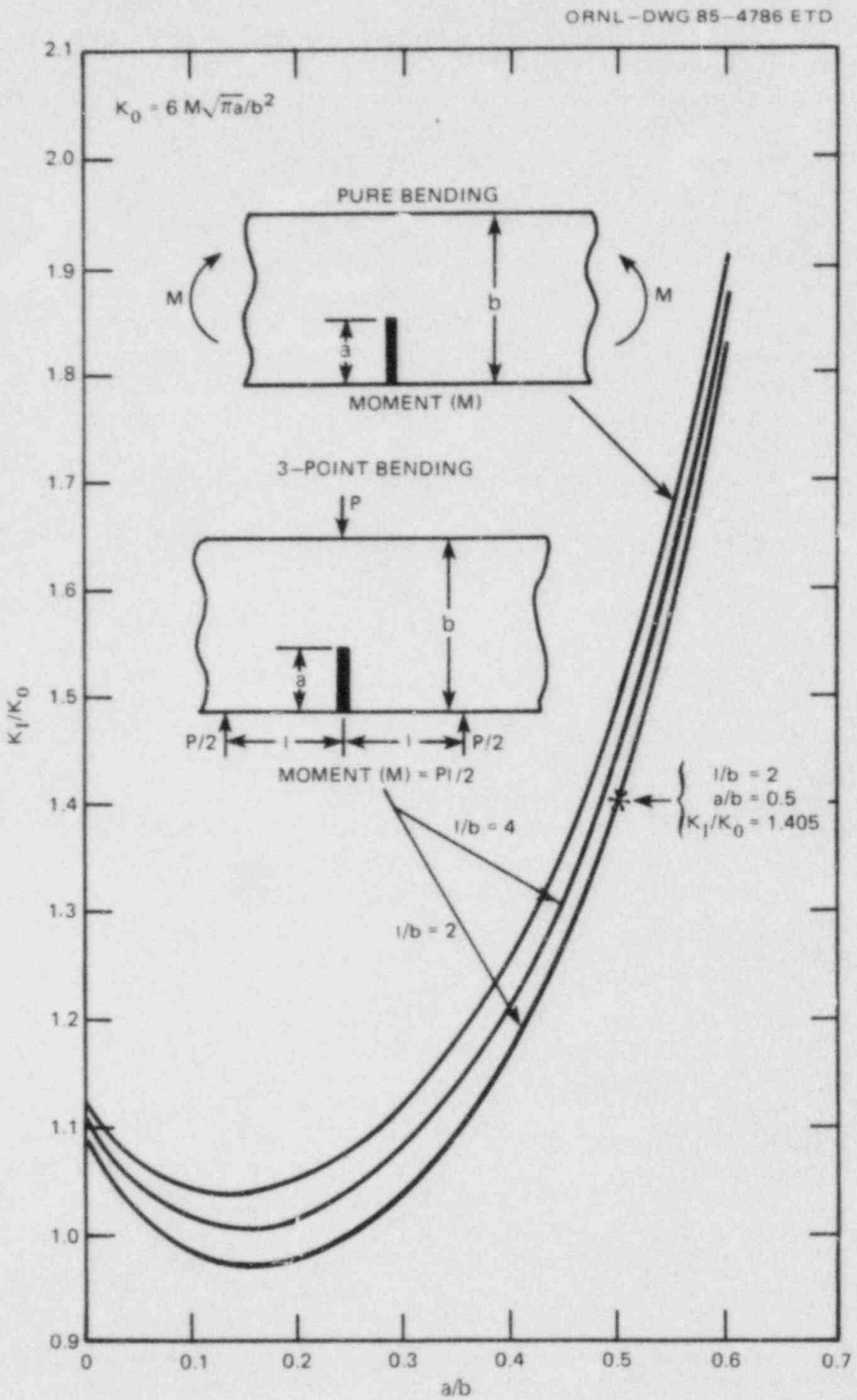

Fig. 2.6 K_I for an edge crack in finite-width sheet subjected to three-point bending.

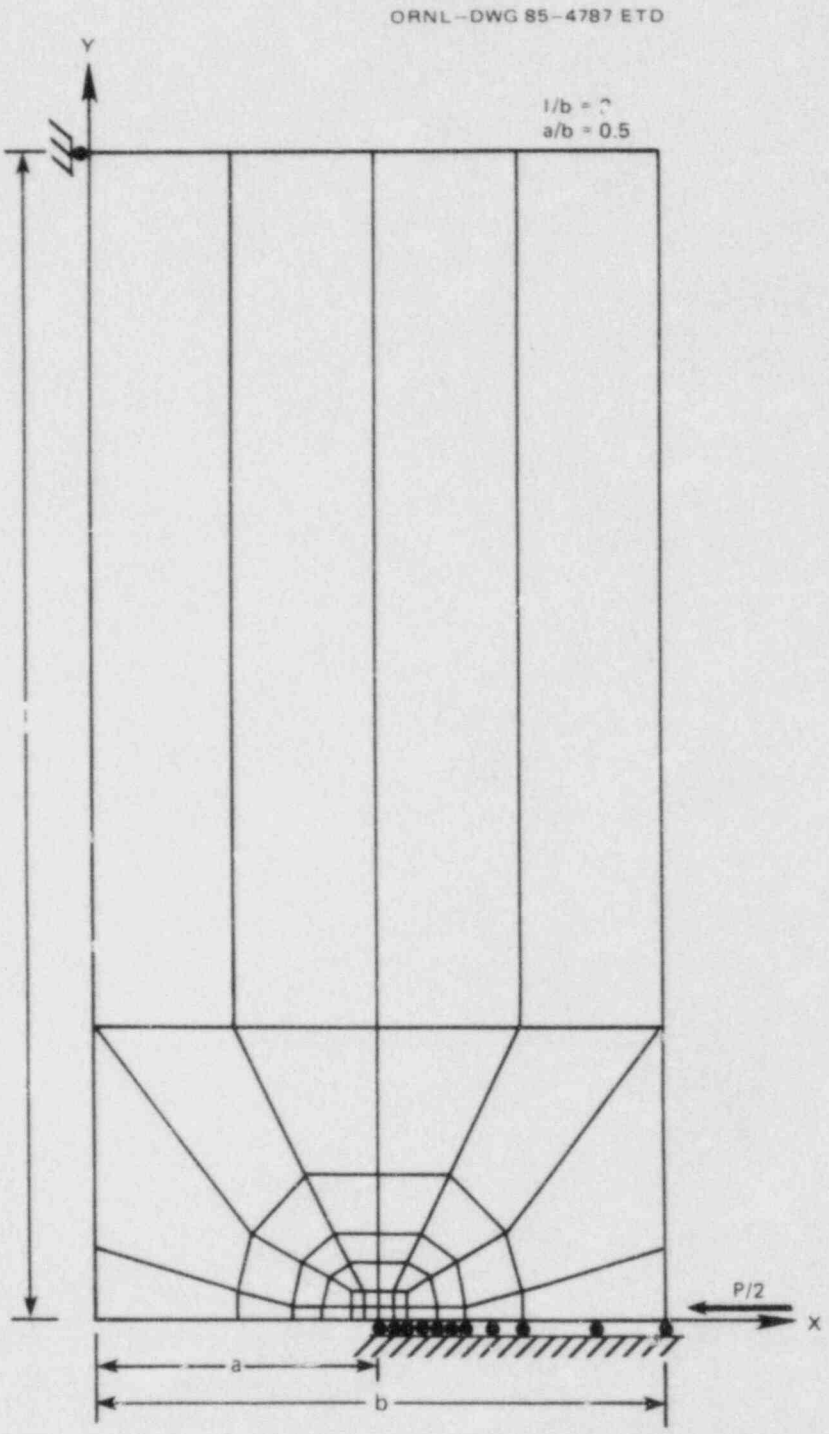

Fig. 2.7 Finite-element mesh employed for edge crack in a finite-width sheet subjected to three-point bending.

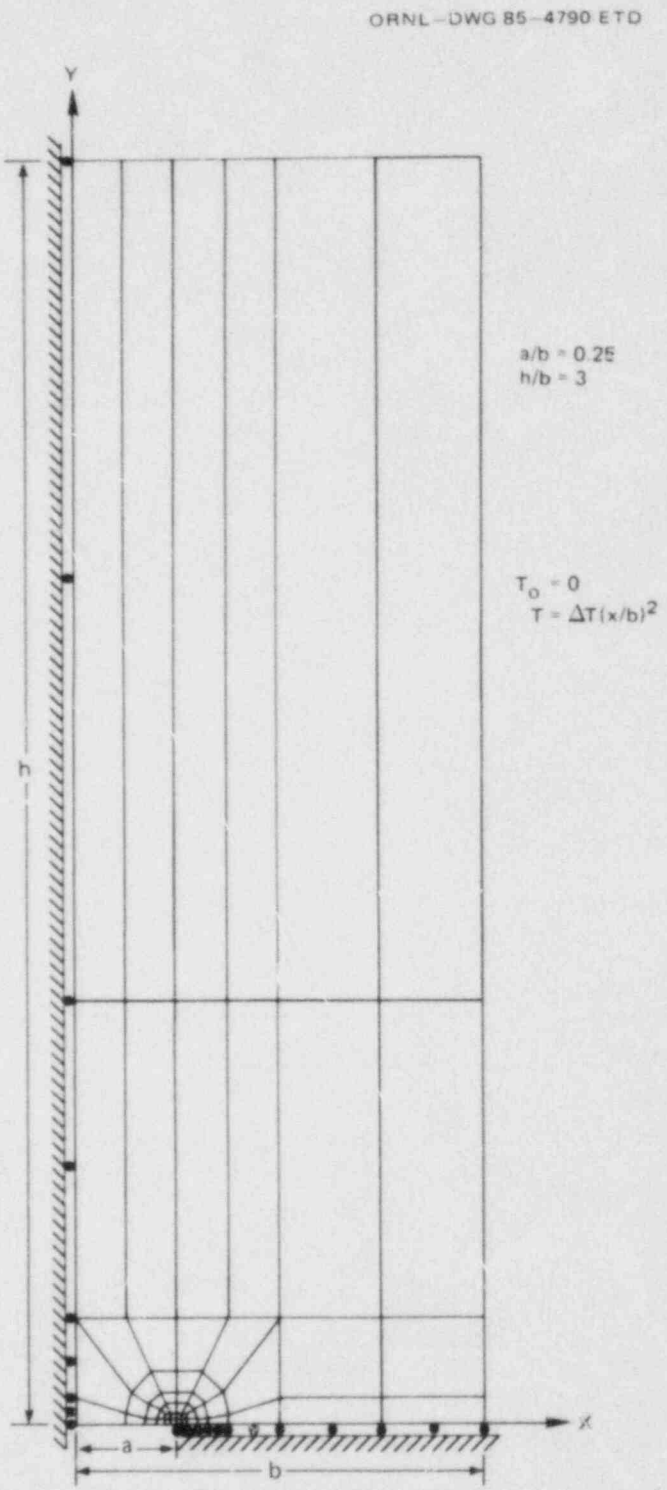

Fig. 2.8 Finite-element mesh employed for center-cracked plate, with a parabolic transverse temperature distribution.

distribution $T = (\Delta T)(x/b)^2$, which gives rise to a known[20] mode I stress-intensity factor

$$K_I = 0.557 E\alpha\Delta T\sqrt{a} \ . \tag{2.9}$$

For $a = 10$ and $\Delta T = 200$, $K_I = 100$ if $E\alpha = 0.2839$. Using these values, ORVIRT.PC computes $K_I = 99.9$ for a 0.1% deviation from the known solution.

2.3 Examination of the Parameters J_D and J_M as Measures of Toughness Controlling the Ductile Tearing Resistance Curve

J. G. Merkle

The currently prescribed method for calculating the value of the J-integral for a compact specimen undergoing stable crack growth[21] is based on the assumptions of the deformation theory of plasticity. Thus, the value of J is assumed to be independent of the loading path, the variables of which are load, displacement, and crack length, and is dependent only on the current values of those variables, as if the current crack length had existed since the start of loading. The value of J so calculated is termed J_D, where the subscript D stands for deformation theory. It is assumed that

$$J_D = \frac{\eta A}{bB} \ , \tag{2.10}$$

where b is the current ligament size, η corresponds to b, and A is the area under the load-displacement curve corresponding to a ligament of constant size b. Thus, A is not $\int P d\Delta$, and an adjustment must be made to calculate J_D.

Ernst et al.[22] outlined a procedure, which can be derived by differentiating J_D to obtain

$$dJ_D = \left(\frac{\partial J_D}{\partial \Delta}\right)_a d\Delta + \left(\frac{\partial J_D}{\partial a}\right)_\Delta da \ . \tag{2.11}$$

Then by using Eq. (2.10),

$$dJ_D = \frac{\eta \left(\frac{\partial A}{\partial \Delta}\right)_a d\Delta}{bB} + \frac{1}{B}\left[\frac{\partial \eta}{\partial a}\frac{A}{b} + \frac{\eta A}{b^2} + \frac{\eta}{b}\frac{\partial A}{\partial a}\right]_\Delta da \ . \tag{2.12}$$

Substituting for A in terms of Eq. (2.10) and recognizing that

$$\frac{1}{B}\left(\frac{\partial A}{\partial a}\right)_{\Delta} = -J_D \ , \tag{2.13}$$

Eq. (2.12) becomes

$$dJ_D = \frac{\eta P d\Delta}{Bb} - J_D\left(\eta - 1 - \frac{b}{W}\frac{\eta'}{\eta}\right)\frac{da}{b} \ . \tag{2.14}$$

Writing

$$dJ_f = \frac{\eta P d\Delta}{bB} \ , \tag{2.15}$$

where J_f is termed the far-field value of J, and defining

$$\gamma = \left(\eta - 1 - \frac{b}{W}\frac{\eta'}{\eta}\right) \ , \tag{2.16}$$

Eq. (2.14) becomes

$$dJ_D = dJ_f - \gamma J_D \frac{da}{b} \ . \tag{2.17}$$

For the compact specimen, it has been shown[23,24] that η can be represented by

$$\eta = 2 + 0.522\left(\frac{b}{W}\right) \ , \tag{2.18}$$

so that by using Eq. (2.16),

$$\gamma = 1 + 0.522\left(1 + \frac{1}{\eta}\right)\left(\frac{b}{W}\right) \ . \tag{2.19}$$

Because γ turns out to be a slowly varying function of b/W, using the value of η near b/W = 0.45 as an approximation,[22]

$$\gamma = 1 + 0.76\left(\frac{b}{W}\right) \ . \tag{2.20}$$

Because of the occasional occurrence of size effects and negative slopes in J_D-based R curves, Ernst[25] subsequently suggested a modified J parameter, termed J_M, based on a suggestion of Rice, Drugan, and Sham,[26] that

$$\left(\frac{\partial J_p}{\partial a}\right)_{\Delta_p} = 0 \ . \tag{2.21}$$

Using this condition replaces the assumption of load-path independence with the observation that plastic work cannot be recovered from a specimen and that, at least for a rigid plastic specimen, a crack cannot extend in ductile tearing without an increase in the load-point displacement. Thus, replacing the total area A in the second term of Eq. (2.12) with A_e leads to

$$dJ_M = dJ_f - \gamma G \frac{da}{b} \ . \tag{2.22}$$

An equation for converting J_D values to J_M can be obtained by combining Eqs. (2.17) and (2.22) to give

$$dJ_M = dJ_D + \gamma (J_D - G) \frac{da}{b} \ , \tag{2.23}$$

so that

$$J_M = J_D + \int_o^a \gamma J_D \left(1 - \frac{G}{J_D}\right) \frac{da}{b} \ . \tag{2.24}$$

Comparing Eqs. (2.23) and (2.17) shows that when G becomes small relative to J_D, J_M approaches J_f, the far-field value of J with no correction for crack extension.

An alternate expression for J_M can be developed by separating J_M into elastic and plastic parts[27] and then differentiating to obtain

$$dJ_M = \left(\frac{\partial G}{\partial \Delta_e}\right)_a d\Delta_e + \left(\frac{\partial G}{\partial a}\right)_{\Delta_e} da + \left(\frac{\partial J_{M,p}}{\partial \Delta_p}\right)_a d\Delta_p + \left(\frac{\partial J_{M,p}}{\partial a}\right)_{\Delta_p} da \ . \tag{2.25}$$

Noting that, according to Eq. (2.21), the last term in Eq. (2.25) is zero[27] and that the first two terms are a total differential, Eq. (2.20)

becomes

$$dJ_M = dG + \left(\frac{\partial J_{M,p}}{\partial \Delta_p}\right)_a d\Delta_p \ . \tag{2.26}$$

Because

$$\left(\frac{\partial J_{M,p}}{\partial \Delta_p}\right)_a = \frac{\eta P}{bB} \ , \tag{2.27}$$

Eq. (2.26) becomes

$$dJ_M = dG + \frac{\eta P d\Delta_p}{bB} \ , \tag{2.28}$$

so that

$$J_M = G + \int_0^{\Delta_p} \frac{\eta P d\Delta_p}{bB} \ , \tag{2.29}$$

where G is calculated according to American Society for Testing and Materials (ASTM) E399, using the current values of load and crack length. Equation (2.29), recently proposed by Ernst,[28] should agree with Eq. (2.24) and appears to be a convenient expression for calculating J_M when the input is experimental data and values of J_D are not available or needed.

Using J_M as a resistance curve parameter reduces or eliminates size effects on the R curves and ensures non-negative R-curve slopes. However, this usage creates a consistency problem with respect to methods of calculating J for toughness specimens and flawed structures that needs to be evaluated.

The difference between J_M- and J_D-based R curves can be appreciable, at least in terms of slopes, as illustrated by Table 2.2 and Fig. 2.9 for the low-shelf-weld metal of ITV-8A.[29] These data provide a good example for illustrating the conversion of J_D to J_M values. A convenient rearrangement of Eq. (2.24) for calculational purposes is

$$J_M = J_D + \int_{\ln a_i}^{\ln a} \frac{\gamma J_D \left(1 - \frac{G}{J_D}\right)}{\left(\frac{b}{a}\right)} d \ln a \ . \tag{2.30}$$

Table 2.2. J_I-R data for specimen V8AJ2

Δa (mm)	E813 J_D (kJ/m²)	J_M (kJ/m²)
0.07	2	2
−0.04	5	5
−0.01	11	11
0.04	19	19
0.07	27	27
0.15	37	37
0.25	48	49
0.42	59	61
0.63	70	73
0.94	80	85
1.30	90	99
2.25	95	112
2.64	104	124
3.16	114	140
3.61	123	155
4.14	136	173
4.65	146	191
5.23	155	208
5.80	162	226
6.32	169	242
7.08	177	263
7.99	177	282
8.68	180	299
9.20	186	317
9.56	193	333
9.92	200	349
10.46	203	368
10.95	207	384

For specimen V8AJ2, W = 50.8 mm, and a_i = 31.37 mm. Approximate calculations can be made by using selected values from Table 2.2 and the trapezoidal rule for estimating areas. Using the values listed in Table 2.3 and the simplifying assumptions that $G/J_D \sim 0$ for $\Delta a > 1.30$ mm and $J_M \sim J_D$ for $\Delta a \leq 1.30$ mm, at $\Delta a = 10.95$ mm,

$$J_M \sim 207 + \frac{(205 + 389)}{2}(0.082) + \frac{(389 + 1190)}{2}(0.176)$$

$$= 207 + 163 = 370 \ \frac{kJ}{m^2} .$$

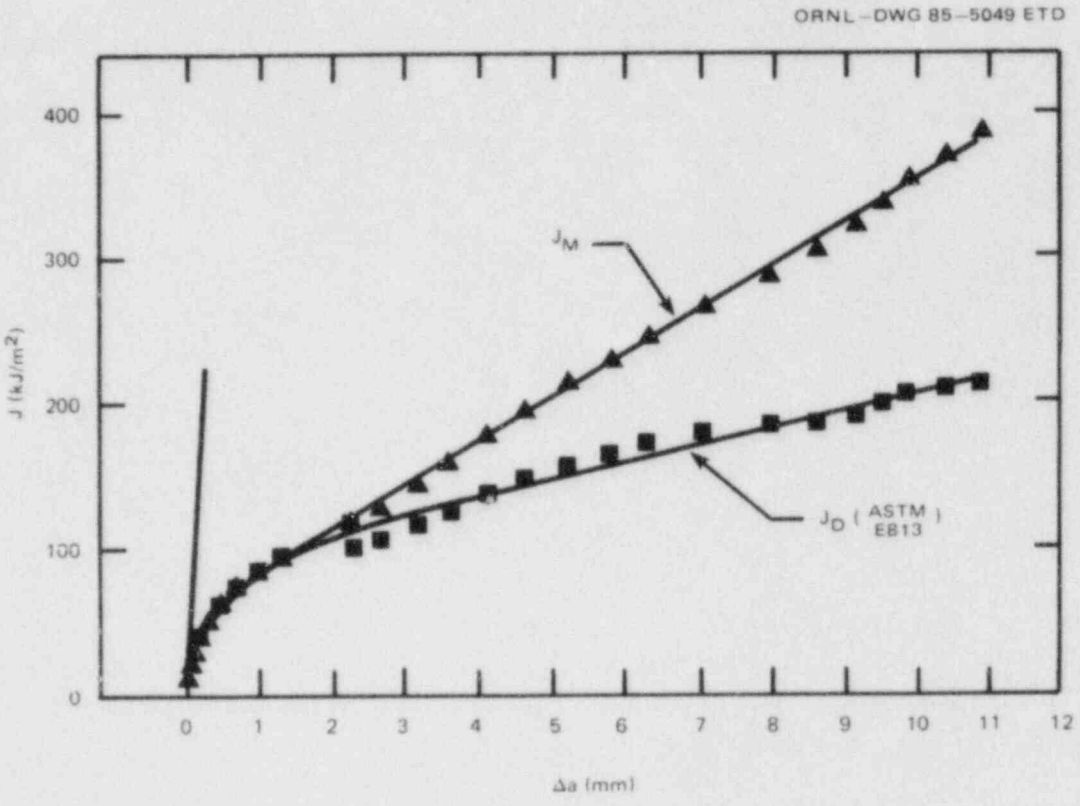

Fig. 2.9. J_I-R curves for specimen V8AJ2 at 149°C.

Table 2.3. Values used for approximate conversion of J_D to J_M values at Δa = 10.95 mm for specimen V8AJ2

Δa (mm)	a (mm)	b (mm)	$\frac{b}{W}$	γ	J_D (kJ/m²)	$\gamma J_D/(b/a)$ (kJ/m²)	Δ ln a
1.30	32.8	18.3	0.36	1.27	90	205	0.082
4.14	35.6	15.2	0.30	1.23	136	389	0.176
10.95	42.4	8.4	0.17	1.13	207	1190	

2.4 Elastodynamic and Viscoplastic-Dynamic Fracture-Mechanics Analyses*

M. F. Kanninen† J. H. Fitzgerald†
S. J. Hudak, Jr.† J W. Cardinal†
K. W. Reed† J. D. Achenbach‡
R. J. Dexter† C. H. Popelar§

2.4.1 Objectives and approach

The purpose of this research is to assist the Heavy-Section Steel Technology (HSST) Program in obtaining reliable procedures for the prediction of crack arrest at the high upper-shelf toughness conditions occurring in postulated pressurized thermal shock (PTS) events. This is being accomplished through research that combines elastodynamic and viscoplastic-dynamic finite-element analyses with material characterization testing, mathematical analyses, elastic-plastic tearing instability analyses, and small-scale fracture experimentation. The focal point of the work is the development of a versatile viscoplastic-dynamic finite-element analysis model. There are two reasons for requiring this level of complexity. First, unless the crack jump length is small, dynamic effects can significantly influence a run-arrest event. Second, rapid crack propagation induces rate-sensitive inelastic deformation that requires strain-rate effects to be taken into account. The basic research issue centers on the quantification of a kinetic crack-growth criterion for these conditions.[30]

The research being performed can be considered in four categories: (1) the development of a versatile viscoplastic-dynamic finite-element analysis model; (2) the development of test methods to obtain dynamic crack propagation/arrest data on high-toughness materials, using small-scale laboratory specimens; (3) asymptotic crack-tip and small-scale yielding analyses of steady-state, viscoplastic-dynamic crack propagation; and (4) elastic-plastic pipe fracture analyses. These activities are being carried out independently with the expectation of integrating the findings into the finite-element model later in this program. In addition to progress in these areas, some preliminary results obtained by applying the viscoplastic-dynamic finite-element model in a posttest analysis of a wide-plate test performed at the National Bureau of Standards (NBS) are also reported in the following sections.

---

*Work sponsored by the HSST Program under subcontract 37X-997306C between Martin Marietta Energy Systems, Inc., and the Southwest Research Institute.

†Engineering and Material Sciences Division, Southwest Research Institute, San Antonio, Texas.

‡Department of Civil Engineering, Northwest University, Evanston, Illinois.

§Engineering Mechanics Department, The Ohio State University, Columbus, Ohio.

2.4.2 Viscoplastic-dynamic finite-element analysis model

A versatile new finite-element model for the analysis of dynamically propagating cracks in viscoplastic materials has been developed. The program is designed for analyses of the compact specimen tests conducted in this research, the wide-plate experiments carried out at NBS, and, eventually, of a PTS event in a pressure vessel. The model is unique because it provides the means for both prediction and interpretation of crack run-arrest-reinitiation histories by using a variety of postulated crack-propagation, arrest, and reinitiation criteria in a variety of viscoplastic and internal-variable type materials. Its main purpose is that of a tool for researchers interested in determining appropriate fracture-related structural integrity assessment procedures.

The model is based on standard stiffness and consistent mass matrix formulations. A nonstandard feature is that the nodes along the crack path are held closed by a combination of artificial springs and masses. These are "released" sequentially by removal of the springs and masses as the crack progresses. As described in Ref. 30, the time-of-node release may be specified at the outset from experimental data (generation-phase analysis) or determined on the basis of a specified crack propagation criterion (application-phase analysis). To minimize spurious high-frequency "ringing" following a node release, the force on a node at the time of its release is removed gradually. The details of this procedure constitute a node-release algorithm.

In addition to the node-release algorithms, special techniques were developed for incorporation of the viscoplastic material model into the finite-element analysis. Because viscoplastic models have not found wide acceptance in engineering, no unifying principles seem to exist among the numerical methods that have been devised to treat them. Two general approaches have been employed in the past. The first and most direct is called the "initial-load" method; the second approach encompasses a variety of "forward-gradient" methods. The principal drawback of the initial-load method is that it is only conditionally stable. Thus, for many realistic materials, unreasonably small time-step limits must be employed. The forward-gradient schemes were devised to overcome these time-step restrictions. They accomplish this, however, only at the expense of reforming and refactoring the global stiffness matrix at each time step (a computation that is not necessary in the initial-load method) and with a loss of accuracy in the transient stress regime.

It has been found that "small" problems (fewer than 1000 degrees of freedom) are most efficiently solved by using the forward-gradient method. For larger problems the time-step restrictions tend to be less critical than the cost of continually refactoring the global matrix. Because the analyses for which the present program was designed typically fall into the "large" problem category, an initial-load approach is called for. However, the Bodner-Partom viscoplastic model used in this work[31] exhibits such extremely short relaxation times that even this optimal approach is impractical, even on a supercomputer. Thus, a new semiexplicit initial-load method for integration of the viscoplastic constitutive equations was developed. The new technique captures the principal advantage (stability) of the forward-gradient method while retaining the efficiency and directness of the initial-load method. This new

method is unconditionally stable for the isotropic-hardening Bodner-Partom model used in this project, although the accuracy of the method depends on the strain-increment size (as with all unconditionally stable methods). Using this algorithm, viscoplastic-dynamic crack-propagation analyses can be performed for the problems intended with only slightly greater effort than elastodynamic analyses.

Other measures taken to improve the efficiency of the code for large problems include the ability to use different constitutive behavior in different parts of the model (i.e., eliminating stress and viscoplastic calculations where they are not needed) and the ability to use reduced integration in the calculation of the viscoplastic initial-load term. It is anticipated that a lumped-mass capability will be added to the code to enable significantly finer meshes to be used in future analyses. Because the run-arrest-reinitiate sequence is controlled by logical variables within the program, a crack may arrest and reinitiate an indefinite number of times. This feature can be used in both generation- and application-phase analyses. Finally, a special model for uneven crack fronts (e.g., tunneling) has been implemented.

2.4.3 Dynamic crack propagation/arrest testing

The objective here is to provide data on the dynamic fracture toughness of A 533 grade B class 1 steel as a function of crack velocity V and temperature T, using small specimens. The specific objectives are to determine the limitations of small compact specimens for measuring $K_{ID}(V,T)$ and to provide a basis for evaluation of viscoplastic-dynamic crack-propagation criteria, using generation-phase analyses. The unique feature of the approach is the use of a compliant loading system that maximizes the stored elastic energy in the system. Consequently, greater amounts of energy can be recovered than is possible with the conventional split-pin loading used in the proposed ASTM standard crack-arrest test. However, this approach requires that specimen boundary conditions and the crack velocity be measured dynamically. Much of the effort thus far has been put into the development and verification of techniques to make these measurements on high-toughness materials.

Specimen boundary conditions are being characterized in terms of the specimen load-line displacement. This quantity is measured dynamically during the crack-propagation event by using an eddy-current technique. The dynamic calibration of this transducer by using a Hopkinson-type experiment was described previously.[32] The calibration was conducted using a stationary transducer and a moving target. However, during dynamic crack-propagation testing, it is convenient to attach the transducer to one specimen arm and use the opposite arm as the target. Under these conditions the transducer experiences accelerations that could affect the transducer output.

A series of tests examined this potential problem by obtaining measurements during dynamic crack propagation on a high-strength steel. The specimen was instrumented with a single moving transducer, as well as with two stationary transducers. The experimental set-up for these experiments, along with a comparison of the measured results, is shown in

Fig. 2.10. The output from the moving transducer exhibits three resolvable characteristic frequencies: 0.5, 2.6, and 30 kHz. The two lower-frequency oscillations are also present in the summed output from the two stationary transducers; the high-frequency oscillations, however, appear to be absent from these measurements.

The high-frequency oscillations are believed to be due to Rayleigh surface waves that propagate along the specimen notch. Because the moving transducer is located along the notch, the transducer captures these oscillations. It might be expected that the stationary transducers, being both remote from the crack tip and unattached from the specimen, should exhibit few or none of these high-frequency Rayleigh waves. Apart from these explainable differences, the two curves in Fig. 2.10 show very similar responses. Both curves are in phase, and the maximum deviation in amplitude is about 7% while the average deviation is even less. Thus, the eddy-current gage is free from inertia effects during dynamic crack-propagation testing and can, therefore, be relied on in this research.

The development of a gage to monitor dynamic crack propagation in tough materials has been a two-step process. First, commercially available gages were adapted to dynamic crack measurements. Then, when it became clear that these would be inadequate, the development of a new gage was undertaken. Dynamic fracture experiments on both 4340 and A 533 grade B steel were used throughout both of these endeavors.

Two commercially available gages — a KRAK gage, based on an indirect electrical potential drop technique, and a Micro-Measurements ladder gage — were found to perform adequately in tests of smooth-sided 4340

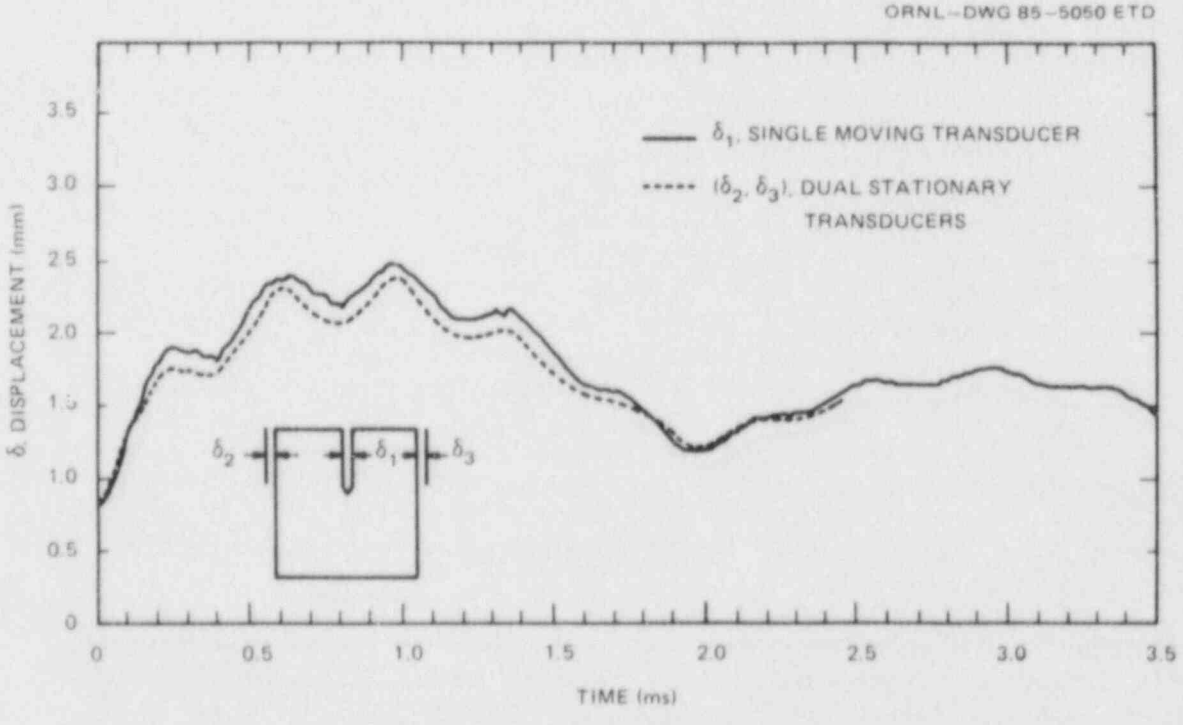

Fig. 2.10. Dynamic response of a compliant loaded specimen measured with both moving and stationary eddy current transducer.

steel. However, debonding between the conductive foil and the insulative backing was occasionally found to cause electrical shorting in the former gage. Preliminary tests on A 533 grade B steel demonstrated the need to employ side-grooved specimens to control crack branching. Both of the commercial gages exhibited debonding problems between the insulative backings and the specimen when they were applied within the side grooves.

Because the major problem with the commercial gages appeared to be the excessive thickness, and, thus, stiffness, of the backing, it was decided to develop a gage having a thinner backing. The preferred approach was to apply a thin coating of varnish or epoxy directly on the specimen, then apply a conductive grid to produce a ladder-type gage. Both a photographic technique and a silk-screen technique of producing the gage were explored. The photographic technique was eventually abandoned due to incompatibility between the photographic emulsion and conductive paint. The silk-screening technique worked well on smooth-sided specimens where it could be applied directly to the specimen. However, this direct technique could not be used within side grooves.

An indirect method of applying the silk-screen gage within side grooves was developed next and consisted of first applying a coating of epoxy insulation, followed by the silk-screen gage, to a release paper. Subsequently, the insulation and silk-screen gage were peeled from the release paper and applied to the specimen, using a second coating of epoxy for adhesion. Dynamic crack-propagation experiments on smooth-sided 4340 steel specimens were used to demonstrate that measurements with the newly developed gage were equivalent to those from the indirect electrical potential KRAK gage. Subsequent experiments on side-grooved specimens of A 533 grade B steel were performed to further verify the gage performance.

Table 2.4 provides a summary of the experiments on A 533 grade B steel. The initial experiments established the advantage of using electrodischarge-machined (EDM) notches instead of conventionally machined (CM) notches. These experiments also demonstrated the need for specimen side grooving to control crack branching and to increase constraint. As indicated in Table 2.4, the use of EDM notches in Hardex N weld-embrittled material was successful in producing dynamic crack propagation and arrest at −50°C in both 100- and 200-mm compact specimens. Unfortunately, triggering problems precluded data acquisition in these experiments. In Experiment 3 premature triggering occurred when the local deformation near the starter notch broke the triggering strand of the silk-screen gage before the crack-propagation event. This problem was circumvented by moving the triggering strand farther from the starter notch. In Experiment 5 premature triggering that again occurred was believed to be caused by premature cracking of the epoxy insulation under the triggering strand. A more ductile insulating coating is now being used for these low-temperature experiments.

The fact that dynamic propagation could not be achieved at 25°C in this plate of A 533 grade B steel is believed to be due to the exhibition of multiple cracking upon loading in the weld-embrittled material at the starter notch. Consequently, a very diffuse region of cracking was introduced into the tough test material, which resulted in slow, stable tearing rather than rapid, unstable crack propagation. It is anticipated that this can be overcome by the proper selection of an alternative

Table 2.4. Summary of exploratory dynamic-fracture experiments on A 533 grade B steel

Experiment No.	W (mm)	B (mm)	B_N/B	T (°C)	Notch diameter (mm)	Notch condition[a]	Result
1	100	25	1.0	−50	1.0	CM	No growth, plastic deformation
2	100	25	1.0	−50	1.0	EDM	Growth, excessive branching
3	100	25	0.75	−50	0.3	EDM/WE	Growth, arrest
4	200	75	0.75	25	0.3	EDM/WE	Limited tearing, plastic deformation
5	200	75	0.75	−50	0.3	EDM/WE	Growth, arrest

[a]CM = Conventionally machined
EDM = Electro-discharge machined
WE = Weld-embrittled starter notch

starter notch that enables more energy to be stored in the system prior to initiation. Thus, it is anticipated that the compliant loaded compact specimen has the potential to generate data at considerably higher temperatures in this material than demonstrated by this experiment.

2.4.4 Crack-tip fields in a Bodner-Partom solid

The fields of stress and deformation at a crack tip generally exhibit singular behavior no matter which constitutive model is used. Because the fracture behavior is controlled by the near-tip fields, it is important to explicitly determine these fields for use in finite-element analyses. The near-tip fields for a crack in a Bodner-Partom solid are more intricate than for most classical rate-independent solids and certainly more intricate than for a linear-elastic solid. These fields have been investigated for isothermal, as well as for variable temperature conditions. The dependence of material properties on temperature and the production of heat by plastic deformation and crack propagation have been taken into account in the formulation.

In the Bodner-Partom model the plastic-strain rate is given by

$$\dot{\varepsilon}^p_{ij} = D_o \exp\left[-(Z^2/3J_2)^n/2\right] s_{ij}/(J_2)^{1/2} , \qquad (2.31)$$

where D_o and n are material constants, Z is a hardening parameter, s_{ij} is the stress deviator, and $J_2 = 1/2\, s_{ij}s_{ij}$. It can be seen that $\dot{\varepsilon}^p_{ij}$ is always bounded. Even if s_{ij} is singular (which is the case), the singularity of s_{ij} as $r \to 0$ will be canceled by the singularity of $(J_2)^{1/2}$ in

the terms $s_{ij}/(J_2)^{1/2}$. The term $\exp[-(Z^2/3J_2)^n/2]$ is bounded whether or not J_2 is singular. Thus, Eq. (2.31) implies that the plastic-strain rate is bounded.

As reported earlier, as a consequence of the boundedness of the plastic-strain rate, the stress and the total strain are square-root singular for the Bodner-Partom model. For example, for Mode-I

$$\sigma_{yy} = \frac{K(t)}{(2\pi r)^{1/2}} f(\theta) + \text{higher-order terms} . \qquad (2.32)$$

Here, $f(\theta)$ has the same form as for linear-elastic behavior. The general form of Eq. (2.32) is valid for a stationary, as well as for a propagating, crack and for the quasi-static, as well as the dynamic, case. Two points are of interest: the dependence of K(t) on time and the importance of the higher-order terms. To obtain some insight, a calculation has been carried out for a quasi-static case and a stationary crack tip. The factor K(t), as well as the stress very close to the crack tip at position $x = \Delta x$, was computed. The results, as expected, show that both K(t) and $\sigma_{yy}(t)(2\pi\Delta x)^{1/2}$ decrease with time as viscoplastic flow develops (shown in Fig. 2.11). A substantial difference develops with time

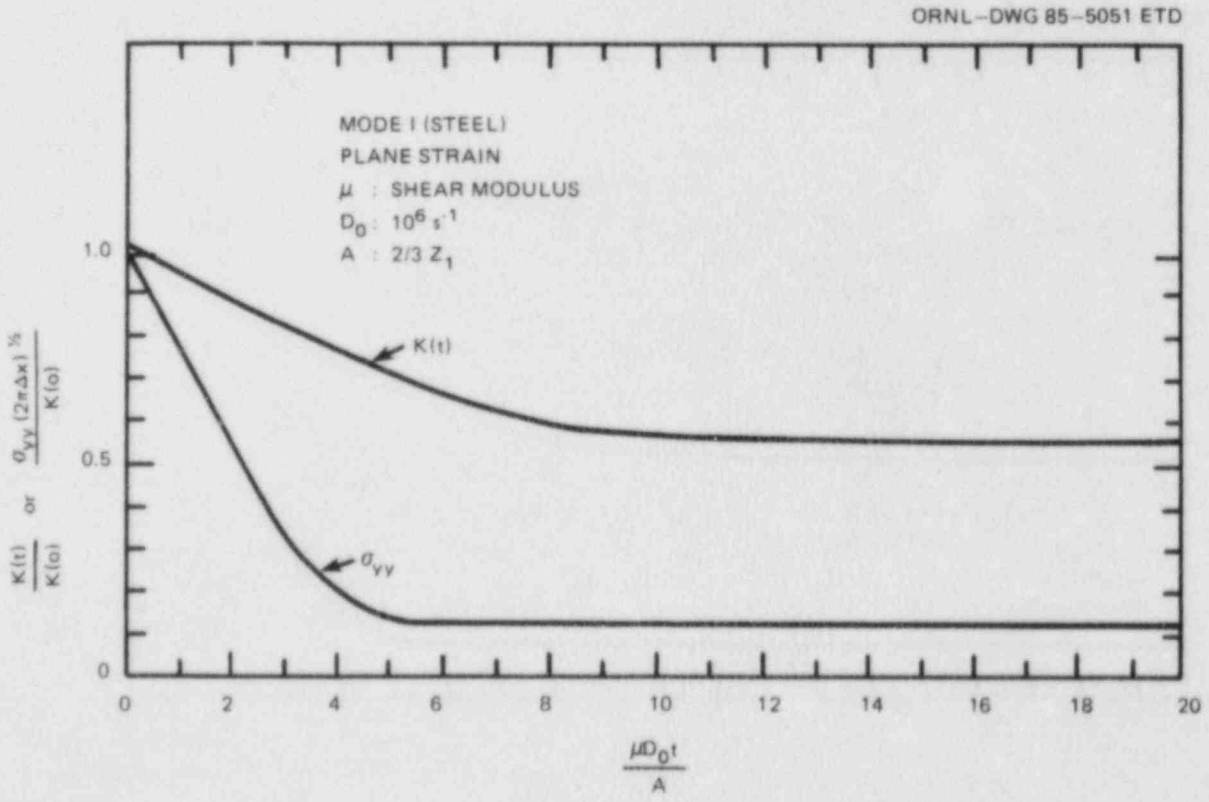

Fig. 2.11. Time-dependent decrease of the stress-intensity factor K(t) and near-tip stress σ_{YY} as viscoplastic flow develops.

between the two quantities, apparently due to the higher-order terms in Eq. (2.32). The analysis of the second-order terms is in progress and will be reported later.

The Bodner-Partom model accounts for the temperature dependence of the material properties principally through the dependence of the factor n and the parameter Z_0 on temperature. For A 533 grade B steel suitable relations have been determined in previous work,[32] as follows when the temperature is expressed in degrees kelvin:

$$
\begin{aligned}
Z_0 &= \frac{2.44 \times 10^4}{T} + 1084 \ (\text{MPa}) \ , \\
n &= \frac{175}{T} + 1.35 \ , \\
Z_1 &= 1550 \ (\text{MPa}) \ , \\
Z &= Z_1 + (Z_0 - Z_1) \exp(-mWp) \ (\text{MPa}) \ , \\
m &= 0.061 \ (1/\text{MPa}) \ , \\
Wp &= \int_0^t s_{ij} \dot{\varepsilon}^p_{ij} \, dt \ .
\end{aligned}
\tag{2.33}
$$

Figures 2.12–2.14 show plastic-strain rates vs σ/Z for uniaxial tension and different values of the temperature-dependent parameter n. Up to a "crossover" value of σ/Z, a higher temperature gives a higher strain rate. Beyond the crossover value the opposite (physically unrealistic) behavior (i.e., lower strain rate at higher temperature) occurs. Consequently, the crossover value is considered to be an artifice of the model.

In most problems, the stresses should remain well below the crossover value, and the artifice can be ignored. However, near the crack tip the stresses become very high, and the model must be adjusted to give physically realistic results. Because the dependence on temperature is weak at high stresses and no accurate experimental information is available in this regime, it is recommended to use the curve for a single value of n (e.g., n = 3.96) for all temperatures when σ/Z is beyond the crossover value. As a consequence of the weak dependence of $\dot{\varepsilon}^p$ on T, the stress-intensity factor will be almost independent of the crack-tip temperature. For example, the result for K(t) shown in Fig. 2.11 is valid at all temperatures. Other quantities near the crack tip may depend on temperature. This point is under further investigation.

The temperature of the material affects its properties. Thus, different externally imposed temperatures will give rise to different rates

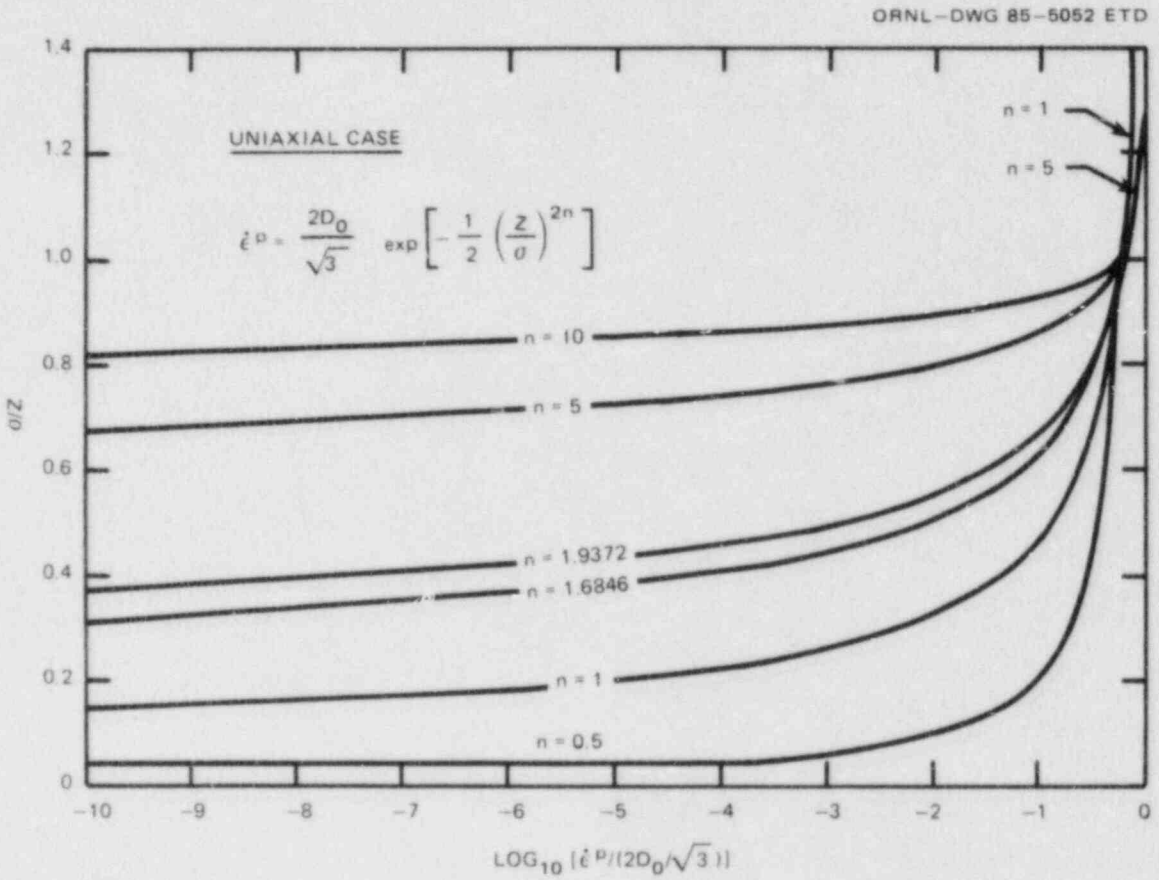

Fig. 2.12. Plastic-strain rates for uniaxial tension given by Bodner-Partom model.

of plastic flow (except right at the crack tip). The question remains whether heat production by plastic work or by rupture phenomena near the crack tip is significant. To start, consider the temperature distribution in a 2-D geometry, governed by

$$k\nabla^2 T - \rho c \frac{\partial T}{\partial t} = -\{W_p + (F - 2\gamma\dot{a})\delta[x_1 - a(t)]\} , \qquad (2.34)$$

where $T(x_1, x_2)$ = temperature, k = thermal conductivity, ρ = density, c = specific heat, $\dot{W}_p$ = rate of dissipation of mechanical energy per unit volume, F = flux of energy into the crack tip, λ = specific surface energy, and a(t) = position of crack tip. Note that $\dot{W}_p(x, y, t)$ is a distributed quantity, while the difference between the flux of energy into the crack tip minus the rate of surface energy ($2\gamma\dot{a}$) acts as a propagating concentrated heat source. Heat production by coupled thermoelastic effects has been neglected.

Consider the heat production terms in Eq. (2.34) in more detail. The dissipation rate of mechanical energy is the rate of plastic work,

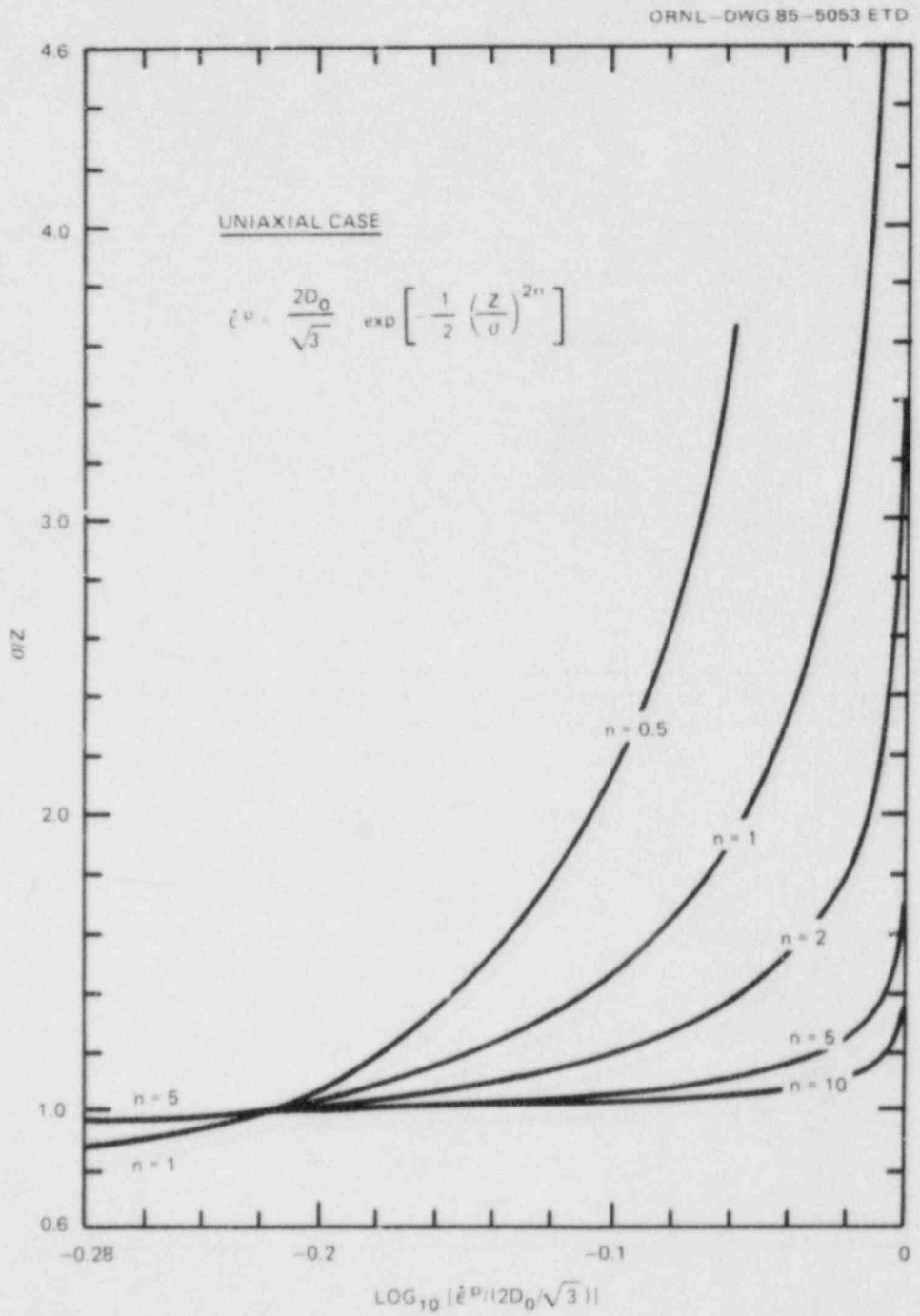

Fig. 2.13. Plastic-strain rates for uniaxial tension given by Bodner-Partom model.

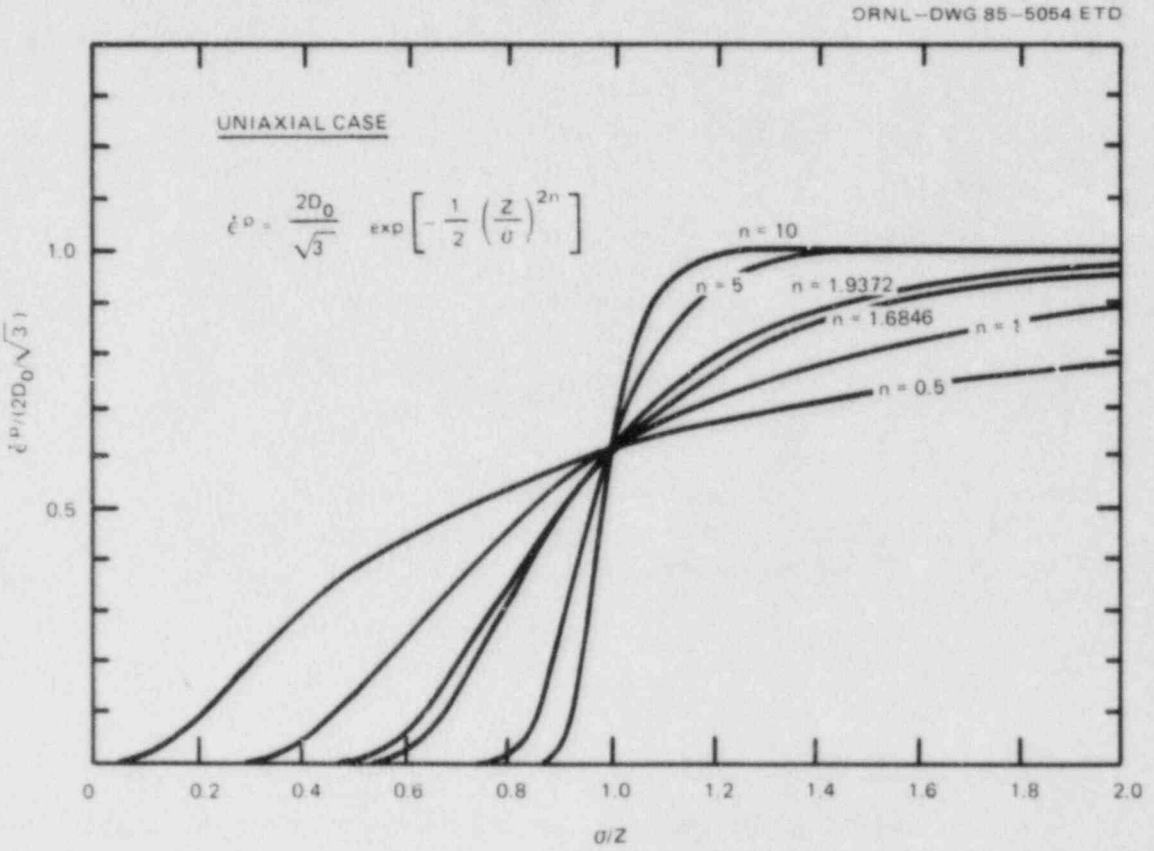

Fig. 2.14. Plastic-strain rates for uniaxial tension given by Bodner-Parton model.

which may be expressed as

$$\dot{W}_p = \sigma_{ij}\dot{\varepsilon}_{ij}^{(p)} \quad , \tag{2.35}$$

where σ_{ij} and $\dot{\varepsilon}_{ij}^{(p)}$ are the components of stress and plastic-strain rate, respectively. To determine the flux of energy into the crack tip, consider that the singular behavior at the crack tip is of the square-root type (as it is for the Bodner-Partom model). For the Mode-I case,

$$F = -\frac{\dot{a}^3(1-\alpha^2)^{1/2}\,[K_I(t,\dot{a})]^2}{2\mu_T^2 D(\alpha,\beta)} \quad , \tag{2.36}$$

where

$$\alpha = \dot{a}/c_L \quad , \quad c_L = [(\gamma + 2\mu)/\rho]^{1/2} \quad , \tag{2.37}$$

$$\beta = \dot{a}/c_T \ , \quad c_T = (\mu/\rho)^{1/2} \ , \tag{2.38}$$

$$D(\alpha, \beta) = (\beta^2 - 2)^2 - 4(1 - \alpha^2)^{1/2} (1 - \beta^2)^{1/2} \ , \tag{2.39}$$

and K_I $(t, \dot{a})$ is the dynamic stress-intensity factor. Equation (2.36) simplifies at small values of $\dot{a}$ when the material inertia may be neglected. Finally, linear momentum can be expressed as

$$(\lambda + \mu)\nabla\nabla \cdot \underset{\sim}{u} + \mu\nabla^2\underset{\sim}{u} - 2\ddot{\mu}\nabla \cdot \overset{\cdot p}{\underset{\sim}{\varepsilon}} - \alpha(3\lambda + 2\mu)\nabla T = \rho\ddot{\underset{\sim}{u}} = 0 \ , \tag{2.40}$$

where α is the coefficient of linear thermal expansion.

It can now be shown that for a propagating crack the δ-function terms in Eq. (2.34) will dominate and give rise to a singular crack-tip temperature of the form

$$T \neq \dot{a} \ \ell n \ r \ . \tag{2.41}$$

For a stationary crack ($\dot{a} \equiv 0$), the crack-tip temperature becomes bounded. For both cases the displacements, stresses, and particle velocities have the same singular behavior as for the purely linear-elastic case; i.e:

$$u_i \neq r^{1/2} \ , \quad \dot{u}_i \neq r^{-1/2} \ , \quad \sigma_{ij} \neq r^{-1/2} \tag{2.42}$$

for the dynamic case and

$$u_i \neq r^{1/2} \ , \quad \dot{u}_i \neq r^{-1/2} \ , \quad \sigma_{ij} \neq r^{-1/2} \tag{2.43}$$

for the stationary case.

2.4.5 Small-scale yielding crack growth in a viscoplastic medium

Freund and Hutchinson[33] recently performed a small-scale yielding analysis of steady-state rapid crack propagation in a rate-dependent material. They were able to relate the global (i.e., far-field) dynamic energy release rate G to the local crack-tip value G_{tip}. While G is more readily calculated, it is G_{tip} that is thought to govern the growth of the crack. Thus, it is clearly advantageous to develop a quantitative relation between these two quantities. The objective of this phase of this research is to extend the work of Freund and Hutchinson to the Bodner-Partom model.[31]

The material model used by Freund and Hutchinson requires a yield criterion. Moreover, the plastic-strain rate in their analysis depends upon nonlinear viscous behavior. As a consequence, the strain rate becomes unbounded with the stress. In contrast, a yield criterion is unnecessary in the Bodner-Partom model, and, in addition, the plastic-strain rate is always bounded. Therefore, there are sufficient differences between the two material models to warrant extending the Freund-Hutchinson analysis to the Bodner-Partom model.

A key development in this analysis is the relation

$$G_{tip} = (1 - m)\, G_S - \frac{6\sqrt{3}}{n}\, 2^{3/2n}\, \Gamma\left(\frac{3}{2n}\right) D_o\, \frac{\mu\sqrt{\mu\rho}}{Z^3}\, D(m)\, G_{tip}^2 , \qquad (2.44)$$

where G_S is the remote static energy release rate. In Eq. (2.44), $\Gamma(x)$ is the gamma function, μ is the shear modulus, ρ is the mass density, while D_o, Z, and n are parameters in the Bodner-Partom model. The function $D(m)$ depends upon the crack Mach number $m = V/C_R$, where C_R is the Rayleigh wave speed. This function is tabulated in Freund and Hutchinson.[33]

If crack propagation is postulated to be governed by a critical value of G_{tip} (i.e., $G_{tip} = G_{tip}^c$), it then follows from Eq. (2.44) that

$$\frac{G_S}{G_{tip}^c} = 1 + D(m)\, P_c , \qquad (2.45)$$

where

$$P_c = \frac{6\sqrt{3}}{n}\, 2^{3/2n}\, \Gamma\left(\frac{3}{2n}\right) \frac{D_o \mu\sqrt{\mu\rho}}{Z^3}\, G_{tip}^c . \qquad (2.46)$$

It can be seen that P_c depends only upon material parameters. Plots of G_S/G_{tip}^c vs crack speed for representative values of P_c are in Fig. 2.15. In this figure, G_{tip}^c is assumed to be independent of crack speed. For A 533 grade B steel P_c varies from about 20 to 40 over the temperature range from −100 to 250°C for values of the material parameters reported in Table 2.5.

In the development that led to Eq. (2.46), it was necessary to neglect hardening to obtain a closed-form solution. For A 533 grade B steel there is only about a 25% difference between the material parameters Z_0 and Z_1 that define, respectively, the lower and upper limits of the hardening. While this simplification seems justified, bounding calculations are nevertheless useful. In this spirit, it is clear from Fig. 2.15 that there exists a minimum value of G_S required to produce steady-state crack growth. Let G_S^* denote this value. Further assume that G_S^* can be identified with K_{Ia}. To establish the value of G_{tip}^c for

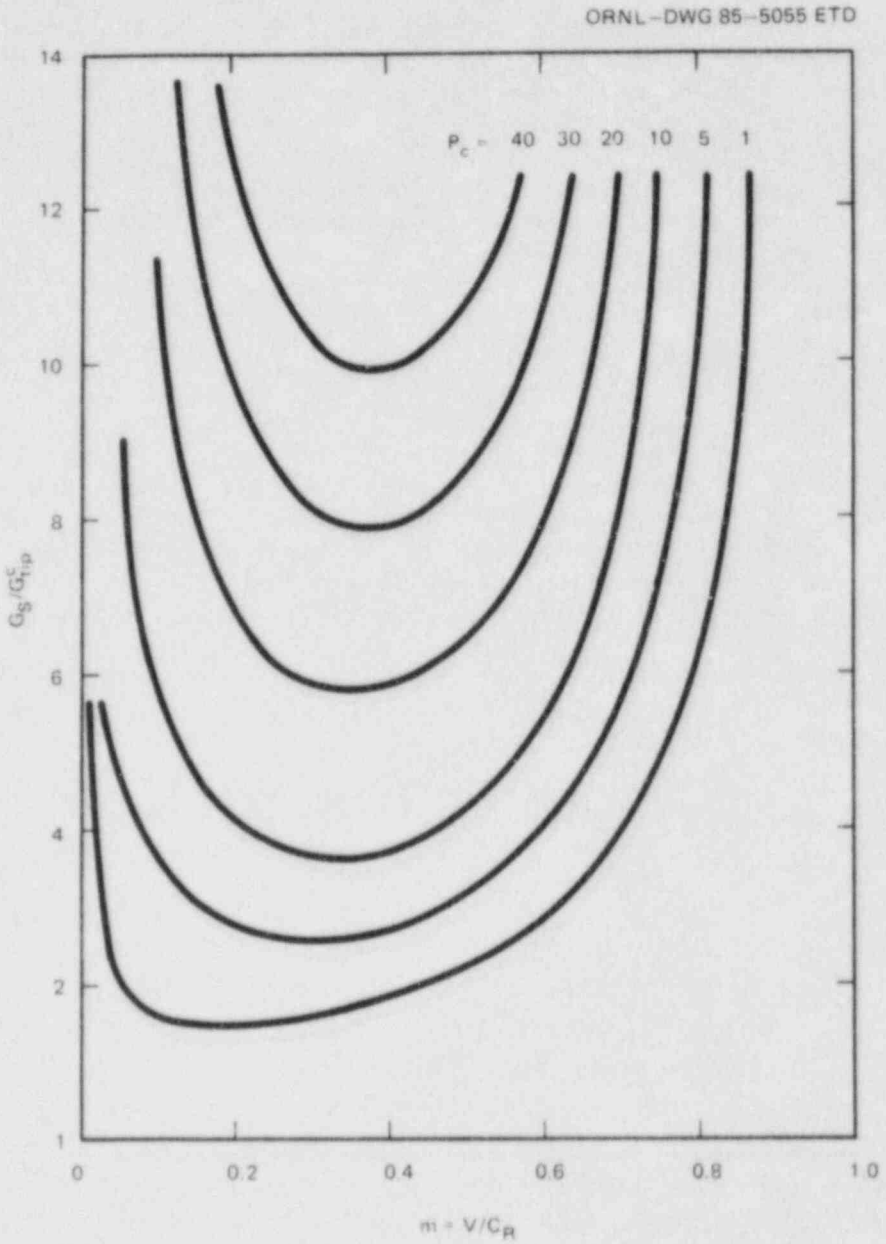

Fig. 2.15. G_S/G^c_{tip} vs m for representative values of P_c.

A 533 grade B steel, assume that $G^*_S = 19.6 \times 10^{-3}$ MPa·$\sqrt{m}$. This corresponds to K_{Ia} = 66.8 MPa·$\sqrt{m}$ at RT_{NDT} = −23°C. The resulting value of G^c_{tip} is 2.97×10^{-3} MPa·$\sqrt{m}$ or, equivalently, K^c_{tip} = 26.0 MPa·$\sqrt{m}$.

In establishing G^c_{tip}, G^*_S was associated with K_{Ia} at a particular temperature. Because this temperature is arbitrary, the calculation should also reflect the dependence of K_{Ia} on temperature. Clearly, the observed temperature dependence of K_{Ia} for A 533 grade B steel is much greater than that obtained from Eq. (2.45) and Fig. 2.16. It follows that

Table 2.5. Bodner-Partom model parameters for A 533 grade B steel

Temperature (°C)	n	Z_0 (MPa)	Z_1 (MPa)	m (MPa^{-1})	D_o (s^{-1})
−60	2.20	1200	1550	0.061	10^6
−10	2.00	1170	1550	0.061	10^6
50	1.90	1160	1550	0.061	10^6
100	1.77	1150	1550	0.061	10^6
175	1.75	1140	1550	0.061	10^6

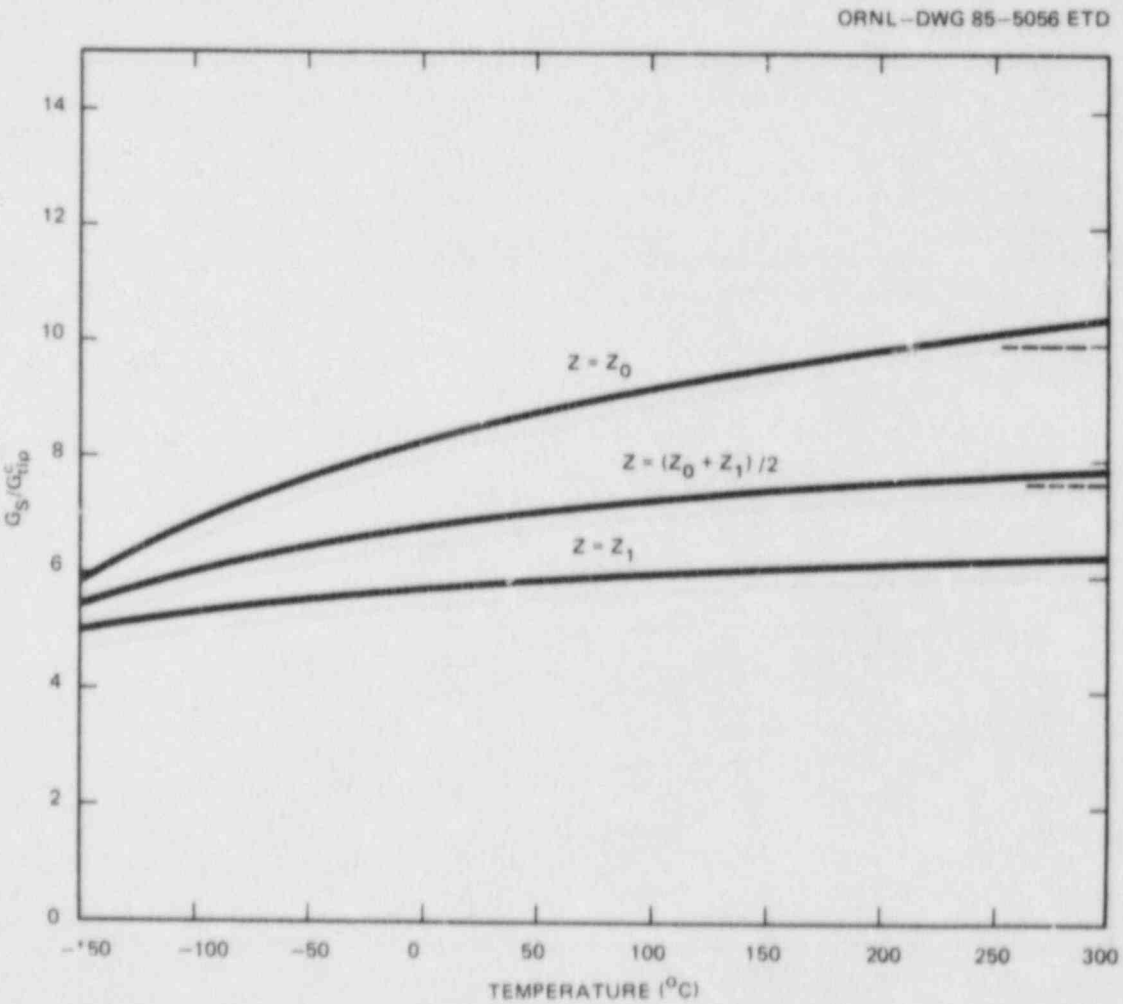

Fig. 2.16. Minimum static driving force required to drive a crack in A 533 grade B steel as a function of temperature.

the ductile-brittle transition cannot be explained solely on the basis of viscoplastic constitutive behavior, a fact to be expected because the constitutive relation does not incorporate the change in mode from cleavage to ductile fracture. Within the confines of the present model, the rapid increase in fracture toughness observed as the ductile-brittle temperature is approached can only be accommodated with an increase of G^c_{tip} with temperature.

Values of the material parameters in the Bodner-Partom viscoplasticity model are given in Table 2.5 for A 533 grade B steel. In establishing values for these parameters, it has become commonplace to select D_o to be several orders of magnitude greater than the anticipated maximum plastic-strain rate. When the stress field is everywhere nonsingular, experience has shown that predictions are relatively insensitive to the precise value of D_o that is chosen. However, this is not the case for fracture problems. For example, the small-scale yielding solution depends strongly on D_o. The stress singularity of the crack tip produces plastic-strain rates there that equal D_o. Thus, a more rational basis for selecting D_o is required.

Presently, no precise measurement exists of the limiting plastic-strain rate that a material can support. This value is apparently limited by the maximum mobile dislocation density that can be generated. Based on estimates of this density, the value of D_o is on the order of 10^8 s^{-1}. Therefore, this value would seem more realistic for fracture problems. In particular, changing the value of D_o results in a change of the parameter n and none of the other parameters in the Bodner-Partom model. The modest dependence of n on D_o for A 533 grade B steel is depicted in Table 2.6.

Table 2.6. Dependence of the parameter n on D_o in the Bodner-Partom model for A 533 grade B steel

Temperature (°C)	n		
	$D_o = 10^4$ (s^{-1})	$D_o = 10^6$ (s^{-1})	$D_o = 10^8$ (s^{-1})
−60	2.02	2.20	2.34
−10	1.83	2.00	2.13
50	1.74	1.90	2.02
100	1.62	1.77	1.88
175	1.60	1.75	1.86

2.4.6 Fracture of welded pipes

In support of the Committee on Safety in Nuclear Installations (CSNI)/Nuclear Regulatory Commission (NRC) Workshop on Ductile Piping

Fracture Mechanics,[34] detailed elastic-plastic, finite-element fracture-mechanics analyses were conducted on a 40.6-mm-diam Type 304 stainless steel pipe containing a circumferential through-wall crack located in a girth weld. Calculations were performed to analyze the welded pipe treated as (1) a monolithic pipe entirely composed of the base metal and (2) a composite of base metal and weldment. In the latter, each constituent was assigned distinct mechanical and fracture properties. In both solutions applied J-values were calculated for a fixed axial load combined with a monotonically increasing applied bending moment.

Material J-resistance curves appropriate for the two problems were used to initiate and grow the initial crack in a stable manner until fracture instability occurred under load control. The analyses were performed using a modified version of ADINA capable of calculating elastic-plastic energy release rates. Implementation of the energy release-rate calculations into the ADINA code generally followed the virtual crack-extension methodology originally introduced by Parks.[35] An analytical expression for the energy release rate more suitable for numerical analysis of general three-dimensional (3-D) crack configurations, subsequently derived by deLorenzi,[36] was used in the SwRI version of the ADINA code.

Table 2.7 shows that the extent of stable crack growth and the applied loads at fracture instability were distinctly different in the two analyses. Specifically, the monolithic pipe model was found to withstand an applied J-value three times that of the composite pipe model prior to reaching instability. The extent of stable crack growth at fracture instability was calculated to be 7.62 mm for the monolithic pipe model but only 2.54 mm for the composite pipe model. These results must be interpreted in light of the fact that the finite-element mesh spacing ahead of the crack was only 2.54 mm. A model containing a finer mesh

Table 2.7. Summary of elastic-plastic finite-element fracture analysis results for the CSNI/NRC workshop problem

	Monolithic pipe model	Composite pipe model
Initiation moment, kN-m	227	178
Rotation[a] at initiation, deg	0.46	0.26
Amount of stable crack growth, mm	7.62	2.54
Instability moment, kN-m	286	227
Rotation[a] at instability, deg	1.02	0.41
Instability J, kJ/m^2	2065	654

[a]Pipe rotation was calculated using the length of the finite-element model (2.03 m).

ahead of the crack tip, as is planned for subsequent work, would provide a more precise calculation for the amount of stable crack extension and would also refine the instability load prediction. Nevertheless, these results clearly indicate the importance of considering the weldment as a distinct entity.

In the analysis of crack growth in the weldment of a pipe or a fracture specimen, precise numerical computations of the J-integral usually necessitate using not only the stresses and deformations of the weldment, but also those of the base metal. This raises concern about the validity of the computed J-values. However, by exploiting the path independence of J for a contour lying wholly within the weldment and noting that J vanishes for any closed path contained entirely within either the weldment or the base metal, it can be shown that the J-integral is path independent for weldment cracks that are parallel to the weld line. This independence allows the virtual crack extension method to be used in elastic-plastic finite-element analyses of fracture instability in welded pipes. Subsequent work will exploit this result.

2.4.7 Preliminary viscoplastic-dynamic analysis of WP-1.3

A preliminary generation-phase analysis was made of the NBS wide-plate test WP-1.3. The specimen, pull plate, and tabs were modeled using 240 eight-noded, isoparametric, plane-stress elements. The thickness of each section was adjusted as reported previously. In this analysis, the first three rows of elements along the crack path were viscoplastic, using the previously calibrated Bodner-Partom model. The next four rows were linear elastic with stresses retained at all times during the computation. This particular partitioning of elements into viscoplastic and elastic is based on quantitative examination of elastodynamic results. The present results verify the complete adequacy of this partitioning.

Gaussian quadratures (3 × 3) were used on all of the elements in the specimen. The remaining elements were elastic with stresses not retained during the computation. The analysis used conventional stiffness and consistent mass matrices coupled with Runge-Kutta fourth-order time integration (except for the quasi-static solution, for which Euler integration was used). The time-steps for the dynamic integration were 2 μs. The initial conditions were taken as given by the linear-elastic solution. Boundary conditions were fixed-grip. The crack-length history data are identical to those used at ORNL in the third and "best" generation-phase analysis. The CPU time on SwRI's VAX 11/780 (no floating-point accelerator) for the dynamic-viscoplastic calculation was 6.5 h.

The results of the analysis indicate first and foremost that significant viscoplasticity is confined to a small zone around the running crack tip. In fact, the mesh used in this analysis (1500+ degrees of freedom) is too coarse to resolve crack-tip plasticity. Also, with the fixed-grip condition, the loads decrease during the propagation of the crack, and no extended plastic zone appears in the ligament. As compared with an elastic analysis for the same mesh, the crack-opening displacements for the viscoplastic analysis are approximately an order of magnitude smaller. More significantly, the crack profile in the latter treatment is essentially straight, which is intuitively correct because it is in agreement with other inelastic analyses. The comparison is shown in Fig. 2.17.

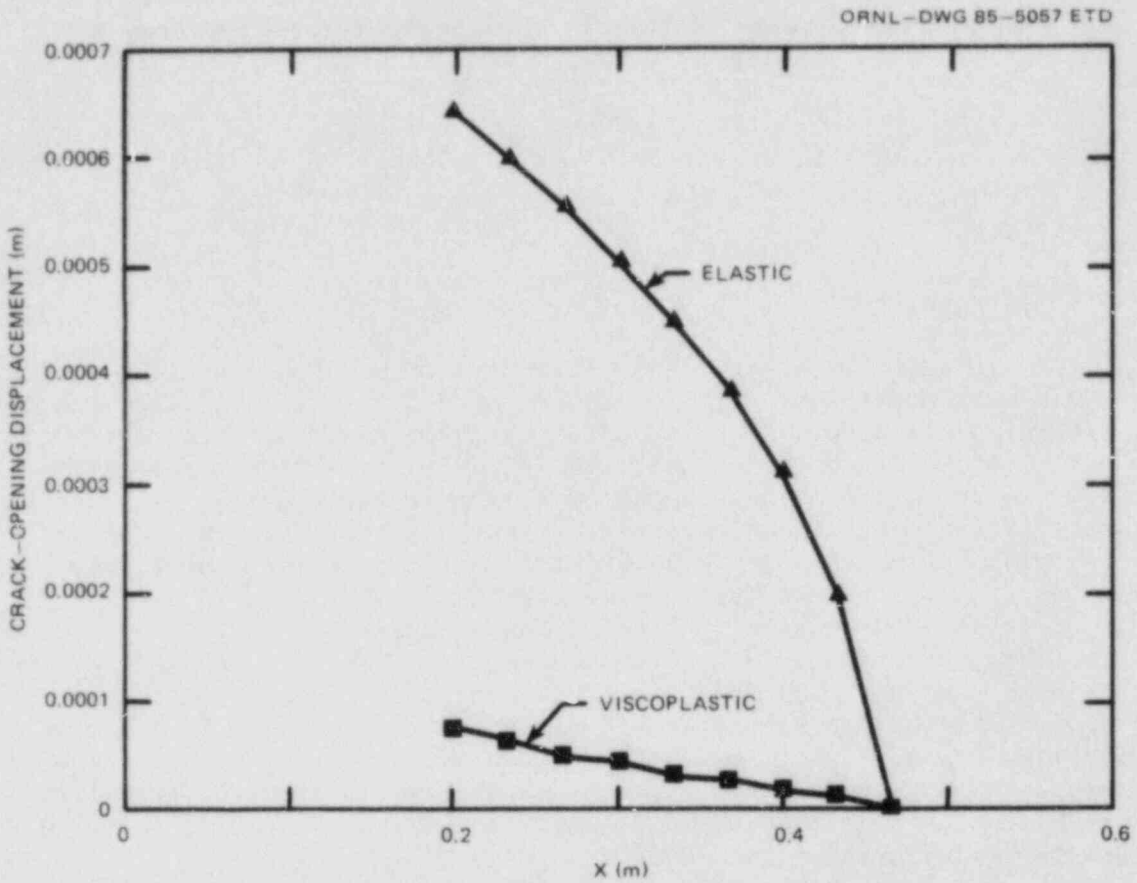

Fig. 2.17. Comparison of crack-opening profiles in WP-1.3 calculated using elastodynamic and viscoplastic-dynamic analyses time = 552 μs (a = 0.47 m).

The most pronounced viscoplastic effect seen in this analysis is the relaxation of stresses from the initial loads. This effect is an oversimplification. Because the quasi-static solution was found by a single Euler increment, it reflects no viscoplastic effects whatsoever. Viscoplasticity only becomes active at the instant of first-node release. This shortcoming, which is much more severe than had been anticipated, will be improved upon in the near future with a fully viscoplastic analysis of the initial loading.

Thermoelastic effects were ignored in this preliminary analysis; however, the temperature distribution was properly accounted for in the viscoplastic material model. Thermoelastic effects will also be accounted for in future analyses. Analyses using significantly finer meshes than those used here will only be possible using the VAX by implementation of lumped mass matrices. This task will be initiated in the near future.

2.5 Investigation of Damping and of the Cleavage-Fibrous Transition in Reactor-Grade Steel*

W. L. Fourney† G. R. Irwin†
D. B. Barker† R. Chona†
J. W. Dally† R. J. Sanford†
C. W. Schwartz‡ X-J. Zhang†

2.5.1 Introduction

The research program at the University of Maryland is aimed at increasing the understanding of crack run-arrest events in nuclear reactor pressure vessel steels. An intensive metallographic and fractographic study is being conducted of the behavior of various steels and heats of steels to investigate the transition from pure ductile fracturing at high temperatures to brittle cleavage at lower temperatures. In particular we are trying to assess what is responsible for the conversion of slow fibrous fracturing into rapid cleavage.

This study is being conducted by examining specimen halves obtained from tests conducted in situations where very compliant loading machines were used. Single- and double-width Charpy tests are also being used to evaluate fracture toughness and to determine the temperature above which slow fibrous fracturing could be expected for the steels under investigation. This research into transition behavior is aimed at formulating a mechanistic model that could be used to aid the understanding of this complicated transition behavior.

The research program also involves calculations performed with a dynamic finite-element computer code (SAMCR) to predict run-arrest events in standard specimen geometries and thermal-shock cylinders and to perform pretest and posttest analyses in support of the wide-plate crack-arrest tests. Crack-arrest and rapid-crack initiation studies are being supported with stress analysis capabilities by testing polymeric and steel models.

During the current report period, investigations of the cleavage-fibrous transition in a low-upper-shelf weldment material have continued. Support for the HSST wide-plate testing program at NBS with dynamic analyses and small-scale laboratory testing has continued, and recommendations with regard to data acquisition and instrumentation on WP-1.3 and WP-1.4 have also been provided. In addition, laboratory testing has begun to investigate high loading-rate initiation, and administration of the ASTM Crack-Arrest Round-Robin Program has continued.

---

*Work sponsored by the HSST Program under Subcontract No. 7778 between Martin Marietta Energy Systems, Inc., and the University of Maryland.

†Department of Mechanical Engineering, University of Maryland, College Park.

‡Department of Civil Engineering, University of Maryland, College Park.

2.5.2 Cleavage-fibrous transition studies

Since March an intensive review of information on cleavage-fibrous behaviors of reactor pressure vessel (RPV) steels and a weld metal has been in progress. A topical report is in preparation that will provide substantiating evidence for the following conclusions.

1. Fracture surface and underlying microstructure examinations reveal a good correlation between the spacing of small holes and the spacing of carbide clusters in ductile hole-joining fractures. Vertical-section views showed actual contact of carbide clusters with cavity bottoms.

2. Rapid fibrous crack extension assists cleavage initiation. This was first illustrated by loss-of-cleavage temperature studies in A 36, A 514, A 533 grade B, and A 508 steels. Spring-in-series loading was used to obtain rapid fibrous separation that, in turn, initiated continuing cleavage after various lengths of rapid hole-joining. It was observed that planar hole-joining separation in a high-carbide density region could play the same role in assisting cleavage initiation. Substantial elevation of the loss-of-cleavage temperature was observed with an increased degree of constraint.

3. Continued cleavage fracturing requires the spread of the initial cleavage initiation across a critical-sized region. In the transition temperature range, an initiation of cleavage must spread rapidly across a region much larger than several grain sizes to overcome barriers and produce continuing cleavage.

4. The largest cleavage facets were found in the largest ferrite grains with aligned carbide clusters. The cleavage was more interrupted and irregular in high-carbide regions, which had smaller grain size and less alignment of carbide clusters.

5. The greatest likelihood of initiating continuing cleavage occurs near the boundary between high- and low-carbide regions. At such locations, a segment of rapid hole-joining fracture can serve to elevate the stress and strain rates in adjacent regions. In those regions where the ferrite grains are larger, the expected extent of rapid spreading of cleavage is greater.

In terms of understanding the wide scatter in fracture-toughness measurements in the transition region, note that the degree of likelihood of continuing cleavage fracture varies widely. There is an uncertainty of location and degree of planar hole-joining associated with high carbide regions, which is combined with the uncertainty of initiation and continued spreading of cleavage in adjacent low-carbide regions. The interaction of these two phenomena gives rise to the large scatter that is observed.

2.6 Modifications of the ORMGEN/ORVIRT Fracture-Mechanics Analysis System

B. R. Bass S. Brosi*
D. A. Steinert G. Saurer*
R. W. Wanner*

During a 1-year assignment to the HSST program, R. Wanner of the Swiss Federal Institute for Reactor Research (EIR) performed thermal-shock calculations on nozzle cracks in the Heiss Dampf Reaktor (HDR)[37] under cyclic-thermal loading. Part of this work was carried out by S. Brosi and G. Saurer, also of EIR. During preparation for these studies, it was determined that the ORMGEN/ORVIRT[11,13] fracture-mechanics analysis system developed at ORNL would require extensive modifications to accommodate the nozzle-crack geometry of the HDR model. These modifications, which provide for a more accurate analysis of a wider variety of crack geometries for both EIR and ORNL projects, are described in the following sections.

2.6.1 Modifications of the ORMGEN mesh-generating program

The original ORMGEN program was designed to automatically generate a three-dimensional (3-D) finite-element model for six different crack geometries. These geometries are flat plates with straight or curved surface cracks and cylinders with part-through cracks on the outer or inner surface. The new version of the program, ORMGEN-II, offers more flexibility in the allowable crack shapes and an expanded range of structural geometries, including nozzle-cylinder intersections of the type being analyzed in the HDR project.

Mesh generation in the original ORMGEN program is established in four steps, illustrated in Fig. 2.18 for a simplified mesh. First, a regular grid is defined [Fig. 2.18(*a*)]. Second, the regular grid is mapped into a 2-D mesh that models the crack-geometry configuration in the plane of the crack [Fig. 2.18(*b*)]. Third, the 2-D mesh is replicated in a series of planes to produce a 3-D structure [Fig. 2.18(*c*)]. Fourth, nodal coordinates and element connectivities are defined using the nodal points of the replicated planes [Fig. 2.18(*d*)]. To generate a model with ORMGEN, the user provides the regular grid in Step 1 and selects a mapping function incorporated into the program for performing Step 2. The options in ORMGEN for the mapping in Step 2 are limited to plates and cylinders containing straight or part-through surface cracks. The remaining steps are automatically executed by the program.

In the ORMGEN-II program, this mesh generating procedure is modified by eliminating Step 1 and allowing the user to directly enter the 2-D mesh of Step 2 as part of the input to the program. The latter alternative significantly increases the amount of data preparation required of the user but offers much greater latitude in the types of crack contours and structural geometries that can be modeled by the program. As indicated in Fig. 2.19, the initial step in ORMGEN-II requires that the user

*Swiss Federal Institute for Reactor Research (EIR).

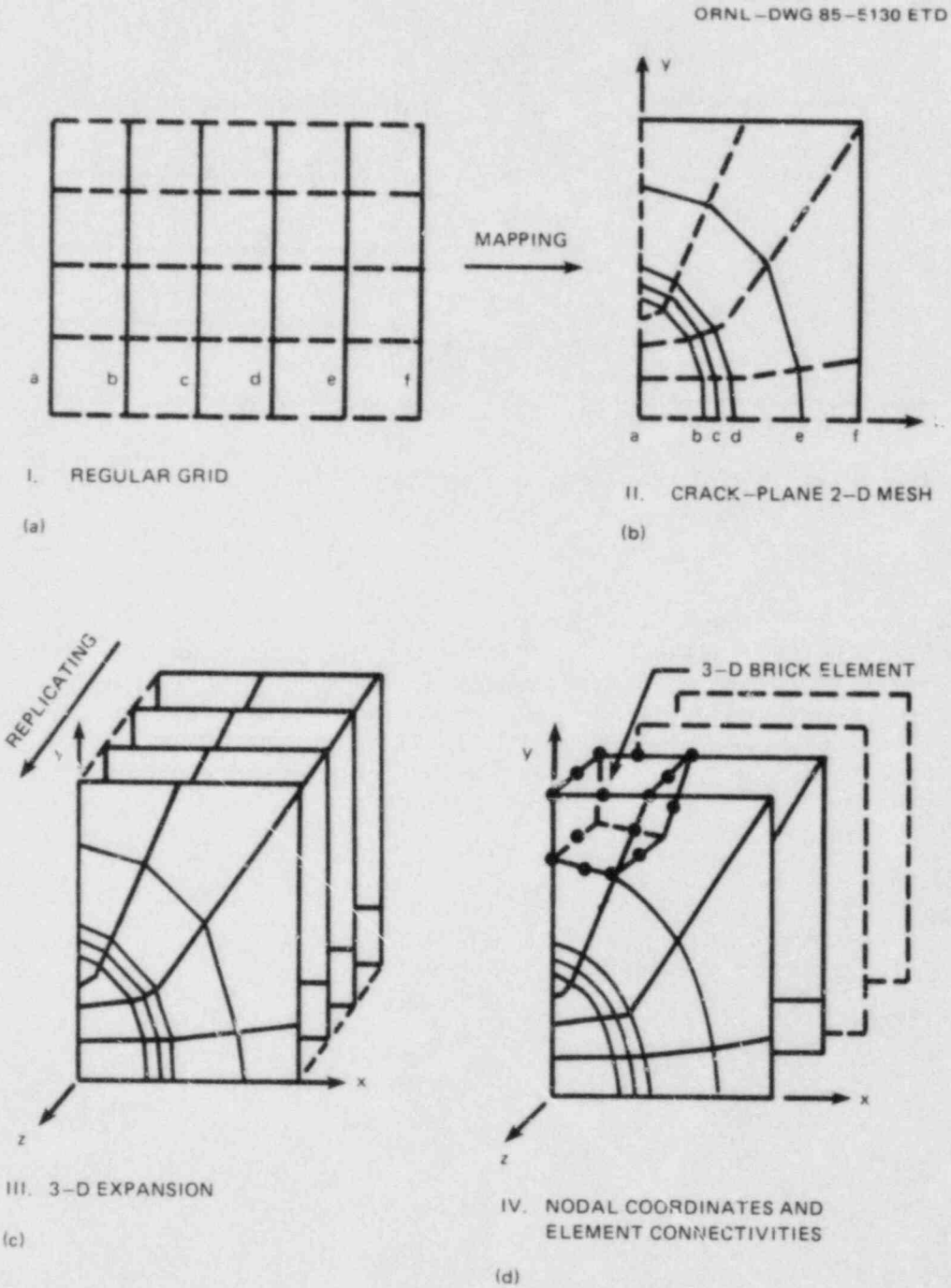

Fig. 2.18. Four major steps for ORMGEN finite-element mesh generation. (*a*) Regular grid, (*b*) crack plane 2-D mesh, (*c*) 3-D expansion, (*d*) nodal coordinates and element connectivities.

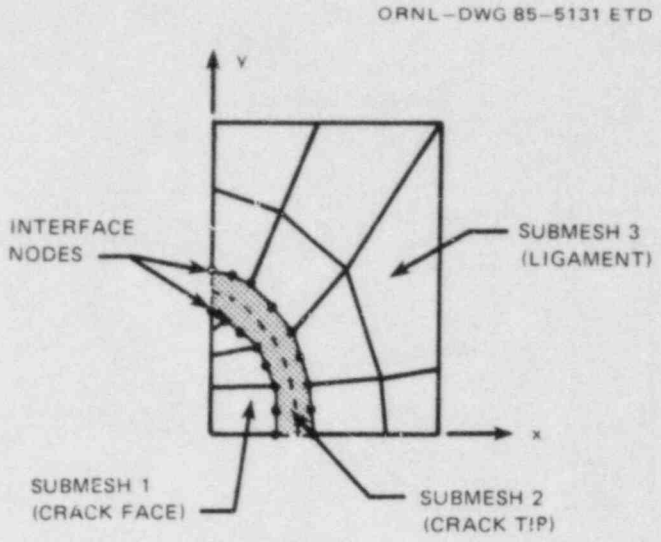

Fig. 2.19. Two-dimensional submeshes with connecting interface nodes for model generation in ORMGEN-II.

define three 2-D submeshes, Submesh 1 (crack face), Submesh 2 (crack tip), and Submesh 3 (ligament), which are connected by interface nodes. Submeshes 1 and 3 are arbitrary, whereas Submesh 2 must have a constant number of elements parallel to the crack front. The shape of the elements of Submesh 2 may be irregular, as shown in Fig. 2.20 for a center cracked plate and in Fig. 2.21 for the HDR nozzle crack. Steps 3 and 4

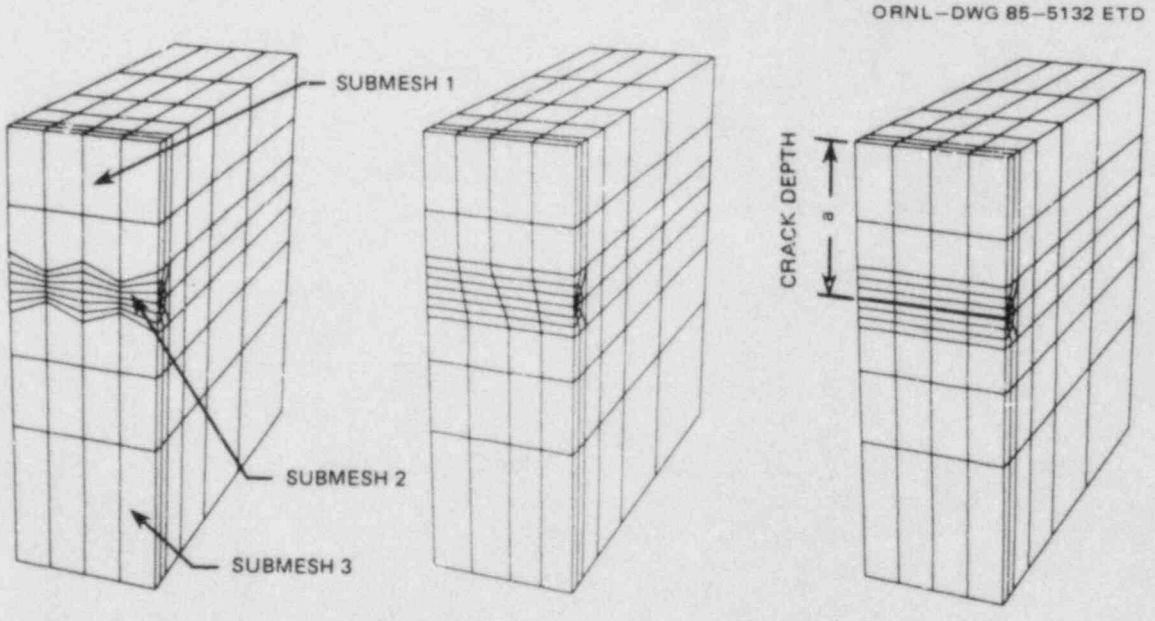

Fig. 2.20. Three different configurations of Submesh 2 for a center-cracked plate generated by ORMGEN-II.

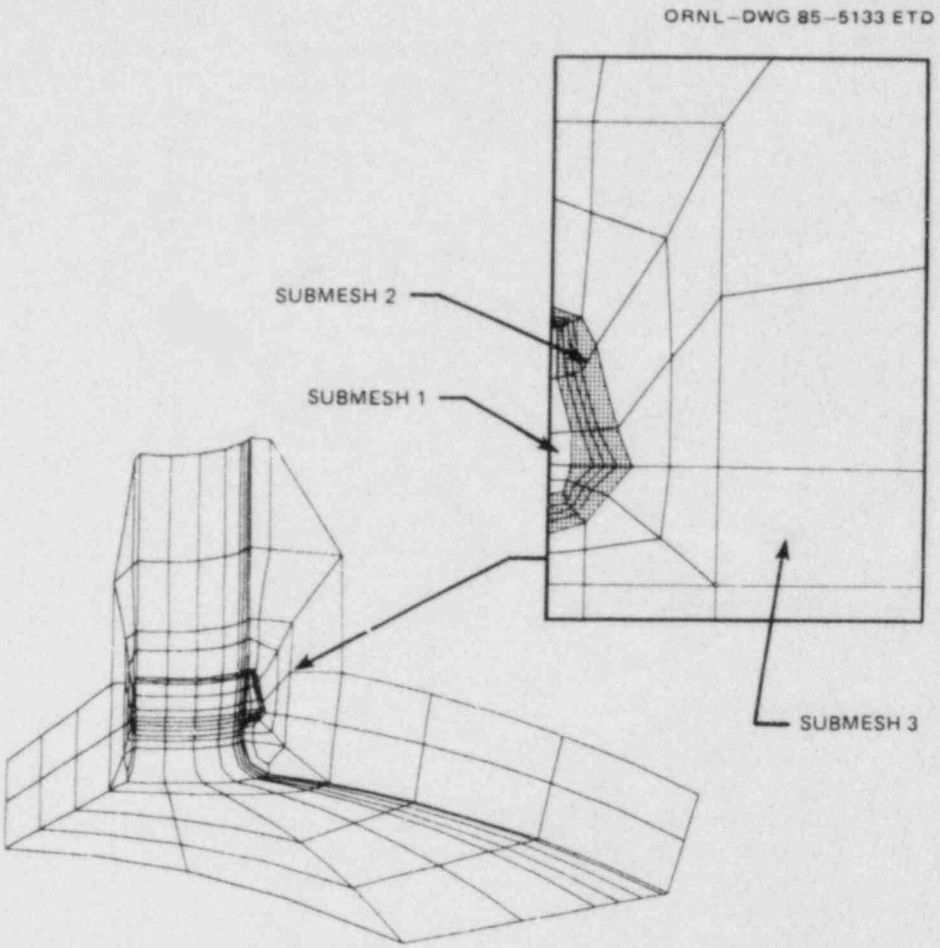

Fig. 2.21. Submeshes 1, 2, and 3 for the finite-element model of the HDR A2 nozzle generated by ORMGEN-II.

from the original procedure remain essentially unchanged in the ORMGEN-II program. The ADINAT,[38] ADINA, and ORVIRT input files for thermal stress and fracture analysis are automatically generated by the ORMGEN-II program. Additional details concerning the capabilities of ORMGEN-II will be described in a future document.

2.6.2 Modifications of the ORVIRT fracture-mechanics analysis program

The ORVIRT program was developed at ORNL to perform energy-release-rate calculations for both 2-D and 3-D nonlinear models of crack configurations in engineering structures. The thermomechanical formulation of the energy release rate in ORVIRT was derived by Bass and Bryson[13] from the isothermal technique of deLorenzi.[36] Average and local values of the energy-release rate are evaluated, respectively, from uniform and local virtual extensions of the crack front (see Fig. 2.22).

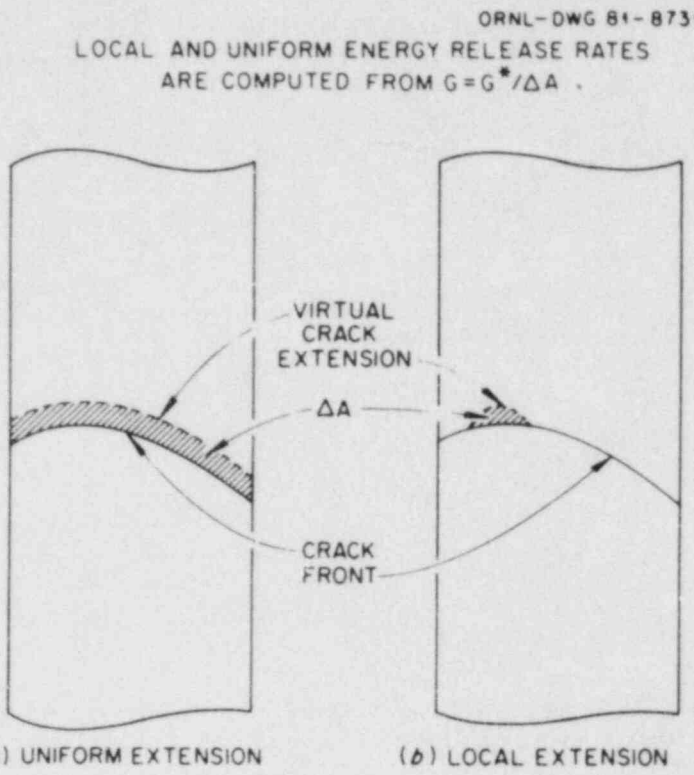

Fig. 2.22. Virtual crack extension for calculating energy release G for (*a*) uniform extension and (*b*) local extension.

The perturbation scheme proposed in the virtual crack extension technique of deLorenzi and implemented in the original version of ORVIRT is represented by the quadratic shape functions depicted in Fig. 2.23(*a*) and identified as IPER = 1. While this local perturbation is adequate for "smooth" semielliptical crack fronts, the technique can generate unrealistic negative energy-release values for crack fronts defined by curves with points of discontinuity in the slope. These negative values are due primarily to the negative area increments associated with perturbations of the element corner node at the point of discontinuity in slope [see Fig. 2.23(*a*)]. This difficulty is illustrated in Fig. 2.24 by an analysis of an HDR nozzle corner crack subjected to crack-face pressure. The solution for the stress-intensity factor vs position on the crack front derived from the quadratic perturbation of Fig. 2.23(*a*) is identified in Fig. 2.24(*b*) as IPER = 1. To improve the accuracy of these calculations, two additional perturbation schemes have been implemented in a new version of the code, ORVIRT-II, and are illustrated in Fig. 2.23(*b*) and (*c*). The second scheme, IPER = 2, was developed by W. Schmitt[39] at the Institut für Werkstoff-Mechanik and represents a smoothing of the energy-release values over several nodes. The third scheme in Fig. 2.23(*c*), IPER = 3, was derived at ORNL to produce a more localized perturbation of the crack front and, consequently, a more accurate pointwise energy-release value. In the latter case, the integration of the energy-

ORNL-DWG 85-5134 ETD

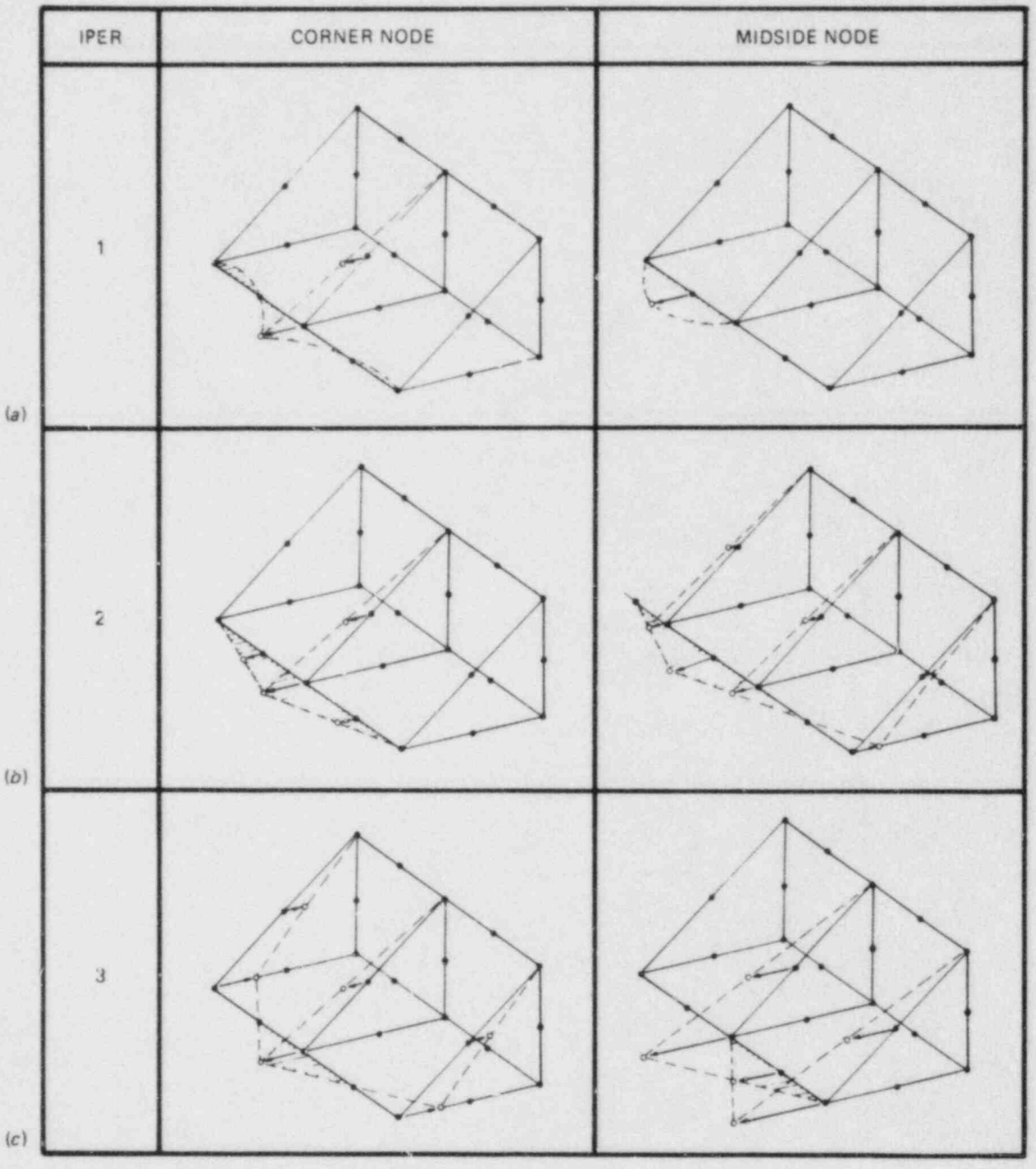

Fig. 2.23. Three perturbation schemes implemented in the ORVIRT-II fracture-analysis program.

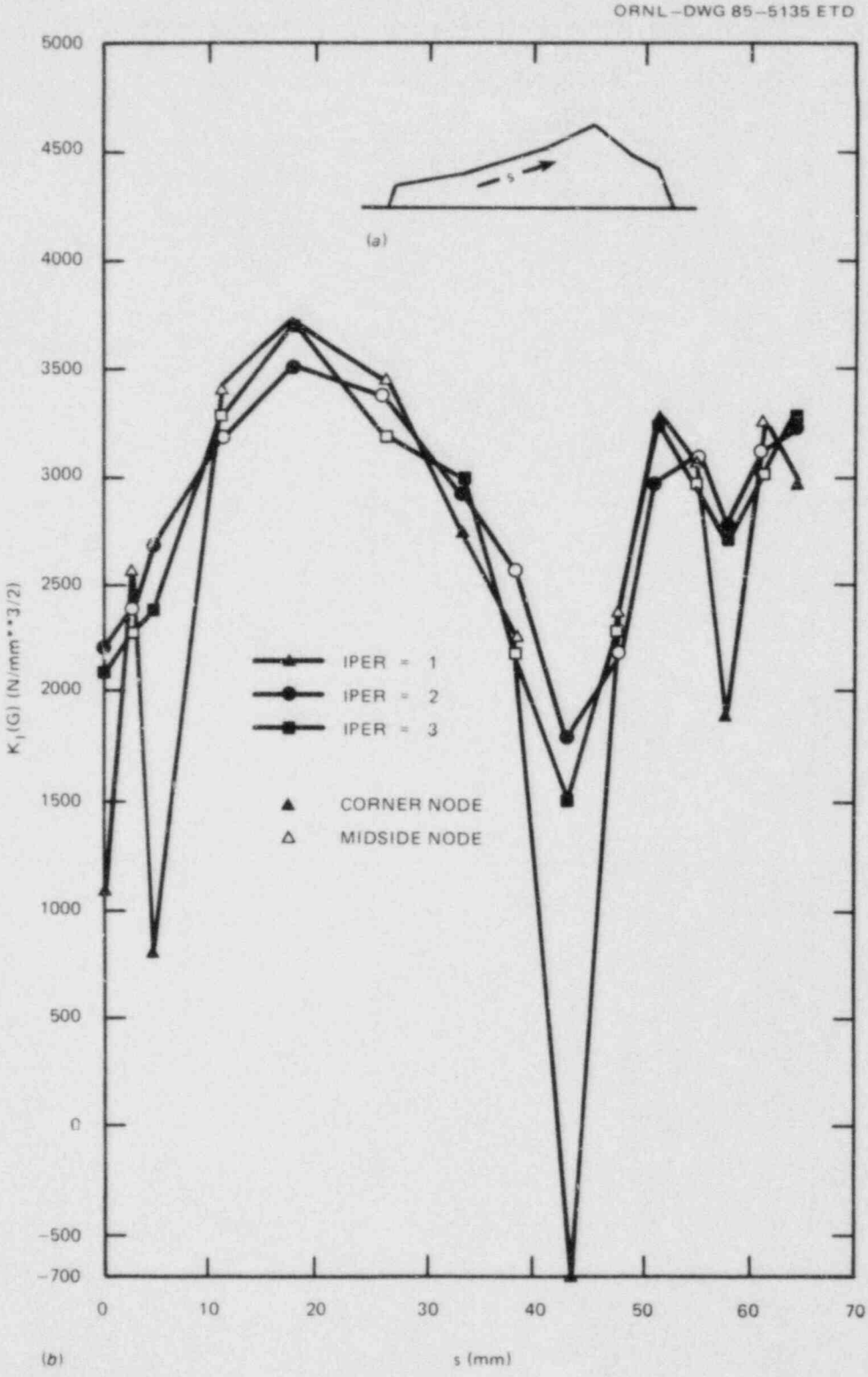

Fig. 2.24. Stress-intensity factor vs position (s) along crack front for HDR nozzle crack. (*a*) HDR nozzle-crack configuration, (*b*) stress-intensity factor vs s.

release function is performed only in the part of the element with positive virtual displacement. Results for all three perturbation schemes are compared in Fig. 2.24(*b*) for the HDR nozzle corner crack and indicate good agreement between the schemes defined by IPER = 2 and 3. Further details of these and other additions to the ORVIRT-II program will be described in a forthcoming document.

References

1. K. J. Bathe, *ADINA — A Finite Element Program for Automatic Dynamic Incremented Nonlinear Analysis*, Report AE 84-1, ADINA Engineering, Watertown, Mass., December 1984.

2. J. J. McGowan et al., "Properties of Wide-Plate Crack-Arrest Test Material," pp. 82–85 in *Heavy-Section Steel Technology Program Semiann. Prog. Rep. October 1984–March 1985*, NUREG/CR-4219, Vol. 1 (ORNL/TM-9593/V1), Martin Marietta Energy Systems, Inc., Oak Ridge Natl. Lab.

3. J. Jung et al., *Finite Element Analysis of Dynamic Crack Propagation*, presented at the 1981 ASME Failure Prevention and Reliability Conference, Sept. 23–26, 1981, Hartford, Conn.

4. B. R. Bass, W. G. Johnson, and S. V. McGrath, *An Approximation of Finite Element Nodal Point Stresses for Nonlinear Material Models*, K/TS-3798, Union Carbide Corp. Nuclear Div., Oak Ridge Gaseous Diffusion Plant, February 1980.

5. E. Hinton and J. S. Campbell, "Local and Global Smoothing of Discontinuous Finite Element Functions Using a Least Squares Method," *Int. J. Numer. Methods Eng.* 8, 461–80 (1974).

6. B. Brickstad, "A Viscoplastic Analysis of Rapid Crack Propagation Experiments in Steel," *J. Mech. Phys. Solids* 31, 307–27 (1983).

7. P. Perzyna, "Fundamental Problems in Visco-Plasticity," pp. 244–368 in *Recent Advances in Applied Mechanics*, Academic Press, New York, 1966.

8. O. C. Zienkiewicz and I. C. Cormeau, "Visco-Plasticity — Plasticity and Creep in Elastic Solids — A Unified Numerical Solution Approach," *Int. J. Numer. Methods Eng.* 8, 821–45 (1974).

9. D. R. J. Owen and E. Hinton, *Finite Elements in Plasticity*, Pineridge Press Limited, Swansea, United Kingdom, 1980.

10. J. W. Bryson, *ORVIRT.PC: A 2-D Finite-Element Fracture Analysis Program for a Microcomputer*, NUREG/CR-4367 (ORNL-6208), Martin Marietta Energy Systems, Inc., Oak Ridge Natl. Lab., October 1985.

11. B. R. Bass and J. W. Bryson, *Applications of Energy Release Rate Techniques to Part-Through Cracks in Plates and Cylinders, Volume 1. ORMGEN-3D: A Finite Element Mesh Generator for 3-Dimensional Crack Geometries*, NUREG/CR-2997/V1 (ORNL/TM-8527/V1), Union Carbide Corp. Nuclear Div., Oak Ridge Natl. Lab., December 1982.

12. K. J. Bathe, *ADINA - A Finite Element Program for Automatic Dynamic Incremental Nonlinear Analysis*, Report 82448-1, Massachusetts Institute of Technology, Cambridge, Mass., 1975 (rev., December 1978).

13. B. R. Bass and J. W. Bryson, *Applications of Energy Release Rate Techniques to Part-Through Cracks in Plates and Cylinders, Volume 2. ORVIRT: A Finite Element Program for Energy Release Rate Calculations for 2-Dimensional and 3-Dimensional Crack Models*, NUREG/CR-2997/V2 (ORNL/TM-8527/V2), Union Carbide Corp. Nuclear Div., Oak Ridge Natl. Lab., February 1983.

14. B. R. Bass and J. W. Bryson, "Energy Release Rate Techniques for Combined Thermo-Mechanical Loading," *Int. J. Fract.* 22, R3 (1983).

15. H. G. deLorenzi, "On the Energy Release Rate and the J-Integral for 3-D Crack Configuration," *Int. J. Fract.* 19, 183 (1982).

16. D. R. J. Owen and A. J. Fawkes, *Engineering Fracture Mechanics: Numerical Methods and Applications*, Pineridge Press Ltd., Swansea, United Kingdom, 1983.

17. E. Hinton and D. R. J. Owen, *Finite Element Programming*, Academic Press, New York, 1977.

18. B. M. Irons, "A Frontal Solution Program," *Int. J. Numer. Methods Eng.* 2, 5–32 (1970).

19. D. P. Rooke and D. J. Cartwright, *Compedium of Stress Intensity Factors*, The Hillingdon Press, Her Majesty's Stationery Office, London, 1976.

20. R. A. Ainsworth, B. K. Neale, and R. H. Price, *Fracture Behavior in the Presence of Thermal Strains*, Central Electricity Generating Board, Report RD/B/N4152, Research Division, Berkeley Nuclear Laboratories, 1977.

21. ASTM Standard E813-81, "Standard Test Method for J_{Ic}, A Measure of Fracture Toughness," pp. 762–80 in *1983 Annual Book of ASTM Standards*, Sect. 3, Vol. 03.01, American Society for Testing and Materials, Philadelphia, Pa., 1983.

22. H. A. Ernst, P. C. Paris and J. D. Landes, "Estimations on J-Integral and Tearing Modulus T from a Single Specimen Test Record," pp. 476–502 in *Fracture Mechanics: Thirteenth Conference*, ASTM STP 743, American Society for Testing and Materials, Philadelphia, Pa., 1981.

23. J. G. Merkle, Oak Ridge National Laboratory, Oak Ridge, Tenn., personal communication to G. A. Clarke, Westinghouse Research Laboratories, Pittsburgh, Pa., August 1978.

24. G. A. Clarke and J. D. Landes, "Evaluation of the J Integral for the Compact Specimen," *J. Test. Eval.* 7(5), 264–9 (September 1979).

25. H. A. Ernst, "Material Resistance and Instability Beyond J-Controlled Crack Growth," pp. 191-213 in *Elastic-Plastic Fracture: Second Symposium*, ASTM STP 803, Vol. I, American Society for Testing and Materials, Philadelphia, Pa., 1983.

26. J. R. Rice, W. J. Drugan, and T. L. Sham, "Elastic-Plastic Analysis of Growing Cracks," pp. 189-221 in *Fracture Mechanics: Twelfth Conference*, ASTM STP 700, American Society for Testing and Materials, Philadelphia, Pa., 1980.

27. J. G. Merkle, Oak Ridge National Laboratory, Oak Ridge, Tenn., personal communication to H. A. Ernst, Westinghouse Research Laboratories, Pittsburgh, Pa., January 19, 1982.

28. H. A. Ernst, *Further Developments on the Modified J-Integral, J_M*, draft 85-9D7-GUDAS-P1, Westinghouse Research Laboratories (to be published)

29. J. M. Bloom and K. K. Yoon, *Analysis of HSST Intermediate Vessel V-8A Test by the Deformation Plasticity Failure Assessment Diagram Method*, B&W-1814, Babcock & Wilcox Co., Lynchburg, Va., November 1983.

30. M. F. Kanninen and C. H. Popelar, *Advanced Fracture Mechanics*, Oxford Press, New York, 1985, pp. 132–6.

31. S. R. Bodner and Y. Partom, "Constitutive Equations for Elastic-Viscoplastic Strain Hardening Materials", *J. Appl. Mech.* 42, 385 (1975).

32. M. F. Kanninen et al., "Elastodynamic and Viscoplastic-Dynamic Fracture-Mechanics Analyses," pp. 18–28 in *Heavy-Section Steel Technology Program Semiann. Prog. Rep. Oct. 1984–March 1985*, NUREG/CR-4219, Vol. 1 (ORNL/TM-9593/V1), Martin Marietta Energy Systems, Inc., Oak Ridge Natl. Lab.

33. L. B. Freund and J. W. Hutchinson, "High Strain-Rate Crack Growth in Rate Dependent Plastic Solids," *J. Mech. Phys. Solids* 33, 169–91 (1985).

34. M. F. Kanninen, ed., *Proceedings of the CSNI/NRC Workshop on Ductile Piping Fracture Mechanics*, San Antonio, Texas, June 21–22, 1984, to be published by the U.S. Nuclear Regulatory Commission, 1985.

35. D. M. Parks, "A Stiffness Derivative Finite Element Technique for Determination of Crack-Tip Stress Intensity Factors," *Int. J. Fract.* 10, 487 (1974).

36. H. G. deLorenzi, "On the Energy Release Rate and the J Integral for 3-D Crack Configurations," *Int. J. Fract.* 19, 183 (1982).

37. PHDR-Arbeitsbericht Nr. 2.041/81, Auslegungsbericht, *Thermoshockversuche am A2 Stutzen des HDR, V66.0-V66.4*, Kernforschungszentrum Karlsruhe, 1981.

38. K. J. Bathe, *ADINAT – A Finite Element Program for Automatic Incremental Nonlinear Analysis of Temperature*, Report 82488-1, Acoustics and Vibration Lab., Mechanical Engineering Dept., M.I.T., September 1975, rev. December 1978.

39. W. Schmitt, *Anwendung der Methode der Finiten Element unter Besonderer Berücksichtigung Dreidimensionaler und Elastisch-Plastischer Probleme*, Frauenhofer-Institut fur Werkstoff-Mechanik, Nosastr. 9, 7800 Freiburg, January 1982.

3. MATERIAL CHARACTERIZATION AND PROPERTIES

R. K. Nanstad

3.1 Directory to Other Material Properties Reporting

Primarily for internal management and budgetary control purposes, the Heavy-Section Steel Technology (HSST) Program has made a separate task (Task H.3) of the work on material characterization and properties determinations. However, for the readers' convenience some contributions are placed within other chapters according to the larger tasks that correspond to the particular material studies. Therefore, in addition to the work reported here, refer to Sects. 7.1 and 7.2 for nondestructive examination studies and beam experiment work, respectively, in support of cladding evaluations.

3.2 Crack-Arrest Test Results in Support of Wide-Plate Testing

W. R. Corwin W. B. Stines
T. D. Owings, Jr.

Crack-arrest tests were performed at Oak Ridge National Laboratory (ORNL) on HSST Plate 13A for two primary reasons: (1) to supplement the existing data base on the wide-plate test material and (2) to provide an interlaboratory comparison of test results obtained at ORNL and Battelle Columbus Laboratories (BCL) for different specimen types (weld embrittled and duplex) and specimen loading methods (normal vs inverted pin).

All specimens were of the compact-crack-arrest type and were fabricated in the LT orientation, corresponding both to the wide-plate tests being conducted at the National Bureau of Standards (NBS) (see Chap. 5) and the previous data generated at BCL. Weld-embrittled specimens were utilized in the temperature range from about RT_{NDT} (−23°C) to 10°C. Above 10°C, duplex specimens were used because experience has indicated difficulty in initiating fracture more than 20 to 40°C above RT_{NDT}.

The test results are listed in Table 3.1 and compared in Fig. 3.1 with the results from the first four wide-plate tests and K_{Ia} correlations. The K_{Ia} curve in Fig. 3.1 is based on a least-squares fit to BCL small specimen data;[1] the current ORNL crack-arrest data are not included. The RT_{NDT} of this material has been determined to be −23°C.[2] It can be seen that the K_{Ia} correlation corresponds fairly well with both the newly generated crack-arrest data as well as the results from the wide-plate tests (see Chap. 5 for wide-plate results and calculation methods).

Further comparison of the ORNL crack-arrest results with the previously generated BCL results shows excellent agreement (Fig. 3.2). Of particular interest are the data at 0 and 10°C. At both these temperatures, ORNL data were obtained utilizing weld-embrittled specimens, whereas the BCL data were obtained with duplex-type specimens. Considering the scatter inherent in data from crack-arrest testing, the weld-

Table 3.1. ORNL compact specimen crack-arrest data for A 533 grade B class 1 steel, HSST plate 13A

Specimen No.	Temperature (°C)	K_{Ia} (MPa·$\sqrt{m}$)	Pin geometry	Specimen type[a]
AK121	−20	71.4	Normal	MD, WE
AK123	−20	80.1	Normal	MD, WE
AK111	0	65.6	Normal	LG, WE
AK112	0	72.3	Normal	LG, WE
AK131	10	74.2	Inverted	LG, WE
AK132	10	93.1[b]	Inverted	LG, WE
13AK21E	30	121.2[b]	Inverted	MD, DP
13AK21F	30	116.2[b]	Inverted	MD, DP
13AK22A	40	161.6[b]	Inverted	MD, DP

[a]MD = medium size, 33.0 × 152.4 × 152.4 mm
LG = large size, 50.8 × 203.2 × 203.2 mm
WE = weld embrittled
DP = duplex

[b]Did not meet all validity limits of ASTM standard.

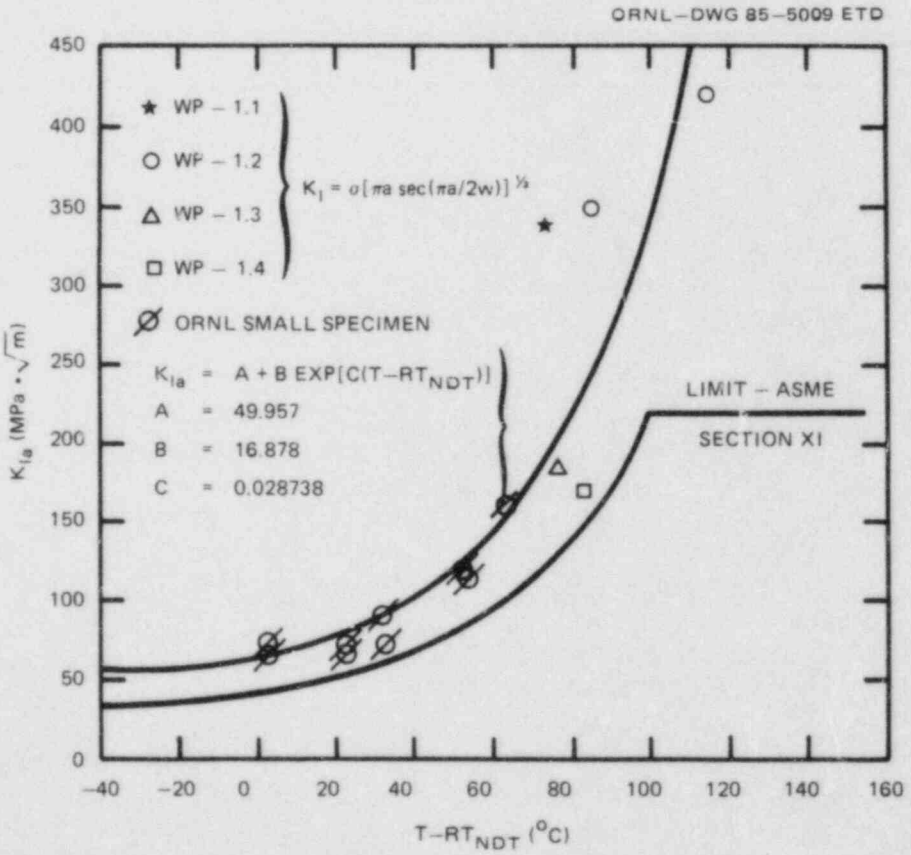

Fig. 3.1. ORNL laboratory-specimen crack-arrest data with K_{Ia} curve generated from BCL data for wide-plate material (HSST plate 13A).

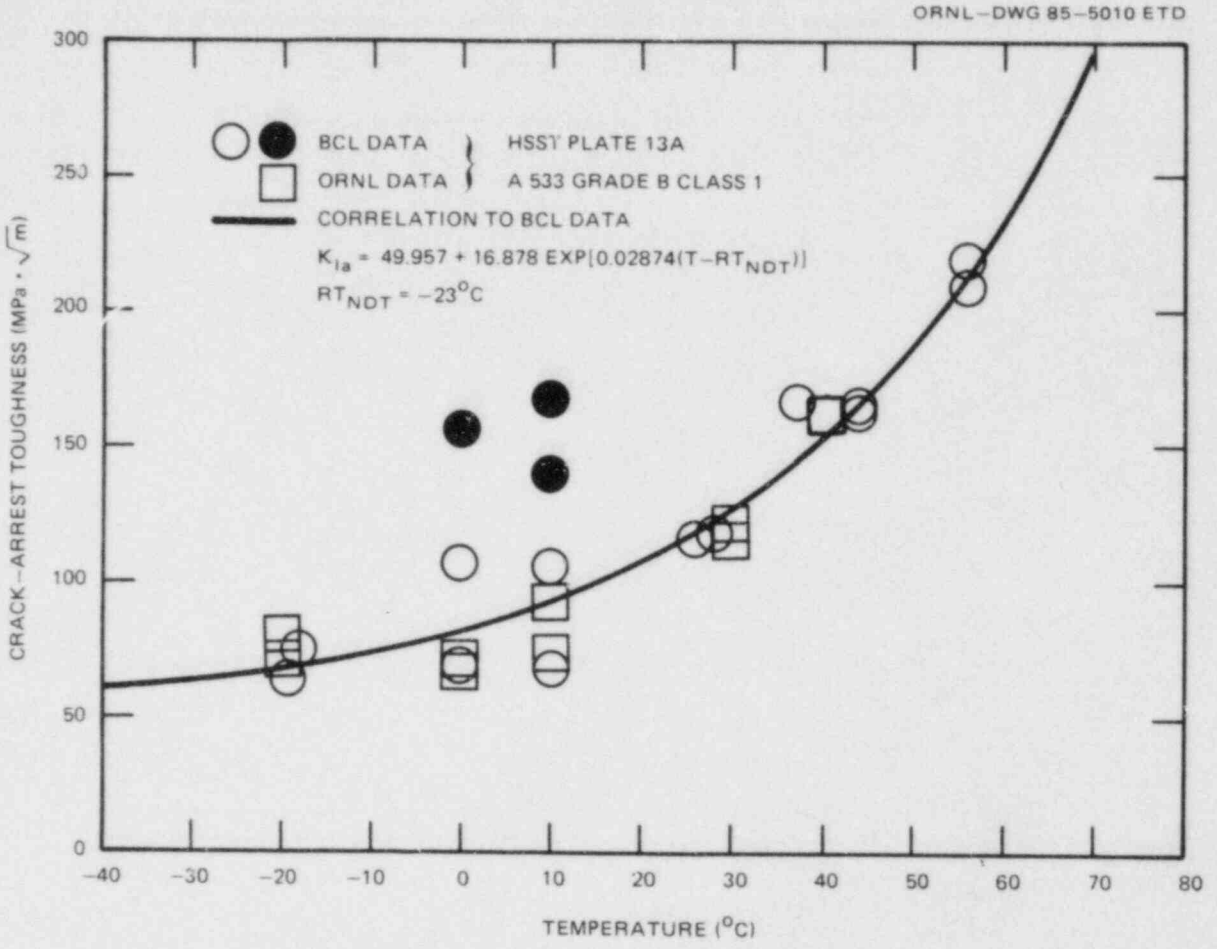

Fig. 3.2. Compact specimen crack-arrest toughness data from ORNL and BCL for A 533 grade B class 1 steel from HSST plate 13A. Line is fit to BCL when solid points are omitted. (Solid points exhibiting unusually high K_{Ic}/K_{IR} values.)

embrittled and duplex specimen data agree very well with one another. The two ORNL data points at 30°C were obtained using duplex specimens. This study will continue into the next report period.

3.3 Round-Robin Crack-Arrest Testing

W. R. Corwin T. D. Owings, Jr.
W. B. Stines

ORNL has completed all of its planned testing for the American Society for Testing and Materials (ASTM)-sponsored international round robin on crack-arrest testing. This includes testing both the full-size specimens specified by ASTM for the round robin (~50 × 200 × 200 mm) as well as subsize specimens machined from their broken halves (~25 × 75 × 75 mm).

In addition to the testing performed with the ASTM-recommended draft procedure that utilizes split pins in a "normal orientation," testing with inverted split pins was also performed.

All specimens were fabricated from blanks of A 514, A 588, and A 533 grade B class 1 steel distributed by the University of Maryland, which is coordinating the round robin. Specimens were of the weld-embrittled type that use a notched brittle-weld nugget as an aid to rapid crack initiation. The full-size specimens contained a brittle weld of Hardex N as recommended by the ASTM Task Group on Crack Arrest. The subsize specimens received a rapidly self-quenching autogeneous electron-beam weld at the root of the notch. The choice of welding procedure did not appear to be significant for the limited conditions examined. Indeed, in most cases the weld bead itself failed prior to the initiation event, which seemed to start in the heat-affected zone (HAZ). Given the historic difficulty in consistently obtaining crack initiation for a given welding process, it would be worthwhile to examine the condition of the HAZ and its relation to rapid crack initiation.

The complete ORNL results for the round-robin specimens have been forwarded to the University of Maryland (see Table 3.2 for a summary of results). All testing temperatures were specified by the responsible ASTM task group. The values of K_{Ia} were calculated using a measured

Table 3.2. Summary of ORNL results for the ASTM crack-arrest round robin

Material	Number of specimens[a]	Temperature (°C)	K_{Ia} (MPa·$\sqrt{m}$)[b]	Specimen size[c]	Pin geometry
A 588	3 (3)	−30	70 (6)	Large	Normal
A 588	4 (4)	−30	48 (3)	Small	Normal
A 514	3 (2)	−30	94 (18)	Large	Normal
A 514	2 (0)	−30	—	Small	Normal
A 514	2 (1)	−30	95 (-)	Small	Inverted
A 533B	3 (3)	10	79 (7)	Large	Normal
A 533B	3 (2)	10	72 (2)	Large	Inverted
A 533B	2 (2)	10	89 (12)	Small	Normal
A 533B	3 (2)	25	82 (5)	Large	Normal
A 533B	4 (3)	25	92 (15)	Large	Inverted
A 533B	1 (0)	25	—	Small	Normal
A 533B	3 (1)	25	68 (-)	Small	Inverted

[a]Number of specimens tested (number of successful run-arrest events).

[b]Value in parentheses is standard deviation.

[c]Large size, 50.8 × 203.2 × 203.2 mm; small size, 25.4 × 76.2 × 76.2 mm.

value of crack-mouth opening that did not include permanent plastic displacement determined from the cyclic test procedure, but did include the quick opening recorded after crack initiation. While this was the analysis method requested by the task group, it is subject to change pending the round-robin results. While a much better picture of any differences of K_{Ia} as a function of specimen size or split pin configuration will be available once all the round-robin data are collected, it does not appear that there are any systematic differences in the ORNL data as a function of size or pin orientation given the overall scatter. A very noticeable difference, however does exist between the full- and subsize A 588 data. It may be that the large plastic deformation prior to the initiation event in the subsize A 588 specimens resulting from its low yield strength (330 MPa) needs to be more fully considered.

References

1. A. R. Rosenfield et al., "Crack-Arrest Studies at Battelle Columbus," pp. 102–9 in *Heavy-Section Steel Technology Program Semiann. Prog. Rep. April–September 1984*, NUREG/CR-3744, Vol. 2 (ORNL/TM-9154/V2), Martin Marietta Energy Systems, Inc., Oak Ridge Natl. Lab.

2. D. P. Edmonds and J. J. McGowan, "Characterization of Wide-Plate Test Material at ORNL," pp. 96-102 in *Heavy-Section Steel Technology Program Semiann. Prog. Rep. April–September 1984*, NUREG/CR-3744, Vol. 2 (ORNL/TM-9154/V2), Martin Marietta Energy Systems, Inc., Oak Ridge Natl. Lab.

4. ENVIRONMENTALLY ASSISTED CRACK-GROWTH TECHNOLOGY*

W. H. Bamford† I. W. Wilson‡
R. J. Jacko‡

4.1 Introduction

The objective of this task is to characterize the crack-growth-rate properties of light-water reactor (LWR) materials exposed to primary-coolant environments. The work now being conducted falls into five major areas:

1. corrosion fatigue crack-growth tests in simulated pressurized-water reactor (PWR) environment,
2. static load K_{ISCC} tests in simulated PWR environment,
3. fractographic examination of specimen fracture surfaces,
4. characterization of environment by measurement of electrochemical potential, and
5. participation in the International Cyclic Crack-Growth Review Group (ICCGR).

The fatigue crack-growth-rate tests are carried out on 2T-CT specimens in autoclaves installed in recirculating water systems. Crack length is monitored through a compliance relationship with the face opening of the specimen, as monitored by an external LVDT. Data acquisition is computer based. The water system is purged of oxygen at the beginning of each test, and the open circuit corrosion potential is monitored by hydrogen and silver-silver chloride electrodes. The water chemistry maintained in the system is given in Table 4.1 of Ref. 1. The systems have a relatively low flow rate. The static load K_{ISCC} specimens are precracked in accordance with American Society for Testing and Materials (ASTM) recommendations, bolt-loaded with bolts of the identical material, and inserted into the fatigue crack-growth test chambers that are set in the bottom. These specimens are removed periodically at the conclusion of crack-growth tests for crack-length measurements.

4.2 Fatigue Crack Growth

Under this task, two aspects of crack growth are being studied: the impact of sulfur content and the relationship between the static and dynamic crack-growth rates observed in heat-affected-zone (HAZ) specimens.

---

*Work sponsored by the Heavy-Section Steel Technology Program under Subcontract 11X-21598C between Martin Marietta Energy Systems, Inc., and Westinghouse Electric Corporation, Plant Engineering Division.

†Westinghouse Electric Corporation, Plant Engineering Division, Pittsburgh, PA 15230

‡Westinghouse Research and Development Laboratories, Pittsburgh, PA 15235.

Earlier tests completed in this program have shown that the material chemistry has an important influence on the level of crack-growth enhancement in a water environment.[2,3] This finding has now been confirmed by a number of other investigators and is generally accepted. A more detailed study of a high-sulfur steel plate is being carried out and is now nearing completion.

The relationship between constant-load cracking and fatigue cracking of HAZ materials has been under study for several years. Findings thus far have shown no discernible relationship. Four HAZs in A 533 grade B plate material have been characterized thus far; the results are discussed in some detail in Sect. 4.3.

4.2.1 High-sulfur material characterization

Now that it is widely understood that high-sulfur materials are more susceptible to environmental enhancement, it is of interest to obtain detailed knowledge of the behavior of a typical high-sulfur steel. To accomplish this goal, a commercially produced reactor pressure vessel steel was chosen, and a matrix of tests was devised to study the effects of R ratio, temperature, frequency, and boron content of the water. Testing on this matrix has been under way now for some time and is nearing completion. The results of this series of tests have important applications because the steels involved represent those used in early construction and are also likely to exhibit the most enhanced crack growth.

The test matrix is shown in Table 4.1. Testing is essentially complete at 204 and 288°C; testing is under way at 93°C and R = 0.2. Specimen CQ2-1B was tested at 1 cycle per minute (0.017 Hz) in simulated PWR

Table 4.1. Test matrix for study of frequency and temperature effects for high-sulfur A 533 grade B steel

Test temperature (°C)	R ratio = 0.2		R ratio = 0.7	
	Frequency (cycles per minute)	Specimen	Frequency (cycles per minute)	Specimen
288	1	CQ2-5	1	CQ2-6
	1	CQ2-8	10	CQ2-11
	1 (borated)	CQ2-9		
204	1 (borated)	CQ2-12	1	CQ2-7
	1[a]	CQ2-15	10	CQ2-10
	10[a]	CQ2-14		
93	1	CQ2-18		

[a]Tests completed during this report period.

environment like the others in the matrix. Boron was not added to the water. The growth rates obtained for these conditions, shown in Fig. 4.1, are about the same as those from the 1-cycle-per-minute tests conducted at 288°C (see Fig. 4.2 of Ref. 1). Fig. 4.1 of Ref. 1 shows that the crack growth rates obtained at 204°C were significantly lower.

4.2.2 Crack-Growth testing of HAZ specimens

Because static-load cracking has been observed in several specimens, the crack-growth-rate behavior of these same materials was investigated to determine if any relationships existed. The materials for which both static and fatigue crack-growth results have been generated are listed in Table 4.2.

Table 4.2. Fatigue crack-growth-rate testing to complement static-load tests

Test material	R ratio = 0.2		R ratio = 0.7	
	Frequency (cycles per minute)	Specimen	Frequency (cycles per minute)	Specimen
Linde 124 weld HAZ				
Material C	1	C-24-HAZ-1	1	C-23-HAZ-1
Material CQ	1	CQ-1 HAZ	1	CQ-2 HAZ
			5	CQ-3 HAZ
Linde 80 weld HAZ				
Material C	1	C-3 HAZ	1	C-4 HAZ
A 533 grade B	1	04A-103	1	04A-102
plate 04	1	04AE 13	1	04AE 15
Linde 0091 weld				
Material D	1	D-1 HAZ	1	D-2 HAZ
		D-3 HAZ	1	D-4 HAZ
			1	D-6 HAZ
Material DD	1	DD-1 HAZ	1	DD-2 HAZ
Linde 124 weld				
Material KH	1	KH-1 HAZ	1	KH-2 HAZ[a]
	10	KH-4 HAZ[a]		

[a]Specimens completed during this test period.

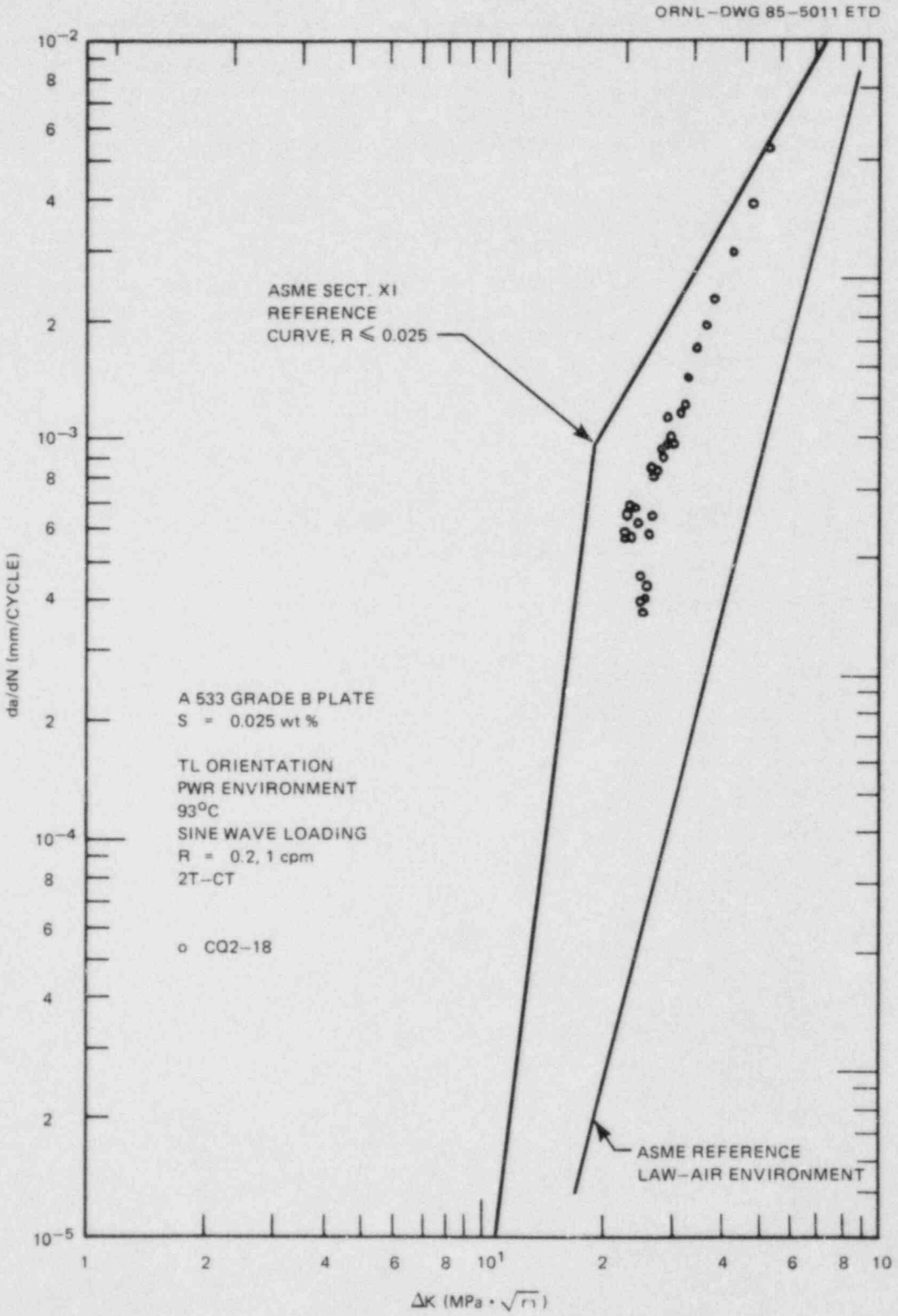

Fig. 4.1. Results of crack growth rate tests of specimen CQ2-18, tested at 93°C in simulated PWR environment, R = 0.2.

During this report period further crack-growth-rate results were obtained for the "KH" HAZ material, which is A 533 grade B class 1 plate material. Figure 4.2 shows the results obtained from two tests at R = 0.2 and 288°C and indicates that a significant frequency effect exists. The growth rates are nearly an order of magnitude higher at 1-cycle-per-minute loading than at 10 cycles per minute. This is consistent with results obtained earlier for plate materials at this temperature.[4] Also note that the crack-growth-rate results obtained at 1 cycle per minute are not as accelerated for HAZ materials with higher sulfur contents[5] under the same test conditions. This is to be expected because the sulfur content for the adjacent base metal is only 0.007 wt % (see Table 4.4 of Ref. 1).

This sulfur effect is also seen for the "KH" HAZ material tested at R = 0.7. Figure 4.3 shows the results for heat KH as well as three other HAZ materials tested earlier under identical conditions. The other three materials had sulfur contents reported ranging from 0.017 to 0.020 wt % (see Table 4.4 of Ref. 1), and the crack-growth ratios were all consistently high. The results for KH-2 HAZ are about an order of magnitude lower, never exceeding 5×10^{-4} m/cycle. Section 4.3 will show that no such differences were found in the static-load cracking behavior of these materials.

4.3 Static-Load Testing

Static-load crack-growth rates (if any) are characterized for these steels by using 2.54-cm-thick bolt-loaded WOL specimens that sit in the bottom of the fatigue chambers. The specimens are precracked in fatigue before loading and are loaded to different values of applied stress-intensity factor K_I. If the crack extends, the load decreases and eventually an equilibrium point, the threshold for static-load cracking identified as K_{ISCC}, is reached. This work has been under way since 1974, with a total of over 25 specimens having been tested. No cracking has occurred in welds or forging materials in over 10 years of testing. On the other hand, cracking did occur in plate specimens and in all the HAZ materials tested thus far. The time to crack initiation for the HAZ materials has averaged ~2000 h, but for the plate material over 37,000 h was required. Note that the initiation times are unrelated to the sulfur content, which has such a marked effect on the crack-growth rates as discussed previously.

During this report period, additional cracking has occurred on several of the specimens. An update of the exposure times is provided in Table 4.3 Specimens where crack extension has occurred are highlighted in the table.

4.4 Examination of Specimens — Sulfur Prints and Detailed Chemistry

As part of the study of sulfur effects, the distribution of manganese sulfide inclusions in a plate is being examined. It is well known that these inclusions migrate to the the center region of the ingot and that

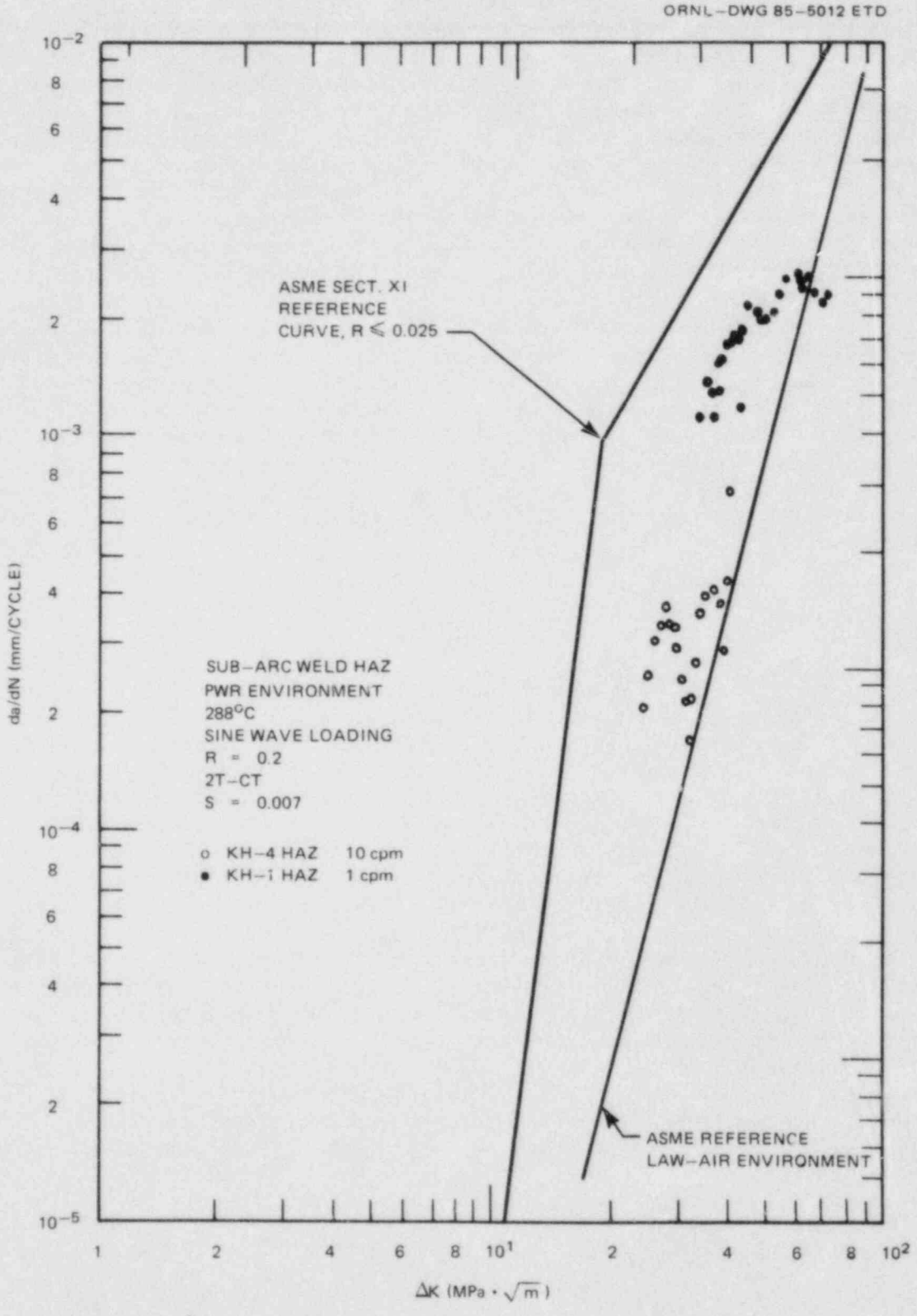

Fig. 4.2. Comparison of crack-growth-rate results for HAZ material "KH," tested at 1 and 10 cycles per minute, R = 0.2.

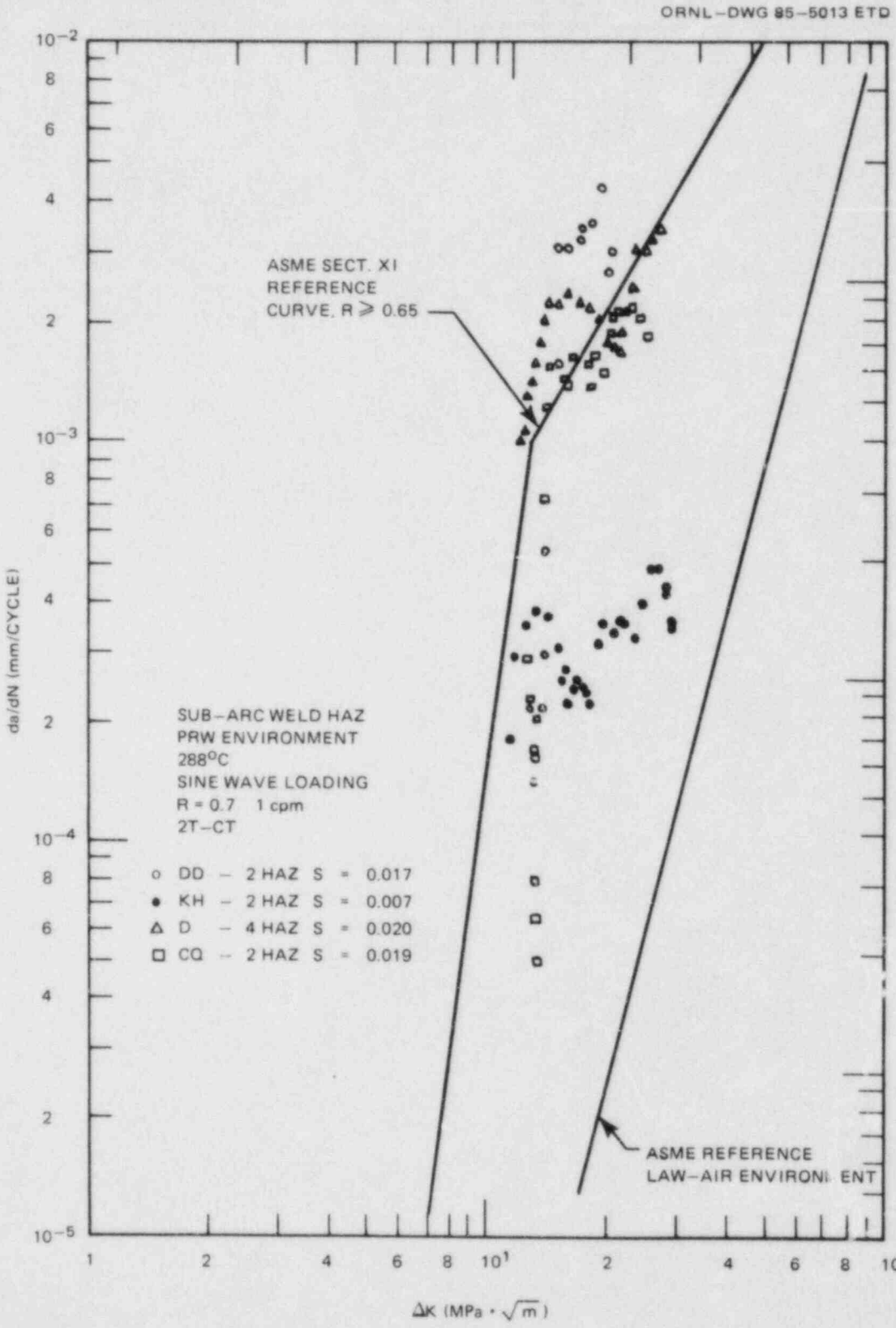

Fig. 4.3. Effect of sulfur content on environmental fatigue crack growth in HAZs of A 533 grade B class 1 steel.

Table 4.3. Status of bolt-loaded specimens in simulated PWR environment (August 16, 1985)

Material	Specimen	Applied stress-intensity factor (Mpa·√m)	Total time loaded to date (h)	Time in environment (h)
A 533 grade B class 1 plate (HSST plate 4)	04A-114[a]	90	74,098	48,994
	04A-116[a]	88	74,098	48,994
A 508 class 2 forging	F-13	110	84,286	56,598
	F-14	99	84,286	58,502
	F-15	88	84,286	58,502
Linde 124 weld	C-13	110	84,286	56,935
	C-14	99	84,286	56,935
Linde 124 weld HAZ	CQ-1-HAZ[a]	110	32,980 (1,816)[b]	14,394 (1,262)
	CQ-2-HAZ[c]	99	37,876 (37,876)[b]	19,562 (19,562)
	CQ-3HAZ[a]	88	33,408 (3,360)[b]	12,274 (2,616)
Linde 0091 weld HAZ	D-7HAZ[c]	99	37,148 (37,148)[b]	28,984 (28,984)
	D-8HAZ[a]	88	37,148 (7,196)[b]	14,384 (4,160)
	D-9HAZ[c]	77	37,148 (37,148)[b]	28,984 (28,984)
Linde 124 weld HAZ	K-3HAZ	66	13,488 (4,320)[b]	8,435 (4,138)
	K-4HAZ	77	13,488 (4,320)[b]	8,435 (4,138)
	K-5HAZ	88	13,488 (4,320)[b]	8,435 (4,138)
Linde 0091 weld HAZ	DD-3HAZ	66	14,928 (5,760)[b]	11,144 (5,280)
	DD-4HAZ[a]	77	14,928 (5,760)[b]	11,144 (5,280)
	DD-5HAZ	88	14,928 (5,760)[b]	11,144 (5,280)

[a]Removed from testing.

[b]Hours at first observed crack extension.

[c]Extension since last report.

the largest concentrations are eliminated by topping the ingot. Those inclusions that remain are rolled into the plate and would, therefore, be likely to remain in the center portion after rolling. Sulfur prints were used to show that this was indeed true for the steel used in this study, CQ2 (see Fig. 4.4).

Figure 4.4 shows a sulfur print of the entire through-thickness slice of the material from which the CQ2 specimens were removed. Note the plate curvature, which corresponds to the curvature of the reactor vessel from which this nozzle dropout was removed. There is a clear concentration of manganese sulfide inclusions near the center of the plate. This figure has been reduced from the full-size print, which was 22.9 cm in height and 55.9 cm long.

Although this print gives a qualitative picture of the distribution of inclusions, it does not quantify the sulfur content or its variation.

ORNL-PHOTO 1769-85

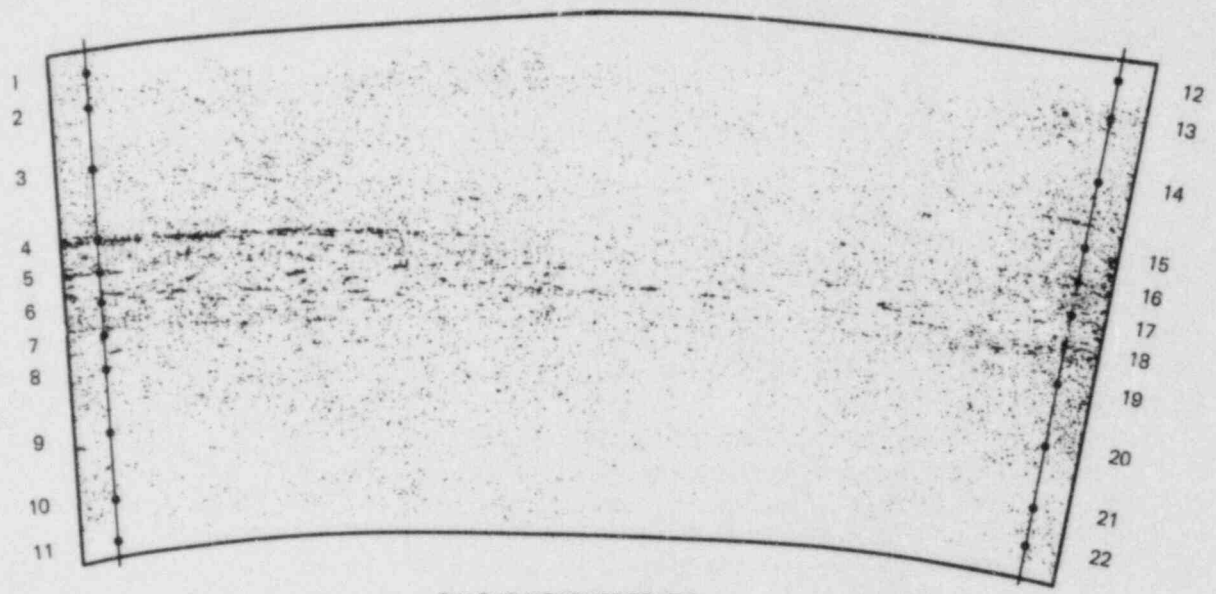

SULFUR MEASUREMENTS

LADLE: 0.019 CHECK: 0.025 WT %

LOCATION	WT %	LOCATION	WT %
1	0.012	12	0.011
2	0.012	13	0.012
3	0.011	14	0.011
4	0.013	15	0.011
5	0.014	16	0.012
6	0.011	17	0.009
7	0.015	18	0.012
8	0.012	19	0.012
9	0.012	20	0.012
10	0.013	21	0.012
11	0.012	22	0.012

Fig. 4.4. Full-thickness sulfur print of heat CQ2, showing concentration of manganese sulfide inclusions near plate center.

To accomplish this, sulfur measurements were taken through the thickness at each end of the sample; the values obtained are shown in the figure as well. A carbide tipped drill was used to remove turnings from 11 positions through the thickness of the plate, as shown in Fig. 4.4. These turnings were carefully cleaned, and ~2 g of each was individually analyzed for sulfur using a Leco combustion apparatus.

As expected, the sulfur content is lower toward the outer surfaces of the plate. The highest levels are observed on either side of the center near the heavier streaks observed on the sulfur print. Note that the readings at one end of the plate are different than those at the other end of the plate, with the higher readings corresponding to the darker areas of the sulfur print. The readings in this set are consistently lower than either the ladle or check analyses on the material test certificate, which are 0.019 and 0.025 wt %, respectively. The differences could have resulted from different sampling locations or measurement techniques because the plate was fabricated in 1972. The sulfur content from the most recent measurements is likely to be most reliable. Nonetheless, the content is high enough to put the material in the category for which significant environmental enhancement would be expected.

4.5 International Cyclic Crack Growth Rate Group

Membership is maintained in the ICCGR review group, which is an interdisciplinary group begun in 1977 to share information on corrosion fatigue. A detailed summary of the background and work of this group has been given in a previous progress report,[5] and a complete report of its status was given recently.[6] Continuing activities of the group are reviewed periodically in these reports; this section reviews the discussions of technical interest.

The group is now composed of 49 member organizations from 12 countries. Over 60 people attended the most recent meeting held in Tokai, Japan, in May 1985. The meeting was hosted by the Japan Atomic Energy Research Institute and was organized into four separate sessions. The group has recently been reorganized to add more emphasis to the applications; the new tasks groups are as follows:

Task group 1. Data Collection and Recent Results
Task group 2. Mechanisms
Task group 3. Applications

In addition to sessions devoted to the task group meetings, the first session was devoted to discussion of round-robin results from all those organized by the group. These round robins are key experiments and will be summarized individually because they are the greatest benefit obtained from participation in the group.

Low R round robin — This was the first round robin. All results have previously been reported, with only three or four specimens now untested. This test has now been adopted as a qualification test for new test rigs.

High R round robin — Most labs have now completed specimens testing but have not reported the results officially to the coordinator, R. Jones. High rates were obtained by 60 to 70% of the laboratories, which approach

the ASME Sect. XI high R water reference line. There appears to be a systematic difference between BWR and PWR environments, with crack growth taking off at a lower ΔK value for BWR than for PWR environments.

Slow strain-rate round robin — Status was given by G. Lloyd, who gave a brief review of the results presented in a formal paper in Sendai, Japan. Over ten labs volunteered for another round robin on this subject.

Bolt-load WOL specimen round robin - This is a new round robin coordinated by W. Bamford and G. Lloyd to study several different materials, beginning with HAZ materials, where observed cracking has been more prevalent. It was decided that a test specification should be prepared for the next meeting and that materials representative of Japanese, French, and U.S. practices were required.

The latest progress of each of the three task groups is reviewed in the following paragraphs.

4.5.1 Data collection and recent results

This task group reviews and compares recent test results and is charged with establishing and maintaining a data base of all available fatigue crack-growth-rate data for pressure vessel steels. Presentation of recent results highlighted the two major variables affecting crack-growth rates, which have been under discussion for the past 2 years: water flow rate and material chemistry. New results were presented from Japan showing that water flow rate had no effect on crack-growth rates in low- and medium-sulfur steels. The trend in results reported in this area now appears to be favoring a smaller effect of this variable than had previously been thought. Additional results were presented on the effect of material type and chemistry, further confirming the effects of manganese sulfide inclusion size and distribution on environmental enhancement of crack growth.

Environmental fatigue crack-growth data for Inconel 600 showed no environmental enhancement. Electrochemical potential measurement techniques were not discussed in detail, having been reviewed in a recent paper by Scott and Bamford.[7] The other area receiving attention was the measurement of static-load crack-growth rates; this discussion was centered around the development of a round-robin test.

4.5.2 Mechanisms

This group has set out to provide a mechanistic basis for the observed trends in fatigue crack-growth rates in water environments. A quantitative model now exists that incorporates anodic dissolution and some hydrogen effects. The model, which was reviewed in detail at the recent meeting, predicts strain and rate effects, and its results are consistent with the ASME code reference crack-growth-rate curves.

Important presentations were made concerning development of a model for hydrogen effects. This was the first attempt at a quantitative model along these lines, and it matches a wide range of observations on corrosion-fatigue behavior in a number of investigations.

4.5.3 Applications

This newly formed group devoted its session to presentations of thoughts on the future directions of the group. Presentations were also made on the status of the EDEAC data base, which now holds results from about 3000 specimens, and on the development of a data analysis code for treatment of the data to develop reference crack-growth-rate laws.

The chairman summed up the need to take the work on applications further. He presented several sets of data to illustrate cases where cracking was observed and where transients and crack extension were measured, including BWR feedwater nozzle cracks and PWR feedwater line cracks.

References

1. W. H. Bamford et al., "Environmentally Assisted Crack Growth Technology," pp. 38–57 in *Heavy-Section Steel Technology Program Semiann. Prog. Rep. October 1984–March 1985*, NUREG/CR-4219, Vol. 1 (ORNL/TM-9593/V1), Martin Marietta Energy Systems, Inc., Oak Ridge Natl. Lab.

2. W. H. Bamford, R. Jacko, and L. J. Ceschini, "Environmentally Assisted Crack Growth in Light Water Reactors," pp. 97–114 in *Heavy-Section Steel Technology Program Quart. Prog. Rep. July–September 1983*, NUREG/CR-3334, Vol. 3 (ORNL/TM-8787/V3), Union Carbide Corp. Nuclear Div., Oak Ridge Natl Lab., February 1984.

3. W. H. Bamford, "Environmental Cracking of Pressure Boundary Materials and the Importance of Metallurgical Considerations," pp. 209–28 in *Aspects of Fracture Mechanics in Pressure Vessels and Piping*, ASME Publication PVP-vol. 58, 1982.

4. W. H. Bamford, "Applications of Corrosion Fatigue Crack Growth Rate Data to Integrity Analyses of Nuclear Reactor Pressure Vessels," *Trans. ASME J. Eng. Mater. Tech.*, pp. 101, 182–90 (July 1979).

5. W. H. Bamford, R. J. Jacko, and L. J. Ceschini, "Environmentally Assisted Crack Growth Technology," pp. 28–45 in *Heavy-Section Steel Technology Program Semiann. Prog. Rep. October 1983–March 1984*, NUREG/CR-3744, Vol. 1 (ORNL/TM-9154/V1), Union Carbide Corp. Nucl. Div., Oak Ridge Natl. Lab.

6. G. Slama and R. Jones, "International Cooperative Group on Cyclic Crack Growth Rate," *Proceedings of the Sixth SMirt Conference Post-Conference Seminar Session 8, Paris, France, 1981.*

7. D. M. Scott and W. H. Bamford, "The Development and Use of Electrochemical Potential Monitoring in Environment Assisted Cracking Tests in High Temperature, High Pressure Aqueous Environments," *Proceedings of IAEA Specialists Meeting on Subcritical Crack Growth, Sendai, Japan, May 1985* (to be published by USNRC in 1985).

5. CRACK-ARREST TECHNOLOGY

5.1 Background Information on HSST Studies

C. E. Pugh

In crack-arrest studies sponsored by the Heavy-Section Steel Technology (HSST) Program, a primary objective has been to obtain reliable fracture-toughness data and to develop procedures for the prediction of crack arrest in materials at temperatures approaching the Charpy upper-shelf regime. Early laboratory studies of crack arrest by numerous investigators have led to the use of test specimens that reduce the dynamic effects of a running crack. The appropriateness of current American Society for Testing and Materials (ASTM) recommendations on laboratory test procedures is being examined through a round-robin test program that is discussed in Sect. 5.7. Battelle Columbus Laboratories (BCL), through an HSST subcontract, have established a data bank of available crack-arrest data, and the status of this effort is discussed in Sect. 5.8. However, small laboratory specimens provide limited constraint of deformation in the crack-plane region and a driving force that decreases with crack extension. These factors have limited the generation of data from these specimens to temperatures below those where arrest is most likely to occur in a pressurized-thermal-shock (PTS) scenario. The HSST Program is measuring crack-arrest data over an expanded temperature range through thermal-shock[1] and PTS (Ref. 2) tests, which also provide validation data under multiaxial transient and high-restraint conditions. Recently, the HSST Program has undertaken the performance of a series of wide-plate tests[3] as an opportunity to obtain a more significant number of data points at affordable costs. These tests are designed to provide fracture-toughness measurements at temperatures approaching or above the onset of the Charpy upper-shelf region, in a rising toughness region and with an increasing driving force.

The HSST wide-plate crack-arrest tests are being performed at the National Bureau of Standards (NBS), Gaithersburg, Maryland, in their 27-MN capacity tensile machine. The first series of six planned tests (WP-1.1 through WP-1.6) use specimens from the HSST plate 13A of A 533 grade B class 1 steel. The overall specimen assembly was described in Ref. 3 and is illustrated in Fig. 5.1. A rising toughness field for crack arrest is achieved by applying a temperature gradient across the plate. The plates are heavily instrumented to record pertinent data during the test. In conjunction with the wide-plate testing, a parallel research effort that combines dynamic-viscoplastic finite-element analyses with small-scale fracture experimentation is under way (see Chap. 2).

While the wide-plate tests are aimed primarily at providing crack-arrest data at temperatures up to or above that corresponding to the onset of the Charpy upper shelf (>50°C for this material), they also provide information on the dynamic fracture process for use in evaluating improved fracture-analysis methods. The single-edge-notched plate specimens are heated on one edge and cooled on the other to give a linear temperature gradient along the crack propagation plane. Upon initiating the

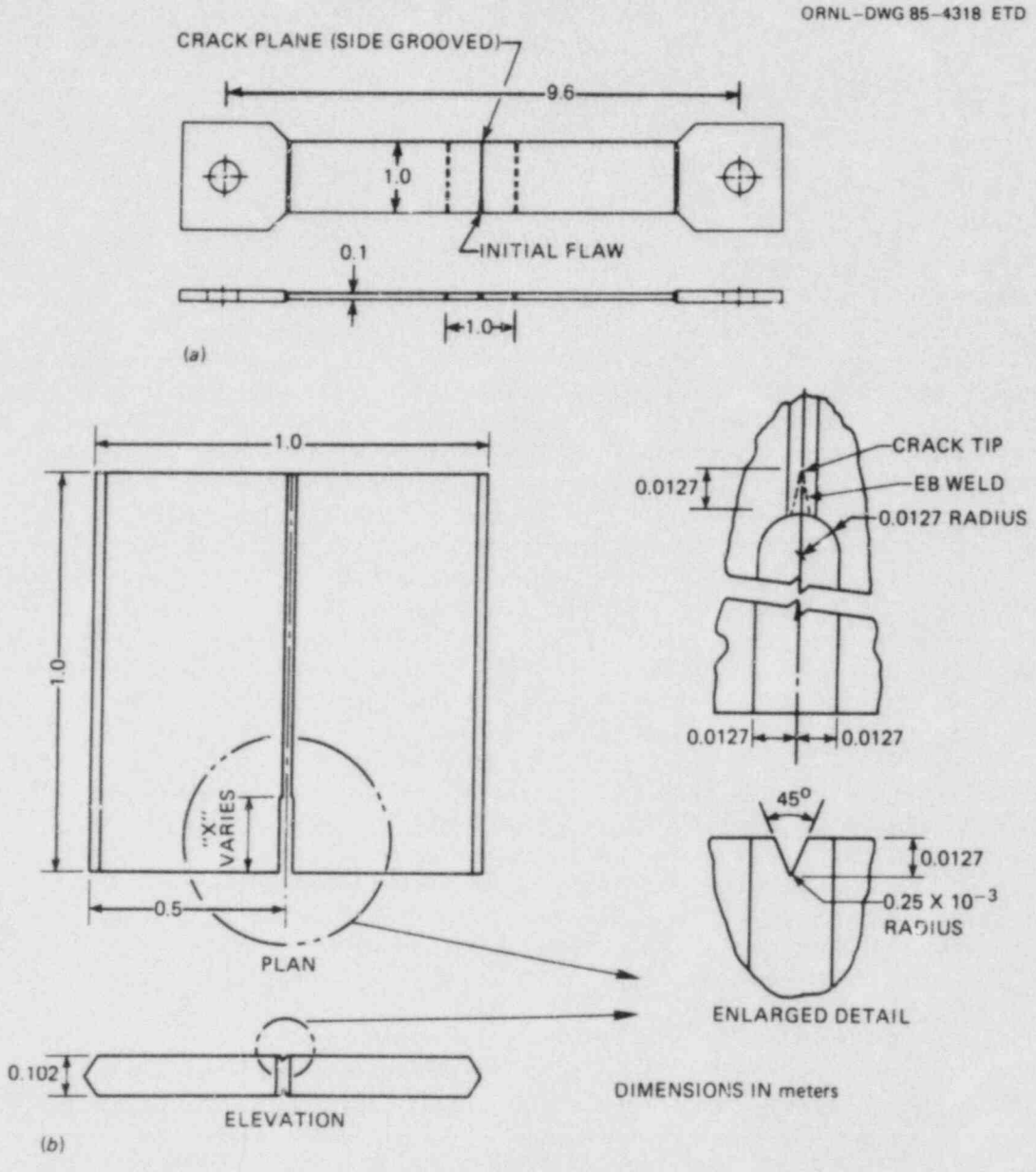

Fig. 5.1. Wide-plate crack-arrest specimen and pull-plate assembly. (*a*) Schematic of assembly, (*b*) detail of test specimen.

crack in cleavage, arrest is intended to occur in the higher-temperature ductile region of the specimen.

Four wide-plate tests have been performed to date, with two tests taking place in this report period: WP-1.3 on May 9, 1985, and WP-1.4 on July 19, 1985. The precracked specimens are provided by Oak Ridge National Laboratory (ORNL), and NBS instruments them with thermocouples and strain gages. Tests WP-1.3 and WP-1.4 are described in Sect. 5.2. Mechanical and fracture properties data for WP-1 material are discussed

briefly in Sect. 5.3. BCL obtained the crack-arrest data, while ORNL performed the other properties tests. Analyses of the wide-plate tests have been performed by ORNL, Southwest Research Institute (SwRI), and the University of Maryland (UM), and these activities are reported in Sects. 5.4–5.6. The fifth test, WP-1.5, has been instrumented and will be performed in October.

5.2 Wide-Plate Crack-Arrest Testing*

R. deWit[†]
S. R. Low III[†]
G. E. Hicho[†]
L. C. Smith[†]
D. Read[‡]
D. McColskey[‡]
D. E. Harne[†]
R. J. Fields[†]

5.2.1 Introduction

Testing procedures, preliminary results, and fractography are included in this section for the third and fourth wide-plate crack-arrest tests (WP-1.3 and WP-1.4) performed for the HSST Program. Detailed specimen dimensions are shown in Figs. 5.2 and 5.3. The length of the pull plates changed from WP-1.3 to WP-1.4 because small amounts of the wide-plate material were left attached to the pull plates in the process of cutting out the WP-1.3 specimen. Dimensions of specimens WP-1.3 and WP-1.4 are listed in Table 5.1.

The third wide-plate test (WP-1.3) was completed on May 9, and the fourth (WP-1.4) on July 19, 1985. Previous wide-plate tests[4] had shown that a simple notch and straight-through crack in a side-grooved plate led to extremely high initiation loads. These loads were so high that while very high arrest temperatures were obtained, the specimen/machine compliances created a mechanically unstable situation that resulted in complete fracture of the specimen. In an effort to obtain a completely stable crack after arrest, several changes were made in WP-1.3 and WP-1.4. At the suggestion of G. R. Irwin of UM, a chevron notch instead of a straight-through notch was used. In addition, G. C. Robinson of ORNL designed and fabricated a "pillow jack" loading device that could fit into the notch and apply a pressure distribution up to 200 MPa (a description of this loading device is given in Sect. 5.2.4). In WP-1.3 only the chevron was effective in reducing the tensile load at initiation because the pressurizing media for the pillow jack froze. In this regard, the load was not reduced enough to obtain a stable arrest. Complete fracture occurred after a 1.9-s hesitation after the first run-arrest event.

---

*Work sponsored by the HSST Program under Interagency Agreement No. DE-AI05-84OR21432 between the U.S. Department of Energy and the National Bureau of Standards.

[†]Fracture and Deformation Division, National Bureau of Standards, Gaithersburg, Maryland.

[‡]Fracture and Deformation Division, National Bureau of Standards, Boulder, Colorado.

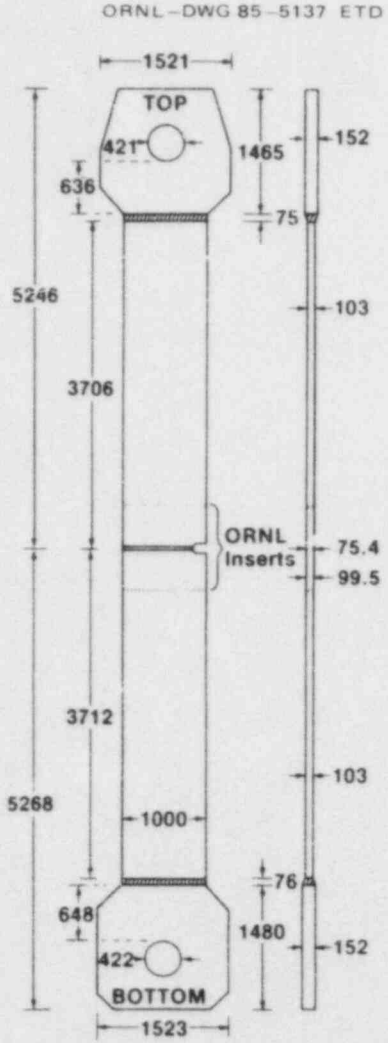

Fig. 5.2. Specimen dimensions for third wide-plate crack-arrest test WP-1.3. (All dimensions are in millimeters ± 2 mm.)

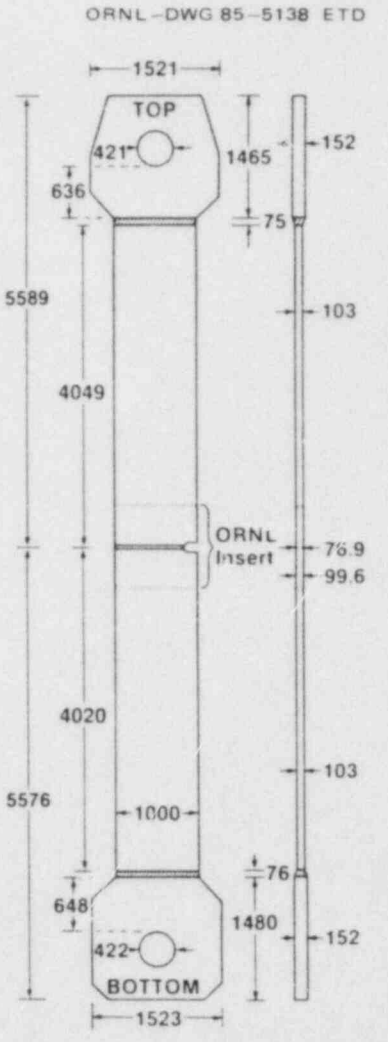

Fig. 5.3. Specimen dimensions for fourth wide plate crack-arrest test WP-1.4.

Table 5.1. Detailed dimensions of wide-plate crack-arrest specimens

Specimen feature	Dimensions (mm)	
	WP-1.3	WP-1.4
Width, w	1000	1000
Thickness, B	99.5	99.6
Side-grooved thickness,[a] B_N	75.4	76.9
Notch length	185	202.0
Initial crack length, a_o	197	207.5
Thickness at crack tip[b]	47.5	33.8

[a]Specimens were side grooved by 12.5% on each side.

[b]The crack-tip region was ground to a chevron configuration to enhance the stress concentration.

By using a fluorocarbon pressurizing instead of ethanol medium, the ORNL pillow jack initiated crack propagation in WP-1.4 with a tensile load that was low enough to obtain a completely stable arrest. The load was maintained constant for several minutes after arrest without further consequence. The load was then increased until a second run-arrest event occurred. This second arrest was not completely stable because a tearing fracture occurred in about 30 s.

5.2.2 Test descriptions

5.2.2.1 Test WP-1.3. Three steps were taken in WP-1.3 in attempts to initiate crack propagation at tensile loads lower than had been experienced in WP-1.1 and WP-1.2. The first step was to cut the crack front into a chevron configuration with the expectation that the stress-intensity factor would be elevated approximately by the square root of the ratio of the original crack-plane width to the chevron crack width. Three-dimensional (3-D) pretest analyses confirmed that this was approximately correct. In particular, pretest 3-D analyses predicted that a 50% reduction in the crack-front width would lead to a 35% increase in K_I. The actual crack front on specimen WP-1.3 was cut to a width of 4.75 cm from the original crack-plane width of 7.62 cm.

The second step was to impose on the specimen a temperature gradient that would have the temperature at the crack tip somewhat lower than for either of the previous tests. The target temperature distributions for the first four tests (WP-1.1 through WP-1.4) are illustrated in Fig. 5.4.

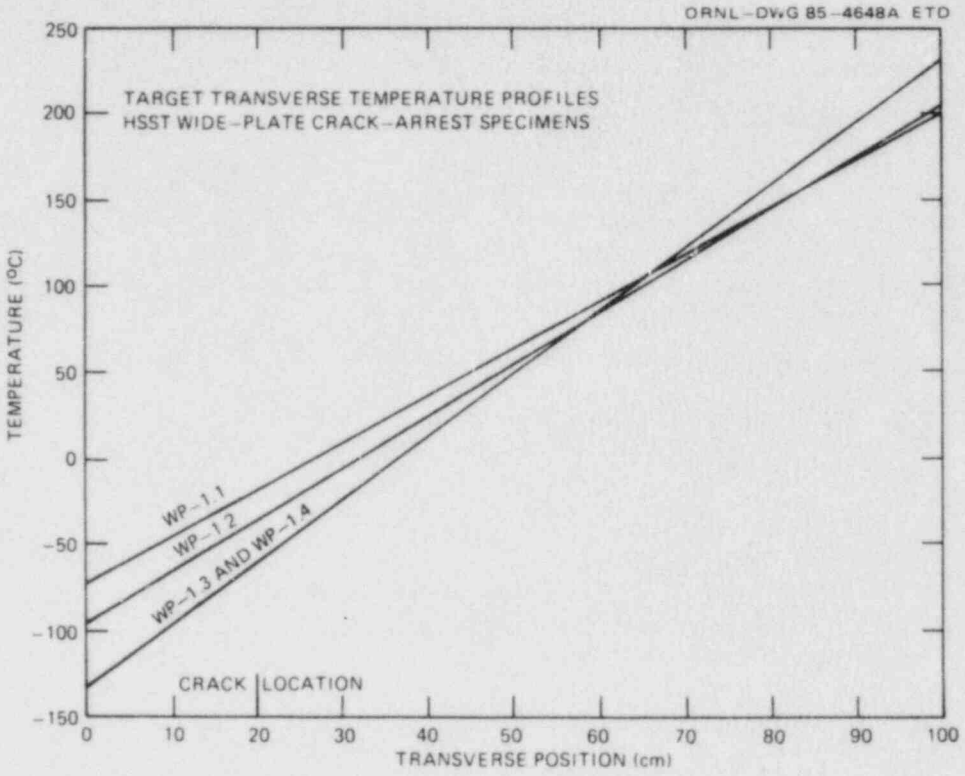

Fig. 5.4. Target temperature profiles for the first four wide-plate tests.

The target crack-tip temperatures were −18, −33, −60, and −60°C for WP-1.1, -1.2, -1.3, and -1.4, respectively. The lower temperature would, of course, lower the initiation load by lowering K_{Ic}. On the basis of the $K_{Ic}(T)$ correlation used in this study (see Sect. 5.3), a change of temperature from −33 to −60°C reduces K_{Ic} from 85 to 65 MPa•$\sqrt{m}$.

The third step was that a pillow jack (Sect. 5.2.4) was designed and fabricated by ORNL to apply pressure loading along the faces of the specimen notch. The first part of the loading plan for WP-1.3 was to apply the tensile load at a rate of 13 KN/s up to a maximum load of 10 MN. If crack propagation had not occurred at this point, the notch was to be pressure loaded by the pillow jack. If the crack tip was at −60°C, pretest analyses suggested that a notch pressure of about 25 MPa would be sufficient for initiation. Figure 5.5 shows a schematic of the pillow-jack design, while Fig. 5.6 shows pretest results of tensile load vs pressure load to give specified K_I values for WP-1.3. Figure 5.6 includes the effects of reducing the crack width in a chevron configuration to 50% of the specimen width. It was expected that initiation would occur prior to 188 MPa•$\sqrt{m}$. As will be seen in Sect. 5.4, actual initiation occurred at 173.5 MPa•$\sqrt{m}$.

The temperature gradient was imposed on the specimen after all instrumentation and insulation were installed. Liquid nitrogen cooling of the notched edge of the specimen was begun at 1:00 a.m. on May 9 and continued until 7:30 a.m. when the crack-tip temperature had reached −60°C

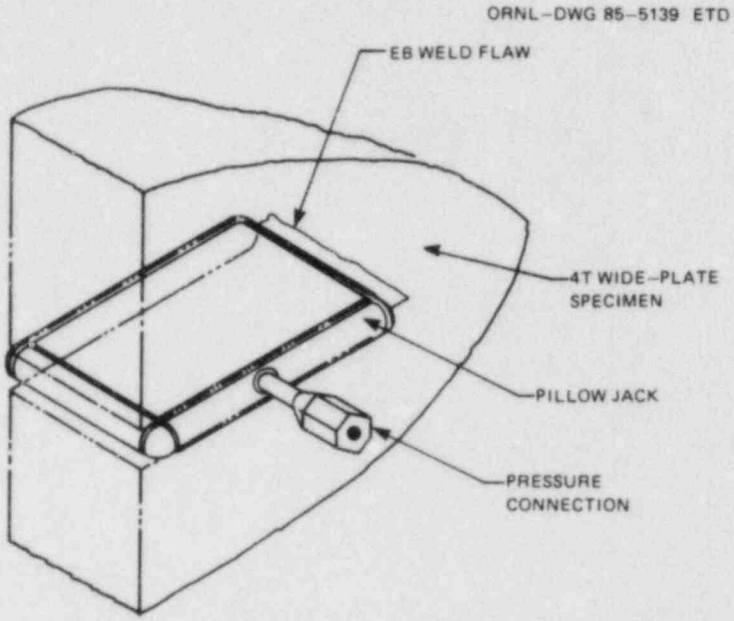

Fig. 5.5. Schematic of a pillow jack designed to apply pressure loading to the flat notch faces of WP-1.3.

(see Table 5.2). At this point, heating of the other edge was initiated. After about 5 h, the target temperature was being approached, and final calibration of the strain gages was undertaken. When this was completed, the system was ready for the test at about 2:15 p.m.; however, the temperatures over the cold half of the specimen were about 10°C above the target (see Table 5.2). An attempt was made to quickly reduce the crack-tip (20-cm location) temperature (T_{CT}) to the target value, but the heat flow conditions at this point did not allow T_{CT} to fall even after several minutes of severe cooling of the specimen's edge. At this point, approximately 3:45 p.m., specimen loading was initiated with the temperature distribution shown in Table 5.2.

The axial load and the crack-opening-displacement (COD) gage (at the 125-mm location, as described in Sect. 5.2.3) histories prior to crack propagation are shown in Figs. 5.7 and 5.8. Loading took place at ~13 KN/s. At 10 MN, a pause in the axial loading took place while an attempt was made to initiate crack propagation by use of the pillow jack installed in the notch. While the remotely controlled, high-pressure pump functioned as expected, the pressurizing media in the jack froze during the final (1-h) attempt to drop the crack-tip temperature. If more time had been taken to develop the final adjustment to the temperature gradient, this freezing would not have occurred, and initiation would have taken place at the target tensile load. Tensile loading was continued as shown in Figs. 5.7 and 5.8, and crack propagation occurred shortly thereafter at a load of 11.25 MN (2.53×10^6 lb). The temperature gradient at this time is shown in the final column of Table 5.2. After the major fracture event, it was found that the specimen had not broken entirely in two. Reloading took place, and final separation of the specimen occurred at a load of 0.912 MN (205 kips).

Table 5.2. Temperature gradient along crack plane at various times during wide-plate crack-arrest test WP-1.3

Thermocouple No.	Distance from cold edge (cm)	Temperature (°C)				
		Target profile	7:30 a.m., heaters turned on	2:15 p.m.	3:47 p.m., start of load application	4:20 p.m., crack propagation
0	0	−133	−115	−152	−175	−183
1	10	−97	−89	−96	−105	−110
2	20	−60	−60	−51	−51	−51
3	30	−24	−41	−18	[a]	[a]
4	40	13	−27	14	23	24
5	50	50	−17	46	57	59
6	60	86	−9	80	92	94
7	70	123	−3	120	131	132
8	80	159	1	160	168	169
9	90	196	4	201	205	206
10	100	233	5	233	233	233

[a]Thermocouple No. 3, which was located 30 cm from the cold edge of the plate, became inoperative during the test.

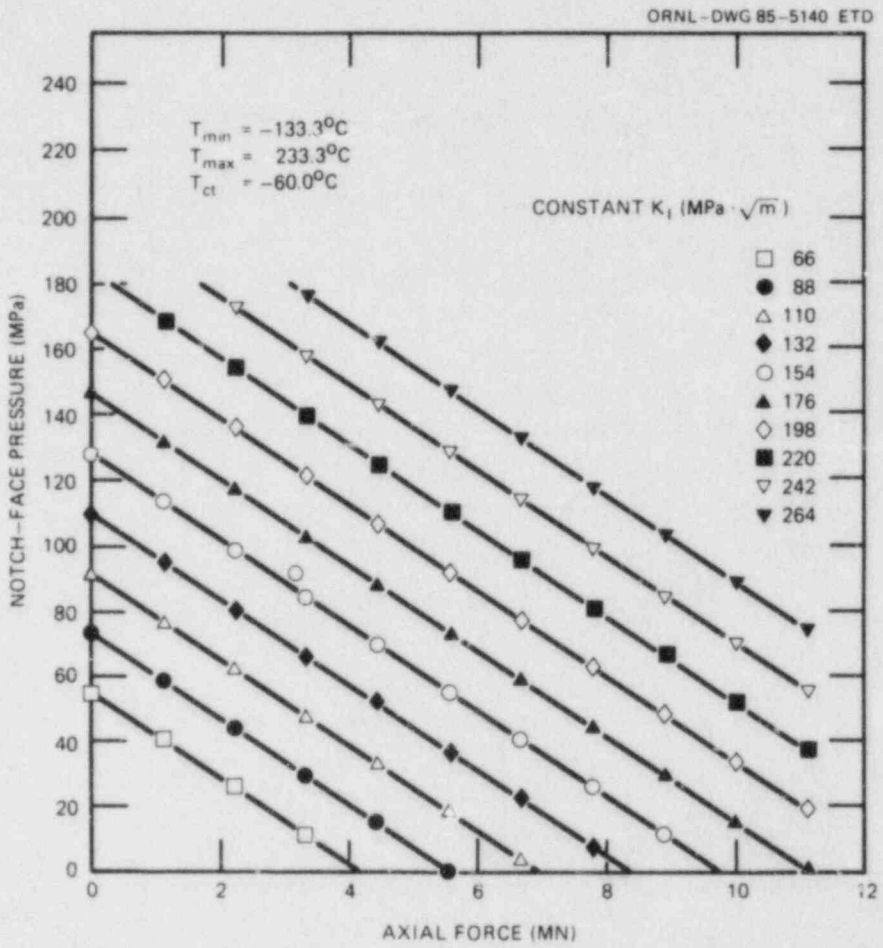

Fig. 5.6. Combination of notch-pressure loading and tensile loadings to give various K_I values for WP-1.3 (including chevron notch width to specimen width ratio of 0.5).

5.2.2.2 Test WP-1.4. The test plan adopted for WP-1.4 was essentially the same as the original plan for WP-1.3 but with the axial load at initiation set low enough to ensure a crack run-arrest event that was completely stable with respect to tearing and tensile criteria described in Refs. 4 and 5. The crack front was again cut into a chevron configuration to elevate the stress-intensity factor above that corresponding to a through-thickness crack-plane width. The actual crack front on specimen WP-1.4 was cut to 3.4 cm from the original width of 7.7 cm. The target temperature distribution was the same as that for test WP-1.3, as indicated in Fig. 5.4. For a target crack-tip temperature of −60°C, the $K_{Ic}(T)$ correlation used in this study (see Sect. 5.3) gives an initiation value of 65 MPa·$\sqrt{m}$.

The first part of the loading plan for WP-1.4 called for application of the tensile load up to a maximum of 8 MN. If crack propagation had not taken place at this point, notch-pressure loading was to be applied with the pillow jack. Pretest analysis indicated that for a crack-tip temperature of −60°C and an axial load of 8 MN, the wide-plate specimen

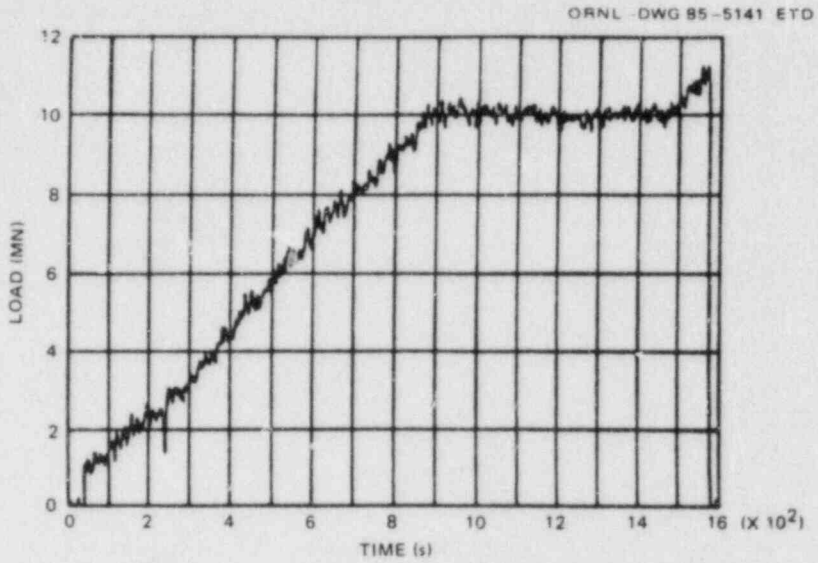

Fig. 5.7. Tensile load vs time plot for WP-1.3.

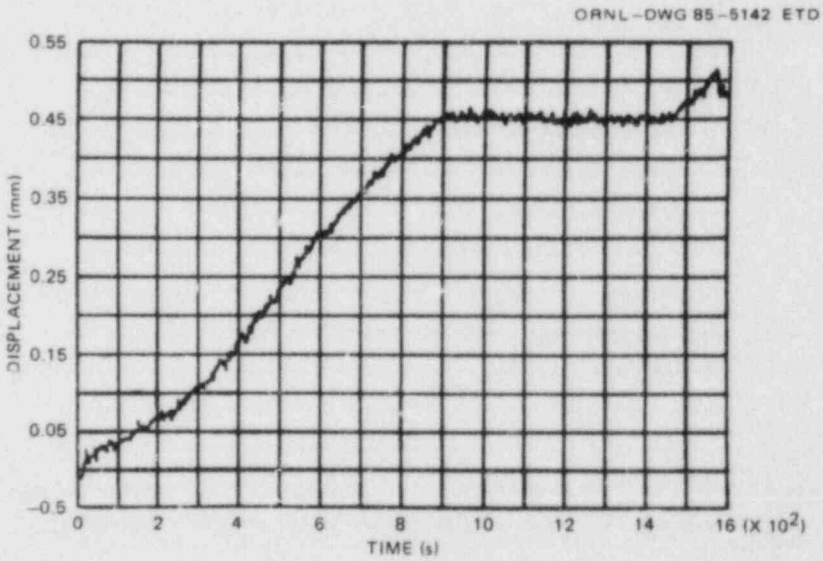

Fig. 5.8. Notch-opening displacement (at 120 mm from cold edge) vs time response for WP-1.3 during application of tensile load.

would require a minimum notch pressure of 35 MPa for crack initiation. This estimate was based on an initiation ratio K_I/K_{Ic} from test WP-1.3 of ~2.5 (see Sect. 5.4). Posttest results in Sect. 5.4 indicate that actual initiation for WP-1.4 occurred at K_I = 213 MPa$\cdot\sqrt{m}$, giving a K_I/K_{Ic} ratio of 3.3.

The WP-1.4 test was performed at NBS on the morning of July 19, 1985. After the desired temperature gradient was obtained, application of the axial load commenced at 10:15 a.m. with the temperature distribution shown in Table 5.3. The average loading rate was 15.5 MN/s. The

Table 5.3. Temperature gradient along crack plane at various times during wide-plate crack-arrest test WP-1.4

Thermocouple No.	Distance from cold edge (cm)	Temperature (°C)				
		Target profile	10:15 a.m., start of load application	10:30 a.m., first run-arrest event	10:35 a.m., second run-arrest event	10:35:31 a.m., final fracture event
0	0	−134	[a]	[a]	[a]	[a]
1	10	−98	−112	−108	−106	−106
2	20	−61	−66	−65	−67	−66
3	30	−24	−25	−26	−26	−26
4	40	12	14	14	14	14
5	50	49	52	51	50	53
6	60	86	89	88	87	88
7	70	122	126	125	125	124
8	80	159	162	162	161	161
9	90	196	198	198	198	198
10	100	233	222	222	223	223

[a]Thermocouple 0, which was located on the cold edge of the specimen, was inoperative.

loading history and COD histories from two (a large and a small) COD gages (see Sect. 5.2.3 for the positions of these gages) are shown in Fig. 5.9 for the complete test. At 7.952 MN (1.788×10^6 lb) the tensile load was maintained constant for 104 s while the pillow jack was pressurized. Crack initiation occurred at a measured pressure of about 63.4 MPa (9200 psi) in the pillow-jack system. As planned, the running crack arrested in a stable configuration. The load fell abruptly to 7.618 MN but was returned to 7.892 MN in 43 s and held there for 97 s. At the end of this period, axial loading was resumed, and a second initiation took place at a tensile load of 9.720 MN (2.185×10^6 lb) with zero pillow-jack pressure. The crack appeared to arrest in a stable fashion at a load of 6.885 MN (1.548×10^6 lb). This arrest load was maintained over a period of 30 s at which time the specimen became plastically unstable and tore nearly in two. A final loading to 0.835 MN (187,700 lb) was required to completely fracture the specimen. The temperature gradients appropriate to these events are also shown in Table 5.3. The temperatures recorded by all of the thermocouples at the time of the first run-arrest event in WP-1.4 are shown in Table 5.4.

Table 5.4. Measured temperatures over the specimen and pull plates for wide-plate crack-arrest test WP-1.4 at time of first run-arrest event[a]

Thermocouple No.[b]	Temperature (°C)	Thermocouple No.[b]	Temperature (°C)
1	−109	18	−47
2	−65	19	48
3	−26	20	142
4	14	21	44
5	51	22	−61
6	88	23	38
7	125	24	133
8	162	25	−24
9	198	26	147
10	222	27	−61
11	−43	28	133
12	53	29	−35
13	146	30	30
14	56	31	37
15	−24	32	76
16	58	33	7
17	147		

[a]See Fig. 5.11 for locations of the thermocouples.

[b]Thermocouple 0 did not function during this test.

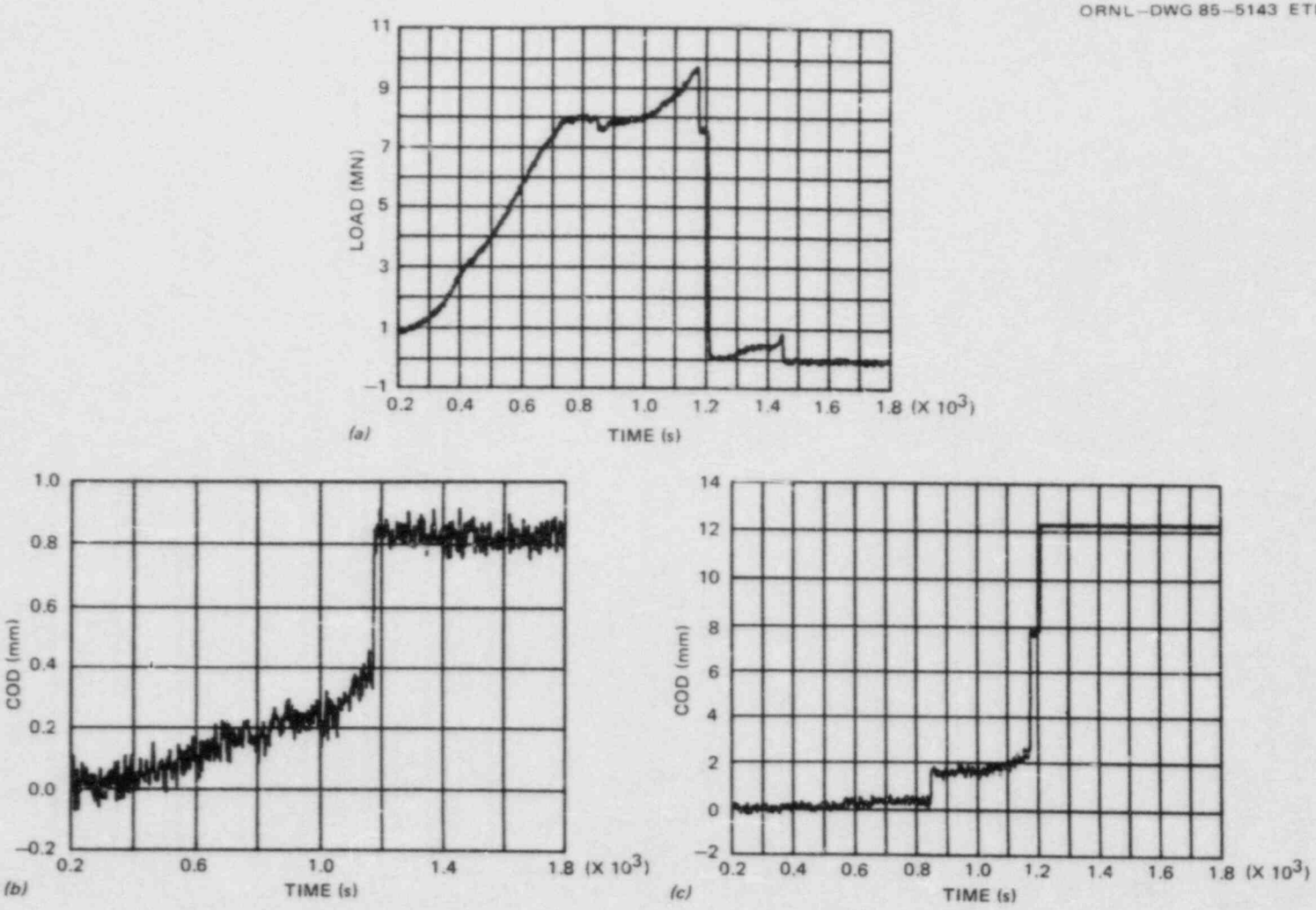

Fig. 5.9. (*a*) Complete load record of WP-1.4, (*b*) complete record of small COD gage, and (*c*) complete record of large COD gage.

5.2.3 Test instrumentation

Thermocouples were placed on WP-1.3 and WP-1.4 as shown in Figs. 5.10 and 5.11, respectively. Small holes (1.5-mm diam and 3 mm deep) were drilled in the plates, and thermocouples were inserted and potted in these. The additional thermocouples used for control of heating and

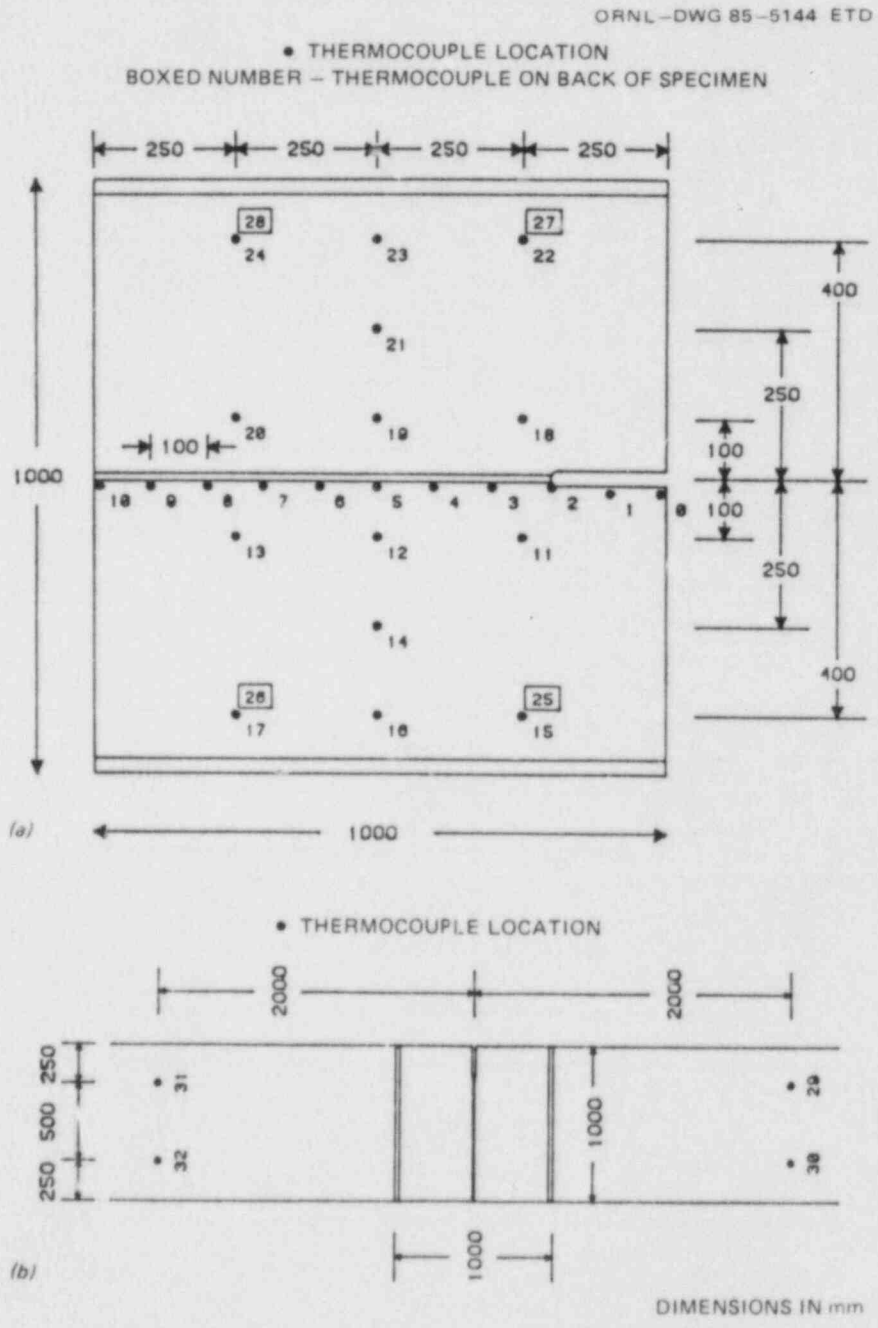

Fig. 5.10. Thermocouple locations for WP-1.3. (*a*) Specimen thermocouples, (*b*) pull-plate thermocouples.

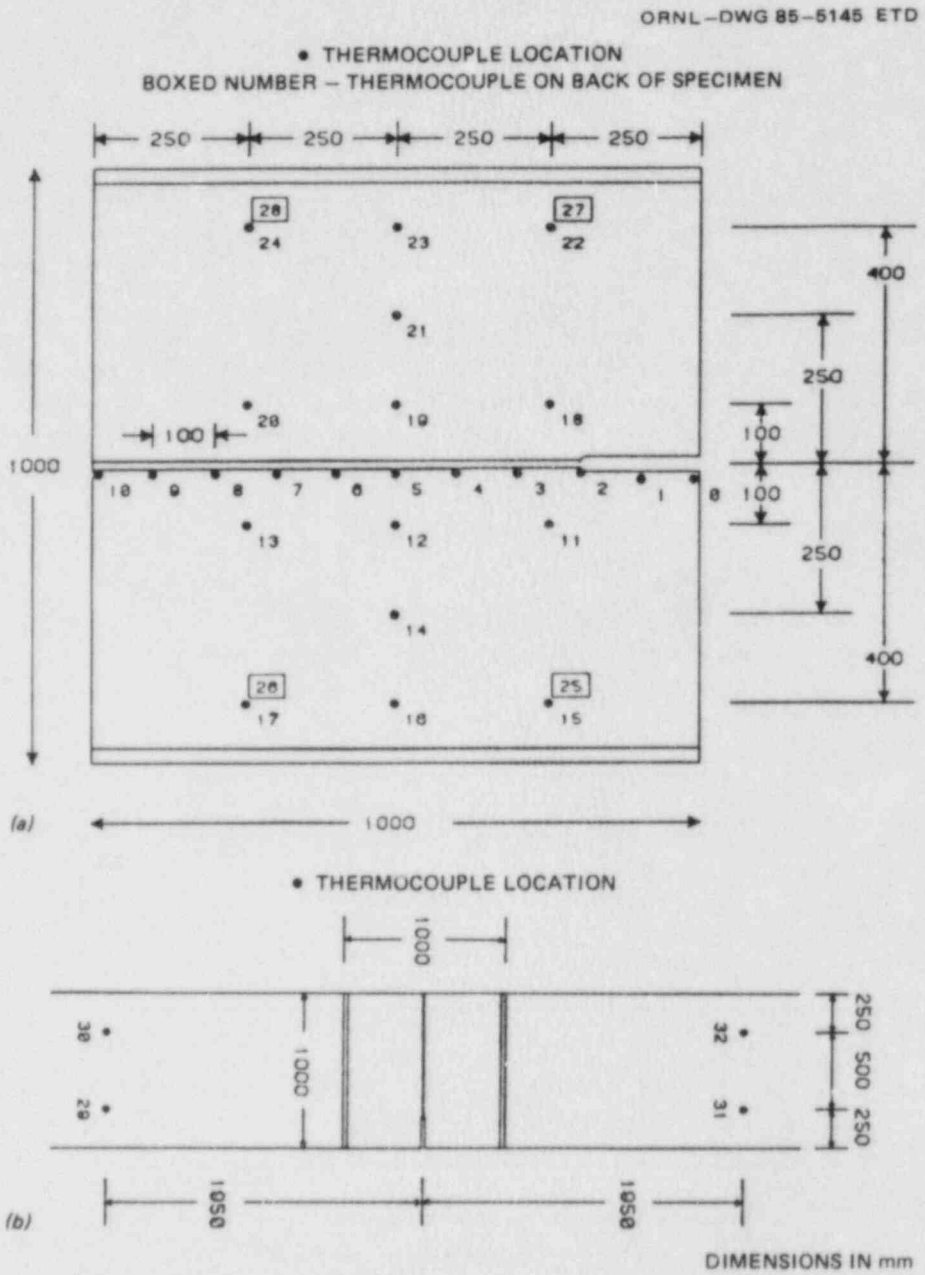

Fig. 5.11. Thermocouple locations for WP-1.4. (a) Specimen thermocouples, (b) pull-plate thermocouples.

cooling are not indicated. All thermocouple wires were connected to copper lead wires in an insulated junction box with the temperature monitored by a thermistor for room-temperature compensation. The thermocouple wires were sequentially monitored on a periodic basis and corrected for room temperature. The results were also viewed on the computer screen that was collecting the data. This data collection system additionally monitored and recorded the load-cell output of the testing machine and the time. For WP-1.3, two COD gages were located at 120 and

175 mm from the cold edge of the plate. For WP-1.4, two COD gages were placed at 150 mm from the cold edge, a small sensitive gage on the back, and a larger gage on the front of the specimen. NBS crack-velocity gages were mounted on the back side of the specimen along the crack-propagation plane in test WP-1.3. The velocity gages were not used in test WP-1.4. For both tests, an acoustic emission transducer was located on the lower pull tab. For both WP-1.3 and WP-1.4, all of the instrumentation functioned through most of the test, and the data were recorded on magnetic tape.

In tests WP-1.3 and WP-1.4, far-field strain gages were mounted as shown in Figs. 5.12 and 5.13. The two three-element, 90° rosettes positioned 250 mm from the edges of the pull plate and 1800 mm above the crack plane in WP-1.3 were replaced by single-element longitudinal gages

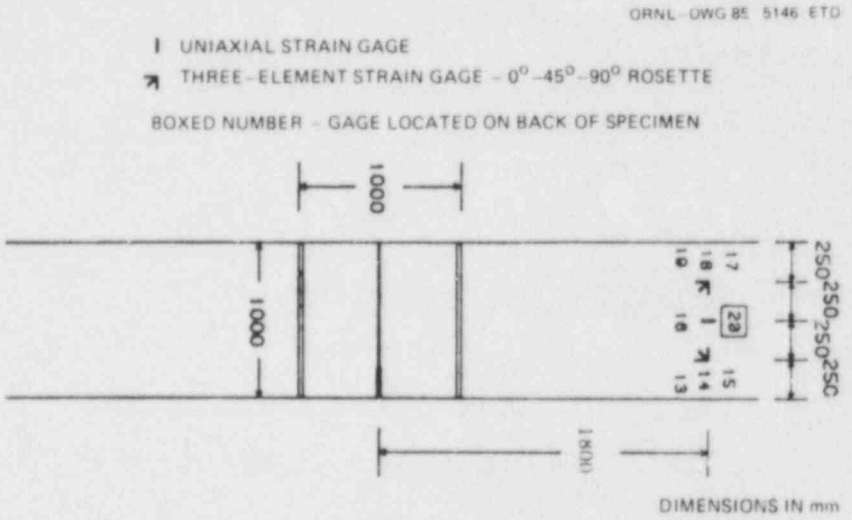

Fig. 5.12. Far-field strain gage locations for WP-1.3.

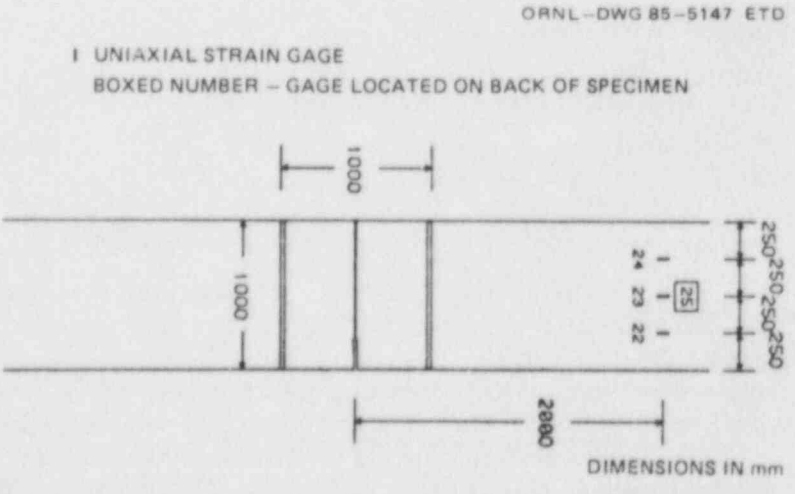

Fig. 5.13. Far-field strain gage locations for WP-1.4.

for test WP-1.4. This change freed four recording channels that could be used for additional crack-line gages in the latter test. These crack-line gages are shown in Figs. 5.14 and 5.15, where the positions of other near-field gages are also defined. As indicated in Figs. 5.14 and 5.15, the 8 pairs of crack-line gages evenly spaced at 65-mm intervals above and below the crack line in test WP-1.3 were replaced by a single row of 12 gages spaced at 40- and 50-mm intervals above the crack line for test WP-1.4. In addition, the crack-line gage closest to the initial crack tip (gage 1) and positioned 300 mm from the cold edge in WP-1.3 was moved to a point 250 mm from the cold edge for WP-1.4. These changes in the number and position of the crack-line gages were intended to provide more accurate data for determining the position of the crack tip as a function of time during the run-arrest events. For both tests, the crack-line gages were two-element, 90°, stacked rosettes of a nickel-chromium alloy grid and connected to the bridges in a fashion to eliminate temperature effects. As a consequence, the crack-line gage outputs are proportional to the difference between the longitudinal and transverse strains. For test WP-1.4, the 90° rosettes numbered 13 through 16 were oriented (2 on the front and 2 on the back) at 45° to the crack line at the request of UM.[6] Mounting at this angle removes the effect of the constant stress term from the strain-gage output and permits K_I to be calculated more accurately from series expansions and the gage data. Additional discussion of this configuration is given in Sect. 5.6.2 of this report.

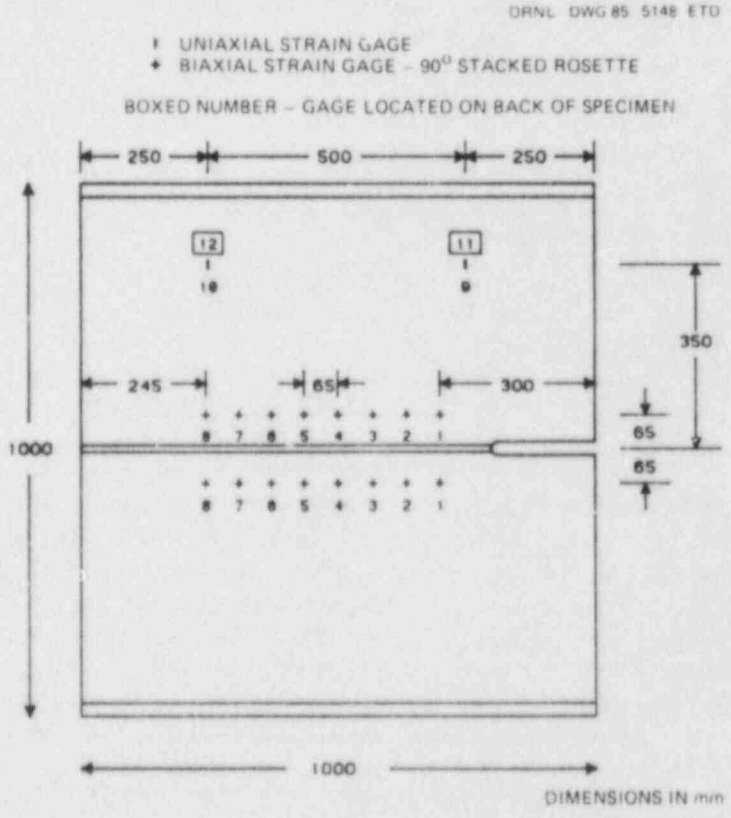

Fig. 5.14. Near-field strain gage locations for WP-1.3.

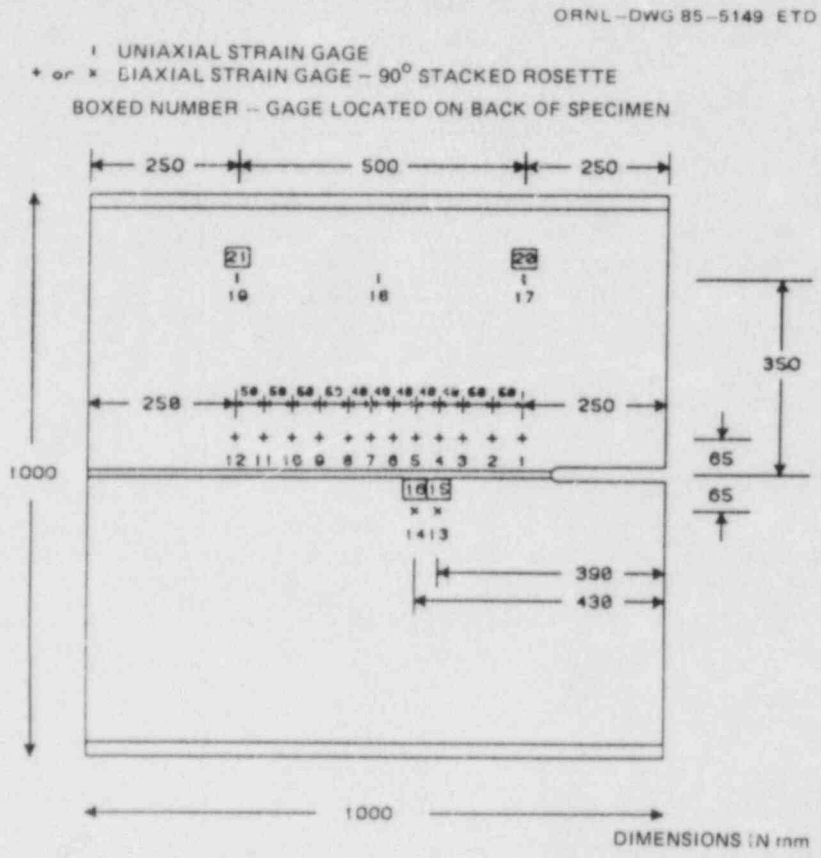

Fig. 5.15. Near-field strain gage locations for WP-1.4.

5.2.4 Wide-plate auxiliary loading device

Because the loadings required to initiate crack propagation in wide-plate crack-arrest specimens WP-1.1 and WP-1.2 were so high, they could not result in stable arrest. Therefore, a pillow-jack device was designed and developed to provide complementary loading in the machined notch of the specimens (Fig. 5.5). It was anticipated that the tensile loading provided by the NBS testing machine could then be reduced sufficiently to result in stable arrest.

ORNL designed the pillow jack, which is essentially a rectangular bellows-type device that employs a solid stainless steel ballast to fill the void volume and is pressurized with a small, portable, air-driven intensifier using ethyl alcohol and silicone oil as a combination pressuring media. The pillow jack fits into the 25-mm-high machined groove in the warm prestressing (WP) specimens that was subjected in the WP-1.3 test to a temperature gradient ranging from −60 to −133°C. The temperature expected at the pressure connection was −97°C, above the freezing point of ethyl alcohol (−117.3°C) and below the freezing point of the silicone oil placed in the intensifier (−55°C). The pillow jack was designed to function as a bellows to provide the load-displacement characteristics desired, with consideration given to the temperature dependence

of the mechanical properties of the type 304L stainless steel material from which the device was made.

Prior to utilizing the device in the WP-1.3 test, ORNL loaded a full-scale, mock-up wide-plate specimen by a pillow jack and cooled it with liquid nitrogen to achieve the WP-1.3 test parameters. Figure 5.16 shows the COD measured 6.35 mm from the cold face as a function of pressure of the pressurizing media. The pressure was increased until the pillow jack failed at 186 MPa, which compared reasonably well with a calculated burst load of 207 MPa. In this mock-up test no provisions were made for the effect of far-field load, and, in particular, the small clearance between the pillow jack and the machined notch was fitted with shims. Analyses showed that these COD measurements were close to expectations.

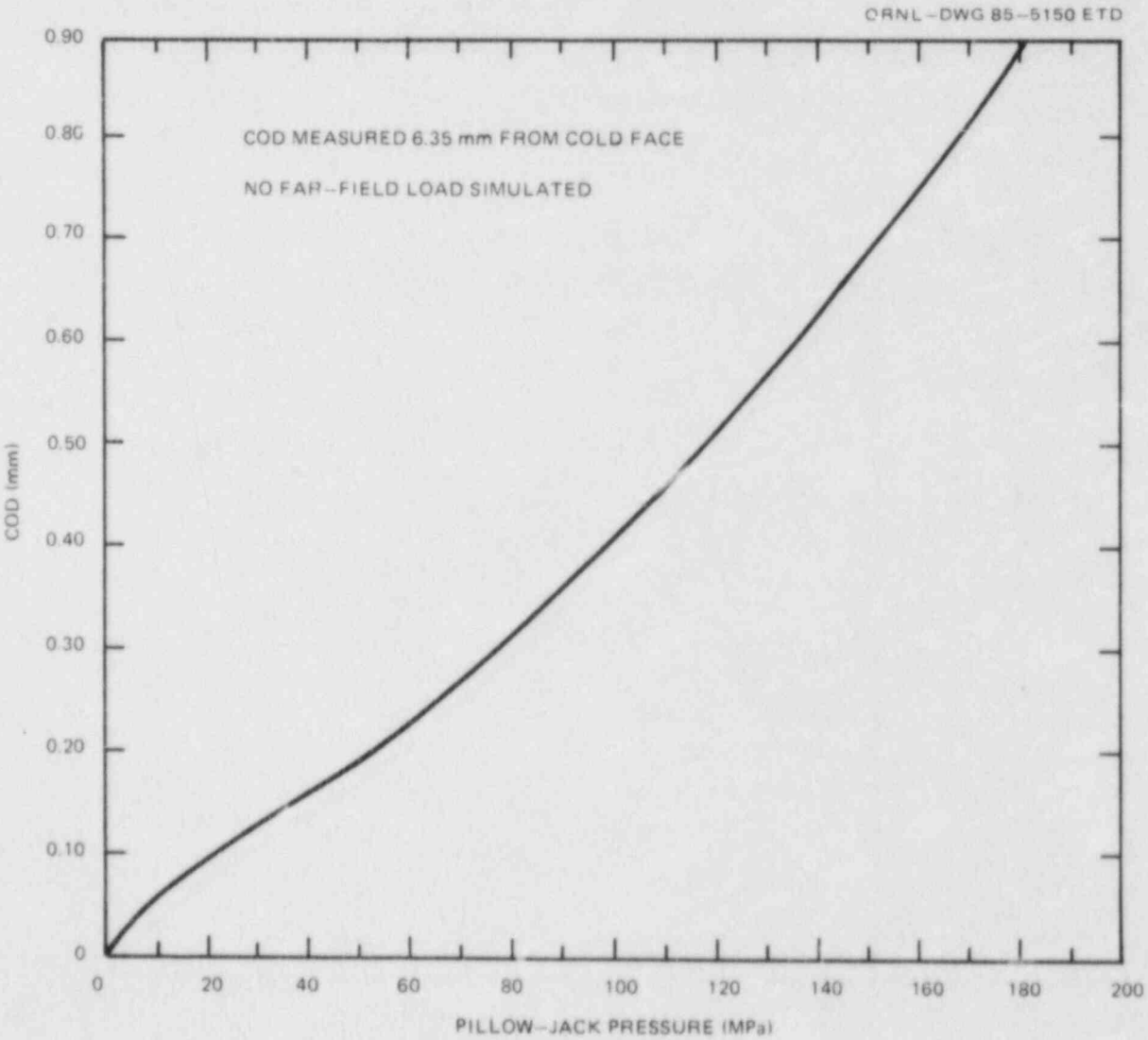

Fig. 5.16. Pressure vs displacement characteristics of a wide-plate specimen undergoing loading by a pillow jack.

The results of Fig. 5.16 coupled with analysis justified the incorporation of a pillow jack in the WP-1.3 test. Unfortunately, the planned temperature distribution for WP-1.3 was not maintained, and the pressurizing media froze. As a result, the complementary loading device was inoperative in WP-1.3. It was concluded that a lower freezing point pressurizing medium would be required.

Because of its substantially lower freezing point (−160°C) and its acceptable toxicity and flammability characteristics, Freon 22* was selected to be used in WP-1.4 in place of ethyl alcohol. Appropriate modifications were made to the pillow-jack design and to the pressurizing equipment, and a mock-up test was performed. In this mock-up, a tensile loading was simulated by using tapered shims between the pillow jack and machined notch so that a linearly varying gap of 0.64 mm at the cold face to zero at the bottom was achieved. Figure 5.17 shows that the COD measured 5.72 mm from the cold face as a function of the pressurizing media. These results justified the application of the equipment in the WP-1.4 test.

*E. I. du Pont trade name.

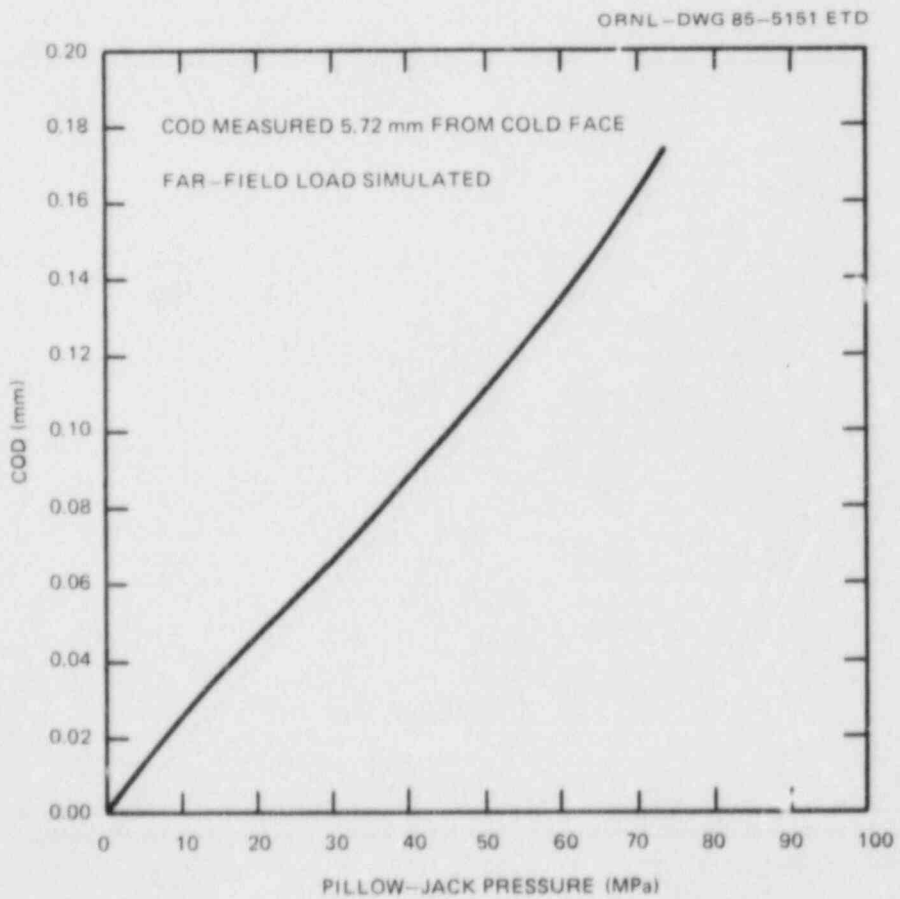

Fig. 5.17. Pressure vs displacement characteristics of pillow-jack loaded wide-plate specimen mockup.

5.2.5 Test results

5.2.5.1 Test data from WP-1.3. The fracture surface for WP-1.3 is shown in Fig. 5.18, and a close-up of the chevron in Fig. 5.19. The initial crack length (notch plus EB weld crack) was 197 mm. The fracture surface reveals that the crack remained in the side-grooved region during propagation. No branching had taken place, and the whole fracture surface is very flat compared with WP-1.1 and WP-1.2. No shear lips are present on the fracture surface. Arrest with a nearly straight-line crack front occurred at a/w = 0.485. After a brief extension by tearing, reinitiation of cleavage fracture occurred on one side of the crack at a/w = 0.495. This cleavage zone spread only one-half of the way through the plate thickness and extended forward to a/w = 0.53. The remainder of the crack extension was fibrous fracture. There is a final region of

ORNL-PHOTO 7082-85A

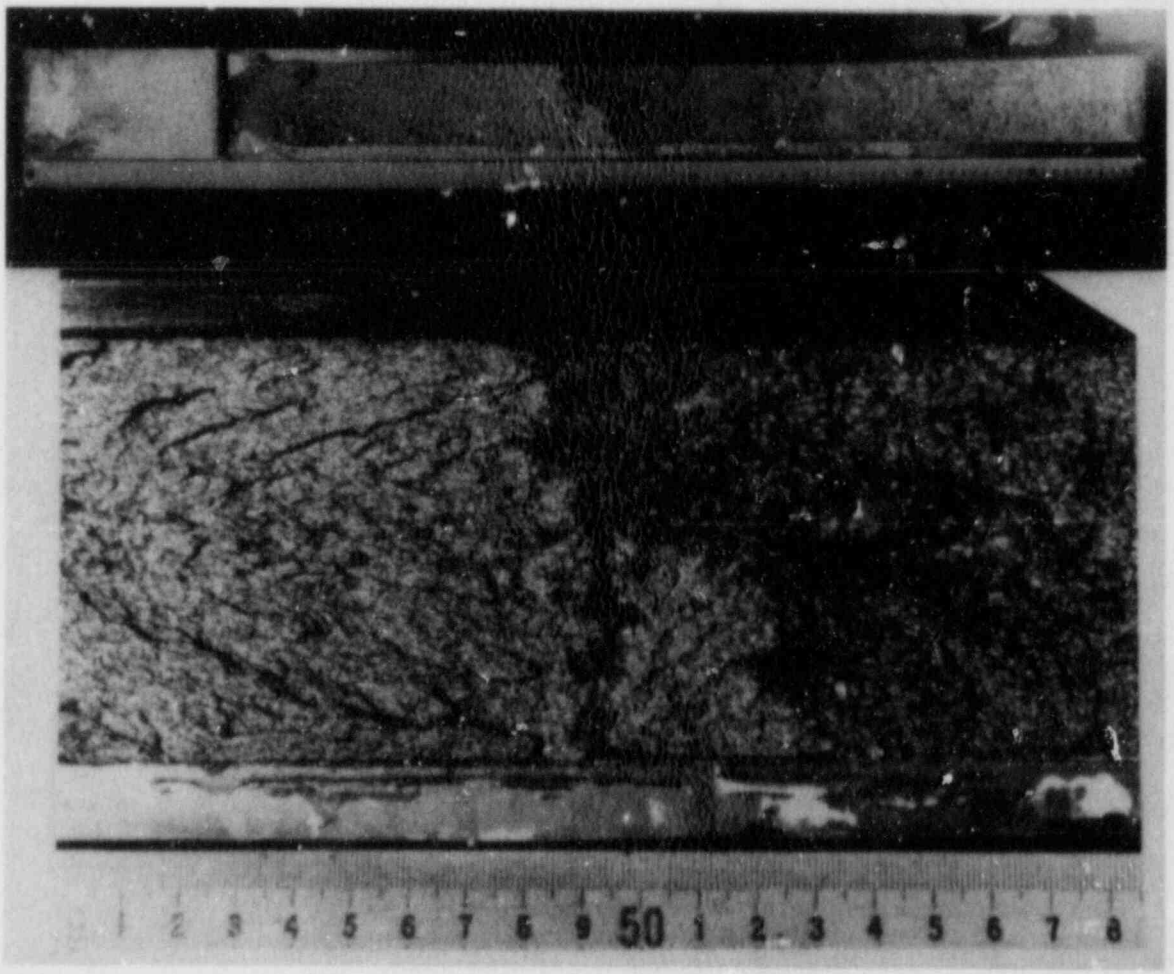

Fig. 5.18. Fracture surface for HSST wide-plate test WP-1.3 showing nearly planar arrest front followed by small amount of tearing and segment of cleavage reinitiation before unstable tearing.

ORNL-PHOTO 7081-85A

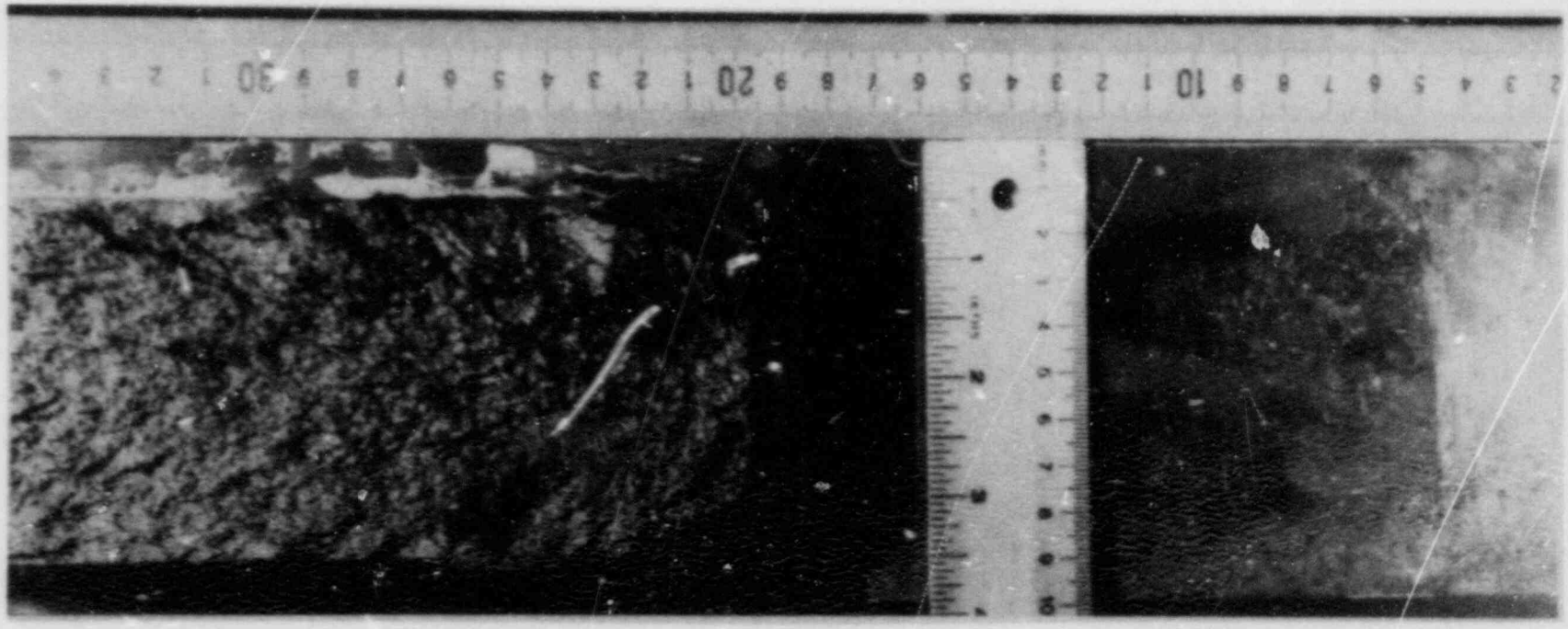

Fig. 5.19. Initial crack for HSST wide-plate test WP-1.3 in a chevron configuration with crack front-to-net section ratio of 0.625.

back-face shear associated with the separation of the specimen into two halves that occurs at a/w = 0.97.

The outputs of the crack-line strain gages are shown in Figs. 5.20–5.22. The strain recorded by the crack-line gages represents the difference between the longitudinal and transverse strain at the positions shown in Fig. 5.14. Vertical and horizontal gage elements were used in the electronic bridge to allow automatic temperature compensation. Figures 5.20 and 5.21(*a*) and (*b*) show the output on different time scales of Gage 4, located just ahead of the point of crack arrest. Similarly, Fig. 5.22 shows the response of Gage 8 over two important intervals of the test: during the early portion of the propagation and the period after the 2-s arrest (or slow tearing) period.

Data from the other strain gages are shown in Figs. 5.23 and 5.24 on the basis of two choices of time scales. Note that Gages 9 and 11, 10 and 12, and 16 and 20 were mounted on the front and back of the plate at common locations. The difference in strain readings was to register any out-of-plane bending. As observed by UM in Ref. 6, the substantial amount of out-of-plane bending present in WP-1.3 can be seen from Gages 9, 10, 11, and 12 (Fig. 5.23) mounted 350 mm above the crack line and Gages 16 and 20 mounted 1800 mm above the crack line. The results are summarized in Table 5.5. The origin of this out-of-plane bending has not been specifically identified, but it could be eccentric loading because of the plate not being centered in the clevis fixtures, residual stresses introduced by the welding procedure, or a nonplanar pull plate.

Table 5.5. Back/front strain ratios for test WP-1.3

Gage pair	Strain at initiation (microstrain)	Back/front strain ratio
9-front	550	1.7
11-back	930	
10-front	280	2.6
12-back	740	
16-front	330	2.2
20-back	720	

Figure 5.25 shows the permanent thickness changes in specimen WP-1.3 as determined by posttest measurements. The plastic deformation began to take place at approximately a/w = 0.43, which corresponds to the region where the cleavage crack propagation slowed prior to arrest at a/w = 0.485.

The velocity gages, which were mounted on the back side-groove of the specimen, were interpreted by NBS, Boulder, Colorado, and the crack

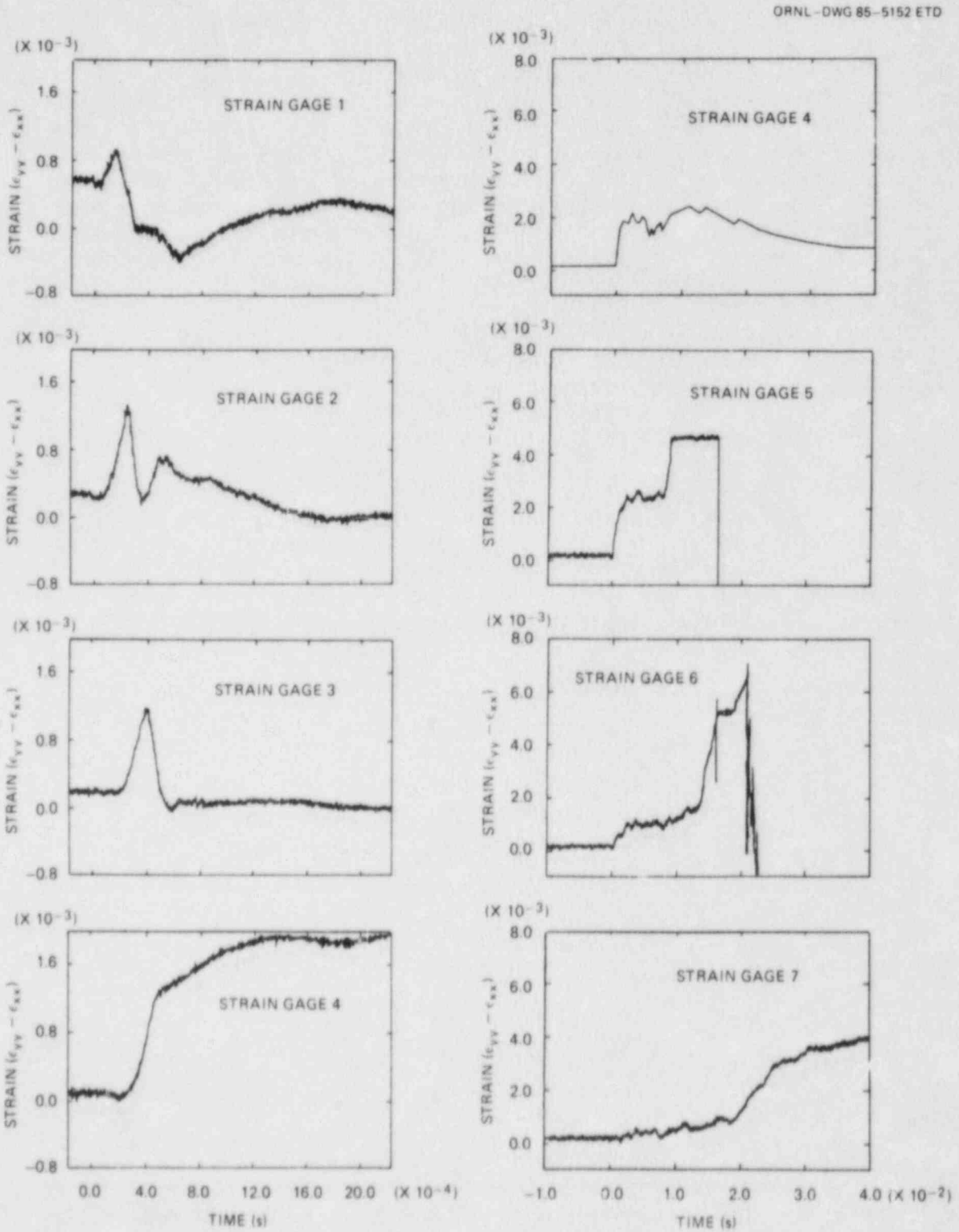

Fig. 5.20. Strain ($\varepsilon_y - \varepsilon_x$) vs time response of crack-line strain gages composed of ε_y and ε_x elements, with a gage above and below crack plane paired to give full-bridge response (Gages 1 through 7 shown) (t = 0 at initiation).

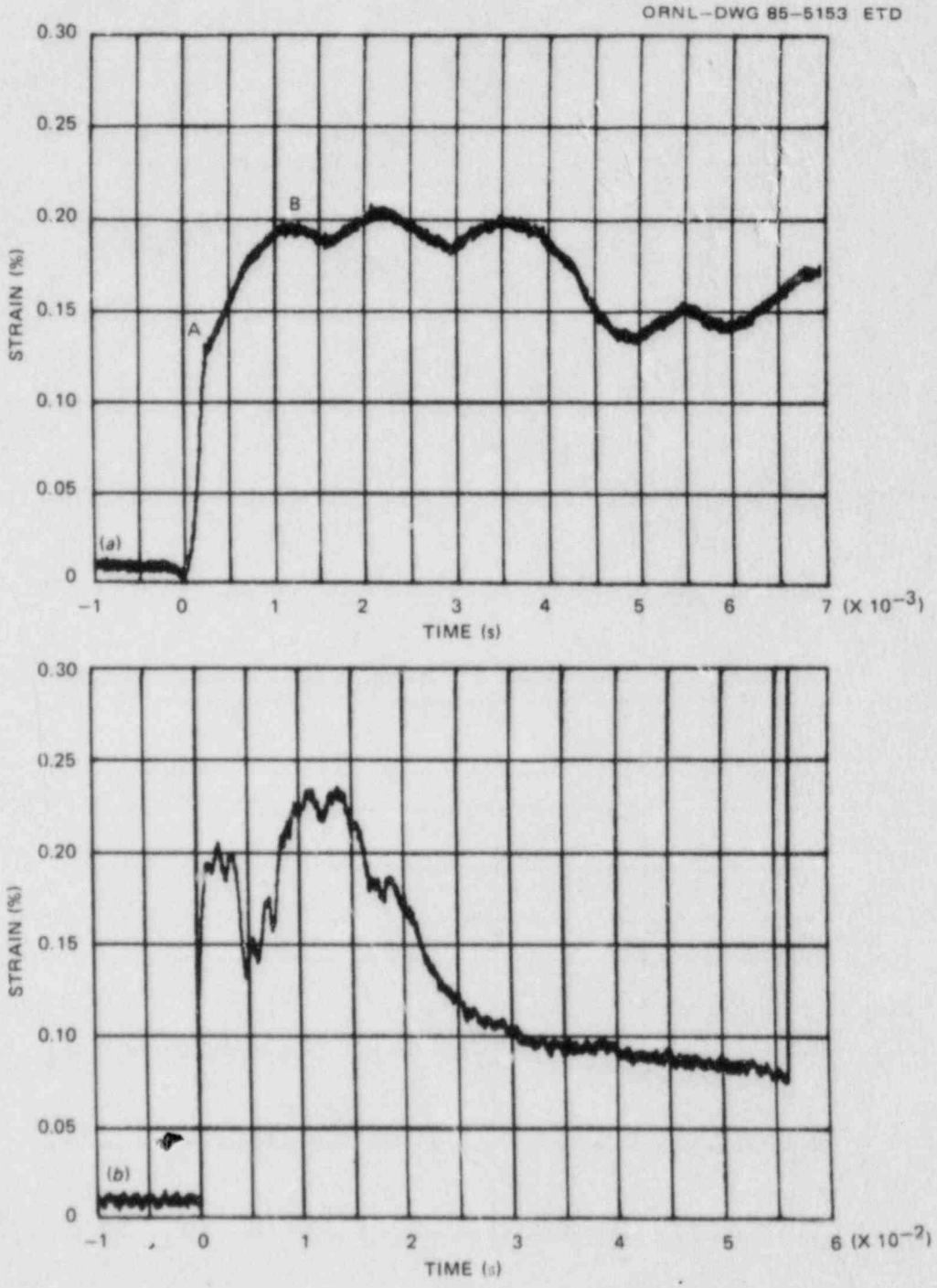

Fig. 5.21. Strain ($\varepsilon_y - \varepsilon_x$) vs time response of Gage 4 located just ahead of arrest point. (*a*) 10^{-3} scale, (*b*) 10^{-2} scale (t = −0.234 ms at initiation).

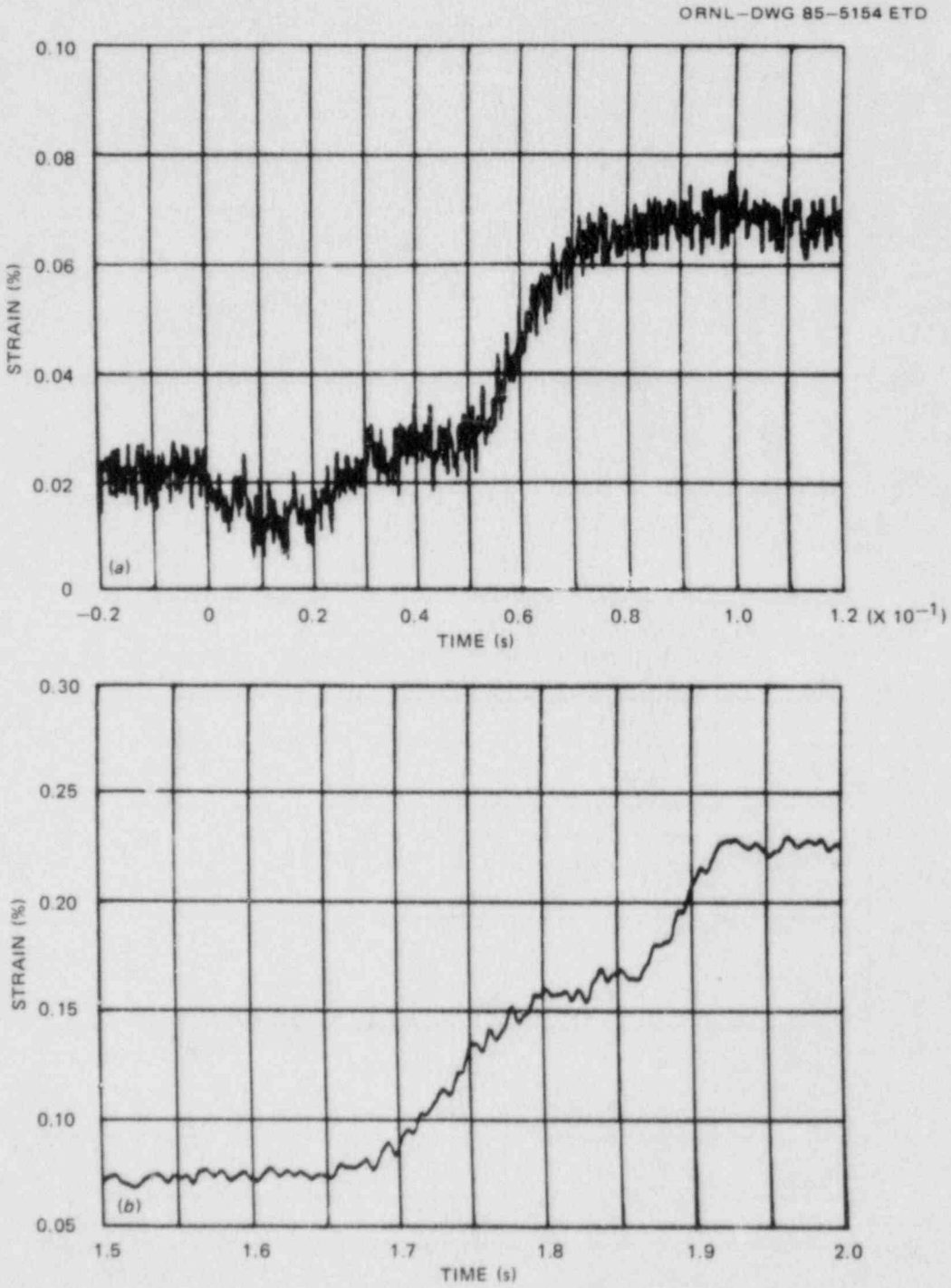

Fig. 5.22. Strain vs time response of crack line Gage 8. (*a*) Time period immediately after initiation, (*b*) time period immediately after 2-s arrest period (t = −0.234 ms at initiation).

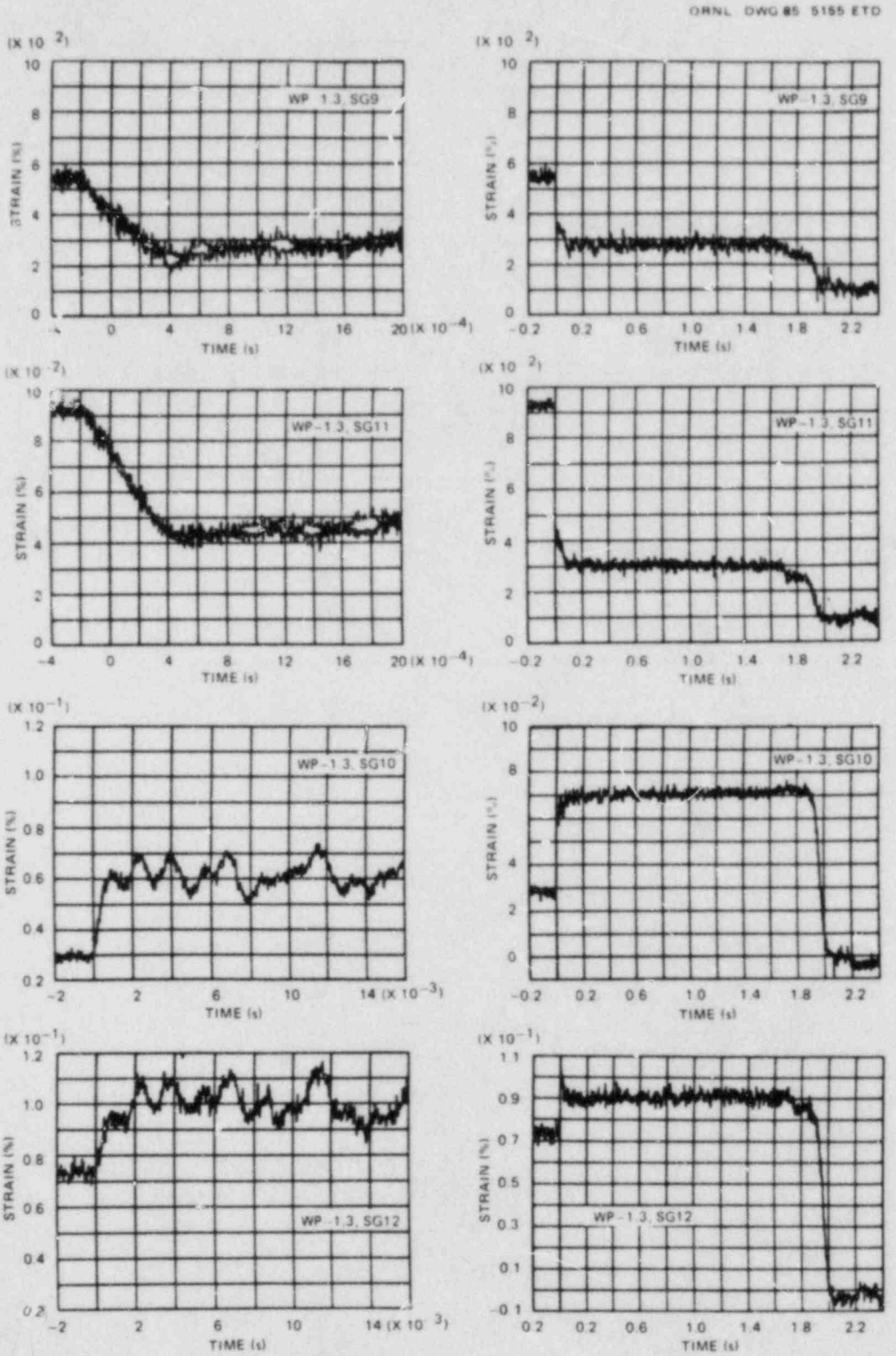

Fig. 5.23. Comparison between strain (ε_y) vs time responses of Gages 9 and 10 on front face and Gages 11 and 12 at same locations on back face of specimen WP-1.3 (t = −0.234 ms at initiation).

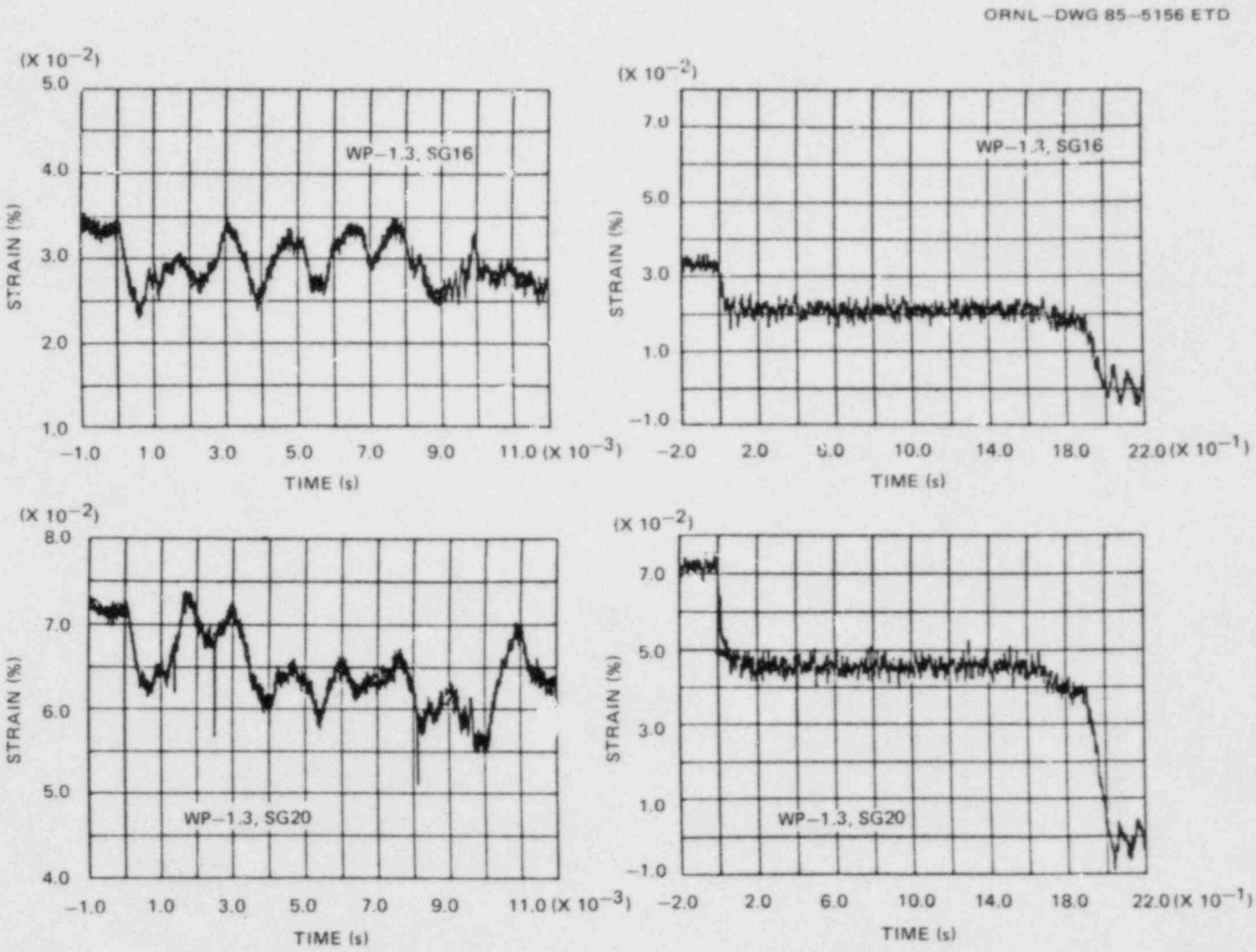

Fig. 5.24. Comparison between strain (ε_y) vs time responses of Gages 16 and 20 on opposite faces of pull plates 1800 mm above crack plane (t = −0.234 ms at initiation).

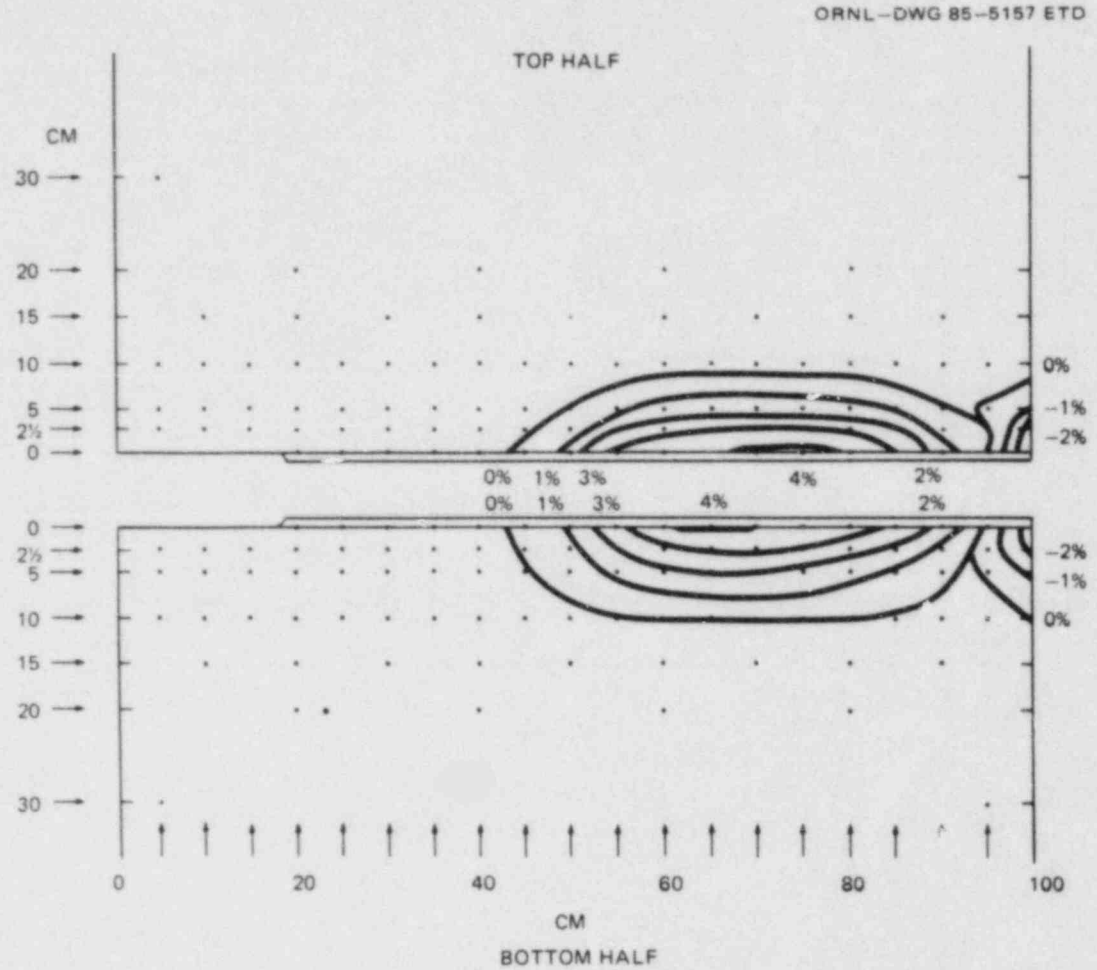

Fig. 5.25. Posttest reduction in thickness contours for specimen WP-1.3.

length vs time results are shown in Fig. 5.26. The agreement between the strain gage results and the velocity gages is fairly good for the early part of the propagation. The velocity gages, however, suggest that high velocities continue for a longer period of time and that crack arrest does not occur until $a/w \approx 0.65$. This may be due, in part, to the plastic zone in front of the crack prematurely breaking the velocity gage.

The record from an acoustic emission device located on the lower pull plate (see Fig. 5.27) shows a burst of high amplitude near time zero, followed by a quiescent period. Then a small amplitude acoustic emission that may be associated with a resumption of ductile tearing occurs. In many respects, this signal is similar to the acoustic emission recorded in WP-1.1 (see Fig. 5.18 of Ref. 4). The main difference is the length of the quiescent period: 2 ms in WP-1.1 vs almost 2 s in WP-1.3. This longer pause is a consequence of the lower load at initiation in WP-1.3. Figure 5.27 also provides a higher time resolution of the first run-arrest event as monitored by the acoustic emission transducer.

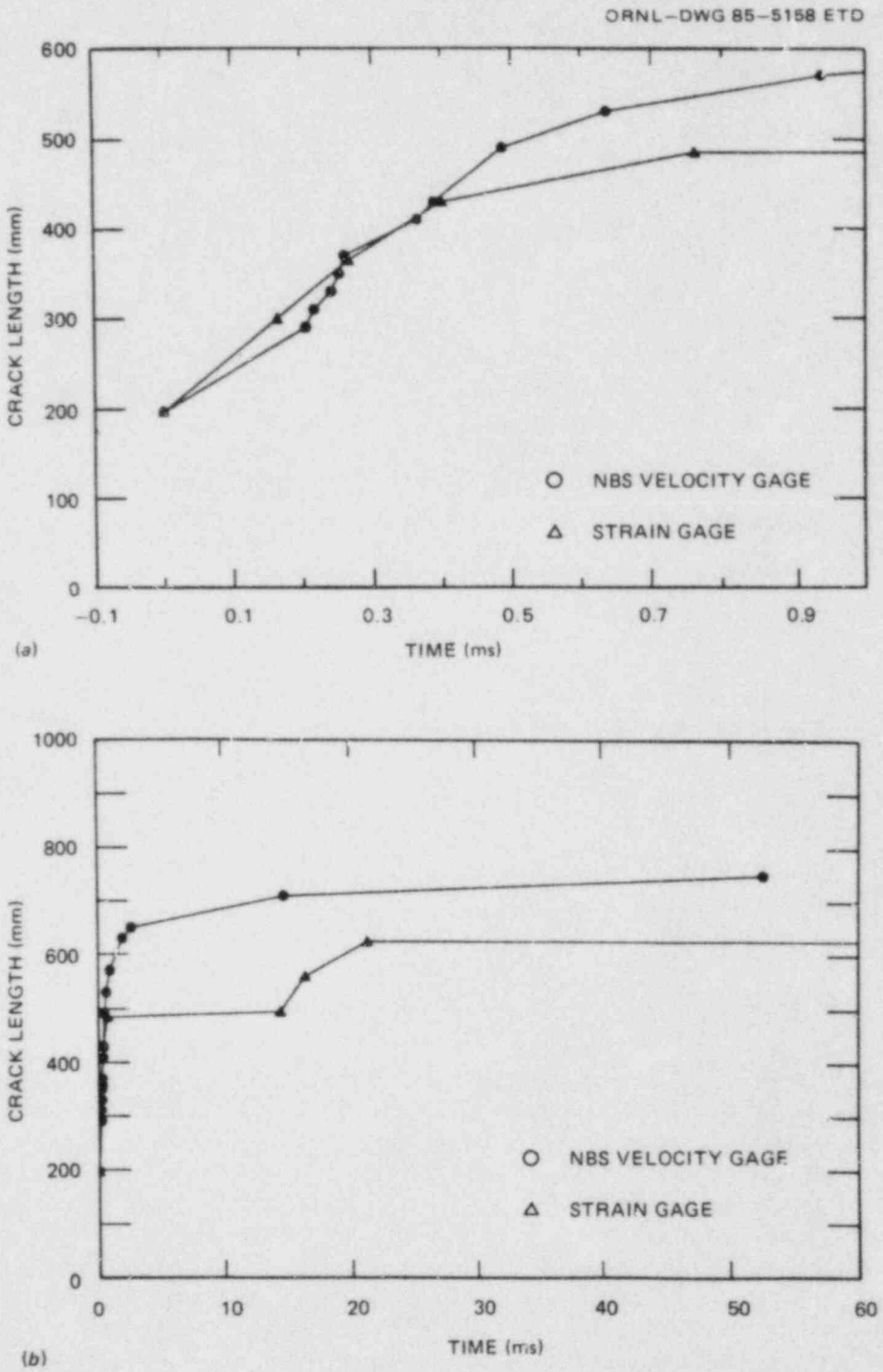

Fig. 5.26. Crack length vs time measurements from crack-line strain gage data and from NBS crack velocity gage (NBS determinations). (*a*) 1-ms scale, (*b*) 60-ms scale.

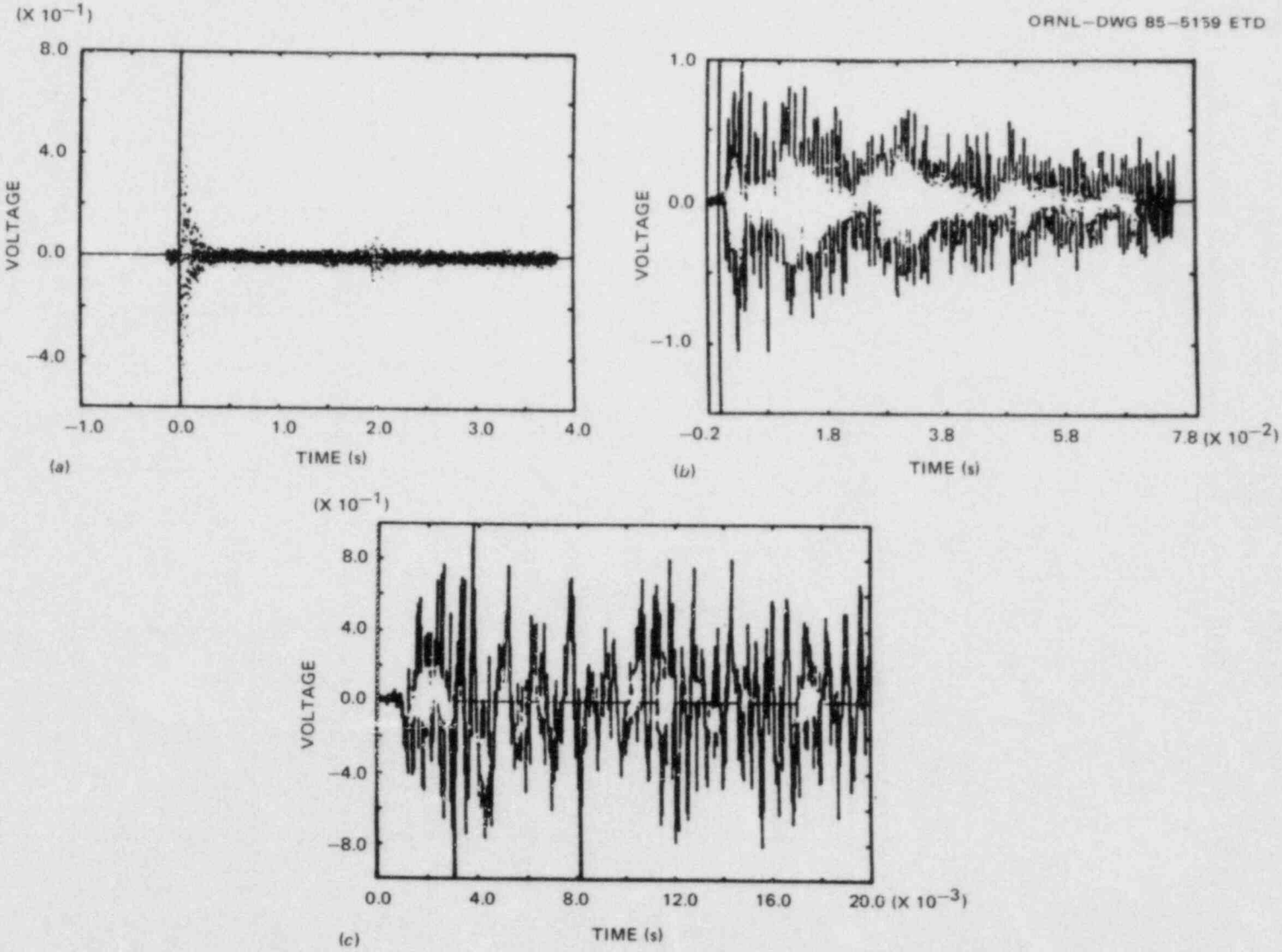

Fig. 5.27. Output of acoustic emission device mounted on lower pull plate for WP-1.3.

Finally, Fig. 5.28 gives the measured COD recorded during fracture at 175 mm from the cold edge of the plate. The voltage output of this gage was converted to distance using a room temperature calibration. Efforts are under way to calibrate this gage at −40°C, which is much closer to the actual application temperature.

5.2.5.2 Data interpretations for WP-1.3 (C. E. Pugh, B. R. Bass, J. G. Merkle, ORNL). Some preliminary interpretations of the test results

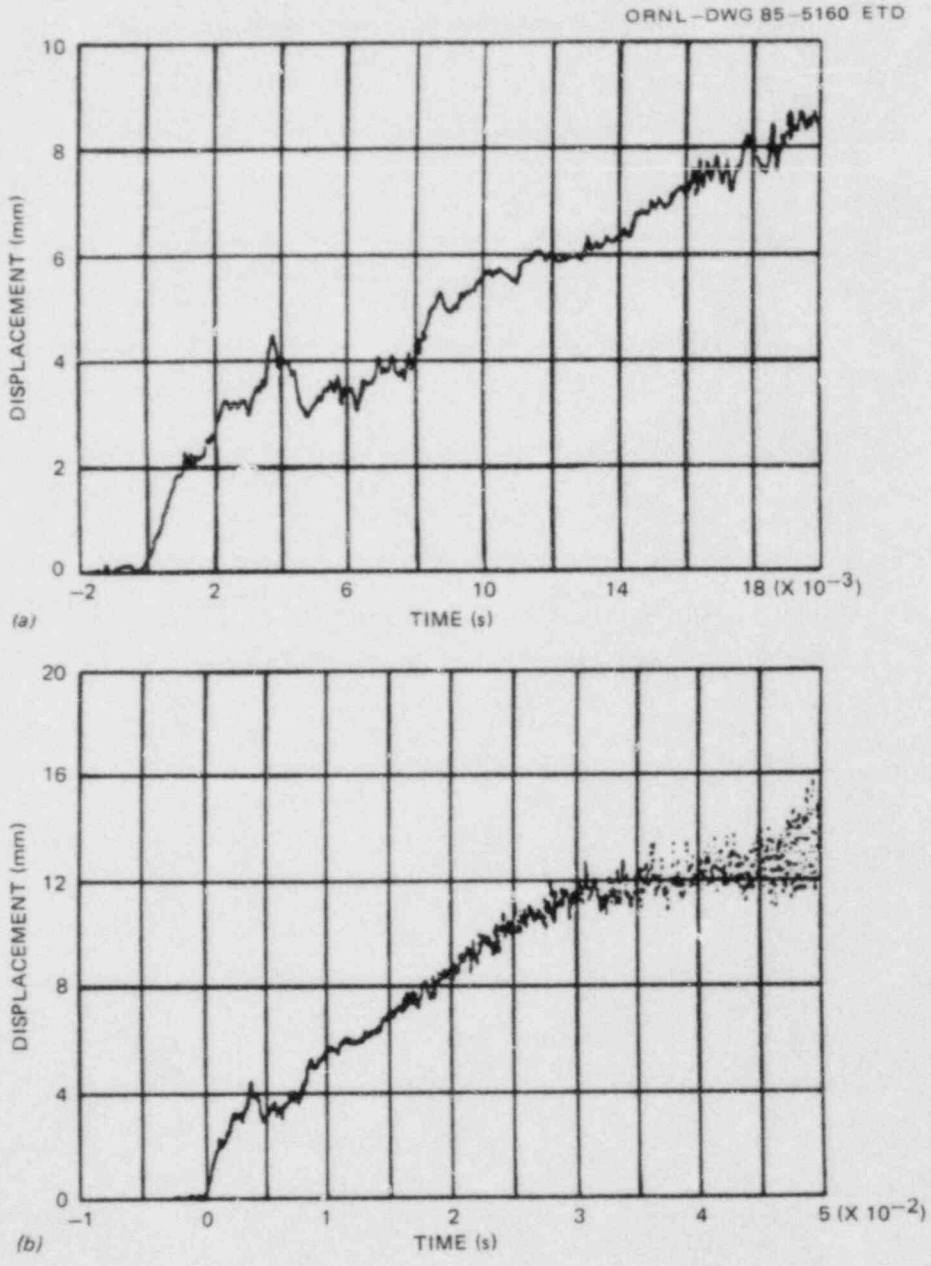

Fig. 5.28. CODs vs time response of WP-1.3 for COD gage located 175 mm from cold edge. (*a*) 18-ms scale, (*b*) 50-ms scale.

are given in this section on the basis of the data obtained in test WP-1.3. Further interpretations on the basis of comparing analytical results with the test data are presented in Sect. 5.4 of this document.

Principal attention has been given to understanding the data from the eight pairs of 90° rosette strain gages located along the crack plane (see Fig. 5.14). The strain-time responses of these gages are shown earlier in Figs. 5.20–5.22, and they have provided the basis for estimating the crack propagation velocities. In this regard, as the crack approaches a gage, the strain rises until the crack passes under the gage location, after which the strain diminishes with time. In particular, it has been assumed here for simplicity that the peak in the strain-time plot for a specific gage gives the time when the crack is directly under that gage. Figures 5.20 and 5.21, therefore, show that the crack propagated past Gages 1, 2, and 3 and was nearing the Gage 4 location when arrest occurred in WP-1.3. Gage 4 is located 495 mm from the cold edge, and the fracture surface shown in Fig. 5.18 suggests that the actual arrest location is at ~485 mm.

The independent NBS and ORNL estimates of the velocity of cleavage crack propagation are shown in Table 5.6 and are average values between adjacent crack-line gage positions. Table 5.6 also includes postcleavage estimates made by NBS. Figure 5.26 is based on the NBS-2 interpretation given in Table 5.6.

Interpretation of the average velocity between Gage 3 and arrest is very difficult to make from Figs. 5.20 and 5.21. For example, if one assumes the crack arrested at a/w = 0.485 at the time when the first slope change [point A in Fig. 5.21(a)] occurred in the ε-time plot for Gage 4

Table 5.6. Average crack velocities for intervals between adjacent crack-line strain gages for test WP-1.3

Gage Nos.	Propagation interval [mm ($a_{n+1} - a_n$)]	Propagation time (ms)			Average velocity (m/s)		
		ORNL	NBS-1[a]	NBS-2[b]	ORNL	NBS-1[a]	NBS-2[b]
0–1	103 (300–197)	0.154	0.165	0.165	669	624	624
1–2	65 (365–300)	0.10	0.10	0.10	650	650	650
2–3	65 (430–365)	0.142	0.135	0.135	458	481	481
3–arrest	55 (485–430)	>0.109 <1.03	0.964	0.362	>53 <505	56	152
Arrest	0		2.88	7.262		0	0
Arrest–4	10 (495–485)		3.97	6.49		2.5	1.54
4–5	65 (560–495)		0.90	1.95		72	33.3
5–6	65 (625–560)		7.4	4.84		8.8	13.4
6–7	65 (690–625)		41.3	1719		1.6	0.04
7–8	65 (755–690)		1862	180		0.035	0.36
8–arrest	215 (970–755)		90	90		2.4	2.39

[a]NBS-1 represents the NBS interpretation given in Ref. 7.

[b]NBS-2 represents the NBS interpretation given in Ref. 9.

(t = 0.5054 ms), then an average velocity of 505 m/s is calculated. This value is, of course, too high and suggests that arrest occurred sometime after point A is reached. However, the crack should have arrested prior to the ε-time plot reaching the first maximum point [point B in Fig. 5.21(*a*) at 1.43 ms after initiation]. This time-of-propagation produces an average velocity of 53 m/s between Gage 3 and the arrest point. Arrest is thought to have occurred prior to point B because the observed strain decrease that occurs immediately after point B probably could not have developed if the crack were still propagating, even at a low velocity, toward Gage 4.

More can be conjectured from the output of Gage 4 by looking at it in conjunction with the fracture surface shown in Fig. 5.18. The crack appears to have arrested in a near planar fashion at an average length of about a_f = 0.485 m. A small amount of stable ductile crack growth followed the arrest and extended the crack length to about 0.495 m. Then an additional segment of cleavage fracture occurred over an area extending a distance of about 3 cm ahead of the first arrest line (to 0.525 m) on one side of the specimen (about 50% across the thickness of the specimen). Finally, the remainder of the net section experienced ductile fracture, which probably began alongside the second cleavage fracture area. The mode conversion from ductile tearing to cleavage after the first arrest was probably aided by crack-tip strain-rate effects caused by the ductile tearing and by the out-of-plane bending that the plate was experiencing. The temperature at the initial arrest depth (0.485 m) was T = 53.8°C, close to the temperature of onset of upper-shelf conditions in the Charpy V-Notch (CVN) test (see Fig. 5.28 of Ref. 4), but the crack-arrest data for HSST Plate 13A show that cleavage fracture is still possible at this temperature (see Fig. 5.27 of Ref. 4).

The run-arrest time, if estimated to be about 1.43 ms, corresponds to the first maximum in the signal from Gage 4. The minor strain oscillations shown in Fig. 5.21 have a period of roughly 1.5 ms, which corresponds reasonably well to the time required for dilatational waves to travel from the crack plane to the loading pins and return (a distance of 8.68 m).

Because the crack-plane strain gages were on the side of the specimen away from the second area of cleavage fracture, Gage 4 would probably not show a sudden strain decrease because of the second cleavage event that extended beyond Gage 4 on the opposite side. Consequently, the initial strain decrease at ~4.5 ms shown in Fig. 5.21(*b*) could be due to the load drop caused by the first crack extension; the second rise and peak could be caused by the effects of the crack tip passing the gage point in ductile tearing.

The change in slope (of Gage 4 response) at point A in Fig. 5.21(*a*) is interpreted here to correspond to the onset of rapid deceleration of the crack extension rather than to arrest of the approaching crack. The responses of Gages 1 through 3 show that the velocity of propagation remains very high for the first 165 mm of propagation. Gage 4 response is interpreted in terms of a relatively high velocity being maintained for 0.505 ms (point A) after which the crack extension slows very quickly, resulting in arrest at an undetermined time between 0.505 and 1.426 ms (Points A and B).

The NBS postcleavage estimates given in Table 5.6 imply some further behavioral characteristics. NBS assumed here (Refs. 7–9) that the crack passed under crack-line Gages 5 through 7 when the abrupt decreases in strain occurred as shown in Fig. 5.20. NBS also surmised that when the cleavage crack propagation arrested at a/w = 0.485, there was an arrest interval of about 7.26 ms (from 0.76 to 8.02 ms). Such a period of inactivity is present in the strain-time records of Gages 5 through 7 in Fig. 5.20, after which slow propagation continued to take place. The responses of Gages 6 and 7 suggest that the propagation from the 625- to 690-mm location was extremely slow or there was indeed an arrest interval that ended when the compliance of the specimen assembly allowed sufficient bending to develop for the resumption of ductile tearing. About 1.7 s was required for the crack to extend over this 65-mm interval. As seen from the fracture surface in Fig. 5.18, this relatively long pseudo-arrest interval occurred within the region of ductile tearing and not at the point of cleavage crack arrest. Again, the cleavage-arrest interval was interpreted to last for only slightly more than 7 ms in contrast to this 1.7-s interval.

Strain Gages 11 and 12 were located on the back face of the specimen directly opposite Gages 9 and 10, respectively. The outputs of these gages are compared in Fig. 5.23 and show that the longitudinal surface strains on the back face of the specimen were about 50% greater at the beginning of the test and during the cleavage propagation. The strains in Gages 9 and 11 became nearly the same during the 2-s arrest period because the crack has passed under their locations. Gages 16 and 20 are on the opposite side of the pull plates, 1.8 m from the crack plane, and they also show substantial out-of-plane bending. These strains do not become close together during the 2-s arrest period. As indicated previously in Table 5.5, the output from these gages differs by approximately a factor of two. The reason for this bending is not understood. The out-of-plane bending suggested by these strain differences is, however, consistent in sign with the segment of cleavage reinitiation occurring on the more highly loaded (back) side of the plate.

An equivalent out-of-plane eccentricity of the specimen can be calculated from the front and back surface strain readings by using the equation

$$\frac{e}{B} = \frac{1}{6} \frac{(\varepsilon_{max} - \varepsilon_{min})}{(\varepsilon_{max} + \varepsilon_{min})} ,$$

where e is eccentricity and B is specimen thickness. The calculated eccentricities for the three opposite surface gage pairs identified previously range from 4.3 to 7.3 mm.

5.2.5.3 Test data from WP-1.4. The fracture surface and reduction-in-thickness contours for test WP-1.4 are shown in Figs. 5.29 and 5.30. The initial crack length was measured to be 207.5 mm [notch plus electron beam (EB) weld]. An inspection of the fracture surface revealed that the cleavage crack did not remain in the side grooves but traveled parallel to them about 1 cm below the side-groove plane. Some branching occurred at crack initiation and extended for about 10 cm from the crack tip. The

ORNL PHOTO 8309-85

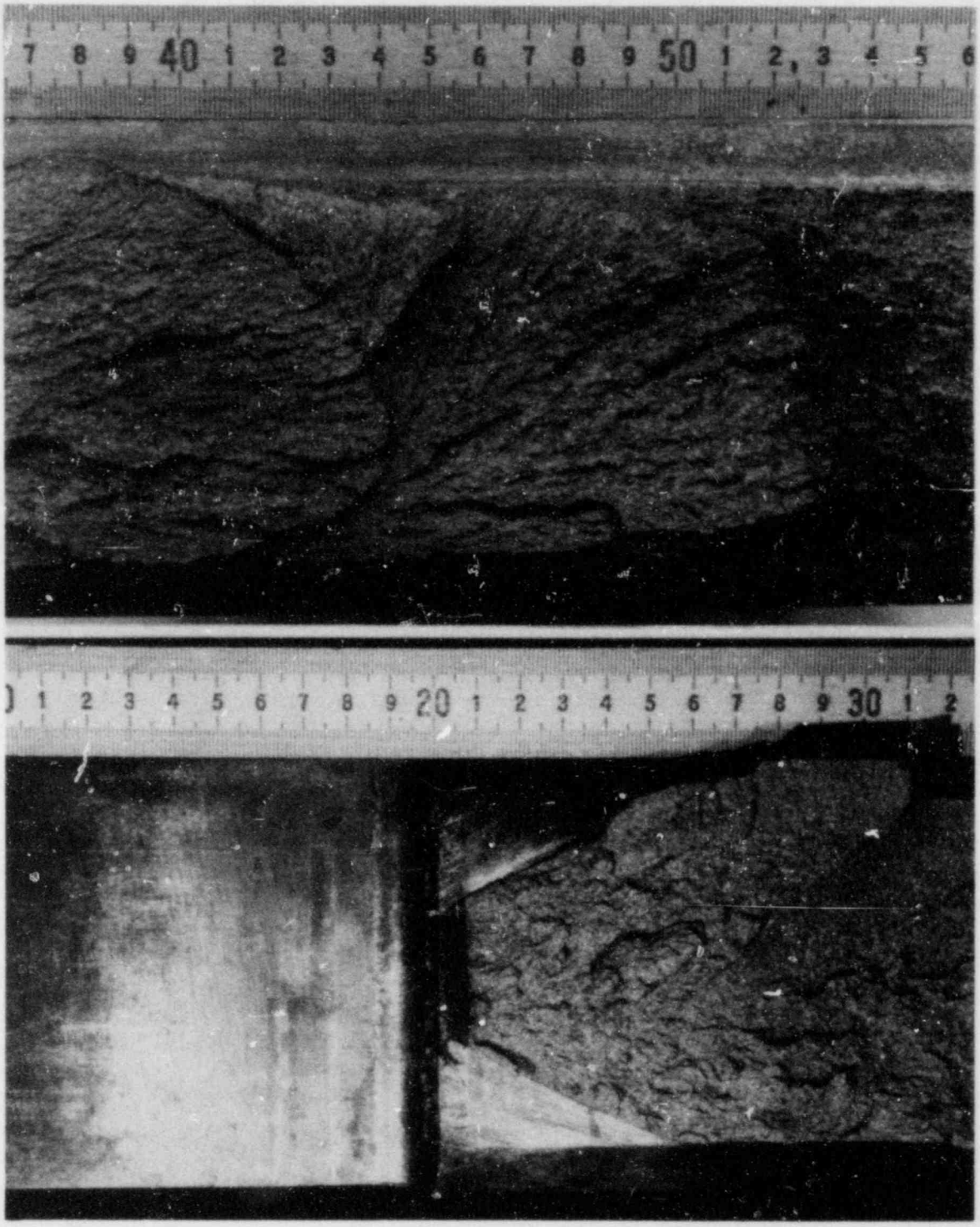

Fig. 5.29. Close-up photographs of first and second arrest positions and chevron notch for WP-1.4.

ORNL PHOTO 8310–85

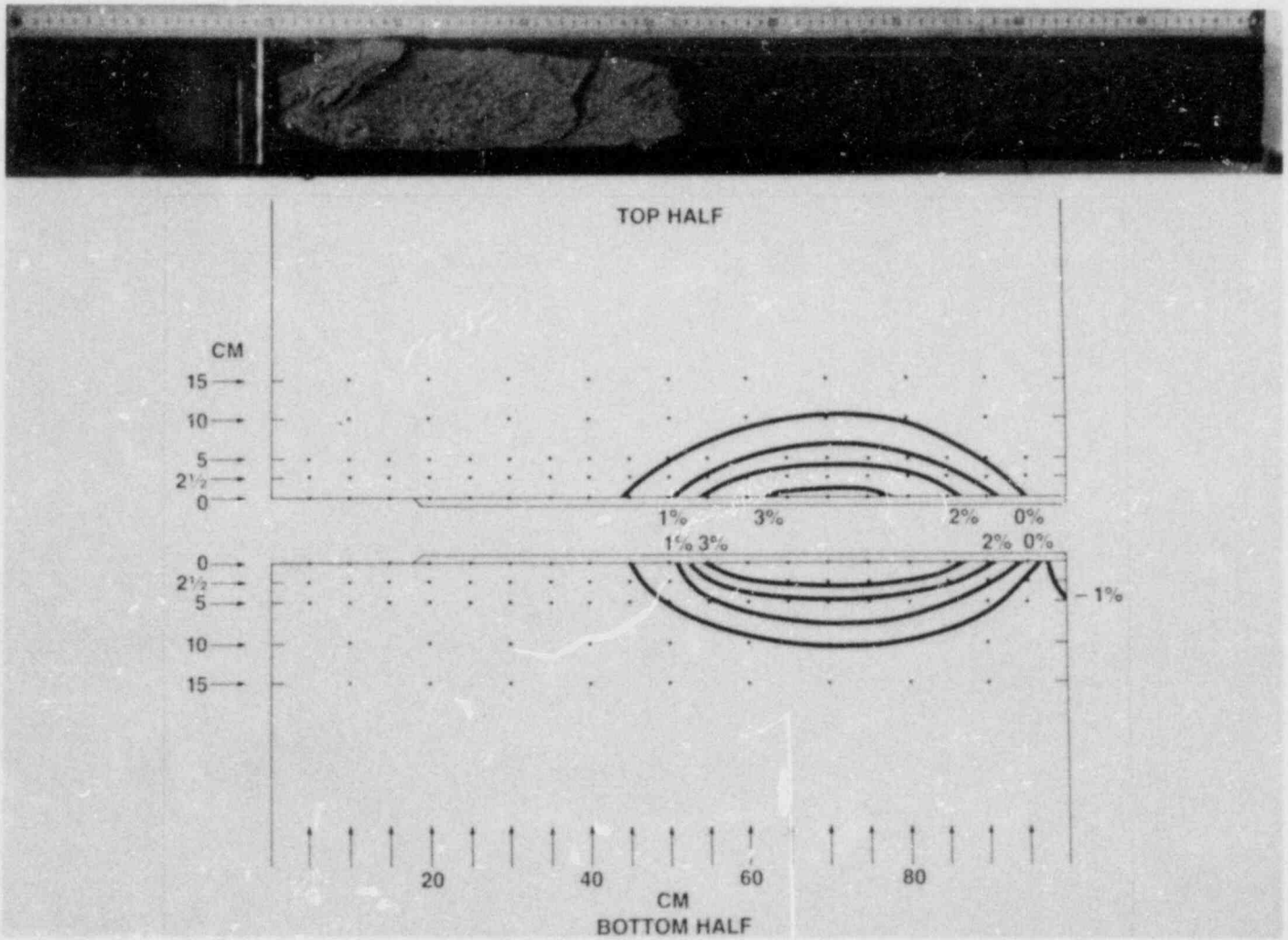

Fig. 5.30. Overall view of fracture surface and reduction-in-thickness contours for WP-1.4.

first run-arrest event terminated in a curved crack front. This arrest position appears to be supported by the strain-gage results presented below. This first crack-arrest locus intersects the front of the specimen at 403 mm and the back of the specimen at 397 mm from the cold edge. The farthest extent of the first arrest is 441 mm from the cold edge. There is no evidence of fibrous fracture at the end of the first event. Presumably, the end of the first arrest is then the initial crack length for the second run-arrest event, which exhibited a transition from cleavage to fibrous fracture at 527 mm in the mid-thickness region. The second crack arrest line intersects the front surface at 526 mm and the back surface at 514 mm and is much less curved than the first crack-arrest line. Again, this arrest position is fairly well supported by the strain-gage results. The strain gages indicate that the crack started moving again slowly after the second arrest. The fracture surface is entirely fibrous after the second arrest, and no particular details are outstanding until the remaining 10- to 15-mm ligament is reached. This ligament begins at 982 mm in the mid-thickness region, 989 mm on the front face, and 991 mm on the back face of the specimen.

The outputs recorded from the strain gages during the first run-arrest event are given in Figs. 5.31–5.35. From these results, the crack position vs time has been deduced by NBS (Ref. 10) and is listed with the calculated velocities in Table 5.7. Because Gage 1 did not show a peak, there is some ambiguity in the exact time when the crack passed under this gage. For this reason, the exact time and velocity deduced from this gage are suspect.

Figure 5.36 gives the strain records from the 90° rosette gages numbered 13 through 16 that were oriented at 45° to the crack line at the request of UM. Gages 13 and 15 and 14 and 16 are paired front to back directly under the crack-line Gages 4 and 5, respectively (see Fig. 5.15). These paired gages exhibit an asymmetric strain history that

Table 5.7. NBS crack-time history for the first run-arrest event in test WP-1.4

Location	Position (mm)	Time (μs)	Velocity (m/s)
a_o	207.5	0	654
Gage 1	250	65	1818
Gage 2	300	92.5	385
Gage 3	350	222.5	777
Gage 4	390	274	183
Gage 5	430	492.5	134
Arrest-1	441	574.5	0

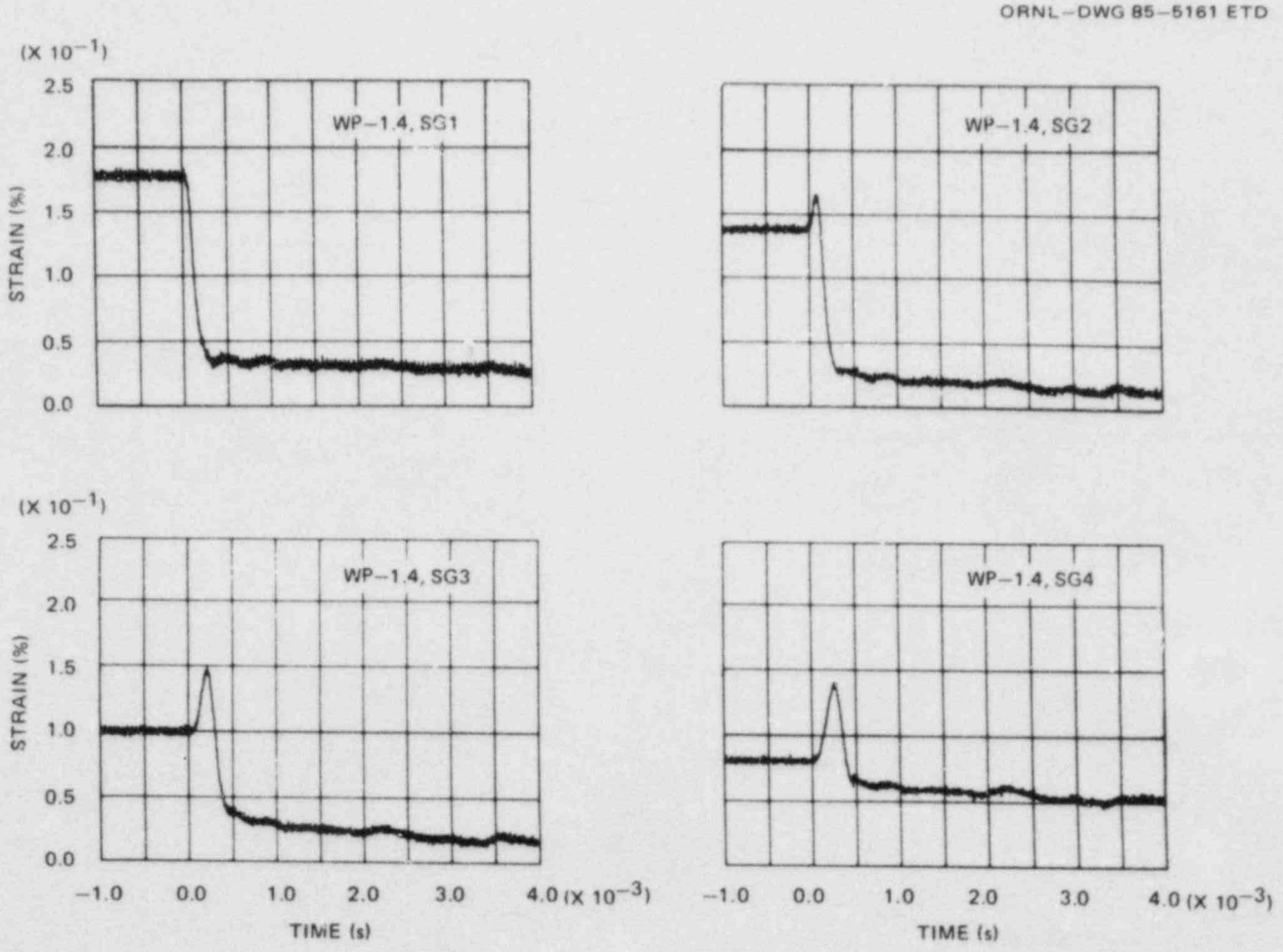

Fig. 5.31. Strain records from Gages 1, 2, 3, and 4 during first run-arrest event of WP-1.4.

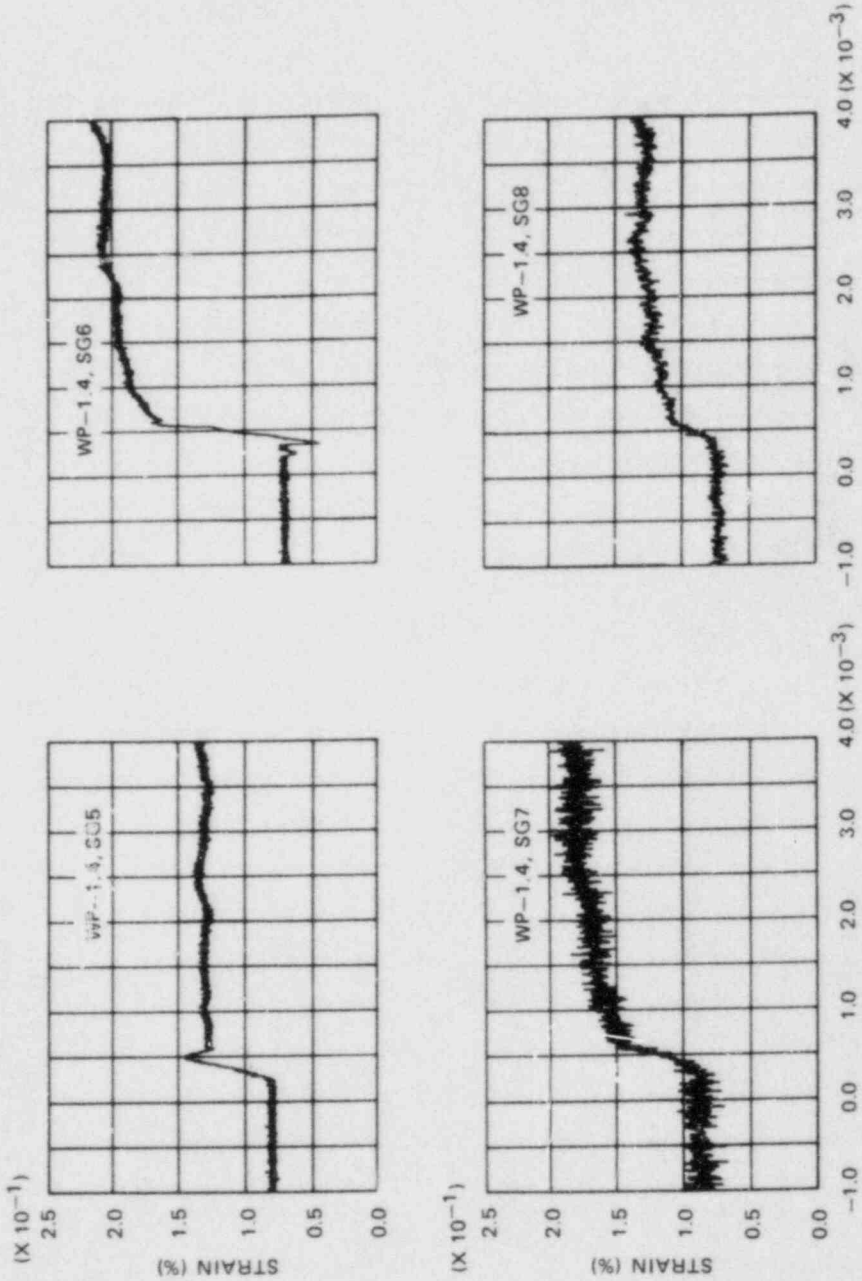

Fig. 5.32. Strain records from Gages 5, 6, 7, and 8 during first run-arrest event of WP-1.4.

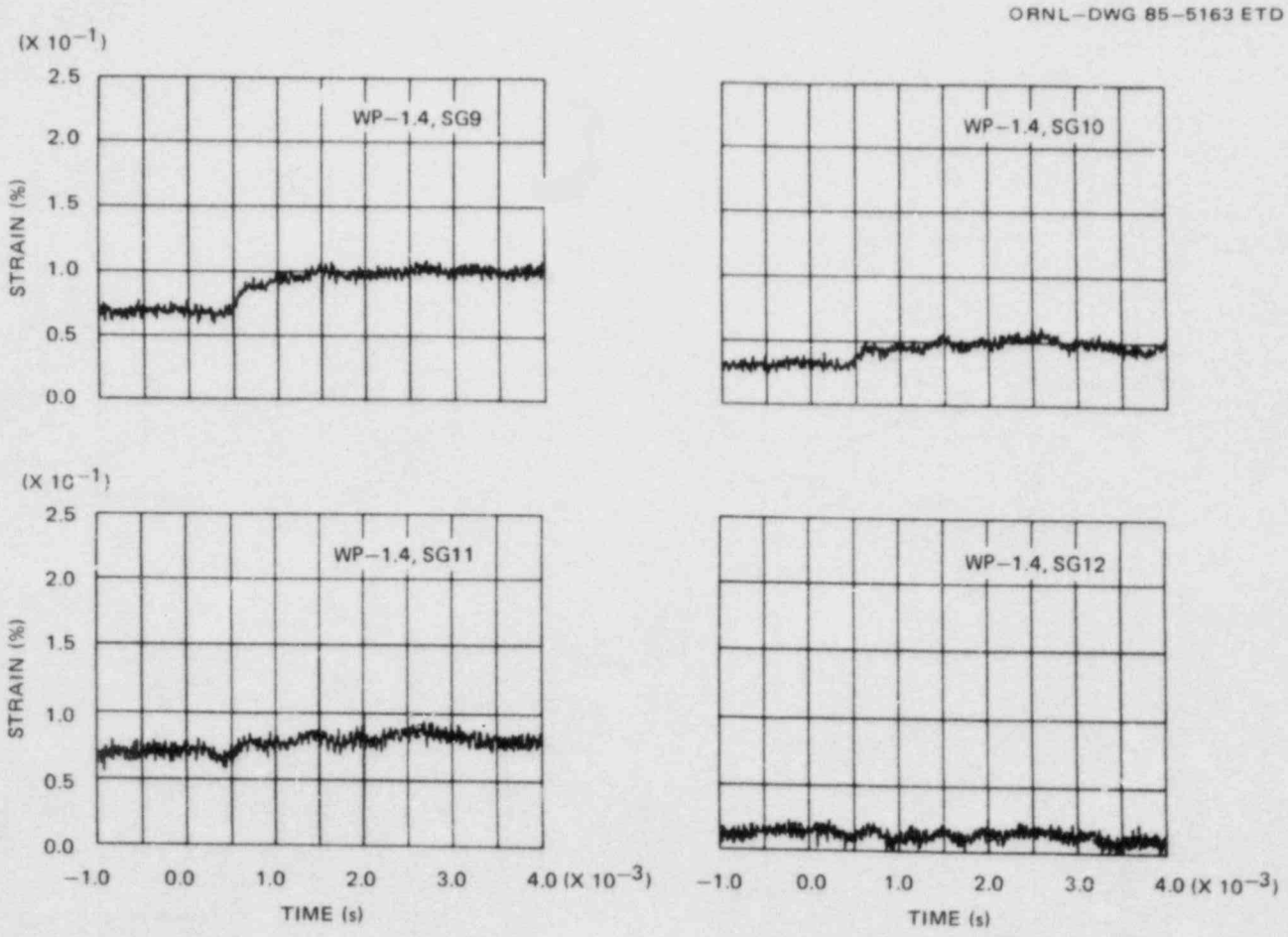

Fig. 5.33. Strain records from Gages 9, 10, 11, and 12 during first run-arrest event of WP-1.4.

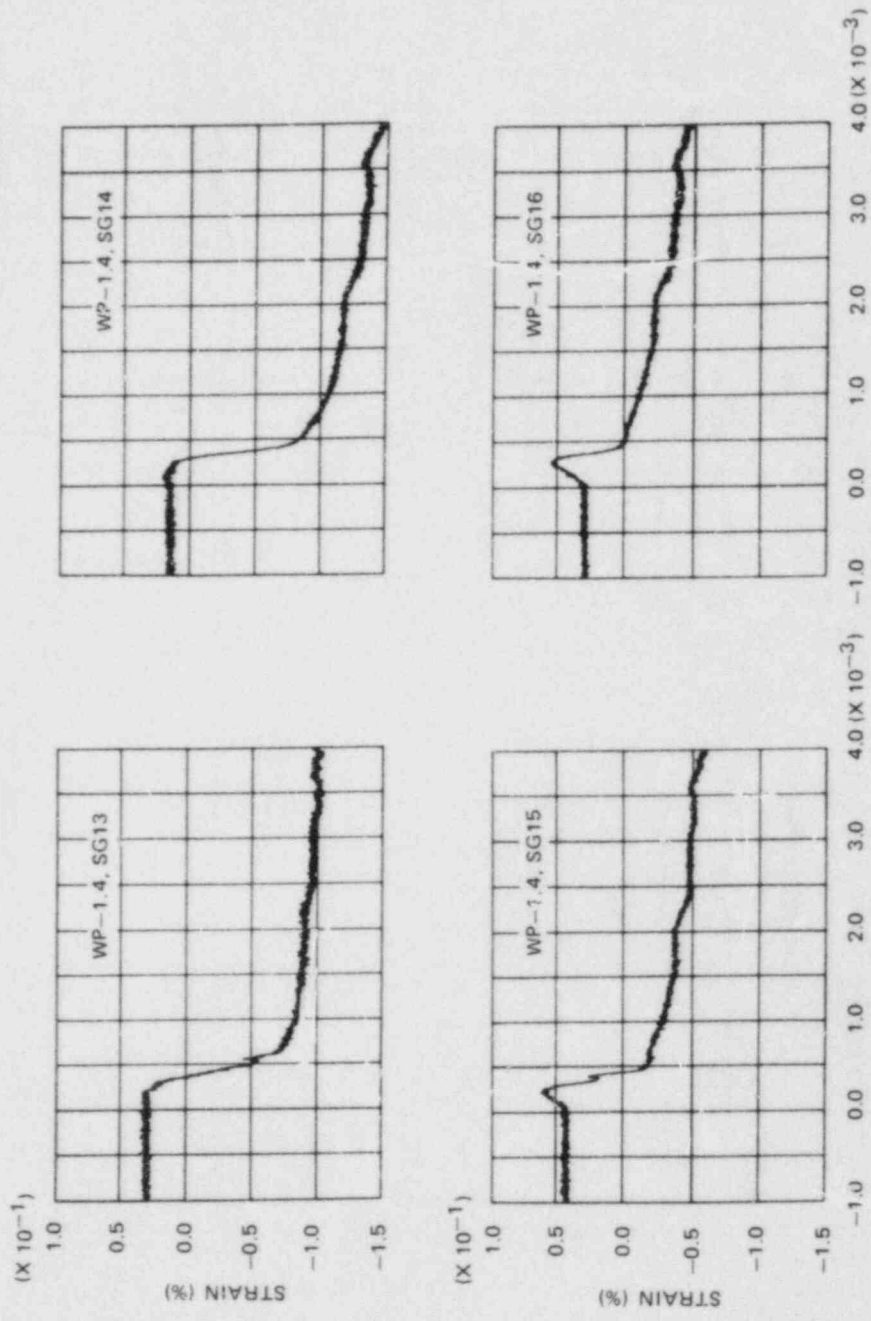

Fig. 5.34. Strain records from Gages 13, 14, 15, and 16 during first run-arrest event of WP-1.4.

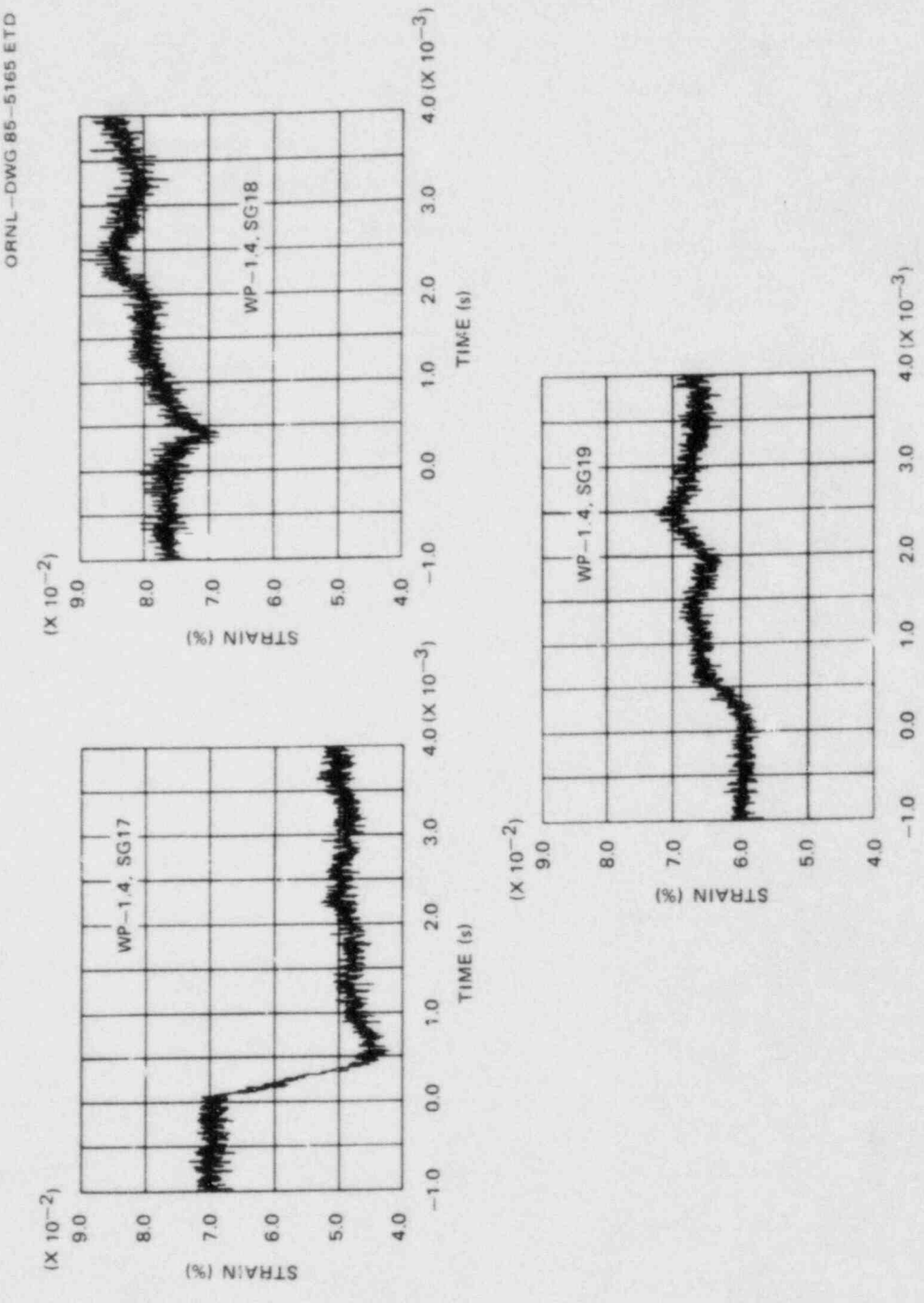

Fig. 5.35. Strain records from Gages 17, 18, and 19 during first run-arrest event of WP-1.4.

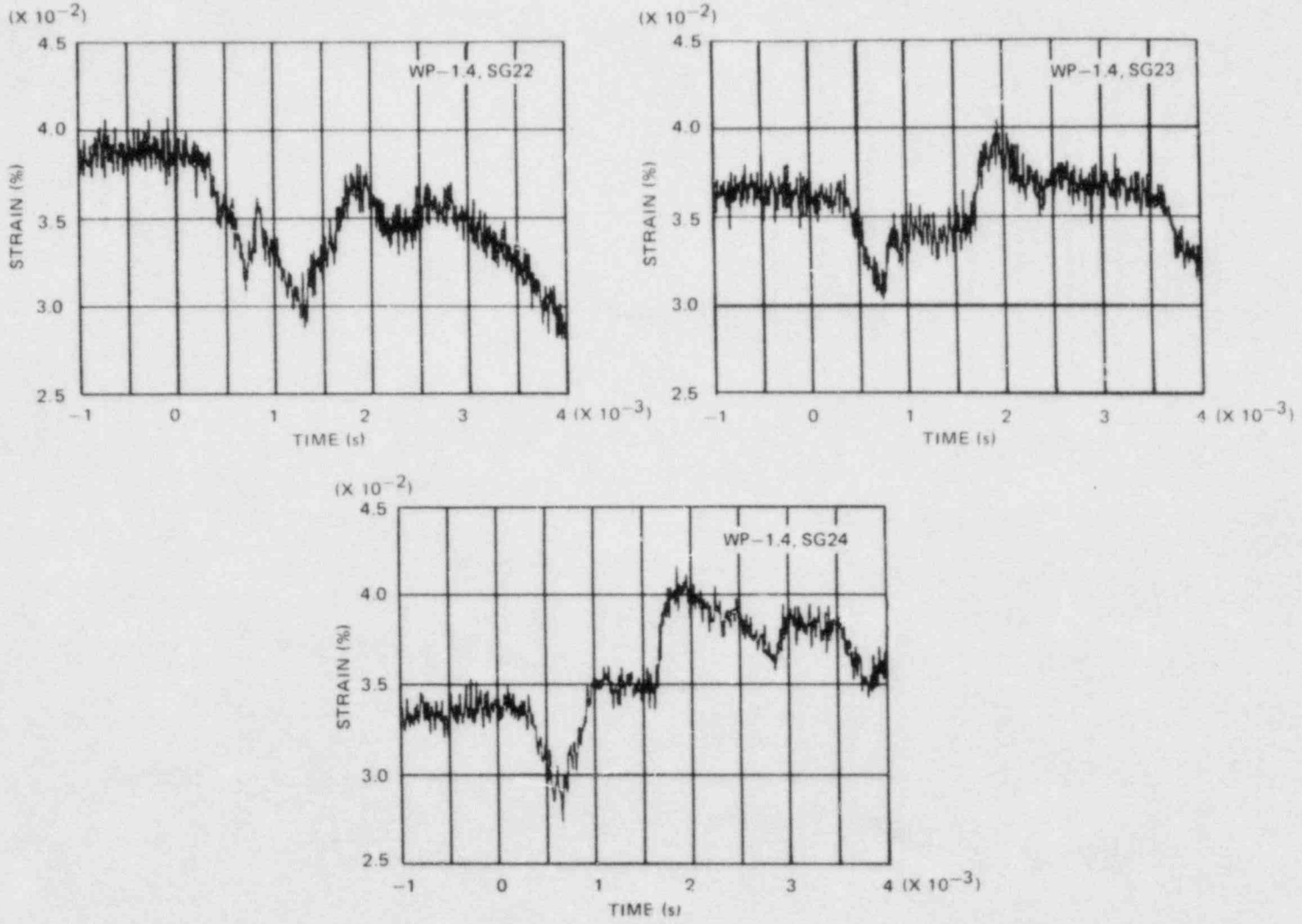

Fig. 5.36. Strain records from Gages 22, 23, and 24 during first run-arrest event of WP-1.4.

could be due to the combined effects of out-of-plane bending and an asymmetric propagating crack front. In addition, the paired Gages 14 and 16 indicate a peak-strain time of ~0.3 ms (Fig. 5.34); Gage 5, however, directly above exhibits a peak strain at ~0.5 ms (Fig. 5.32). This discrepancy could possibly be due to conflicting initiation times selected from the measured data for these strain histories.

The outputs of strain gages during the second run-arrest event are shown in Figs. 5.37–5.41. Because the initial crack front for the second run-arrest is curved, there were strain changes on Gages 4 and 5, but they were not used to deduce crack position during the second event. It also appears that Gage 12 was not functioning during this event. The gage outputs (Fig. 5.42) and the fracture surface suggest that after the cleavage crack arrested, there was a pause of 4.46 ms before a fibrous reinitiation occurred. This fibrous crack passed Gages 8 and 9 before arresting or slowing down to a creeping rate. Because there is no marking on the fracture surface between Gages 9 and 10, it is assumed that no fibrous crack arrest occurred and that the crack continued growing very slowly until the major fracture to zero load took place. The above sequence of events as constructed by NBS (Ref. 10) is listed in Table 5.8.

Table 5.8. NBS crack-time history for the second run-arrest event in test WP-1.4

Location	Position (mm)	Time (μs)	Velocity (m/s)
Arrest-1	441	0	866
Gage 6	470	33.5	259
Gage 7	510	188	3.93
Arrest-2	527	4,518	0
Reinitiation	527	8,898	8.98
Gage 8	550	11,458	1.09
Gage 9	600	57,498	1.59×10^{-3}
Gage 10	650	31.58×10^{6}	7.25×10^{-2}
Gage 11	700	32.27×10^{6}	3.14
Final ligament	983	32.38×10^{6}	0

The output during all three events of the large COD gage located at a/w = 0.15 is shown in Fig. 5.43, where a conversion from voltage to displacement that is appropriate for −40°C is used.

Prior to the application of axial load, the out-of-plane deformation of the wide-plate assembly was recorded as a function of axial position (Fig. 5.44). The maximum deflection of ~44 mm was recorded at mid-length

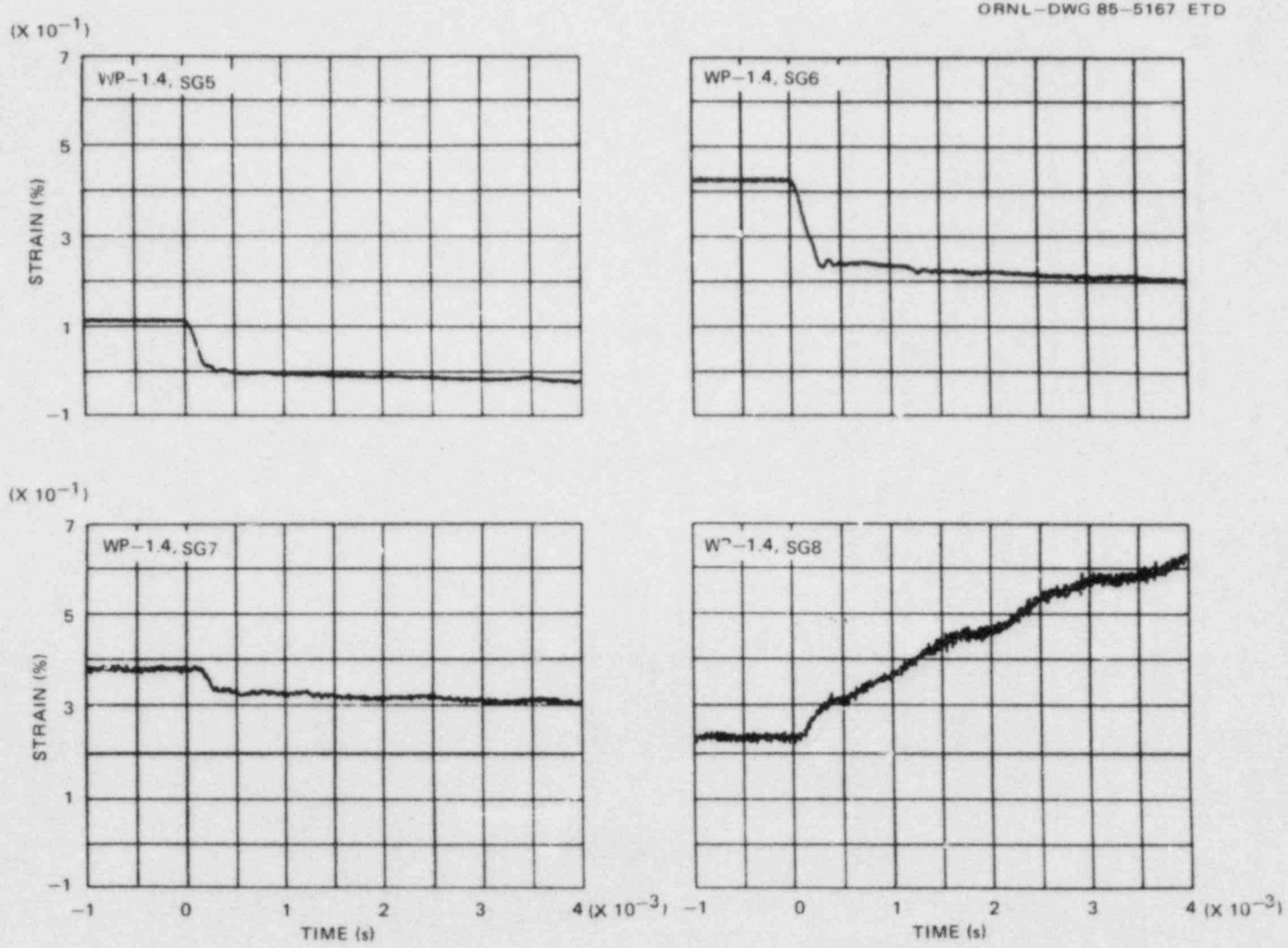

Fig. 5.37. Strain records from Gages 5, 6, 7, and 8 during second run-arrest event of WP-1.4.

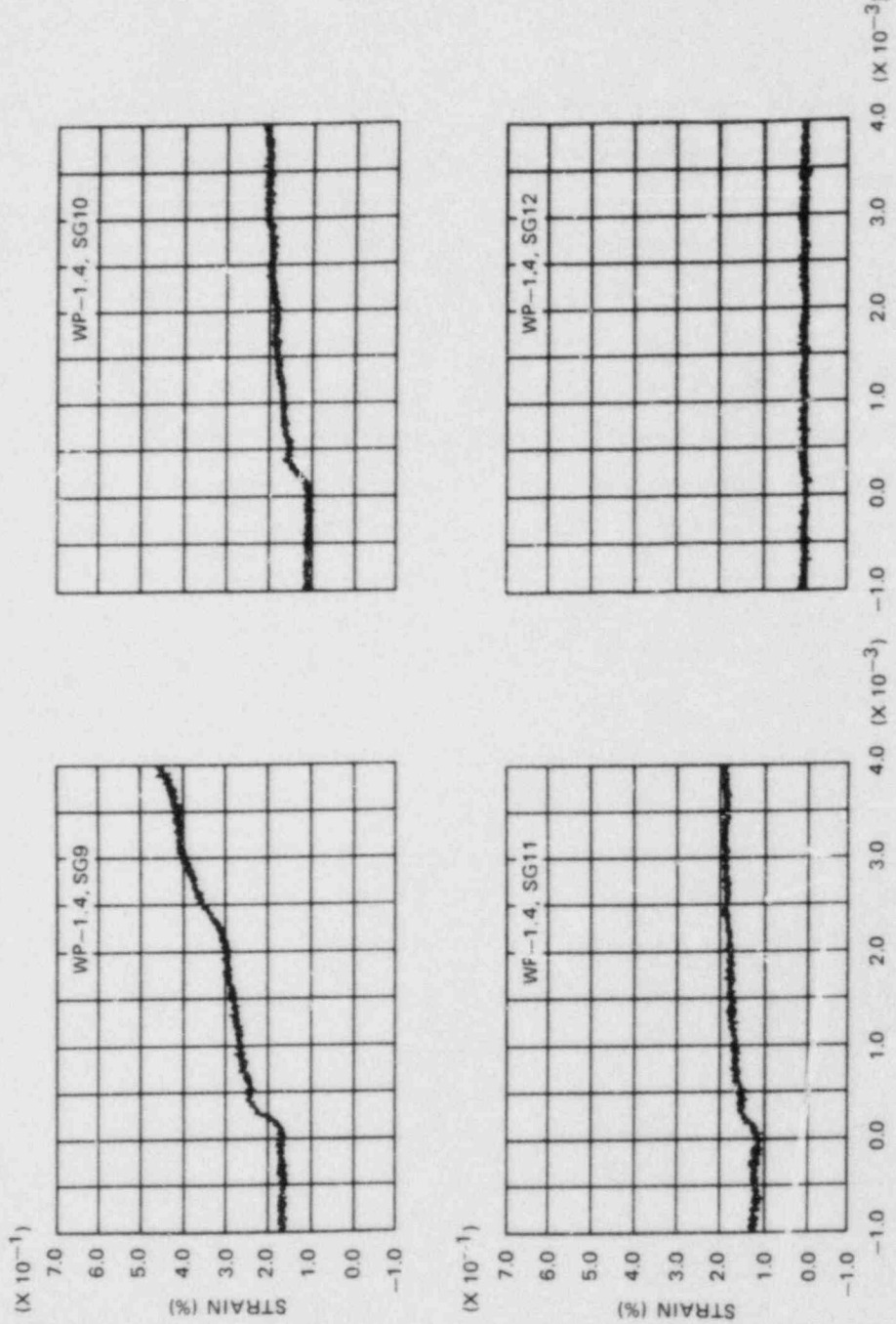

Fig. 5.38. Strain records from Gages 9, 10, 11, and 12 during second run-arrest event of WP-1.4.

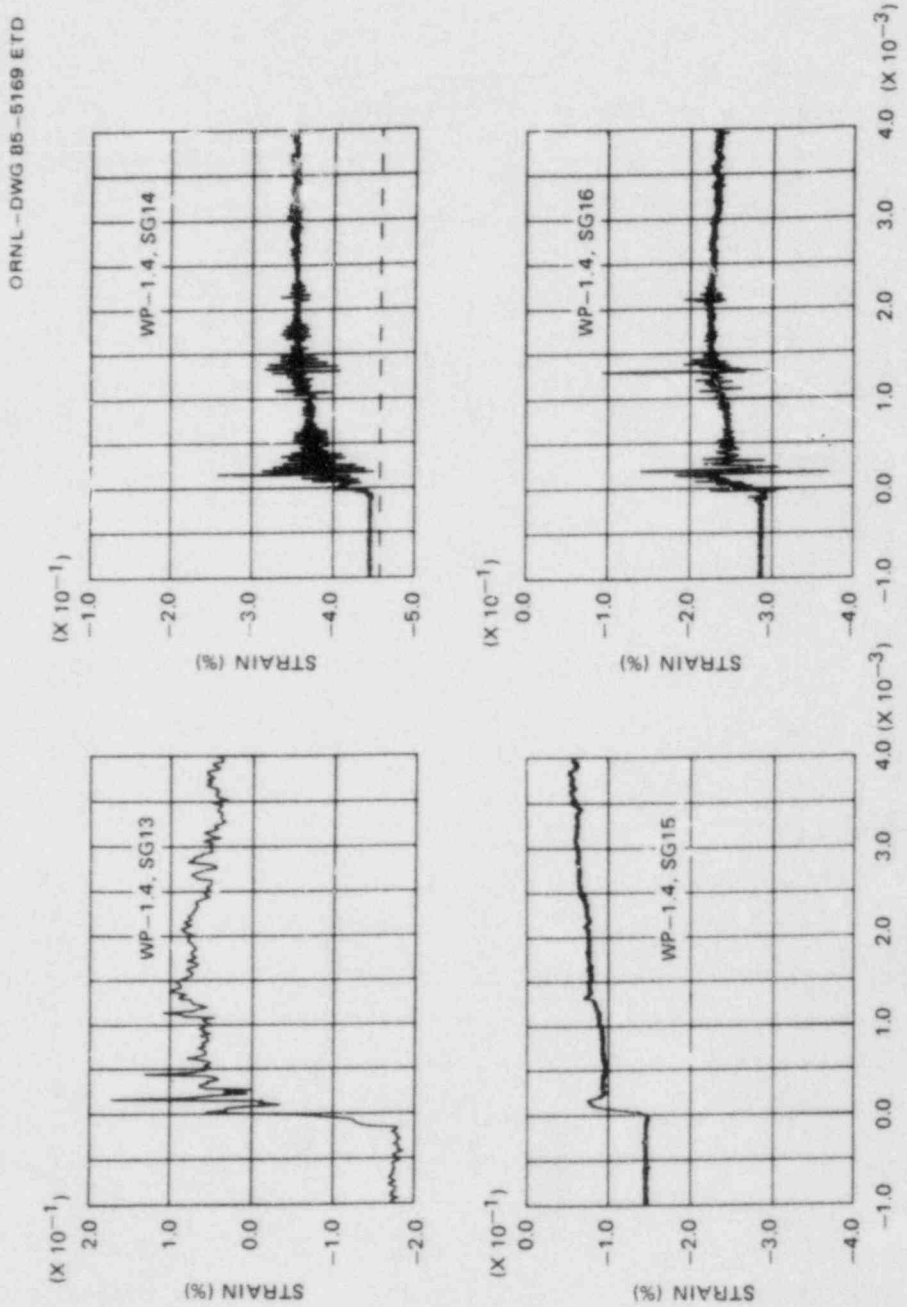

Fig. 5.39. Strain records from Gages 13, 14, 15, and 16 during second run-arrest event of WP-1.4.

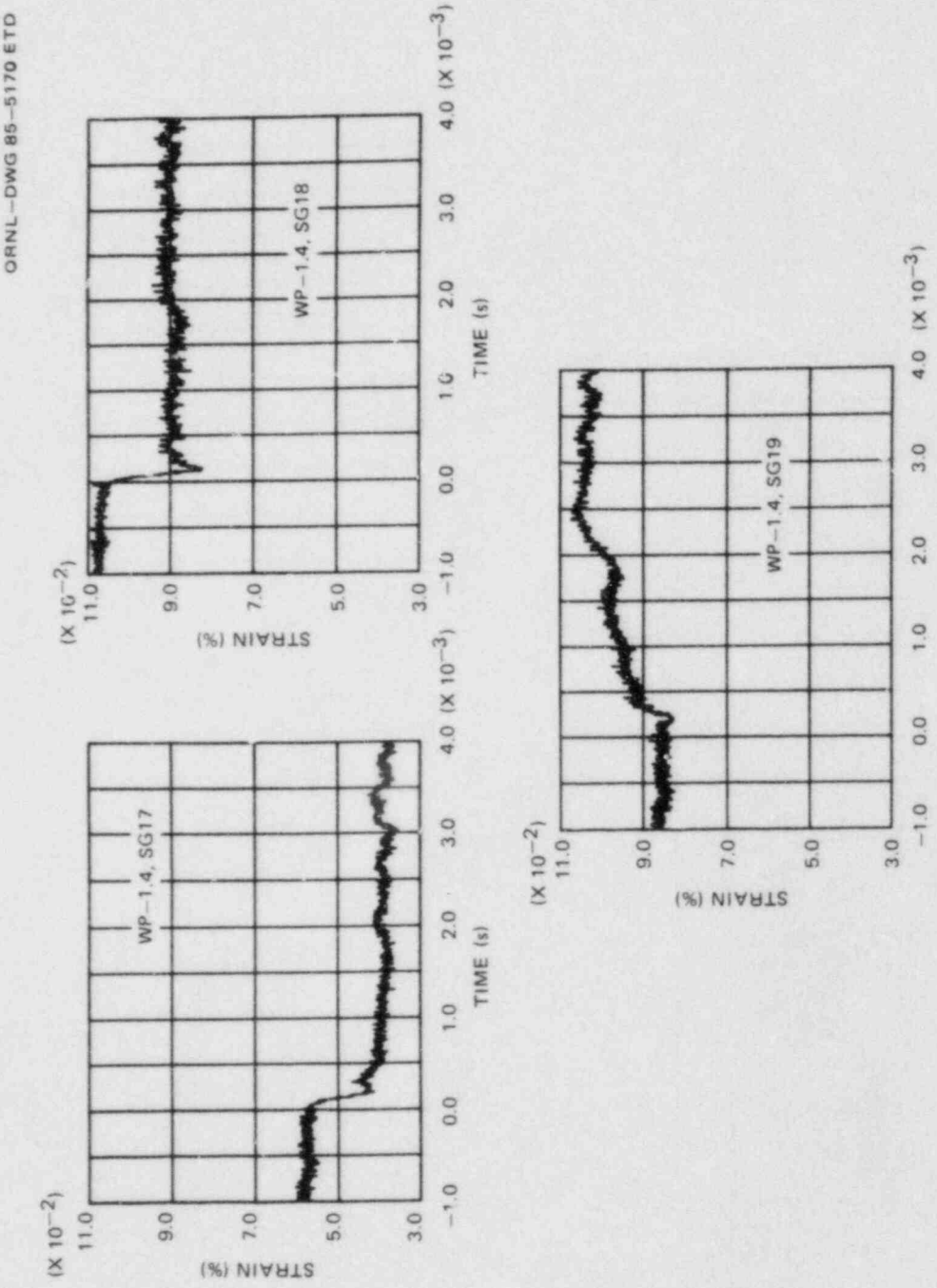

Fig. 5.40. Strain records from Gages 17, 18, and 19 during second run-arrest event of WP-1.4.

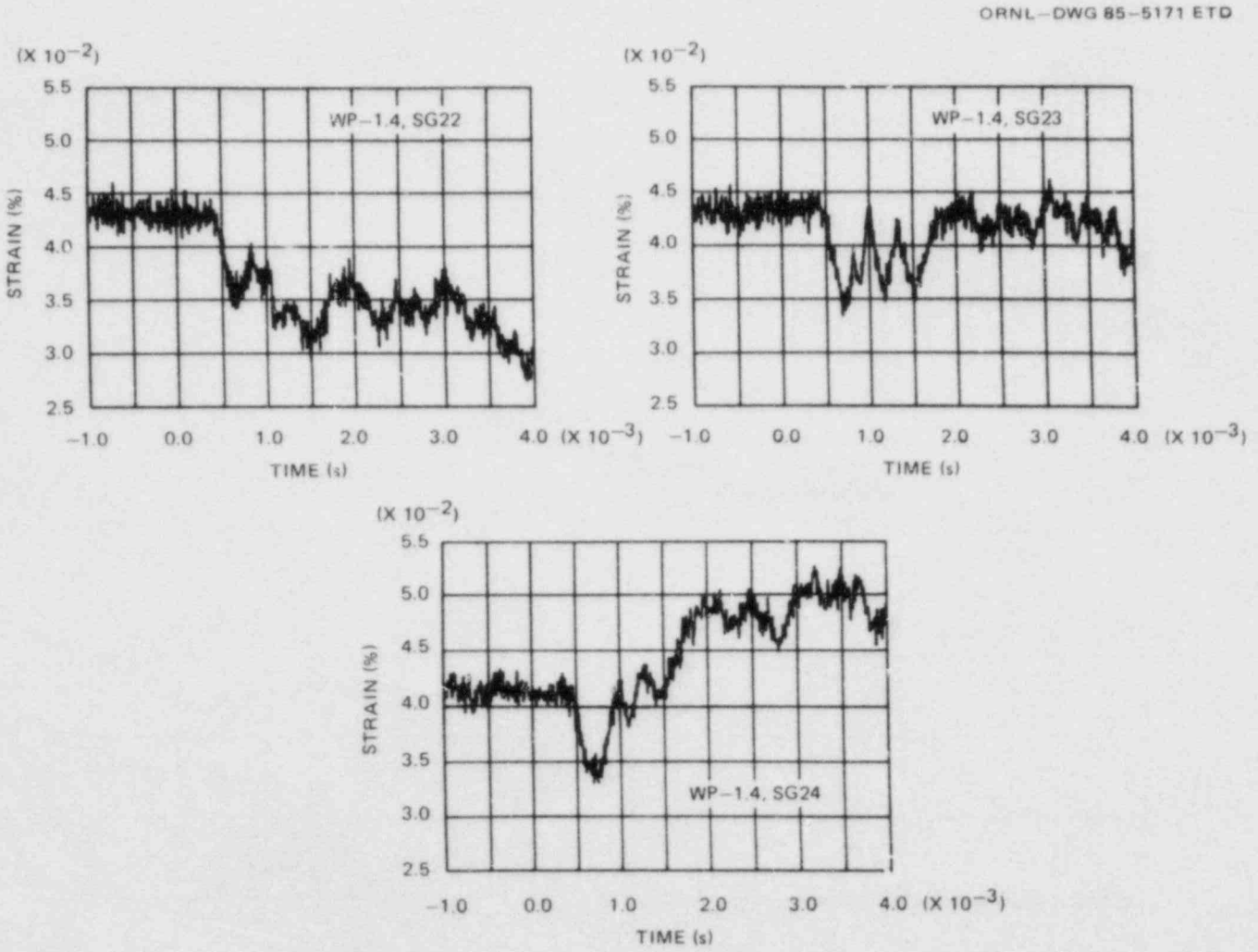

Fig. 5.41. Strain records from Gages 22, 23, and 24 during second run-arrest event of WP-1.4.

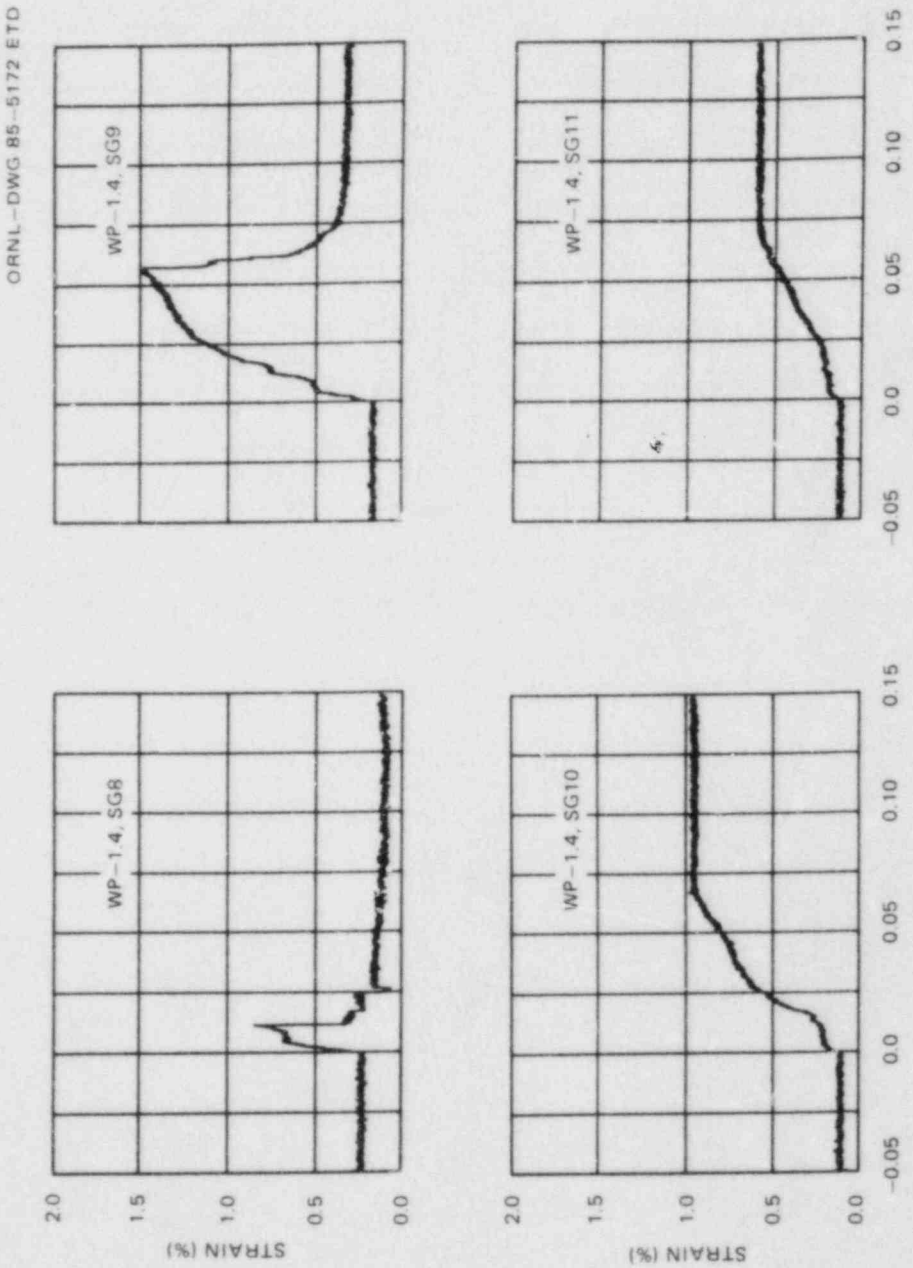

Fig. 5.42. Strain records from Gages 8, 9, 10, and 11, showing second arrest of WP-1.4 followed by pause and start of slow tearing.

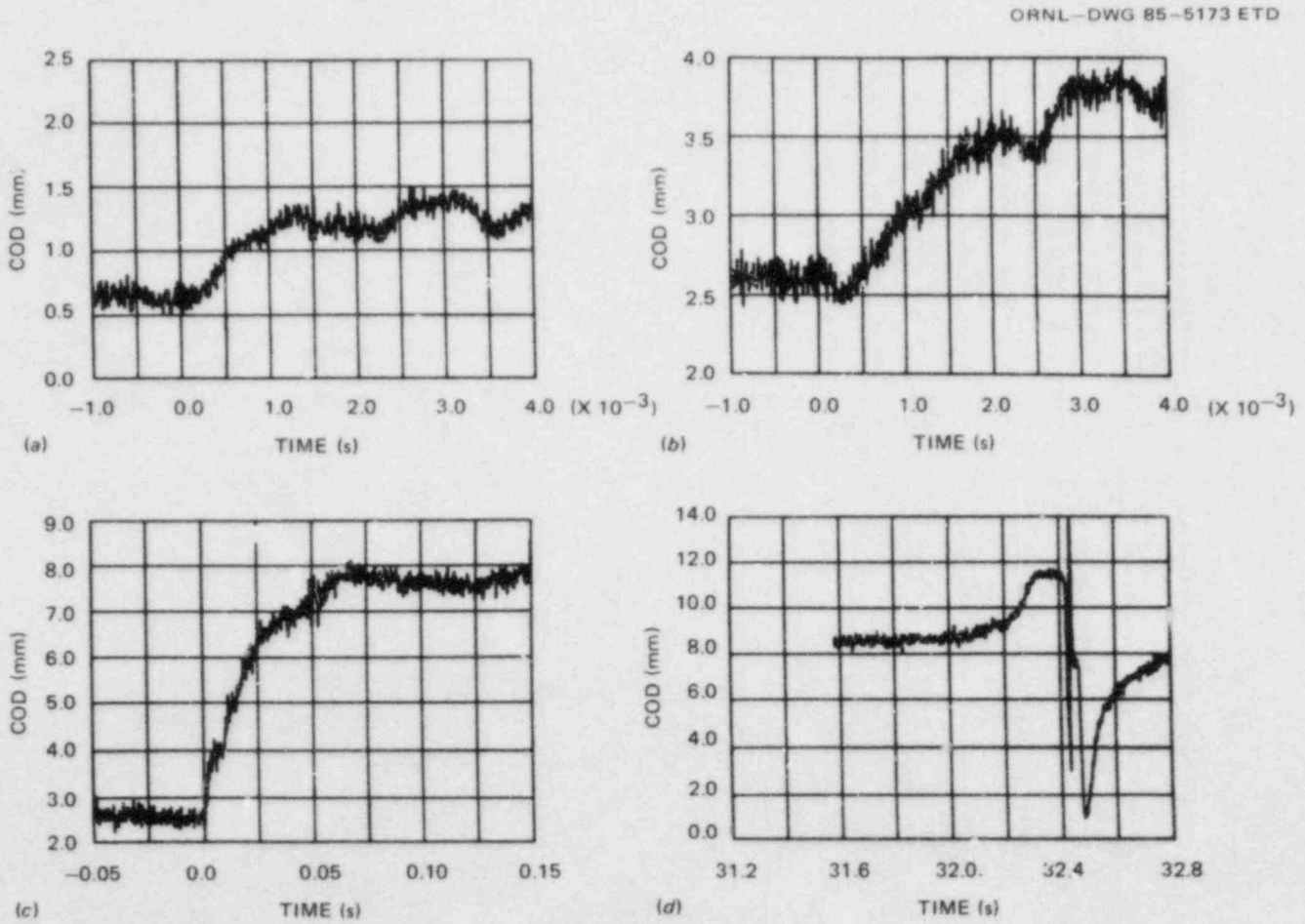

Fig. 5.43. Output of large COD gage on WP-1.4 during (*a*) first event, (*b*) and (*c*) second event, and (*d*) third event. Zero time in (*d*) would correspond to start of second event. Gage broke during third event.

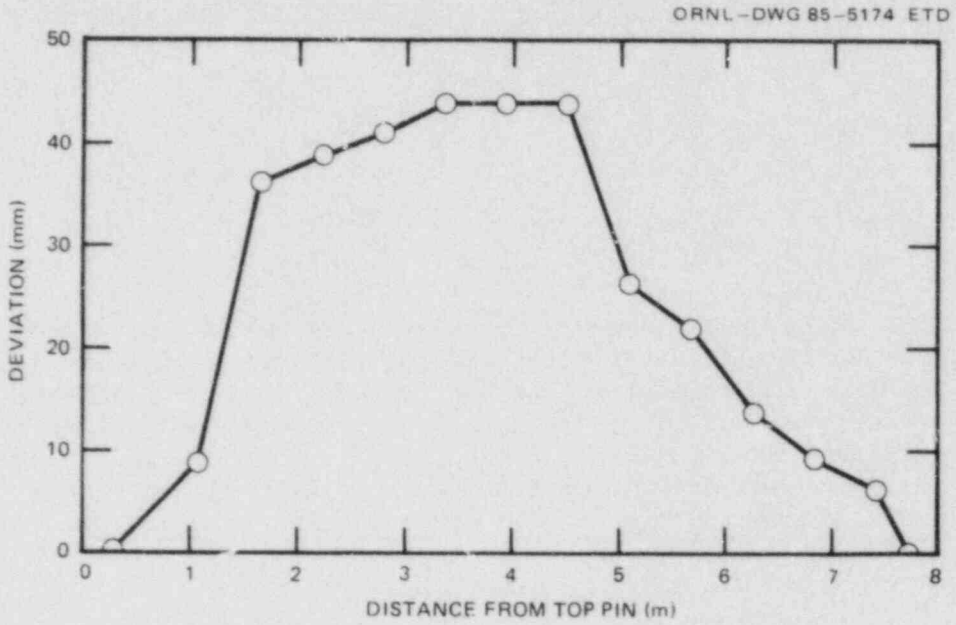

Fig. 5.44. Out-of-plane bowing for WP-1.4 specimen and pull-plate assembly.

of the plate assembly. Presumably, the out-of-plane deformation in the interval from 4.5 to 8 m is due to residual stresses introduced by the welding of one of the pull plates to the plate specimen. The measured deflection in the interval from 0 to 3.5 m possibly indicates an additional problem with out-of-plane warp of one of the pull plates. The effects of the resultant eccentric loading on the run-arrest event are uncertain at this point, partly because strain histories from back-side Gages 20, 21, and 25 were not available for comparison with front-side Gages 17, 19, and 23.

From these results, use of the pillow jack clearly resulted in a stable crack arrest that occurred at a temperature of 29.2°C and a/w = 0.441. In addition, a second, nearly stable, crack arrest was obtained on continued loading at 60.0°C and a/w = 0.527. These temperatures and positions refer to the farthest extension of the crack tip at arrest.

5.3 Properties of Wide-Plate Crack-Arrest Test Material

The initial series of wide-plate crack-arrest specimens is taken from the central portion of the 18.73-cm-thick HSST plate 13A of A 533 grade B class 1 steel that is in a quenched and tempered condition. Properties of this plate include Young's Modulus E = 206.9 GPa, Poisson's Ratio $\nu = 0.3$, thermal expansion coefficient $\alpha = (11 \times 10^{-6})$°C, and density $\rho = 7850$ kg/m^3. Temperature-dependent multilinear representations of stress-strain curves for this material are described in Refs. 5 and 11.

Temperature-dependent fracture-toughness relations for initiation and arrest, based on small-specimen data, are given as follows:

$$K_{Ic} = 51.276 + 51.897\, e^{0.036\,(T - RT_{NDT})}\ , \tag{5.1}$$

$$K_{Ia} = 49.957 + 16.878\, e^{0.028738\,(T - RT_{NDT})}\ . \tag{5.2}$$

Units for K and T are in megapascals times root meters and degrees Celsius, respectively. Drop-weight and Charpy test data indicate that $RT_{NDT} = -23°C$. The small-specimen K_{Ia} data for this material were obtained by BCL (see Ref. 12 and Fig. 5.27 of Ref. 4), and all other data were obtained by ORNL (Ref. 13). CVN results are given in Fig. 5.28 of Ref. 4 for specimens taken from the middle of plate 13A.

Analytical studies have used a dynamic fracture-toughness relation in the following form:

$$K_{ID} = K_{Ia} + A(T)\,\dot{a}^2\ , \tag{5.3}$$

where K_{Ia} is given by Eq. (5.2) and

$$A(T) = [329.7 + 16.25\,(T - RT_{NDT})] \times 10^{-6}\ , \tag{5.4}$$

or

$$A(T) = [121.71 + 1.296\,(T - RT_{NDT})] \times 10^{-6}\ , \tag{5.5}$$

if $(T - RT_{NDT})$ is greater or less than $-13.9°C$, respectively. Units for K_{ID}, A, $\dot{a}$, and T are megapascals times root meters, megapascals times square seconds times meters to the $-3/2$, meters per second, and degrees Celsius, respectively. The form of the K_{ID} expression in Eq. (5.3) and relations for A(T) [Eqs. (5.4) and (5.5)] are derived from Ref. 14 by estimating that $RT_{NDT} = -6.1°C$ for the material used in that study.

5.4 Wide-Plate Analyses at ORNL

B. R. Bass J. K. Walker
C. E. Pugh

5.4.1 ORNL summary of wide-plate crack-arrest tests WP-1.1 through WP-1.4

This section summarizes the static and dynamic analysis results obtained thus far by ORNL for tests that have been performed in the WP-1

series. The results are also compared with those from other large specimen experiments performed in the United States, France, and Japan.

Cleavage initiation was experienced at very high loads in the first two tests, but they exhibited arrest, if for only a small fraction of a second, prior to tearing instability. Test WP-1.2 actually exhibited two such microarrest periods. The initiation loads were reduced further for tests WP-1.3 and WP-1.4. An arrest period of about 2 s was experienced in WP-1.3, and the arrest in WP-1.4 was completely stable. Test WP-1.4 was reinitiated by further increase in load to produce a second cleavage initiation-run-arrest event. Table 5.9 shows the general conditions for these four experiments, and Fig. 5.4 shows the target temperature profiles for each test.

Table 5.9. Summary of HSST wide-plate crack-arrest tests for A 533 grade B class 1 steel

Test No.	Crack location (cm)	Crack temperature (°C)	Initiation load (MN)	Arrest location (cm)	Arrest temperature (°C)	Arrest $T - RT_{NDT}$ (°C)
WP-1.1	20	−60	20.1[a]	50.2	51	74
WP-1.2A	20	−33	18.9	55.5	62	85
WP-1.2B	55.5	62	18.9	64.5	92	115
WP-1.3	20	−51	11.25	48.5	54	77
WP-1.4A	20.7	−63	7.95	44.1	29	52
WP-1.4B	44.1	29	9.72	52.7	60	83

[a]Specimen was warm prestressed by loading to 19 MN while the crack tip drifted from −17 to −9°C.

Crack-arrest toughness values have been determined by static and dynamic analyses, as well as by handbook techniques. Some of the computed values are summarized in Table 5.10. The values computed from

$$K_I = \sigma \left[\pi a \sec\left(\frac{\pi a}{2w}\right)\right]^{1/2}$$

are plotted in Fig. 5.45 against the arrest temperature minus RT_{NDT}. Figure 5.45 also includes the generation-mode dynamic analysis results for tests WP-1.2 through WP-1.4, the K_{IR} curve from Sect. XI of the *American Society of Mechanical Engineers Code*, and the K_{Ia} curve that corresponds to small-specimen data for WP-1 material [Eq. (5.2)]. The trend of the wide-plate test results shows a rapidly increasing toughness at temperatures near and above the onset of the Charpy upper shelf

Table 5.10. Computed crack-arrest toughness values from HSST wide-plate tests on A 533 grade B class 1 steel

Test No.	Crack-arrest toughness values ($MPa\cdot\sqrt{m}$)				
	Static SEN formulas		Alternate static formula[c]	Dynamic finite element	
	Displacement control[a]	Load control[b]		Application mode	Generation mode
WP-1.1	391	813	340	599	NA
WP-1.2A	384	942	349	706.7	440
WP-1.2B	416	1489	419	NA	523
WP-1.3	215	424	185	448	242.8
WP-1.4A	145	248	120	250.9	158
WP-1.4B	331	433	170	NA	396.5

[a] From Ref. 15 (pp. 2.10–2.11) while assuming $a = a_f$ and no further bending occurs because of propagation of the crack.

[b] From Ref. 15 (pp. 2.10–2.11) while assuming $a = a_f$ and full bending according to SEN formula when the final crack depth is used.

[c] $K_I = \sigma\,[\pi a \sec(\pi a/2w)]^{1/2}$ from Refs. 16 and 17 with σ = far-field tensile stress, $a = a_f$ = final crack length, and w = full-plate width.

($T = 55°C$ or $T - RT_{NDT} = 78°C$). The values obtained from tests WP-1.1 through WP-1.4 extend above the limit (220 $MPa\cdot\sqrt{m}$) of the American Society of Mechanical Engineers (ASME) curve. Further, Fig. 5.46 shows that the data from the wide-plate tests and those from other large-specimen experiments form a consistent trend with $(T - RT_{NDT})$. The sources of data other than WP-1 in Fig. 5.46 are discussed in Refs. 2 and 18–21.

5.4.2 Posttest generation-mode analysis of test WP-1.2

Posttest elastodynamic analyses of the wide-plate test WP-1.2 were performed with the ORNL version of the SWIDAC (Ref. 22) dynamic crack-analysis code. Application-mode dynamic analyses of test WP-1.2 were reported previously in Refs. 4 and 5. The two-dimensional (2-D) plane stress finite-element model of the wide-plate configuration used in the analyses is depicted in Fig. 5.31 of Ref. 4. Because of symmetry conditions, only one-half of the plate assembly is included. The model consists of 626 nodes and 180 eight-noded isoparametric elements. A total

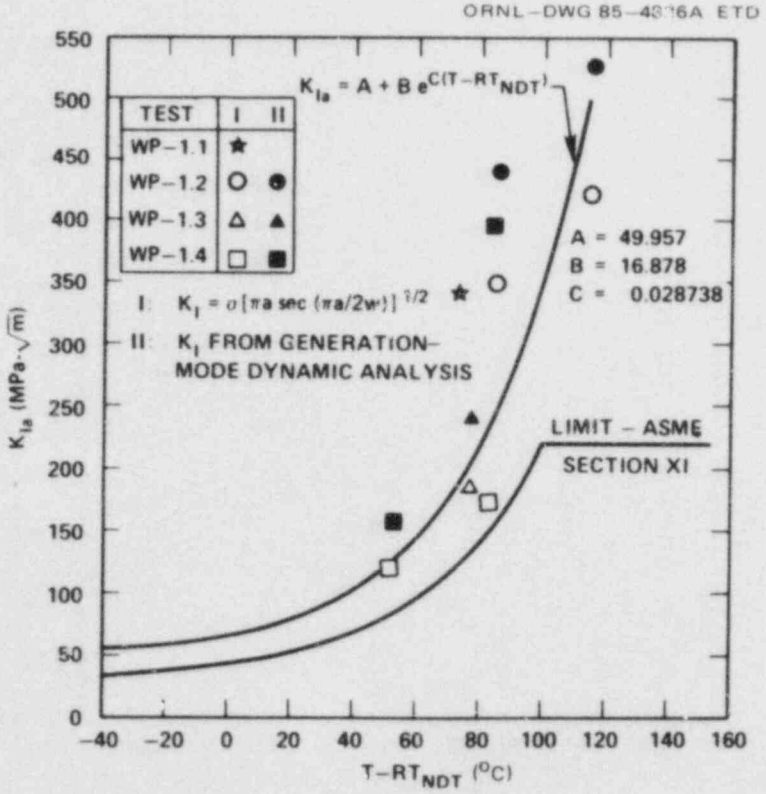

Fig. 5.45. Wide-plate specimen high-temperature crack-arrest data for tests WP-1.1 through WP-1.4.

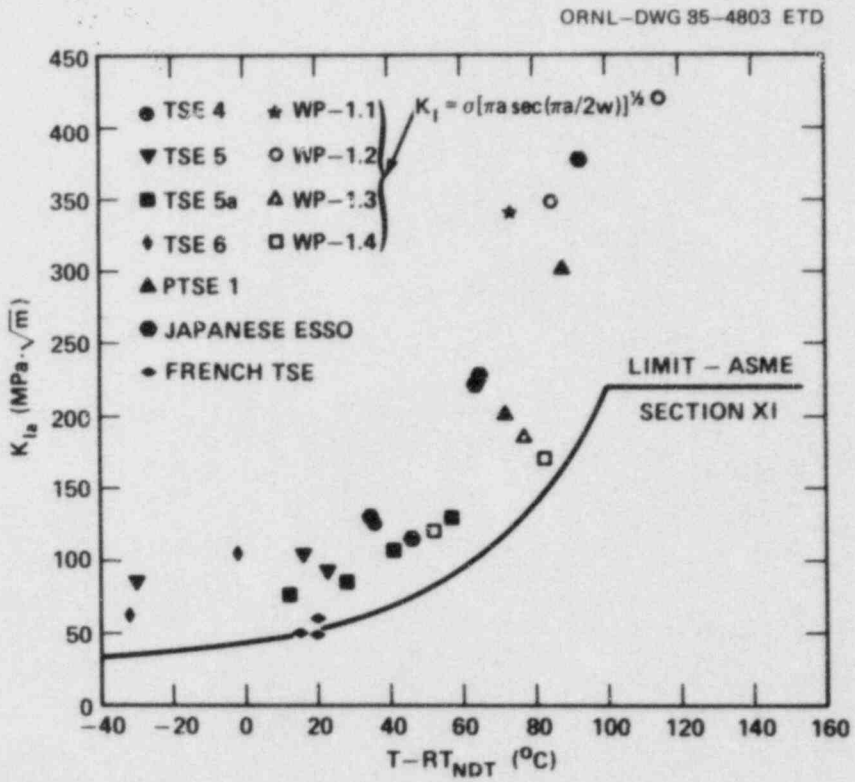

Fig. 5.46. Wide-plate crack-arrest data from consistent trend with data from other large crack-arrest specimen tests.

of 27 spring elements are used in the crack plane to model propagation of the crack tip. Side grooves are taken into account by adjustment of the resulting stress-intensity factor calculated in each time step of the analysis.

The generation-mode analysis of test WP-1.2 described here utilized the temperature gradient of Table 5.11 and the material properties of Sect. 5.3. While the steady state temperature gradient imposed on the plate assembly does not include thermal stresses, the global deformation of the assembly because of thermal strains must be incorporated into the analyses. The thermal boundary conditions assume that the temperatures T_{min} and T_{max} of the cooled and heated edges, respectively, of the plate are fixed along a segment 2.44 m in length, centered relative to the crack plane. The temperature of the edges of the pull-tabs, which extend 90 cm toward the specimen from the center of the pull-pins, are prescribed to be T = 20°C. The remaining surfaces of the assembly are assumed to be insulated. Static thermoelastic analyses were performed with the ADINAT/ADINA (Ref. 23) finite-element codes to determine the thermal deformation of the plate assembly. These thermal displacements were added to the nodal point data defining the finite-element model. Generally, the load-line eccentricity caused by the thermal gradients used in the test elevates the stress-intensity factors for the initial crack (a/w = 0.2) by ~10%.

In the initial static analysis the measured fracture load of F_{in} = 18.9 MN was applied to determine the load point displacement U_{LL} = 0.51564×10^{-2} m and the initiation stress-intensity factor K_I = 251.5 MPa•$\sqrt{m}$. For the dynamic analysis the load point was fixed at the displacement value of the initiation load, and the time step was set at Δt = 10 μs.

Table 5.11. Transverse temperature profile in wide-plate test specimen WP-1.2 at time of crack initiation

Location x (m)	Measured temperature (°C)	Planned temperature (°C)
0	−97	−95
0.1	−60	−66
0.2	−33	−36
0.3	−9	−6
0.4	17	24
0.5	46	55
0.6	77	84
0.7	110	114
0.9	181	174
1.0	207	205

From the strains recorded at the crack-line gages (see Fig. 5.17 of Ref. 4 for gage locations) and from an inspection of the fracture surface, NBS (Ref. 24) constructed the estimate given in Fig. 5.47 of the crack position as a function of time $t \leq 5$ ms. In Fig. 5.47 the curve depicting two measured crack arrests at $a_f = 0.55$ m and at $a_f = 0.645$ m was used as input to SWIDAC for a generation-mode analysis of test WP-1.2. From the SWIDAC calculations the amplitude of the stress-intensity factor as a function of time and crack depth is given in Figs. 5.48 and 5.49, respectively. The generation-mode analysis results for the two arrest events were $a_f/w = 0.55$, $T = 61.5°C$, and $K_{Ia} = 440$ MPa$\cdot\sqrt{m}$; $a_f/w = 0.65$, $T = 93.5°C$, and $K_{Ia} = 523$ MPa$\cdot\sqrt{m}$. Also from the SWIDAC analysis, the second propagation event initiated at $a/w = 0.55$ with a predicted stress-intensity factor $K_I = 577.9$ MPa$\cdot\sqrt{m}$.

The computed strain-time histories from selected points close to crack-line Gages 1 through 8 (Fig. 5.17 of Ref. 4) are depicted in Fig. 5.50. These results indicate that a sharply defined strain peak is associated with the fast-running crack passing under a gage point, with the peak being transformed into a more blunted curve as the crack tip slows down. Figure 5.51 depicts the strain level computed at points near crack-line Gages 1 through 4 expressed as a function of the normalized separation between the crack-tip position and the location of the strain point. These results indicate that the peak value of strain at a point near the crack line in the dynamic model occurs at the time when the moving crack tip is located approximately beneath the gage point. This relation between the time of occurrence of peak strains and the location of the crack tip is important in the determination of crack velocities and crack histories from strain data recorded during the test. The computed

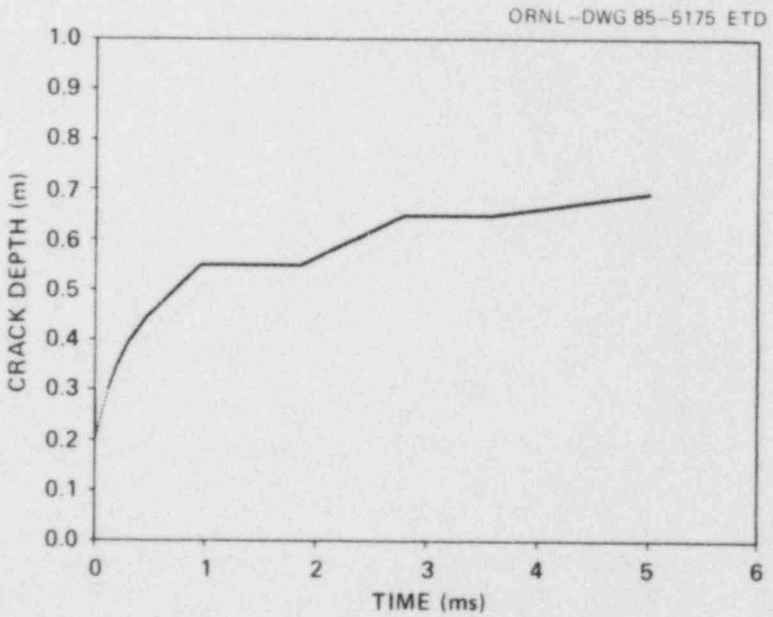

Fig. 5.47. Crack-depth vs time from measured data used as input for posttest generation-mode dynamic analysis of WP-1.2.

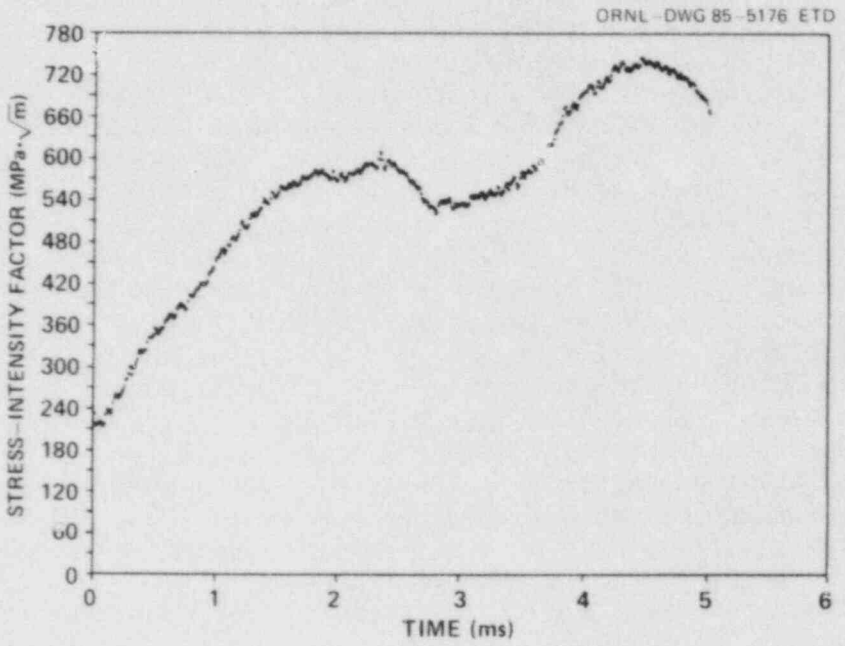

Fig. 5.48. Stress-intensity factor vs time from posttest generation-mode dynamic analysis of WP-1.2.

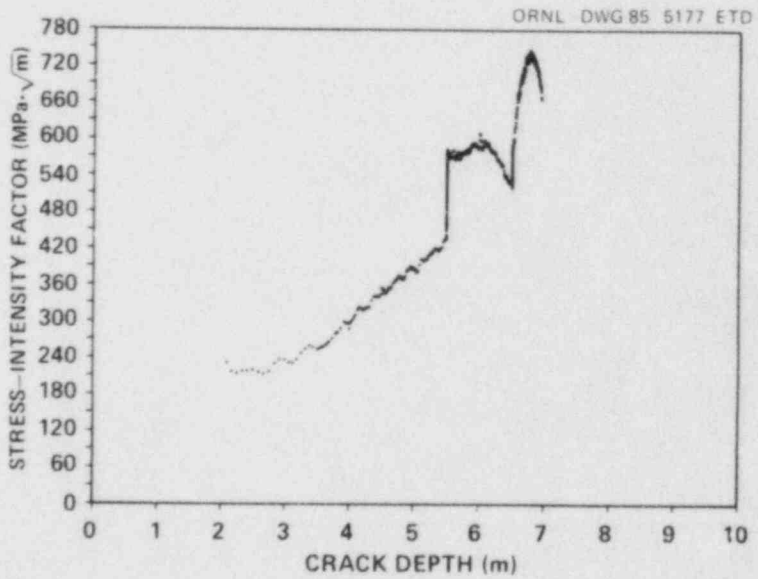

Fig. 5.49. Stress-intensity factor vs crack depth from posttest generation-mode dynamic analysis of WP-1.2.

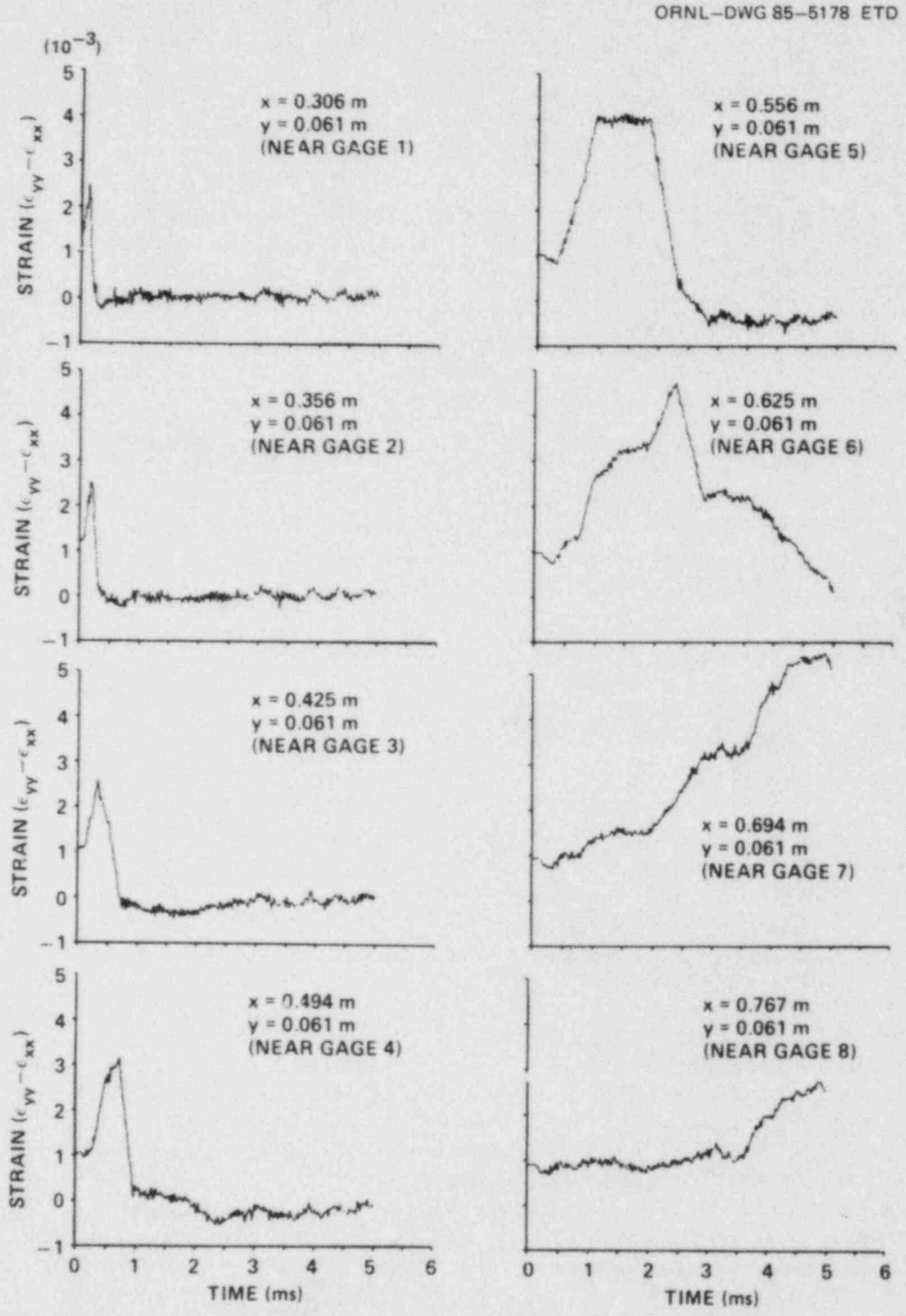

Fig. 5.50. Strain vs time at locations near crack-line gages from posttest generation-mode dynamic analysis of WP-1.2.

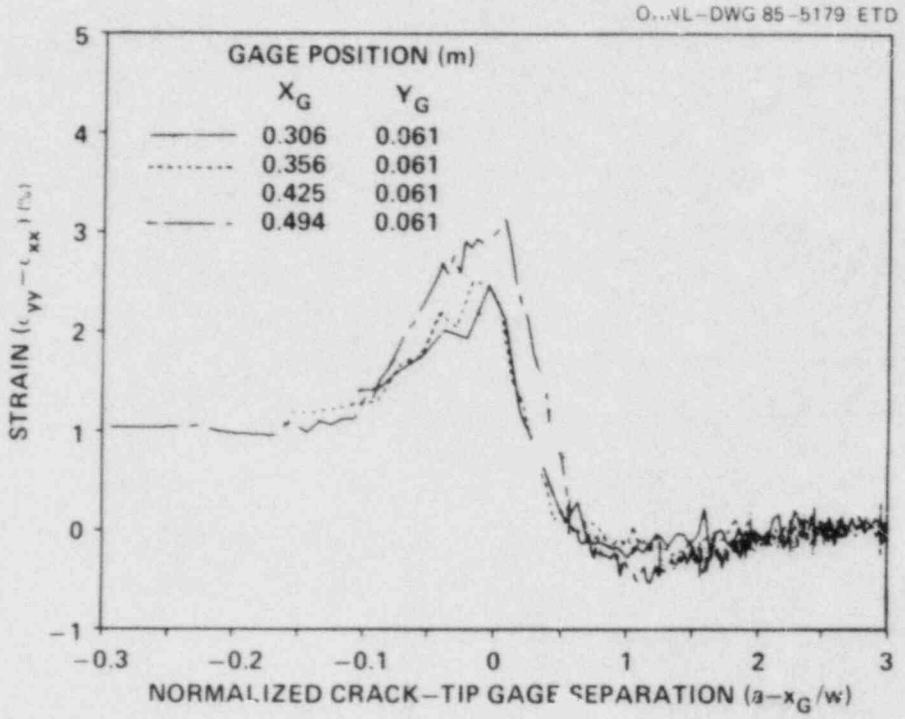

Fig. 5.51. Strain vs normalized crack-tip gage separation from posttest generation-mode dynamic analysis of WP-1.2.

strain-time histories from Gages 1 through 3 and Gage 8 are compared with measured data in Figs. 5.52 and 5.53, respectively. The comparisons in these figures indicate good agreement between measured and computed times for the occurrence of peak strain values.

In Fig. 5.54 the COD calculated at x = 0.175 m from the cold edge in the generation-mode analysis is compared with measured data from test WP-1.2. There is good agreement between the calculated and measured values for the portion of the transient up to t ≈ 2.5 ms, beyond which time the calculated values tend to lag behind the measured data. Figure 5.55 compares the strain-time histories recorded by the far-field Gages 13 and 19 (see Fig. 5.15 of Ref. 4) with the dynamic calculations from selected points close to these gages and indicates generally good agreement through t = 5 ms.

Additional posttest dynamic analyses of the WP-1.2 test performed by the SwRI and UM are presented in Sects. 5.5 and 5.6, respectively, of this report. There is generally good agreement between the generation-mode results from these institutions and the previously stated results obtained by ORNL.

5.4.3 Posttest analysis of WP-1.3

5.4.3.1 Three-dimensional finite-element analysis of test WP-1.3. Three-dimensional (3-D) static finite-element analyses were performed on the WP-1.3 plate assembly to ascertain the static stress-intensity factor

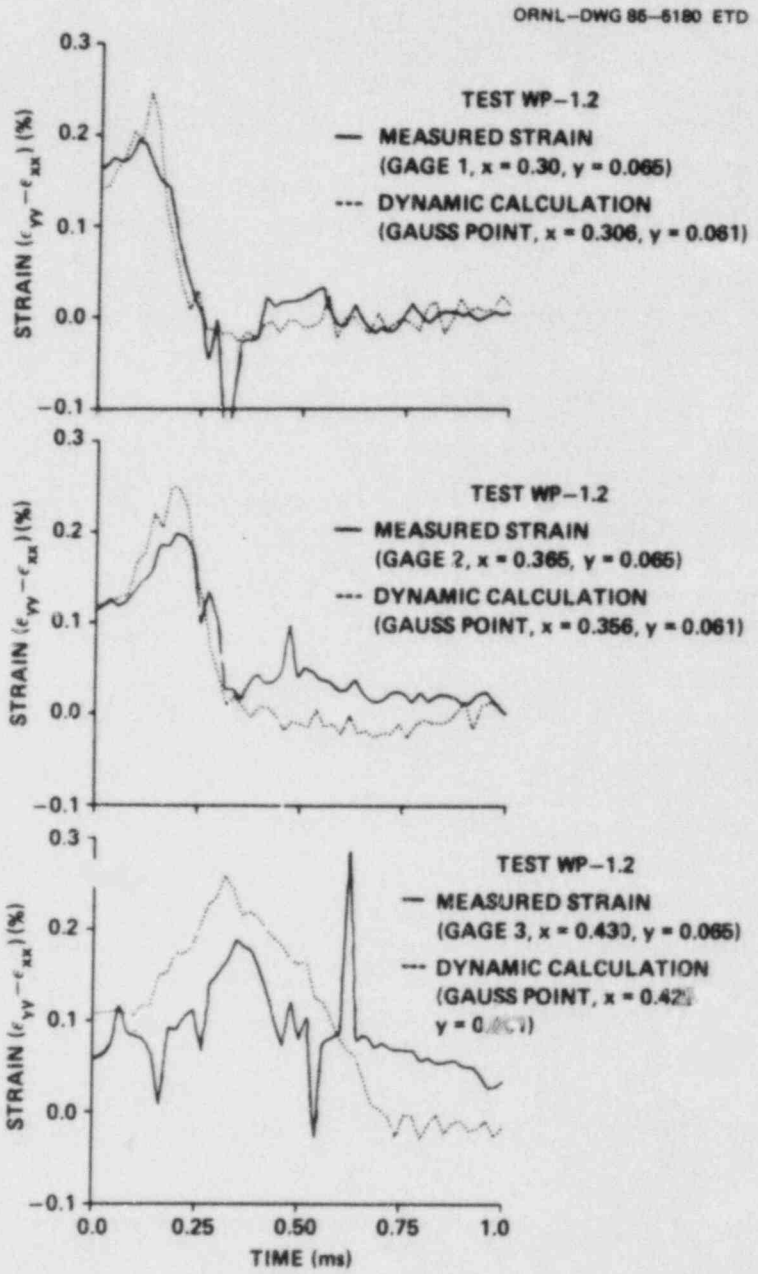

Fig. 5.52. Comparison between strain-time histories from measured data and dynamic calculations at Gages 1, 2, and 3 for generation-mode analysis of WP-1.2.

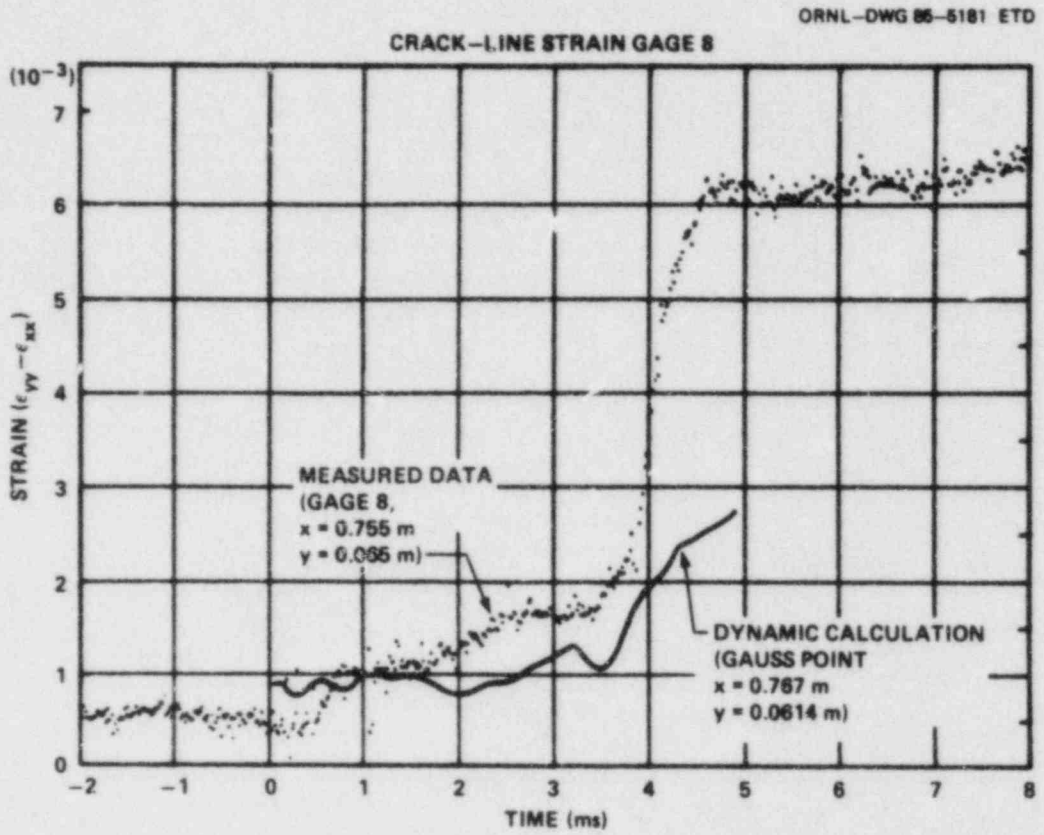

Fig. 5.53. Comparison between strain-time histories from measured data and dynamic calculations at Gage 8 for WP-1.2.

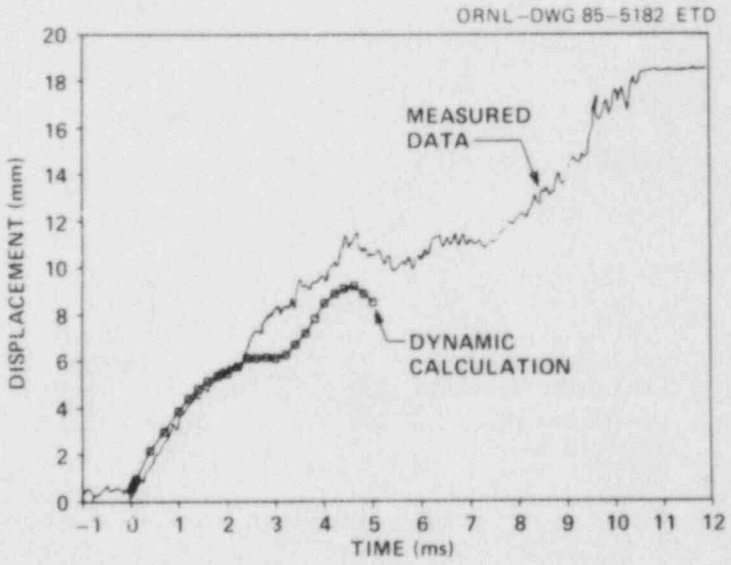

Fig. 5.54. Comparison between COD histories from measured data and dynamic calculations at a/w = 0.175 for generation-mode analysis of WP-1.2.

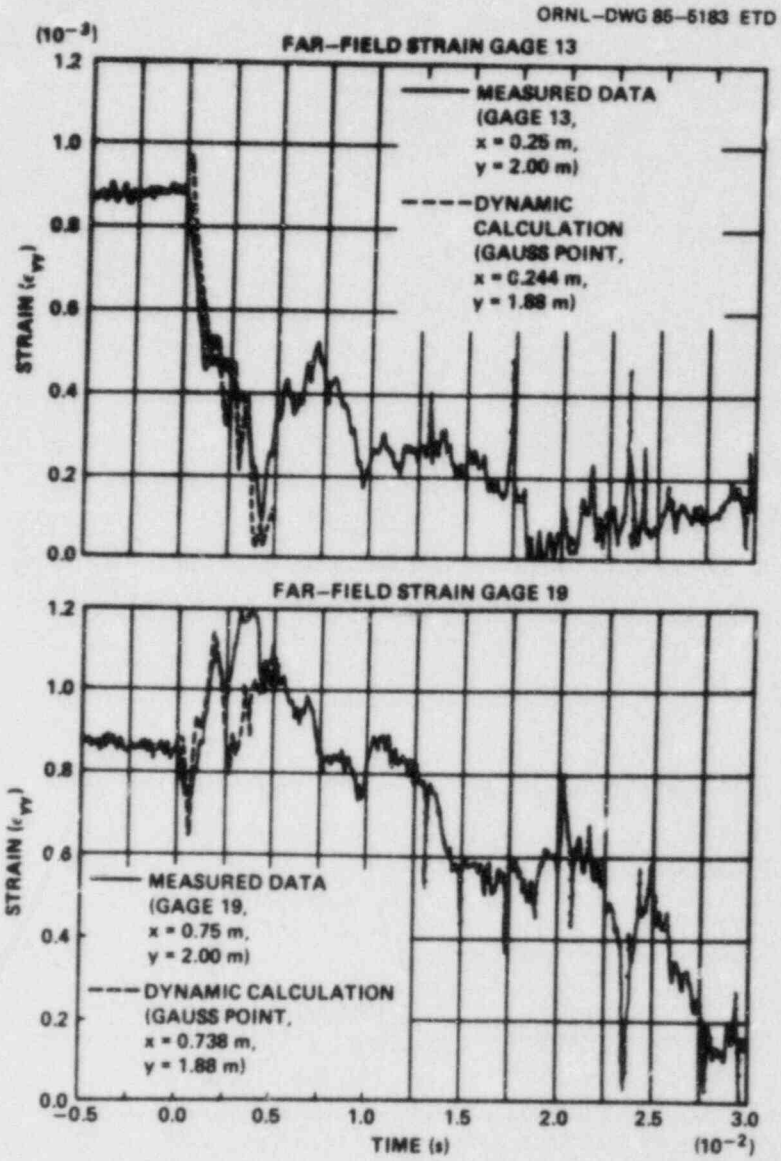

Fig. 5.55. Comparison between strain-time histories from measured data and dynamic calculations at Gages 13 and 19 for WP-1.2.

at the time of crack initiation. These analyses were carried out using the ORMGEN/ORVIRT (Refs. 25 and 26) fracture-analysis system in conjunction with the ADINA-84 (Ref. 23) finite-element code installed on the CRAY-1-S supercomputer at Martin Marietta Energy Systems, Inc.

The portion of the plate modeled in these analyses consists of a segment 4.8 m in length m[illegible]red from the crack plane to the top of the load-pin hole, which, with [illegible]e wings of the pull tab, was not included in the model. A detailed description of the crack-tip region of the model is given in Fig. 5.56, which shows portions of the chevron cutout, the

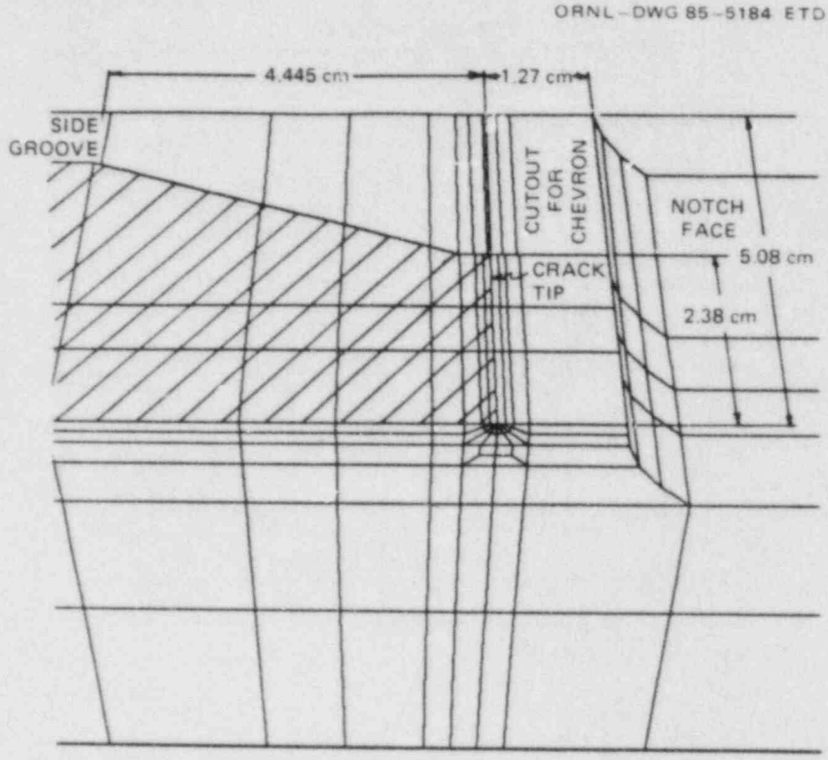

Fig. 5.56. Detail of crack-tip region from 3-D finite-element model of WP-1.3 wide-plate assembly.

side grooving, and the edge notch. Dimensions of the chevron cutout are taken from the photograph of the exposed crack plane in Fig. 5.19. From symmetry conditions, one-quarter of the partial pull-plate assembly is modeled using 3751 nodes and 720 20-noded isoparametric elements.

The thermal deformation computed from a pretest 2-D analysis was superposed on the 3-D finite-element model to account for the in-plane thermal bending effect in the 3-D analyses. The boundary conditions of the 2-D thermoelastic analysis assumed that the heated and cooled edges of the plate were fixed at T_{max} = 233°C and T_{min} = −133°C, respectively, along a 2.4-m length (centered relative to the crack plane) and that the pull-tab edges were prescribed to be T = 20°C. The remaining surfaces of the assembly were assumed to be insulated. Material properties used in both the 2-D and 3-D static analyses are given in Sect. 5.3. The in-plane thermal bending produced a load-line (through the top of the load-pin hole) eccentricity of 2.72 cm relative to the geometric center of the pull-plate assembly.

In the 3-D analyses, thermal stress effects were neglected, and a uniform line-load statically equivalent to the WP-1.3 test initiation load of 11.25 MN was applied at the location corresponding to the top of the load-pin hole. The results of this analysis produced a static stress-intensity factor of K_I = 173.5 MPa•$\sqrt{m}$ at the center plane of the plate. Comparison of this computed K_I value with the static initiation

value of K_{Ic} = 70.1 MPa$\cdot\sqrt{m}$ from Eq. (5.1) evaluated at the crack-tip temperature of T_{CT} = −51°C yields a ratio of K_I/K_{Ic} = 2.48.

5.4.3.2 Static and stability analysis. Posttest analyses of wide-plate test WP-1.3 were carried out using computer codes based on both quasistatic and elastodynamic techniques. For the quasistatic analyses, the ORNL computer code WPSTAT (Ref. 5) was used to perform both crack-arrest and crack-stability analyses. As described in Ref. 5, the WPSTAT code evaluates static stress-intensity factors as a function of crack length a and temperature differential $\Delta T = T_{max} - T_{min}$ across the plate. These factors are computed for fixed-force conditions K_I^F (a, ΔT) and for fixed load-pin displacement conditions K_I^{DSP} (a, ΔT) by superposing contributions from tension and bending finite-element and handbook solutions. In addition, WPSTAT categorizes arrested crack lengths in terms of three types of instability limits that are enumerated in the following.

For the third wide-plate test, the proposed temperature profile was defined by specifying a crack-tip temperature of T_{CT} = −60°C at x = 0.2 m and a mid-plate temperature T_{MP} = 50°C at x = 0.5 m, implying T_{min} = −133.3°C and T_{max} = 233°C. The temperature gradient actually achieved at the time of the run-arrest event deviated from the pretest objective, as indicated in Table 5.2. For the posttest WPSTAT calculations of static factors K_I^F (a, ΔT) and K_I^{DSP} (a, ΔT), a linear approximation of the test temperature profile defined by T_{CT} = −51°C and T_{MP} = 59°C was employed, implying T_{min} = −124.3°C and T_{max} = 242.3°C; the calculations of initiation toughness K_{Ic} and arrest toughness K_{Ia} utilized a piecewise-linear interpolation of the thermocouple data from Table 5.2. For this specified temperature profile, the dependence of the arrested crack length and crack stability upon the applied initiation load F_{in} was investigated with WPSTAT, and the results are presented in Fig. 5.57. Figure 5.57 includes the statically calculated final crack length a_f and the instability-limit crack lengths for reinitiation $a_{rein}(F_{in})$, for tensile instability a_{I1} (F_{in}), and for tearing instability a_{I2} (F_{in}). The tensile instability calculation is based on the average stress in the remaining ligament equal to an ultimate stress of σ_u = 550 MPa, which represents the lowest value for the temperature range of interest. For the tearing instability calculation, the material tearing resistance is assumed given in the form of a power-law J-resistance curve $J_R = C(\Delta a)^m$, where C = 0.3539, m = 0.4708, and the units of J_R and Δa are megajoules per square meter and millimeters, respectively. In Fig. 5.57 the statically computed arrest length corresponding to the measured initiation load F_{in} = 11.25 MN is given by a_f = 0.575 m. The computed arrest point is above the a_{I2} curve, implying that tearing instability is expected for this situation. The measured initial arrest point a_f = 0.49 m is slightly below the tearing instability curve; however, the measured second arrest in cleavage at a_f = 0.52 m is approaching an instability condition.

The complete static and stability analyses are depicted in Fig. 5.58 for the initiation load of F_{in} = 11.25 MN. Included in the figure are curves for initiation toughness K_{Ic}, arrest toughness K_{Ia}, displacement-controlled stress-intensity factor K_I^{DSP}, and force-controlled stress-intensity factor K_I^F. Evaluation of the $K_{Ia}(a_f)$ curve at the initiation

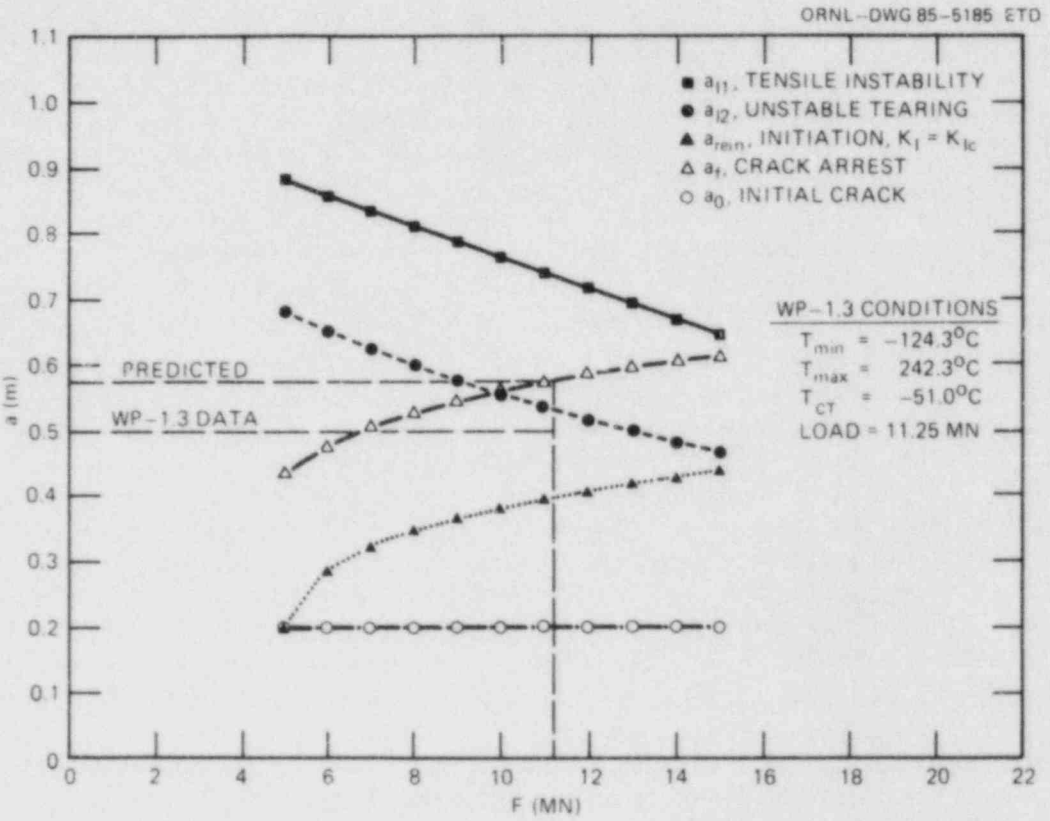

Fig. 5.57. Results of posttest crack-stability analysis of wide-plate assembly showing limits of reinitiation, tearing, and tensile instability.

load F_{in} = 11.25 MN yields an arrest toughness of K_{Ia} = 429 MPa•$\sqrt{m}$ at the predicted arrest point a_f = 0.575 m, where the crack-tip temperature would be T = 85.25°C. The regions of reinitiation, tearing, and tensile instability and the two measured cleavage arrest points are also identified in Fig. 5.58.

5.4.3.3 Application-mode dynamic analysis. Elastodynamic analyses of the wide-plate test WP-1.3 were carried out with the SWIDAC code, using the procedures described in the previous section for WP-1.2. The 2-D plane-stress finite-element model of the wide-plate configuration used in the analyses is depicted in Fig. 5.31 of Ref. 4. A posttest application-mode analysis of the third test WP-1.3 was performed using the temperature gradient of Table 5.2 and the material properties given in Sect. 5.3. In this analysis the crack tip is propagated incrementally according to the following relations:

if $K_I < K_{ID}$ ($\dot{a}$, T), then no propagation;

if $K_I = K_{ID}$ ($\dot{a}$, T), then propagation.

Here, K_I is the dynamically computed stress-intensity factor, and K_{ID} is

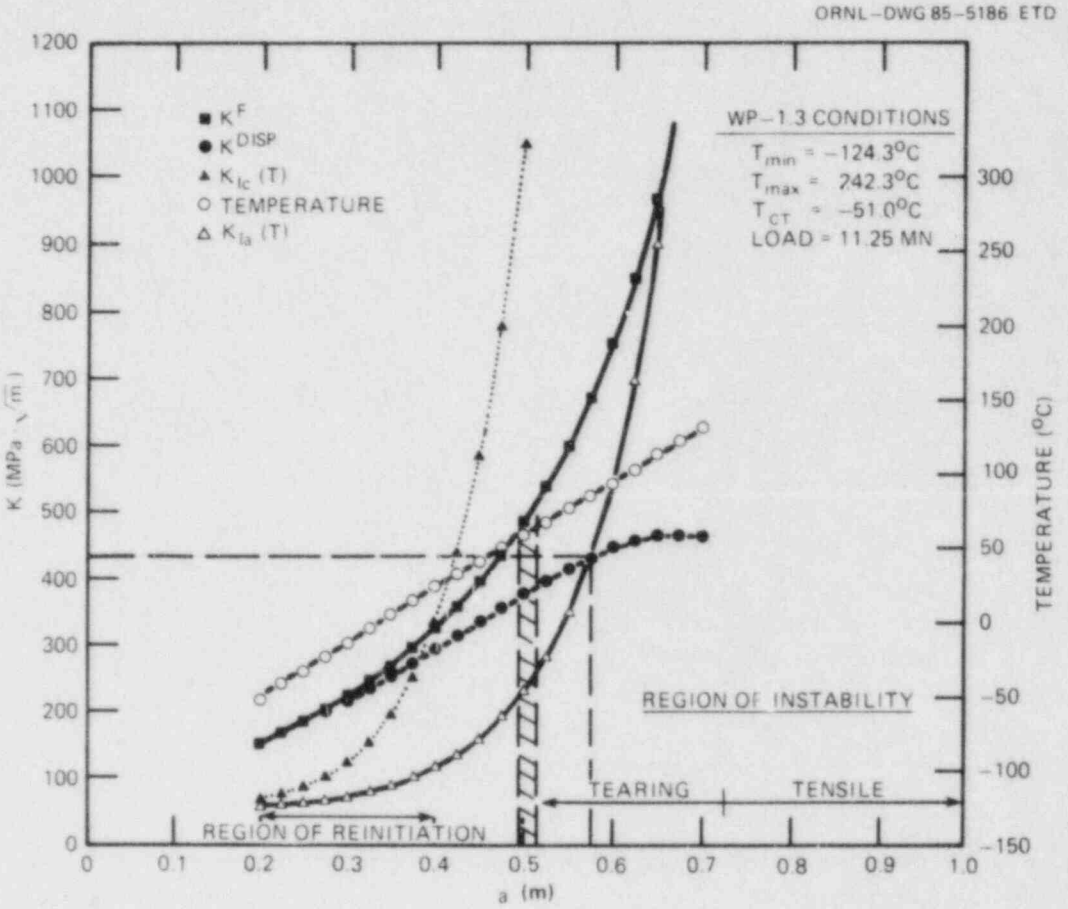

Fig. 5.58. Results of static and stability analyses of wide-plate assembly for measured initiation load F_{in} = 11.25 MN.

a postulated dynamic fracture-toughness relation that is taken to be the function of crack velocity $\dot{a}$ and temperature T given by Eqs. (5.2)–(5.5). The measured fracture load of F_{in} = 11.25 MN was applied at the location of the top of the load-pin hole to determine the load point displacement $U_{LL} = 0.30597 \times 10^{-2}$ m. For the dynamic analysis the load point was fixed at the displacement value of the initiation load, and the time step was set at Δt = 10 μs. Figure 5.59 presents the dynamic factor K_I^{DYN}, the static toughness K_{Ia} [from Eq. (5.2) and Table 5.2], and the crack velocity $\dot{a}$ as a function of instantaneous crack length. The crack propagates into a rising K_I field, followed by arrest at the point a_f = 0.58, where the crack-tip temperature would have been T = 87°C. The arrest toughness at the arrest-point temperature is given by Eq. (5.2) to be K_{Ia} = 448.3 MPa•√m. The computed arrest length exceeds the measured arrest length at a_f = 0.49 m, with crack-tip temperature T = 55.5°C and corresponding arrest toughness K_{Ia} = 211.0 MPa•√m from Eq. (5.2). The analysis results for the quasistatic displacement-controlled factor K_I^{DSP} and for the three previously defined instability limits are also included in Fig. 5.59.

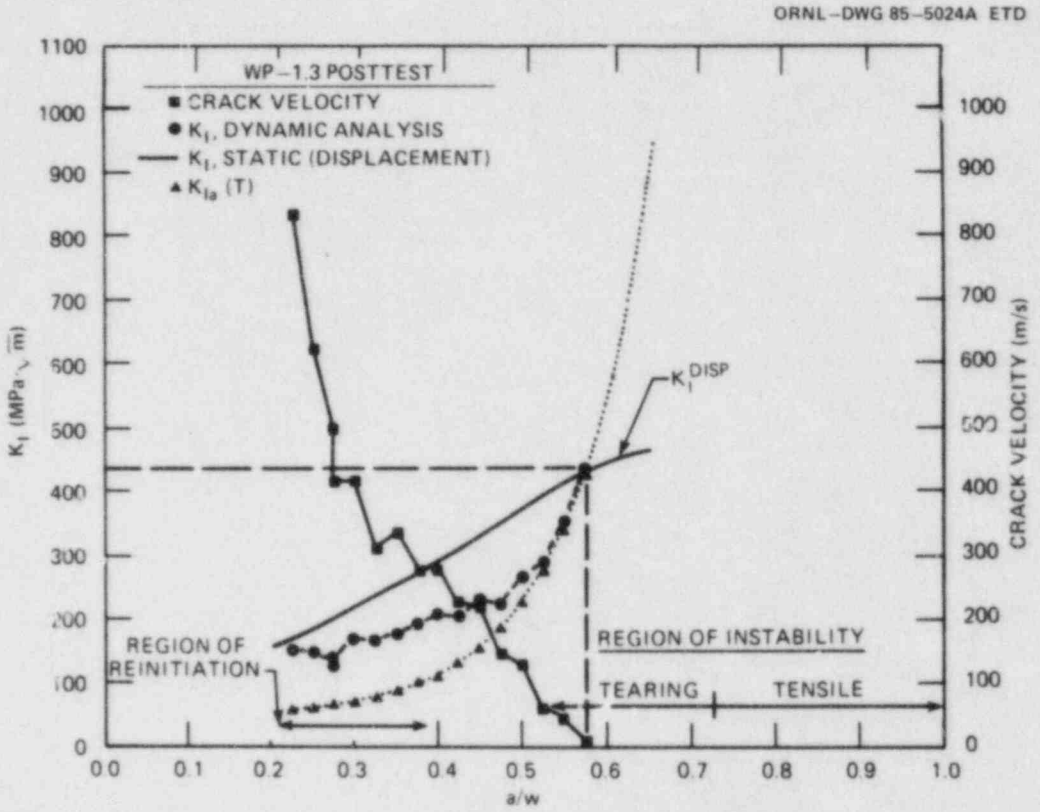

Fig. 5.59. Results of posttest static and dynamic application-mode analysis of WP-1.3.

5.4.3.4 Generation-mode dynamic analysis. From the output of the crack-line gages and from an inspection of the fracture surface, estimates of the crack position as a function of time were constructed by NBS and by ORNL and are given in Table 5.6. Figure 5.60 depicts the NBS-1 estimate of the crack-time curve from Table 5.6 and a modified version of the curve (analysis GM-1 in Table 5.12) that was used as input for a posttest generation-mode dynamic analysis of test WP-1.3. In a generation-mode analysis, the crack tip is propagated incrementally according to a prescribed crack-time history. For the dynamic analysis GM-1, the load point was again fixed at the displacement value of the initiation load, and the time step was set at $\Delta t = 10$ μs.

The computed strain-time histories from selected points close to crack-line Gages 1 through 4 (Fig. 5.14), along with measured data from these gages, are depicted in Fig. 5.61 for analysis GM-1. The comparisons of strain histories in these figures indicate generally good agreement between measured and computed times for the occurrence of peak strain values. In Fig. 5.61(σ) the absence of a sharp peak in the computed strain history at $x = 0.425$ m suggests that the postulated velocity for the crack in the interval $0.4 < a < 0.5$ m is probably too low. To test this conjecture, additional studies were performed to ascertain whether adjustment of the input crack-time history would produce better

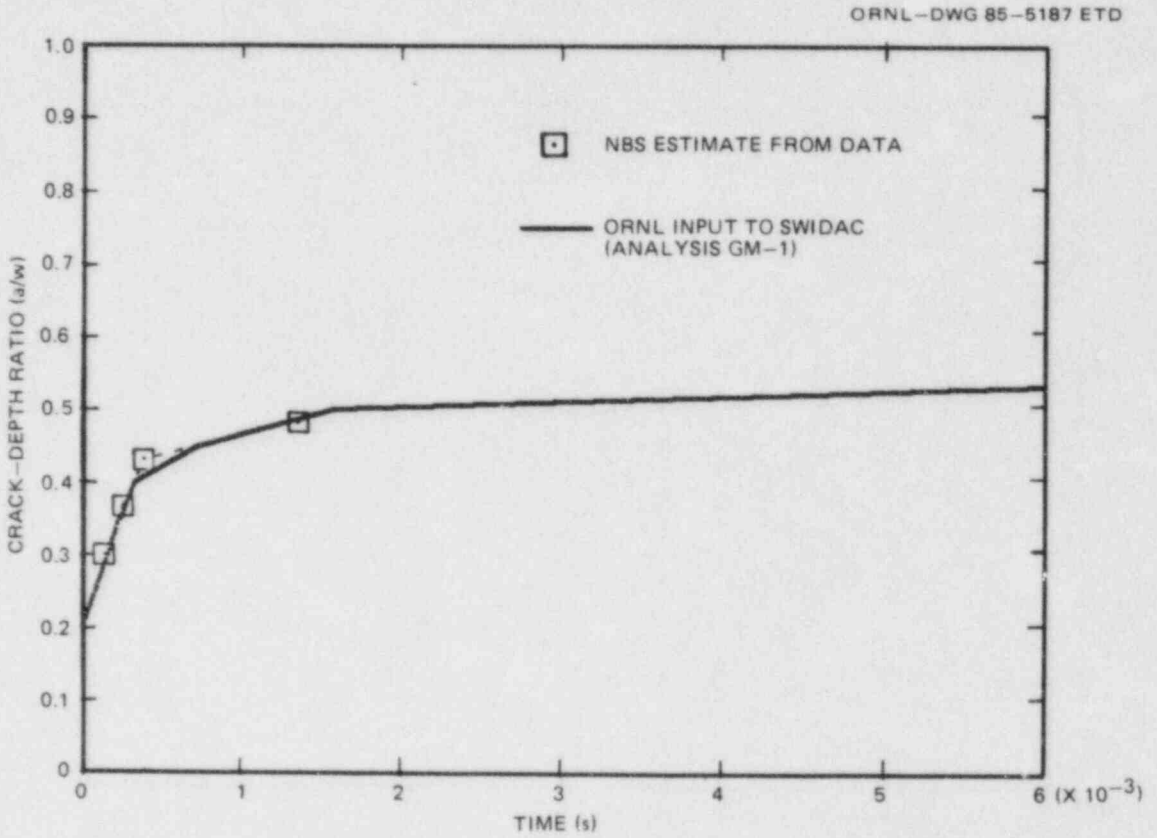

Fig. 5.60. Crack position vs time used in posttest generation-mode dynamic analysis GM-1 of WP-1.3.

Table 5.12. Three crack-time histories employed in generation-mode dynamic analyses of test WP-1.3

Crack position a (m)	Analysis GM-1		Analysis GM-2		Analysis GM-3	
	Time t (ms)	Velocity $\dot{a}$ (m/s)	Time t (ms)	Velocity $\dot{a}$ (m/s)	Time t (ms)	Velocity $\dot{a}$ (m/s)
0.20	0.0		0.0		0.0	
		619.8		619.9		619.8
0.35	0.242		0.242		0.242	
		520.8		520.8		520.8
0.40	0.338		0.338		0.338	
		119.6		190.8		446.4
0.45	0.756		0.600		0.450	
		59.2		50.0		166.7
0.50	1.600		1.600		0.750	
		6.8		Arrest		Arrest
0.55	9.000					

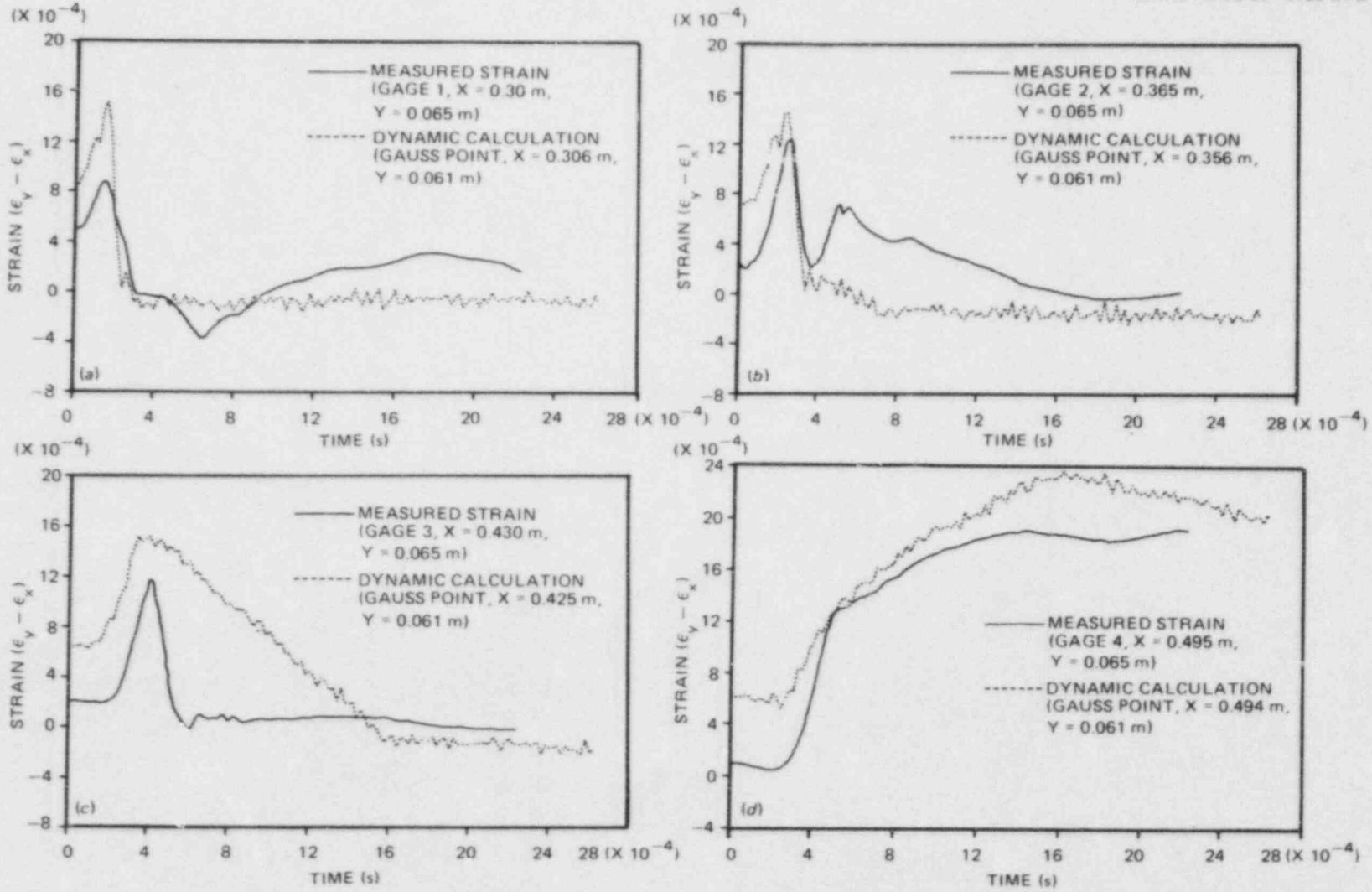

Fig. 5.61. Comparison between strain-time histories from measured data and generation-mode dynamic analysis GM-1 for Gages 1 through 4 (see Fig. 5.14) for WP-1.3.

agreement with measured data from Gage 3. In the second generation-mode analysis (GM-2 of Table 5.12), the crack velocity was adjusted in the interval $0.4 < a < 0.5$ m to obtain the input curve of Fig. 5.62. In Fig. 5.63 the strain history calculated at $x = 0.425$ m by analysis GM-2 shows only marginal improvement when compared with the results from the first analysis and measured data. A third analysis (GM-3 from Table 5.12) utilized the crack-time history of Fig. 5.64, which was constructed as an approximation of the NBS-2 estimate from Table 5.6. As indicated in Table 5.12, the crack velocity was again increased in the interval $0.4 < a < 0.5$ m, and arrest was set to occur at $t = 0.75$ ms. Results from analysis GM-3 for the strain history near Gages 3 and 4 are shown in Fig. 5.65 and indicate improved agreement with measured data. The crack-arrest analysis results were $a_f/w = 0.499$, $T = 59°C$, and $K_{Ia} = 242.3$ MPa$\cdot\sqrt{m}$.

In Fig. 5.66 the COD calculated at $x = 0.175$ m from the cold edge in the generation-mode analysis GM-1 is compared with measured data from test WP-1.3. The divergence between computed and measured values at $t = 6$ ms in Fig. 5.66 is due in part to a sequence of tearing-cleavage-tearing events near $a/w = 0.5$ that are not included in the dynamic model but were previously discussed in Sect. 5.2.5.

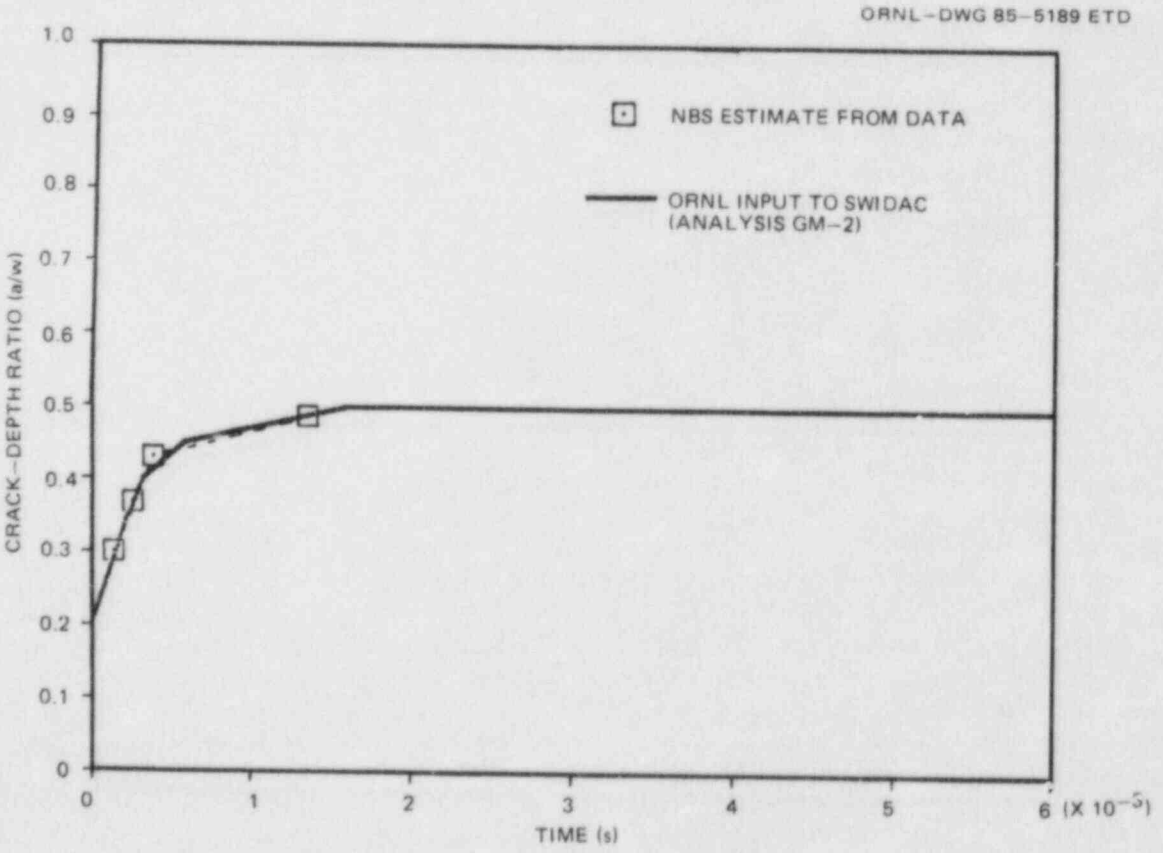

Fig. 5.62. Crack position vs time used in posttest generation-mode dynamic analysis GM-2 of WP-1.3.

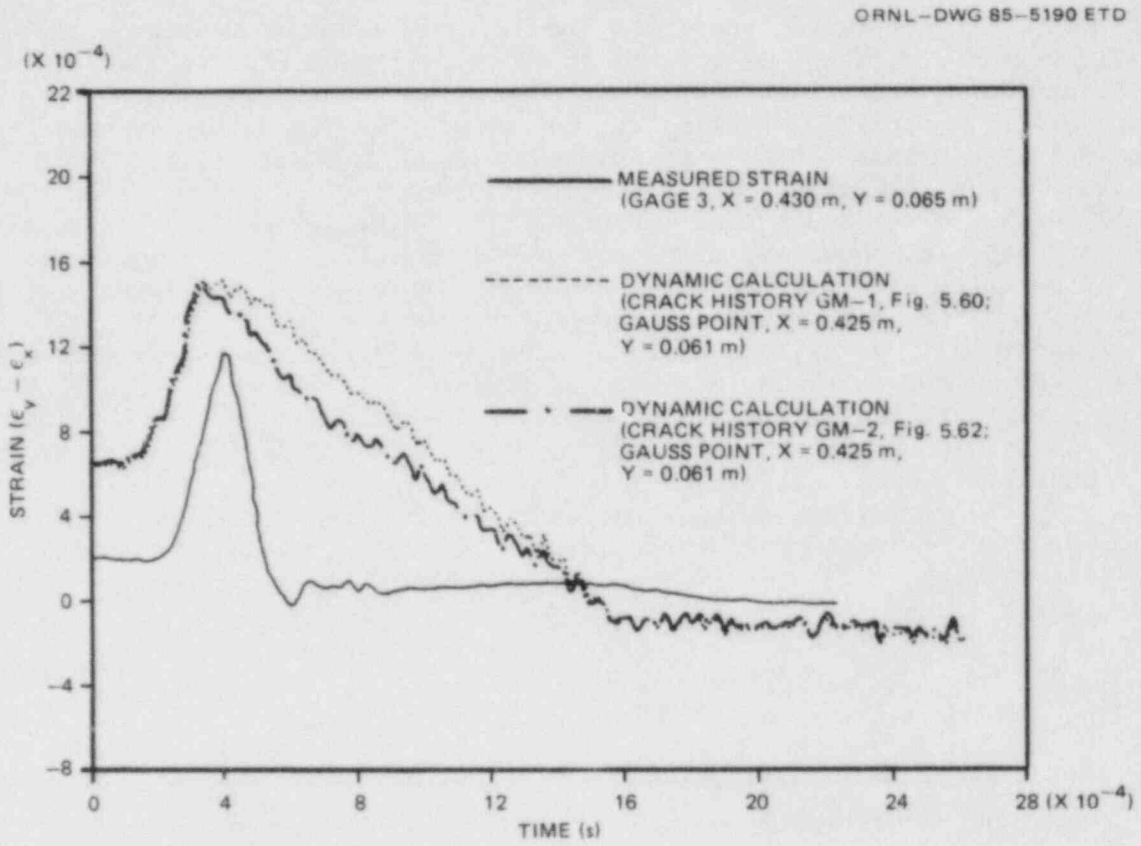

Fig. 5.63. Comparison between strain-time histories from measured data and generation-mode dynamic analyses GM-1 and GM-2 at Gage 3 (see Fig. 5.14) for WP-1.3.

5.4.4 Posttest analyses of WP-1.4

The posttest analyses for test WP-1.4 have been particularly challenging for several reasons, including (1) the complexity of the test in that it exhibits three phases of propagation, (2) the complexities introduced by pressure loading the notch, and (3) difficulties associated with interpreting results from COD gages. Results presented below for test WP-1.4 are preliminary in nature and subject to revision upon review of the data and completion of additional analyses.

5.4.4.1 Three-dimensional finite-element analysis of test WP-1.4. The 3-D finite-element model of the wide-plate assembly incorporated a segment of the plate assembly 5.17 m in length, measured from the crack plane to the top of the load-pin hole. The crack-tip region of the model included the chevron cutout, the side grooving, and the edge notch, the dimensions of which are taken from Figs. 5.1 and 5.29. From symmetry conditions, one-quarter of the partial pull-plate assembly is modeled using 3751 nodes and 720 20-noded isoparametric elements.

The thermal deformations computed from a posttest 2-D analysis were superposed on the 3-D finite-element model to account for the in-plane

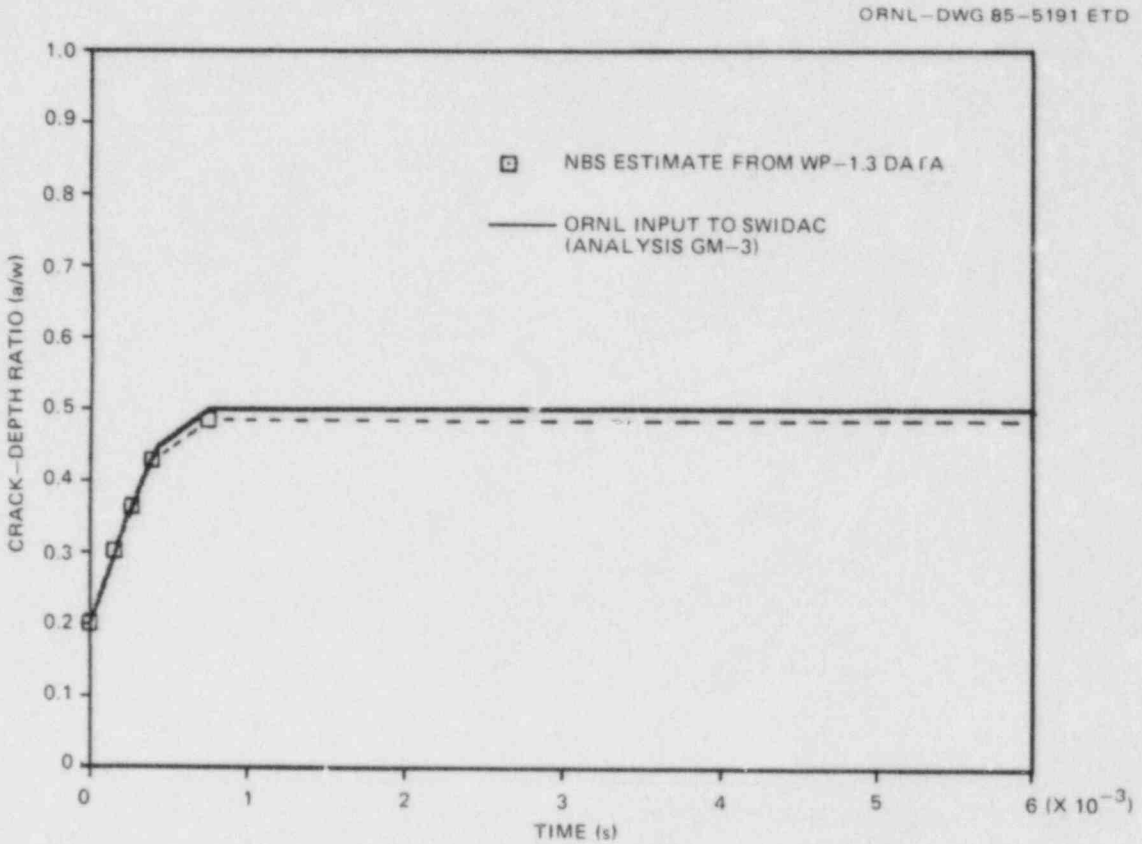

Fig. 5.64. Crack position vs time used in posttest generation-mode dynamic analysis GM-3 of WP-1.3.

thermal bending effect in the 3-D analyses. The boundary conditions of the 2-D thermoelastic analysis assumed that the heated and cooled edges of the plate were fixed at T_{max} = 233°C and T_{min} = −133°C, respectively, along a 2.4-m length (centered relative to the crack plane) and that the pull-tab edges were prescribed to be T = 20°C. The remaining surfaces of the assembly were assumed to be insulated. The in-plane thermal bending produced a load-line (through the top of the load-pin hole) eccentricity of 3.1 cm relative to the geometric center of the plate.

In the 3-D analysis, thermal stress effects were neglected, and two different loading conditions were applied: a uniform axial line load applied at the location corresponding to the top of the load-pin hole and a pressure distribution applied over the face of the notch cutout. Results from these analyses were superposed to provide an estimate of the initiation stress-intensity factor for the WP-1.4 test. Note that the actual pressure loading on the notch face from the pillow jack at the time of initiation is unknown. Consequently, conditions at initiation were estimated from measured data recorded by the large COD gage. Measured data from the large COD gage [Fig. 5.43(*a*)] indicated a deflection of ~0.65 mm at the time of initiation of the first run-arrest event. From analysis of the 3-D model, the axial load of 7.952 MN at initiation produced a

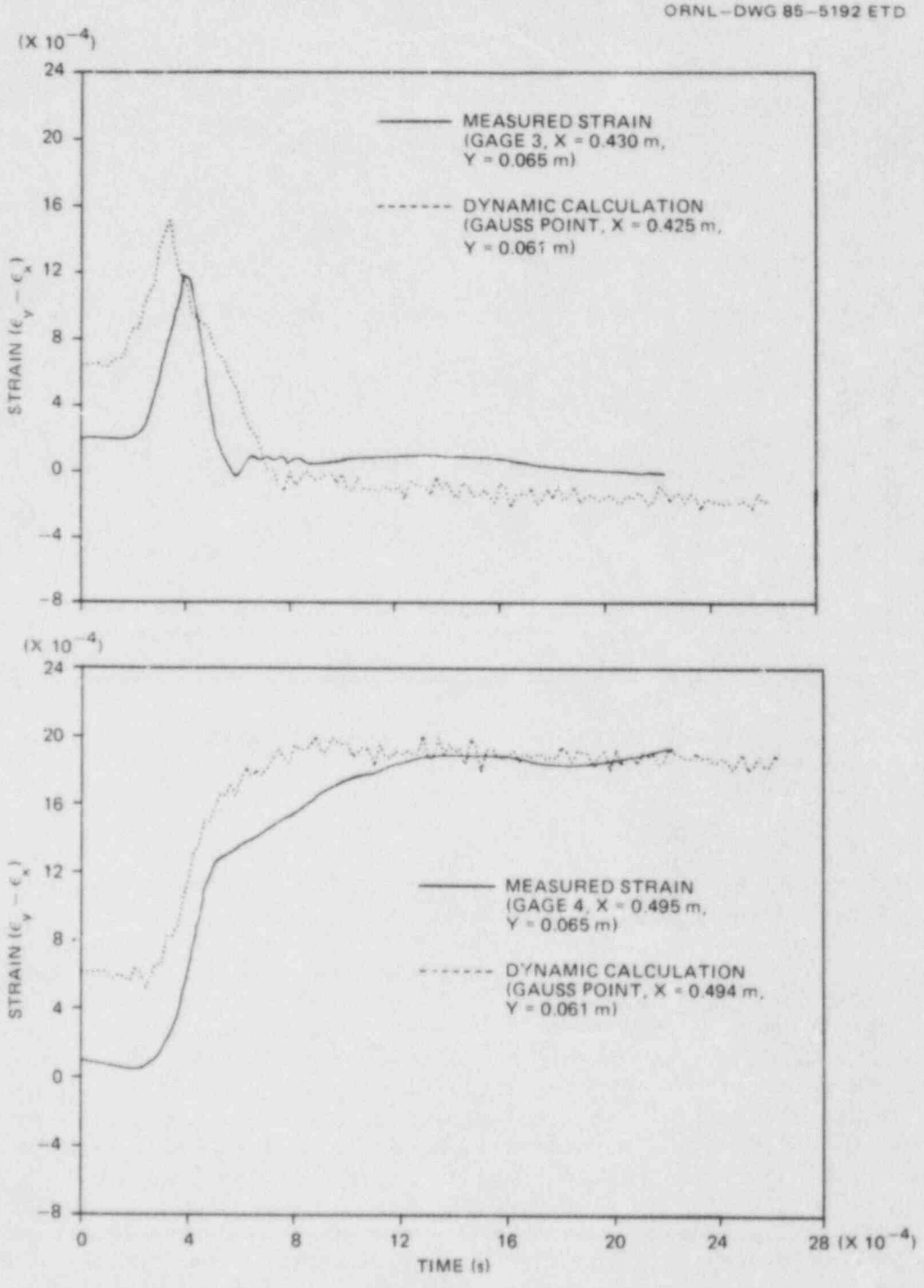

Fig. 5.65. Comparison between strain-time histories from measured data and generation-mode dynamic analysis GM-3 at Gages 3 and 4 (see Fig. 5.14) for WP-1.3.

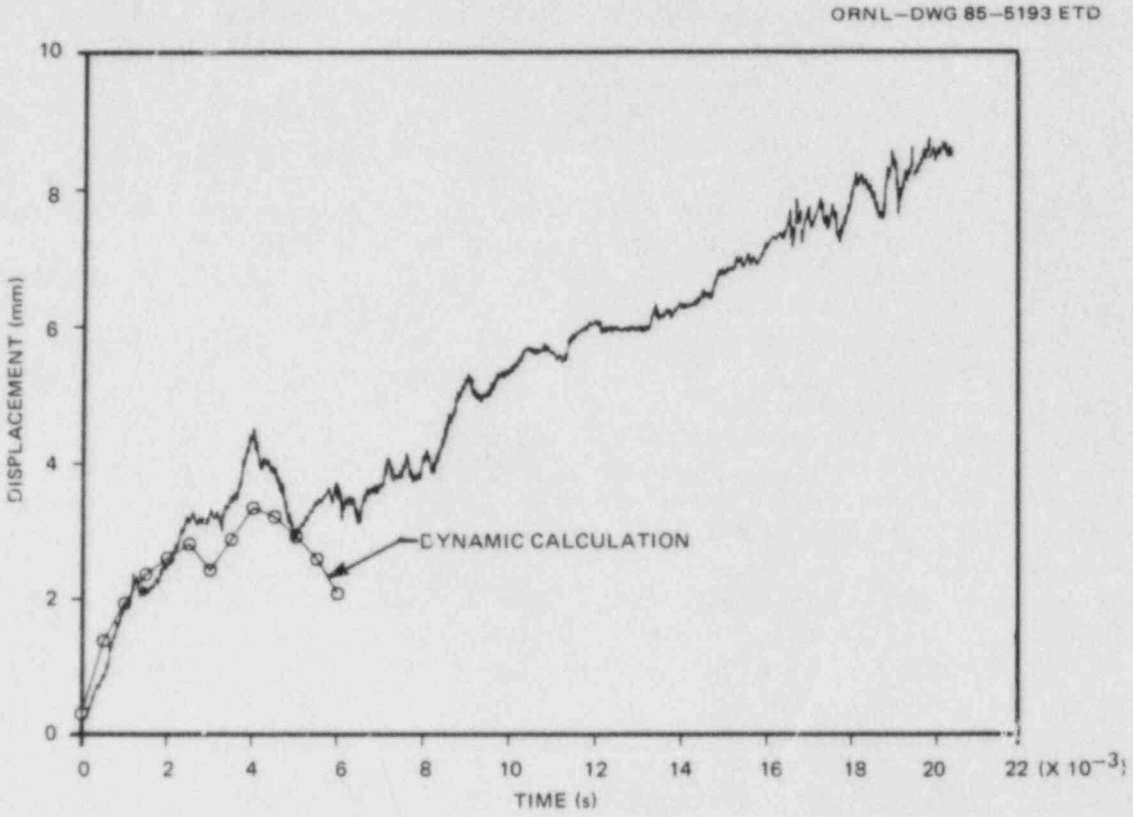

Fig. 5.66. Comparison between measured data and posttest generation-mode dynamic calculation (GM-1) of COD vs time for WP-1.3 (gage located 0.175 m from cold edge with 0.102-m gage length).

COD-gage deflection of 0.431 mm, which corresponds to a stress-intensity factor of K_I = 145.2 MPa•$\sqrt{m}$. The balance of the measured gage deflection, 0.219 mm, was assumed to be due to the notch-face pressure load from the pillow jack. From 3-D analysis of the plate with notch-face pressure loading, the ratio of stress-intensity factor to gage COD was calculated to be 309.5 MPa•$\sqrt{m}$/mm, implying a notch-pressure contribution to the initiation factor of 67.7 MPa•$\sqrt{m}$ for WP-1.4. Superposition of the axial and pressure loadings led to an estimated initiation stress-intensity factor of ~213 MPa•$\sqrt{m}$. This computed K_I value was compared with the static initiation value of K_{Ic} = 63.9 MPa•$\sqrt{m}$ that was determined from Eq. (5.1) with T = T_{CT} = −62.3°C and RT_{NDT} = −23°C, which resulted in a K_I/K_{Ic} ratio of 3.333. This ratio was calculated earlier for WP-1.2 (K_I/K_{Ic} = 251.5/87.5 = 2.87 at T_{CT} = −33°C) and for WP-1.3 (K_I/K_{Ic} = 173.5/70.1 = 2.48 at T_{CT} = −51°C), and WP-1.4 represents the highest calculated ratio thus far.

In the NBS quick-look report to ORNL (Ref. 10, p. 2), the applied tensile load plus pillow-jack pressure was estimated by NBS to be equivalent to a single tensile load (without pillow-jack pressure) of 12.943 MN. If this tensile load is employed in the analysis of the 3-D model with

axial load only, the estimate for initiation stress-intensity factor is 236 MPa$\cdot\sqrt{m}$, resulting in K_I/K_{Ic} = 3.7.

Subsequent to the completion of the NBS quick-look report, additional study of the recorded data was performed by NBS at the request of ORNL to ascertain the effects of the pillow-jack load on the large COD gage readings just prior to the first initiation. In the judgment of NBS, the large COD gage *showed no effects of the pillow-jack load being applied to the notch face*, and the data supplied to ORNL (Ref. 27) tend to confirm this evaluation. This apparent difficulty with the large COD gage data is yet to be resolved.

5.4.4.2 Elastodynamic analysis of WP-1.4. Elastodynamic analyses of wide-plate test WP-1.4 were carried out with the ADINA/EDF dynamic crack analysis code described in Sect. 2.1 of this report. The 2-D plane-stress finite-element model of the wide-plate configuration used in the analyses consists of 712 nodes, 208 eight-noded isoparametric elements, and 25 truss elements in the crack plane to model propagation of the crack tip. Side grooves were taken into account by adjustment of the resulting stress-intensity factor in each time step of the analysis. The in-plane bending of the plate assembly because of the thermal gradient across the plate was also incorporated into the analyses.

For the first of the two cleavage run-arrest events in WP-1.4, a series of analyses was performed with ADINA/EDF, using different mechanical loadings on the notch face in attempts to model the effects of the pillow jack employed in the test. In the first set of calculations, both application- and generation-mode analyses were carried out with fixed load-pin displacement and with initial conditions from a static solution that assumed an axial load of 7.952 MN and zero load on the notch face; in other words, pillow-jack effects were ignored. Results for the application-mode analysis (Case A) were a predicted crack arrest at a_f/w = 0.555, arrest toughness K_{Ia} = 250.9 MPa$\cdot\sqrt{m}$, and arrest temperature T_{ar} = 71°C. For the generation-mode analysis (Case B) based on the NBS estimate (Table 5.7) of crack position vs time (a vs t), the results were a_f/w = 0.44, K_{Ia} = 157.9 MPa$\cdot\sqrt{m}$, and T_{ar} = 29°C. Both analyses were performed using a time step Δt = 10 μs and the Newmark time integration scheme. These analyses were repeated with the SWIDAC code, using the same finite-element model, time step, and integration scheme, and the corresponding arrest toughnesses were calculated to be K_{Ia} = 249.1 MPa$\cdot\sqrt{m}$ [application mode (Case C)] and K_{Ia} = 158.1 MPa$\cdot\sqrt{m}$ [generation mode (Case D)]; the values for a_f/w and T_{ar} were the same as for the ADINA/EDF analyses. All subsequent analyses were performed with the ADINA/EDF code.

The second set of analyses was based on initial conditions derived from a static solution that assumed an axial load of 7.952 MN and a piecewise-linear notch-face pressure distribution defined according to Table 5.13. The pressure distribution of Table 5.13 is strictly conjecture, not based on measured data, and implies that the pillow jack is not fully effective in transferring load to the faces of the notch. Two generation-mode analyses were performed assuming that the notch face is traction free for t > 0 during the run-arrest event. The first analysis (Case E) used the NBS a vs t relation from Table 5.7; the second analysis (Case F) used an ORNL a vs t relation shown in Table 5.14; the NBS relation is also repeated in Table 5.14. For a time step Δt = 10 μs, the

Table 5.13. Notch-pressure distribution assumed to exist at crack initiation in WP-1.4

Distance from cold edge (m)	Pressure (MPa)
0	31.72
0.107	63.43
0.157	63.43
0.207	0.00

Table 5.14. Crack position vs time values used in posttest analyses of WP-1.4

Location	Position (mm)	Time (μs)	
		NBS[a]	ORNL
a_o	207.5	0	0
Gage 1	250	65	65
Gage 2	300	92.5	92.5
Gage 3	350	222.5	289.5
Gage 4	390	274	361
Gage 5	430	492.5	492.5
Arrest-1	441	574.5	574.5

[a]Same as given in Table 5.7.

results were K_{Ia} = 166 MPa•$\sqrt{m}$ (NBS a vs t) and K_{Ia} = 157 MPa•$\sqrt{m}$ (ORNL a vs t). The ORNL a vs t curve in Table 5.14 represents an attempt to obtain better agreement between calculated and measured values of peak strain times.

In the next series of analyses, the pressure loading p′(x), defined in Table 5.13, was maintained on the notch face during the dynamic event, according to the piecewise-linear time history F(t) shown in Table 5.15 so that p(x,t) = p′(x)•F(t). The pressure was maintained at a peak amplitude up to time t = 0.12 ms and then ramped linearly down to zero at t = 0.25 ms to prevent the notch from tending to close early in the transient, as was observed in the previously described cases (E and F). The results for these generation-mode analyses for two different time steps and for the two different a vs t relations of Table 5.14 are given in Table 5.16. For all analyses, a_f/w = 0.44, and T_{ar} = 29°C.

Table 5.15. Piecewise-linear time history of pressure intensity used in posttest analyses of WP-1.4

Time (ms)	F(t)
0	1.0
0.12	1.0
0.25	0
1000	0

Table 5.16. K_{Ia} results from dynamic generation-mode analyses for WP-1.4, using the pressure history of Table 5.15

Time step (μs)	K_{Ia} values for a vs t curves (MPa·$\sqrt{m}$)	
	NBS	ORNL
5	162 (Case H)	149 (Case J)
10	166 (Case G)	157 (Case I)

Finally, a generation-mode analysis was performed for the second run-arrest event (WP-1.4B), using Δt = 10 μs and initial conditions from a static analysis that assumed an axial load of F = 9.72 MN and zero notch-face loading. Assuming an initial crack depth of a_o/w = 0.44 and the NBS a vs t relation given in Table 5.8, the results of the analysis were an arrested crack depth of a_f/w = 0.527, an arrest toughness K_{Ia} = 396.5 MPa·$\sqrt{m}$, and an arrest temperature of T_{ar} = 61°C. This result, along with the other generation-mode analyses for WP-1.2 through WP-1.4, is plotted in Fig. 5.45.

5.5 SwRI Analysis of Wide-Plate Tests*

R. J. Dexter† M. F. Kanninen†

The research at SwRI in support of the HSST program includes both elastodynamic and dynamic-viscoplastic analyses of rapid crack propagation and arrest under conditions corresponding to a PTS event. Specific attention is currently being focused on the wide-plate experiments discussed in Sect. 5.4 and being conducted by NBS. This report summarizes the elastodynamic computations that have been performed for NBS test WP-1.2 (Ref. 4).

The computations in this work employ a kinetic approach and include both application-phase computations (i.e., fracture propagation criterion assumed with crack-growth history computed for the measured boundary and initial conditions) and generation-phase computations (i.e., measured crack-length history and boundary and initial conditions used as input to infer dynamic-fracture toughnesses). Following a description of these computations, comparisons are given between the dynamic and static interpretations of the results for WP-1.2.

A fine-grid finite-element model (364 elements) of the NBS wide-plate test specimen was constructed. The previous SwRI elastodynamic application-phase analysis of WP-1.2 used a model with only 96 elements. Other refinements included modeling the hole in the pull-plate, spreading the load along 17 nodes at the hole, and including the notch geometry. Nevertheless, an application-phase analysis of WP-1.2 using the fine-grid model produced essentially the same results as did the coarser model. These two computations were made using the velocity/temperature relation for K_{ID} that was developed by Kanninen[14] and extended by Merkle and defined in Eqs. (5.2)–(5.5). Table 5.17 compares various computed K values at several a/w values. The K values include (1) the application-phase analysis results, (2) the generation-phase analysis results, (3) the K inferred from the temperature-velocity relation, and (4) a static K solution. These values have been elevated by a factor of 1.155, which is the square root of the ratio of the nominal thickness to the net thickness of the side-grooved specimen. The agreement of generation- and application-phase analyses illustrates the usefulness and reliability of the calculations. These results also show that the dynamically calculated K values are far less than the statically calculated (load-controlled) K values.

Table 5.18 compares the times corresponding to various a/w values from the generation- and application-phase analyses. These times begin to deviate at $a/w > 0.4$ when the velocity is small. Note that the values of K in Table 5.17 from generation- and application-phase analysis at a particular a/w do not necessarily correspond because the time of arrival at that a/w may be different.

---

*Work sponsored by the HSST Program under subcontract 37X-97306C between Martin Marietta Energy Systems, Inc., and the Southwest Research Institute.

†Engineering and Materials Sciences Division, Southwest Research Institute, San Antonio, Texas.

Table 5.17. Comparison of SwRI computed stress-intensity factors for WP-1.2

a/w	K (MPa•√m)			
	Static analysis[a]	Application phase[b]	Generation phase[c]	From assumed K_{ID} relation[d]
0.2	230	227	227	87
0.3	331	227	218	388
0.4	454	292	271	233
0.555	656	385	400	305
0.645	722	534	503	517

[a]From edge-cracked plate solution.

[b]Computed using a fixed displacement boundary condition corresponding to the measured initial load (18.9 MN), the measured temperatures, and Eq. (5.3).

[c]Computed using crack length vs time inferred from NBS data and a fixed displacement boundary condition.

[d]Inferred from Eq. (5.3), using the NBS velocity data and the measured temperatures.

Table 5.18. Comparison of computed crack length vs time results for WP-1.2 experimental data

a/w	Prediction[a] t (μs)	Experiment[b] t (μs)
0.2	0	0
0.3	144	130
0.4	300	320
0.555	636	980
0.645	1400	1800

[a]Computed using a fixed-displacement boundary condition corresponding to the measured initial load (18.9 MN), the measured temperatures, and Eq. (5.3).

[b]Inferred from NBS crack-speed vs crack-length results.

The predictions are in generally good agreement overall with the NBS data[28] except that the first arrest (at a/w = 0.55) is not predicted. However, very reasonable agreement with the second arrest (at a/w = 0.64) was obtained. Good agreement is achieved between the predictions of data sets measured by BCL and NBS (Ref. 28) for the initial stage of the crack propagation event. However, the BCL data are somewhat suspect thereafter (i.e., on the basis that the NBS results conform to the observed surface features on the crack surfaces); the NBS data are probably more correct for the latter stages.

In summary, the prediction of an elastodynamic kinetic approach using the postulated K_{ID} property developed for A 533 grade B class 1 steel by Kanninen and Merkle [Eqs. (5.3)—(5.5)] is in general agreement with the experimental observations in NBS wide-plate test WP-1.2. Some features of the results at variance with these predictions may only be explained via the viscoplastic analyses currently in progress (see Sect. 2.4).

5.6 Analyses and Experiments at University of Maryland in Support of Wide-Plate Tests*

W. L. Fourney† X-J. Zhang†
D. B. Barker† G. R. Irwin†
R. J. Sanford† R. Chona†
C. W. Schwartz‡

5.6.1 Dynamic analyses

Support for the wide-plate crack-arrest testing that is being conducted at NBS (Gaithersburg) is being provided through analytical modeling with the dynamic fracture-analysis computer code SAMCR. During the current report period generation-mode analysis capabilities have been incorporated into SAMCR to permit dynamic stress-intensity factor information to be inferred from experimentally recorded crack-tip position histories.

Such an analysis has been performed for WP-1.2, using the NBS estimates for crack length as a function of time.[28] The stress-intensity variation with time predicted by SAMCR is shown in Fig. 5.67. The two crack-arrest data points inferred from this analysis are shown in Fig. 5.68, superposed on a compilation of data from the thermal shock experiments (TSE) and pressurized-thermal-shock experiments (PTSE) performed at ORNL.

---

*Work sponsored by the HSST Program under Subcontract No. 7778 between Martin Marietta Energy Systems, Inc., and the University of Maryland.

†Department of Mechanical Engineering, University of Maryland, College Park.

‡Department of Civil Engineering, University of Maryland, College Park.

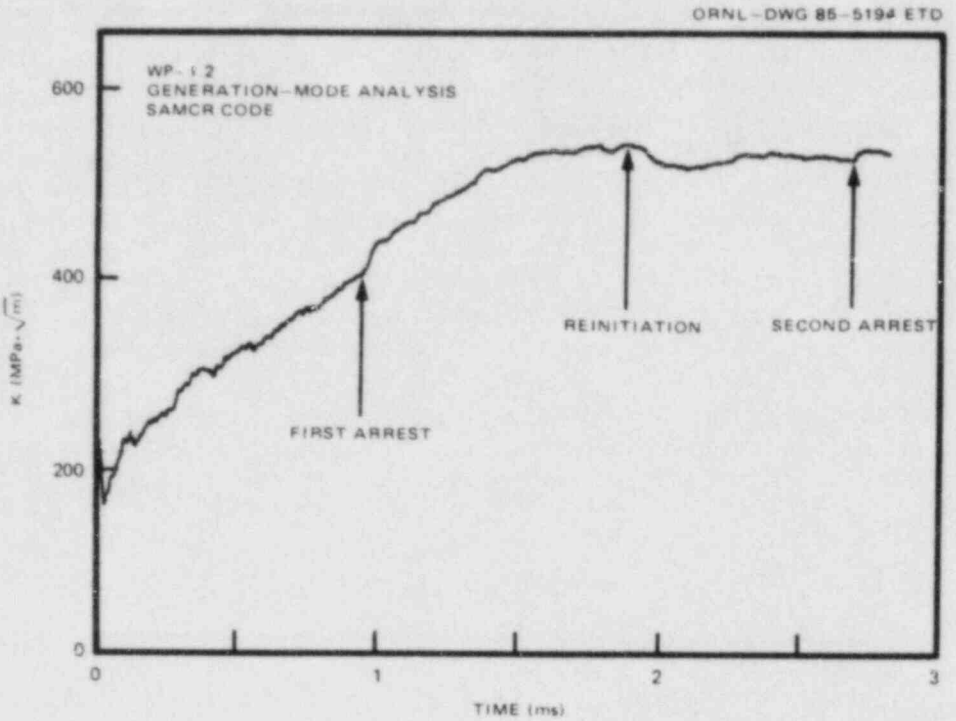

Fig. 5.67. Results for K as function of time obtained from generation-mode analysis of WP-1.2 performed using SAMCR computer code.

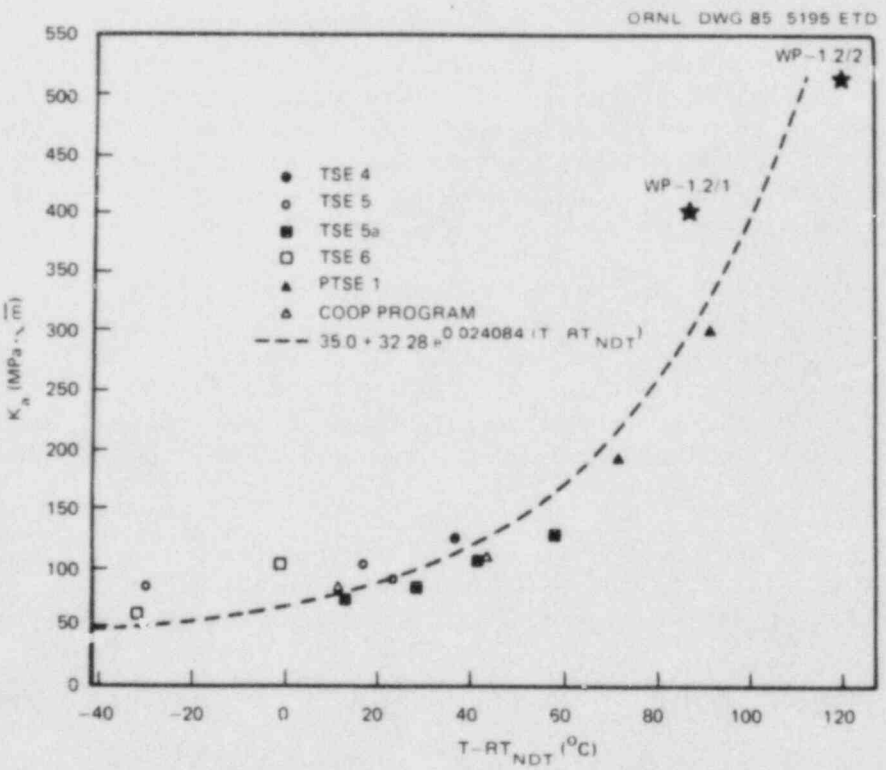

Fig. 5.68. Design curve for K_a as function of temperature used in wide-plate analyses and data obtained from ORNL TSEs.

5.6.2 Determination of stress-intensity factors from strain gages

During this report period several new methods for determining the stress-intensity factor from strain gages were developed analytically and verified experimentally. Three studies are in progress. The first, which has been completed, is the measurement of K_I with a very limited number of strain gages. The second is the determination of K_I using three strip gages containing a total of 30 strain sensors. The third is the simultaneous determination of K_I and K_{II} for the mixed-mode problem. All of these methods take advantage of the fact that for certain orientations of the gages, the influence of the leading nonsingular stress component(s) can be made to cancel. Accordingly, the strain gage output can be directly related to the stress-intensity factor.

Of the several approaches developed, the one of primary interest in the wide-plate test program is the 90° rosette, rotated 45° relative to the crack line. Expressions had previously been developed for the strain components $\varepsilon_y - \varepsilon_x$ being measured in the wide-plate tests, in terms of the coefficients of the dynamic series stress-field representation.[29] Calculations using estimates of the nonsingular term magnitude expected in the wide-plate geometry showed that the constant stress term σ_{ox} would have a large influence on the strain readings. For the rotated rosette configuration the constant stress parallel to the crack line has no influence on the gage output $\varepsilon_y' - \varepsilon_x'$. The next nonsingular term $r^{1/2}$ can then be eliminated by linear extrapolation. A confirming experiment using the ASTM E-399 compact tension (CT) specimen geometry demonstrated the practicality of this approach and correctly determined the stress-intensity factor to within 5%.

5.6.3 Instrumentation

Preliminary results for WP-1.3 were examined and recommendations made to ORNL for changes in the instrumentation layout for subsequent tests with a view toward maximizing the information obtained dynamically for the run-arrest event.[6] Several of these suggestions were implemented on WP-1.4. Four sets of rosettes in WP-1.4 were placed in the rotated configuration, and the results will be studied and compared with those obtained from the alternative orientation.

5.6.4 Dynamic crack initiation

A series of experiments have been conducted to study dynamic crack initiation at very high loading rates by passing two tensile dilatational stress waves over a stationary crack. Preliminary photoelastic experiments are being used to determine the loading rate dK/dt that can be achieved. The initiation toughness K_d determined from these experiments will be compared with K_c determined from small CT specimens. The next series of experiments will simultaneously measure K_d from photoelastic data and strain gages so that the technique can then be applied to steel specimens that are currently being fabricated.

5.7 ASTM Round Robin on K_{Ia} Testing*

W. L. Fourney† R. Chona†

The 20 participants who have completed their testing and forwarded test reports to UM are listed in Table 5.19. Preliminary data compilation has been completed, and two meetings of the working group have been

*Work sponsored by the HSST Program under Subcontract No. 7778 between Martin Marietta Energy Systems, Inc., and the University of Maryland.

†Department of Mechanical Engineering, University of Maryland, College Park.

Table 5.19. Crack-arrest round-robin participants who have completed testing and forwarded test reports

Foreign participants[a]
Ontario Hydro (Canada)
RISO (Denmark)
Technical Research Center (Finland)
MPA Stuttgart (Federal Republic of Germany)
FIWM (Federal Republic of Germany)
BAM (Federal Republic of Germany)
KWU (Federal Republic of Germany)
Nippon Kokan (Japan)
Mitsubishi Heavy Industries (Japan)
SINTEF (Norway)
RIT (Sweden)
Welding Institute (UK)
CEGB (UK)
UKAEA (UK)
U.S. participants[b]
UM
CE Power Systems
ORNL
BCL
Westinghouse Research and Development Center
National Bureau of Standards

[a]Fourteen of sixteen participants have responded.

[b]Six of eleven participants have responded.

held at College Park (one in June and one in August) to discuss the results. Further analyses that are required have been identified and are being performed by UM. A report on the ASTM Round-Robin Program will be presented at the November meetings of ASTM Committee E-24.

Small-specimen data are still lacking and have been received to date from only two participants. However, several laboratories have indicated that results can be expected from them in the next few months. Inverted-pin data have been received from three of the original six volunteers, and one more set is expected shortly.

5.8 Battelle-Columbus HSST Support Program*

A. R. Rosenfield† P. N. Mincer†

5.8.1 Crack-arrest Data Bank

Over the past several years, researchers at BCL have been compiling all of the available crack-arrest-toughness (K_{Ia}) data. The Data Bank contents include information on both base plate and weldments and for both irradiated and unirradiated materials. A draft report summarizing and characterizing this information[30] was submitted during the previous report period.

During the current report period, 33 new data points were added, all for unirradiated base plate. These include four wide-plate data (from NBS) and a PTS result (from MPA, Stuttgart). In addition, more accurate and complete data have been received for some earlier reported inputs. All of this additional information provides the opportunity to update several comments made in our earlier summaries concerning the statistical analysis of the data.[30,31]

The statistical analysis showed that the mean value of K_{Ia} is a temperature-independent multiple of the ASME K_{IR} curve, regardless of material, irradiation, or test method. The standard deviation of K_{Ia} is a temperature-dependent fraction of K_{IR}, but this fraction is greater for welds than for base plate and is greater for data sets containing multiple base-plate/heat-treatment combinations than for those containing a unique material. In the following sections, large-specimen data are discussed in light of these observations.

5.8.2 Thermal-shock experiments

The new PTS result[32] is not strictly comparable to the data already available because it reflects ductile (upper-shelf) behavior and involves stable crack growth. However, Fig. 5.69 shows that its K_{Ia}/K_{IR} ratio is very close to the solid line representing the average ratio obtained from

---

*Work sponsored by the HSST Program under Subcontract 85X-17264C between Martin Marietta Energy Systems, Inc., and Battelle-Columbus Laboratories.

†Battelle-Columbus Laboratories, 505 King Avenue, Columbus, Ohio.

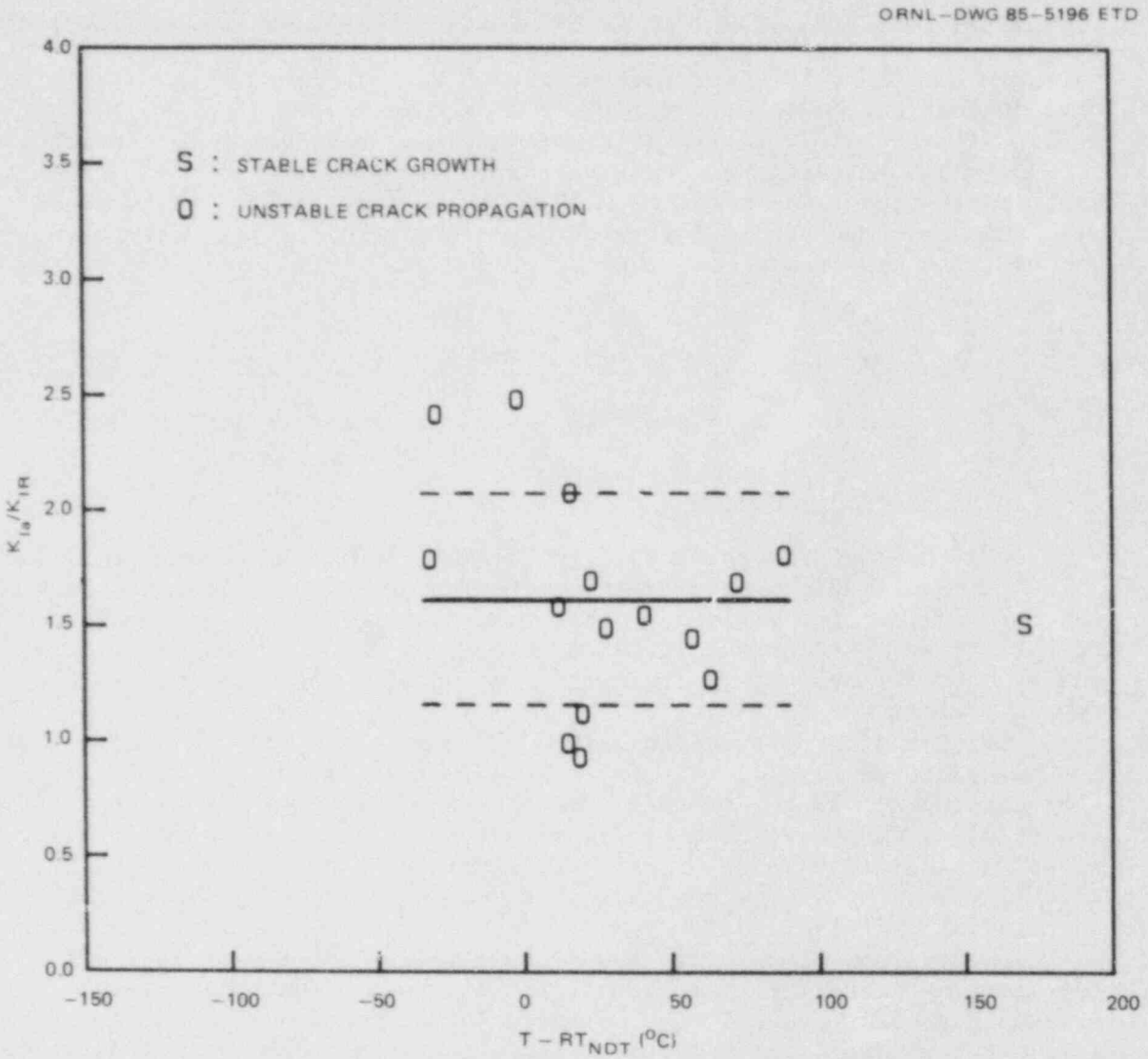

Fig. 5.69. Normalized crack-arrest toughness data from TSEs.

transition-temperature experiments. On the other hand, the absolute value K_{Ia} = 330 MPa•$\sqrt{m}^{1/2}$ is somewhat higher than our preliminary estimate based on extrapolation of a plot of the yield-strength dependence of small-specimen, high-strength-steel, upper-shelf, crack-arrest data for the yield strength of reactor-pressure-vessel steels.[33] Because this MPa result is unique, considerably more high-temperature data are needed before any definitive conclusions are drawn regarding extension of our reference crack-arrest toughness equation to upper-shelf temperatures.

The refinement in the analysis of the PTSE-1 data[34] has caused a slight change in the crack-arrest reference equation from that reported in Ref. 30. The updated equation is

$$K_{Ia} = (1.61 \pm 0.46)\ K_{IR}\ , \qquad (5.6)$$

with the numbers in parentheses being mean and standard deviation, respectively. As indicated by the lines on Fig. 5.69, this equation is believed to be valid from (RT_{NDT} − 35°C) to (RT_{NDT} + 90°C).

5.8.3 Wide-plate experiments

The Data Bank contains 43 wide-plate results, almost all of them from Japan.[35-40] These data are plotted in Fig. 5.70 and compared with both our average reference curve [Eq. (5.6)] and the ASME lower-bound reference curve (K_{IR}). While the points appear to be representative of the thermal-shock line, close examination of Fig. 5.70 suggests that K_{Ia} is more temperature dependent in the wide-plate tests. This difference

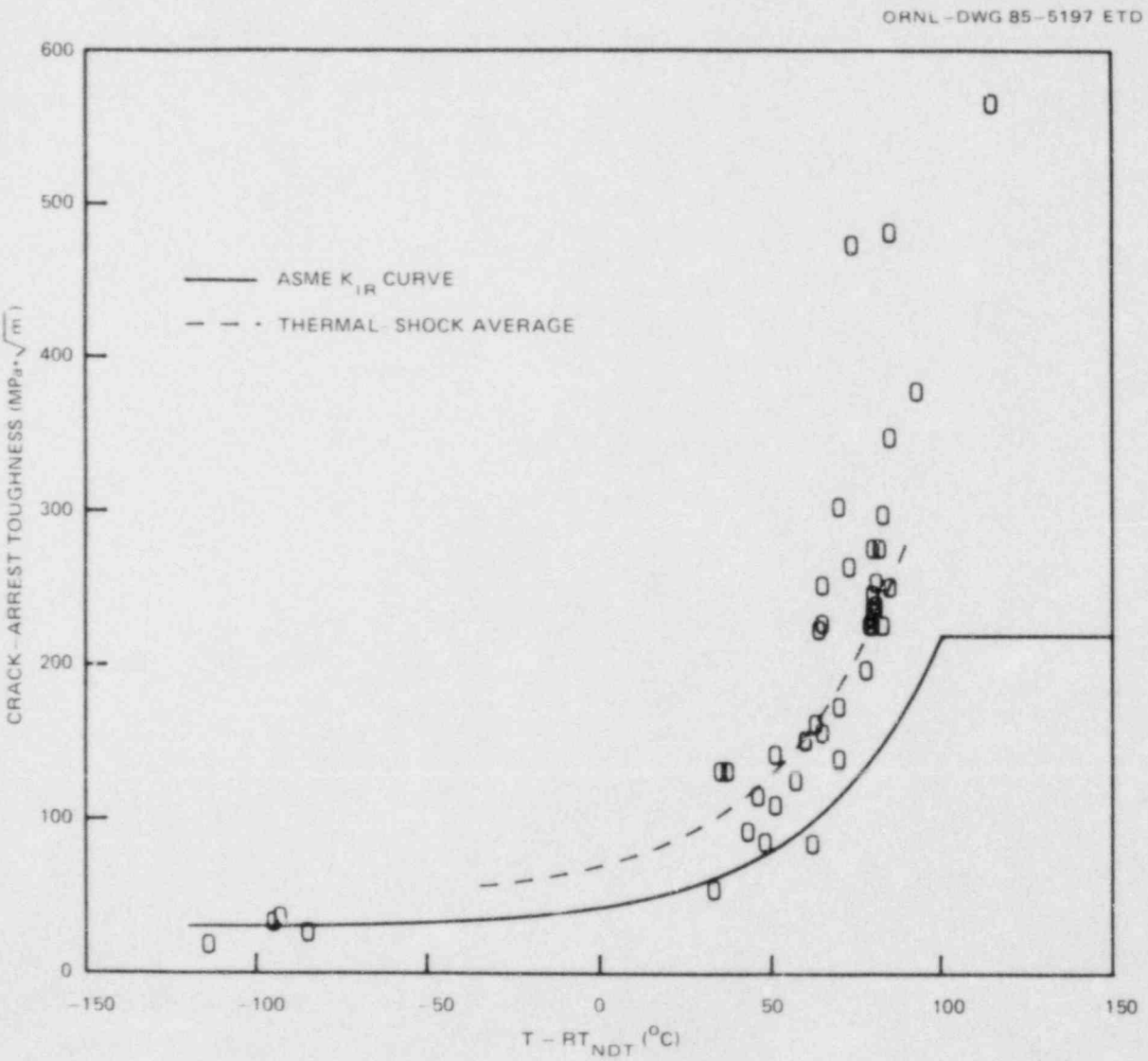

Fig. 5.70. Crack-arrest data bank covering wide-plate experiments.

in slopes becomes apparent when the data are normalized to the ASME reference curve, as has been done in Fig. 5.71. This result is not unexpected because a similar difference in temperature dependence was found when comparing large wide-plate specimen data with small wedge-loaded specimen results.[41] It would appear that the wide-plate geometry is an exception to the general tendency for K_{Ia}/K_{IR} to be temperature insensitive.

This data bank is intended to be updated continually. Additional data are solicited from readers of this report.

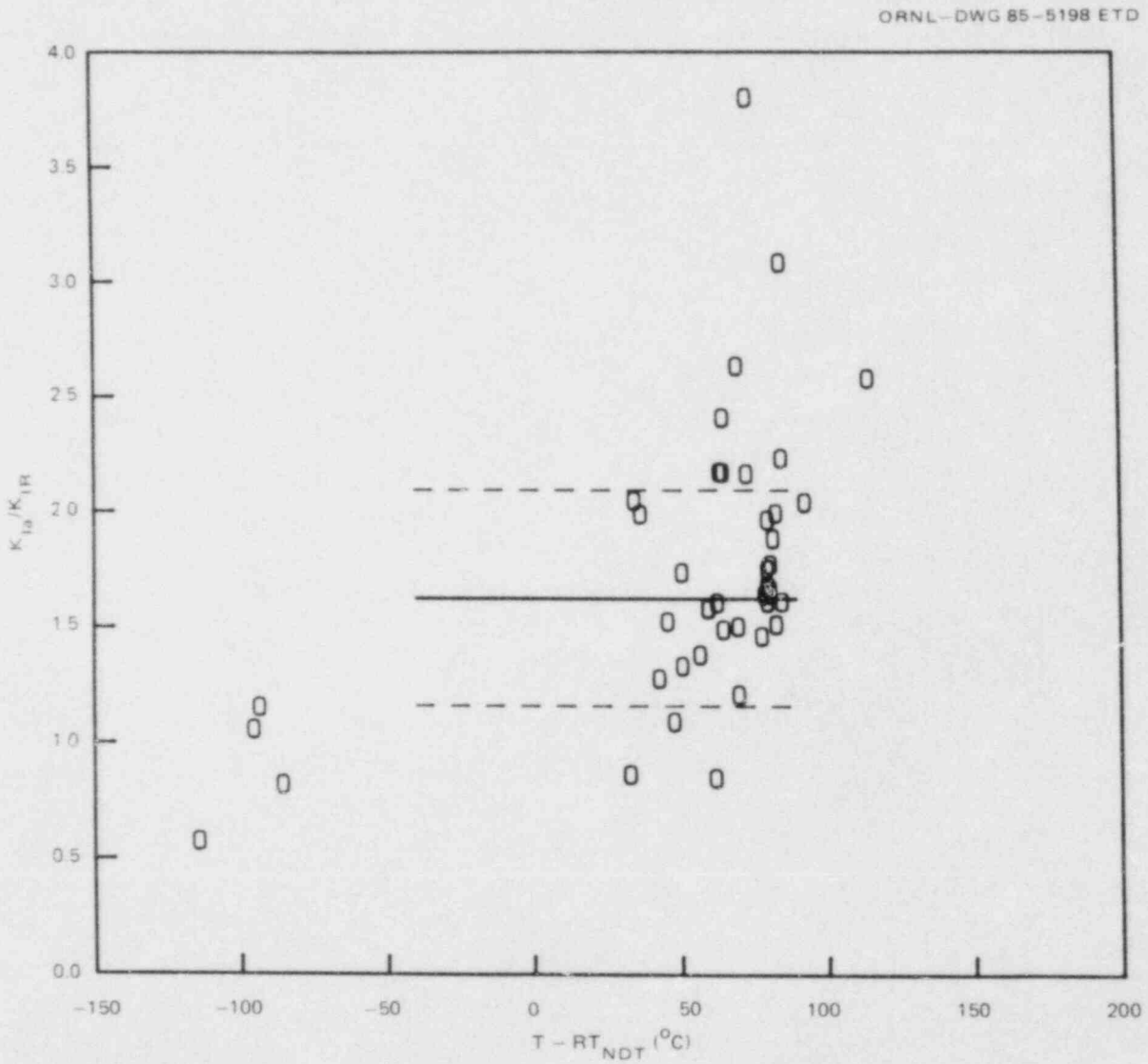

Fig. 5.71. Normalized crack-arrest data, wide-plate experiments. Scatter band represents thermal-shock data.

References

1. R. D. Cheverton et al., "Fracture Mechanics Data Deduced from Thermal-Shock and Related Experiments with LWR Pressure Vessel Material," *J. Pressure Vessel Technol.* 105, 102–10 (May 1983).

2. R. H. Bryan et al., *Pressurized-Thermal-Shock Test of 6-in.-Thick Pressure Vessels. PTSE-1: Investigation of Warm Prestressing and Upper-Shelf Arrest*, NUREG/CR-4106 (ORNL-6135), Martin Marietta Energy Systems, Inc., Oak Ridge Natl. Lab., April 1985.

3. C. E. Pugh, "Crack Arrest Technology," pp. 83–137 in *Heavy-Section Steel Technology Program Semiann. Prog. Rep. April–September 1984*, NUREG/CR-3744, Vol. 2 (ORNL/TM-9154/V2), Martin Marietta Energy Systems, Inc., Oak Ridge Natl. Lab.

4. C. E. Pugh, "Crack Arrest Technology," pp. 58–109 in *Heavy-Section Steel Technology Program Semiann. Prog. Rep. October 1984–March 1985*, NUREG/CR-4219, Vol. 1 (ORNL/TM-9593/V1), Martin Marietta Energy Systems, Inc., Oak Ridge Natl. Lab.

5. B. R. Bass, C. E. Pugh, and H. K. Stamm, "Dynamic Analyses of a Crack Run-Arrest Experiment in a Nonisothermal Plate," pp. 175–84 in *Pressure Vessel Components Design and Analysis*, Vol. 4, ASME PVP, Vol. 98-2, 1985.

6. W. L. Fourney et al., University of Maryland, College Park, memorandum to C. E. Pugh, Oak Ridge Natl. Lab., Oak Ridge, Tenn., "Instrumentation for Future Wide Plate Tests," June 17, 1985.

7. R. deWit and R. J. Fields, National Bureau of Standards, letter report to C. E. Pugh, Oak Ridge Natl. Lab., Oak Ridge, Tenn., "Preliminary Results from the Third Wide Plate Test: WP-1.3," May 21, 1985.

8. R. J. Fields, National Bureau of Standards, letter report supplement to C. E. Pugh, Oak Ridge Natl. Lab., Oak Ridge, Tenn., "Detailed Data from Gage 4 in Test WP-1.3," May 29, 1985.

9. R. J. Fields, National Bureau of Standards, letter report supplement to C. E. Pugh, Oak Ridge Natl. Lab., Oak Ridge, Tenn., "Further NBS Data from WP-1.3," June 11, 1985.

10. R. deWit and R. J. Fields, Natinal Bureau of Standards, letter report to C. E. Pugh, Oak Ridge Natl. Lab., Oak Ridge, Tenn., "Preliminary Results from the Fourth Wide Plate Test: WP-1.4," August 1, 1985.

11. H. K. Stamm, B. R. Bass, and C. E. Pugh, *Fracture Analysis of Plate Crack Arrest Specimens*, Martin Marietta Energy Systems, Inc., Oak Ridge Natl. Lab., in preparation.

12. A. R. Rosenfield et al., "Crack-Arrest Studies at Battelle Columbus," pp. 102–9 in *Heavy-Section Steel Technology Program Semiann. Prog. Rep. April–September 1984*, NUREG/CR-3744, Vol. 2 (ORNL/TM-9154/V2), Martin Marietta Energy Systems, Inc., Oak Ridge Natl. Lab.

13. D. P. Edmonds and J. J. McCowan, "Characterization of Wide-Plate Test Material at ORNL," pp. 96–102 in *Heavy-Section Steel Technology Program Semiann. Prog. Rep. April–September 1984*, NUREG/CR-3744, Vol. 2 (ORNL/TM-9154/V2), Martin Marietta Energy Systems, Inc., Oak Ridge Natl. Lab.

14. M. F. Kanninen et al., *Preliminary Analysis of Japanese Wide-Plate Dynamic Crack Propagation Arrest Experiments*, Subcontract report from Battelle Columbus Laboratories to Oak Ridge Natl. Lab., December 1983.

15. H. Tada, P. C. Paris, and G. R. Irwin, *The Stress Analysis of Cracks Handbook*, Del Research Corp., Hellertown, Pa., 1973.

16. C. F. Fedderson, "Current Status of Plain Strain Crack Toughness Testing of High-Strength Metallic Materials," *Crack Arrest Methodology and Applications, ASTM STP-410*, American Society for Testing and Materials, Philadelphia, Pa., 1967.

17. G. R. Irwin, University of Maryland, College Park, private communication to C. E. Pugh, Oak Ridge Natl. Lab., Oak Ridge, Tenn., "Notes on Testing Arrangements for Crack Arrest Tests Using an SEN Specimen and a Temperature Gradient," October 1983.

18. R. H. Bryan et al., *Pressurized-Thermal-Shock Test of 6-in.-Thick Pressure Vessels, PTSE-1: Investigation of Warm Prestressing and Upper-Shelf Arrest*, NUREG/CR-4106 (ORNL-6135), Martin Marietta Energy Systems, Inc., Oak Ridge Natl. Lab., April 1985, pp. 14–36, 143–51.

19. R. D. Cheverton et al., "Fracture Mechanics Data Deduced from Thermal-Shock and Related Experiments with LWR Pressure Vessel Material," *J. Pressure Vessel Technol.* 105, 102–10 (May 1983).

20. Japan Welding Council, *Structural Integrity of Very Thick Steel Plate for Nuclear Reactor Pressure Vessels*, JWES-AE-7806, 1977 (in Japanese).

21. A. Pellissier-Tanon, P. Sollogoub, and B. Houssin, "Crack Initiation and Arrest in an SA 508 Class-3 Cylinder Under Liquid Nitrogen Thermal-Shock Experiment," Paper G/F 1/8, pp. 132–42 in *Transactions of the 7th International Conference on Structural Mechanics in Reactor Technology*, Chicago, vols. G and H, August 1983.

22. J. Jung, J. Ahmad, and M. F. Kanninen, *Finite-Element Analysis of Dynamic Crack Propagation*, presented at the 1981 ASME Failure Prevention and Reliability Conference, September 23–26, 1981, Hartford, Conn.

23. K. J. Bathe, *ADINA — A Finite Element Program for Automatic Dynamic Incremental Nonlinear Analyses*, Report AE-1, Massachusetts Institute of Technology, Cambridge, Mass., 1984.

24. R. deWit et al., "Wide-Plate Crack Arrest Testing," in *Heavy-Section Steel Technology Program Semiann. Prog. Rep. October 1984—March 1985*, NUREG/CR-4219, Vol. 1 (ORNL/TM-9593/V1), Martin Marietta Energy Systems, Inc., Oak Ridge Natl. Lab.

25. B. R. Bass and J. W. Bryson, *Applications of Energy Release Rate Technique to Part-Through Cracks in Plates and Cylinders, Volume 1, ORMGEN-3D: A Finite Element Mesh Generator for 3-Dimensional Crack Geometries*, NUREG/CR-2997, Vol. 1 (ORNL/TM-8527/V1), Union Carbide Corp. Nuclear Div., Oak Ridge Natl. Lab., December 1982.

26. B. R. Bass and J. W. Bryson, *Applications of Energy Release Rate Technique to Part-Through Cracks in Plates and Cylinders, Volume 2, ORVIRT: A Finite Element Program for Energy Release Rate Calculations for 2-D and 3-D Crack Models*, NUREG/CR-2997, Vol. 2 (ORNL/TM-8527/V2), Union Carbide Corp. Nuclear Div., Oak Ridge Natl. Lab., February 1983.

27. R. deWit, National Bureau of Standards, letter to B. R. Bass and C. E. Pugh, Oak Ridge Natl. Lab., Oak Ridge, Tenn., "Pillow-Jack Loading Versus CMOD Data," Sept. 6, 1985.

28. R. deWit et al., "Wide-Plate Crack-Arrest Testing," pp. 62—82 in *Heavy-Section Steel Technology Program Semiann. Prog. Rep. October 1984—March 1985*, NUREG/CR-4219, Vol. 1 (ORNL/TM-9593/V1), Martin Marietta Energy Systems, Inc., Oak Ridge Natl. Lab.,

29. W. L. Fourney, "Investigations of Damping and Cleavage-Fibrous Transition in Reactor-Grade Steel," pp. 56—59 in *Heavy-Section Steel Technology Program Quart. Prog. Rep. July—September 1981*, NUREG/CR-2141/Vol. 3 (ORNL/TM-8145/V3), Union Carbide Corp. Nuclear Div., Oak Ridge Natl. Lab.

30. A. R. Rosenfield, *Reactor-Pressure-Vessel-Steel Crack-Arrest Data Bank*, Battelle Columbus Report to Oak Ridge National Laboratory, Jan. 28, 1985.

31. A. R. Rosenfield, C. R. Barnes, and P. N. Mincer, "Battelle-Columbus HSST Support Program," pp. 111—14 in *Heavy-Section Steel Technology Program Semiann. Prog. Rep. October 1984—March 1985*, NUREG/CR-4219, Vol. 1 (ORNL/TM-9593/V1), Martin Marietta Energy Systems, Inc., Oak Ridge Natl. Lab.

32. A. W. Sauter, *Experimental and Theoretical Investigation of Pressurized Thermal Shock Loading*, presented at IAEA-Course on Quality Assurance, MPA, Stuttgart, Federal Republic of Germany, 1985.

33. A. R. Rosenfield et al., "BCL HSST Support Program," pp. 7–39 in *Heavy-Section Steel Technology Program Quart. Prog. Rep. July–September 1982*, NUREG/CR-2751, Vol. 3 (ORNL/TM-8369/V3), Union Carbide Corp. Nuclear Div., Oak Ridge Natl. Lab.

34. R. H. Bryan et al., "The Heavy-Section Steel Technology Pressurized-Thermal-Shock Experiment, PTSE-1," submitted to *Eng. Fract. Mech.* (1985).

35. Y. Nakano and K. Tanaka, "Crack-Arrest Toughness of Structural Steels Evaluated by Compact Tests," *Trans. Iron Steel Inst. Jpn.* 22, 147–53 (1982).

36. N. Ohashi et al., "Fracture Toughness of Heavy Section LWR Pressure Vessel Steel Plate Produced by Basic Oxygen Furnace and Ladle Refining Process," pp. 391–401 in *Pressure Vessel Technology*, Institution of Mechanical Engineers, London, 1980.

37. H. Susukida et al., "Fracture Toughness of Heavy Section Steel for Nuclear Reactor Pressure Vessels," *Trans. Iron Steel Inst. Jpn.* 17, 497–505 (1977).

38. Japan Welding Engineering Society, *ESSO Experiment*, tr. no. OLS-81-212 by Language Services, Knoxville, Tenn., from pp. 232–33 in Report JWES-AE-7908, otherwise unidentified.

39. K. Iida et al., "Applicability of JIS SPV50 Steel to Primary Containment Vessels of Nuclear Power Stations," pp. 403–9 in *Pressure Vessel Technology*, Institution of Mechanical Engineers, London, 1980.

40. R. Fields and R. deWit, unpublished poster presentation at *18th National Symposium on Fracture Mechanics*, Boulder, Colo., June 1985.

41. A. R. Rosenfield et al., "BCL HSST Support Program," pp. 12–37 in *Heavy-Section Steel Technology Program Quart. Prog. Rep. for January–March 1983*, NUREG/CR-3334, Vol. 1 (ORNL/TM-8787/V1), Union Carbide Corp. Nuclear Div., Oak Ridge Natl. Lab.

6. IRRADIATION EFFECTS STUDIES

R. K. Nanstad

6.1 Fourth HSST Irradiation Series

J. J. McGowan R. L. Swain

The cooperative testing program with Materials Engineering Associates (MEA) has been completed on specimens from the first three capsules. Statistical analysis of fracture mechanics results has been initiated. An exponential fit of the form

$$K_{Jc},\ K_{\beta c} = A + \exp(B \times T + C)\ , \tag{6.1}$$

with T in degrees Centrigrade, is being used in the transition region. A linear fit of the form

$$K_{Jc},\ T_{avg} = D \times T + E \tag{6.2}$$

is being used for the fracture toughness and tearing modulus on the upper shelf. Nonlinear least-squares fitting techniques are being developed to give accurate confidence limits on all parameters. Marquardt's method[1] will be used to solve the nonlinear equations.

The testing of the specimens from capsule 4 (KS07 LSTM material) is now under way. Testing of the Charpy V-notch (CVN) and tensile specimens has been completed. Scoping tests on unirradiated and irradiated 1T-CS specimens have been completed.

6.2 Fifth HSST Irradiation Series

J. J. McGowan R. K. Nanstad
B. H. Montgomery

The characterization of the unirradiated welds in this program continued. The tensile tests are complete, and testing of the CVN specimens has been completed by both Oak Ridge National Laboratory (ORNL) and MEA. The impact energy results of the tests are shown in Figs. 6.1 and 6.2 for welds 72W and 73W, respectively. The solid curves shown in these figures are nonlinear regression fits to the ORNL and MEA data using hyperbolic tangent functions. The fabrication of all fracture specimens is complete with precracking of the 150- and 200-mm specimens to begin shortly. A comparison of the fracture specimens in the program is shown in Fig. 6.3. Testing of the 25- 50-, and 100-mm specimens is 50% complete. The results of the fracture mechanics tests are shown in Figs. 6.4 and 6.5 for

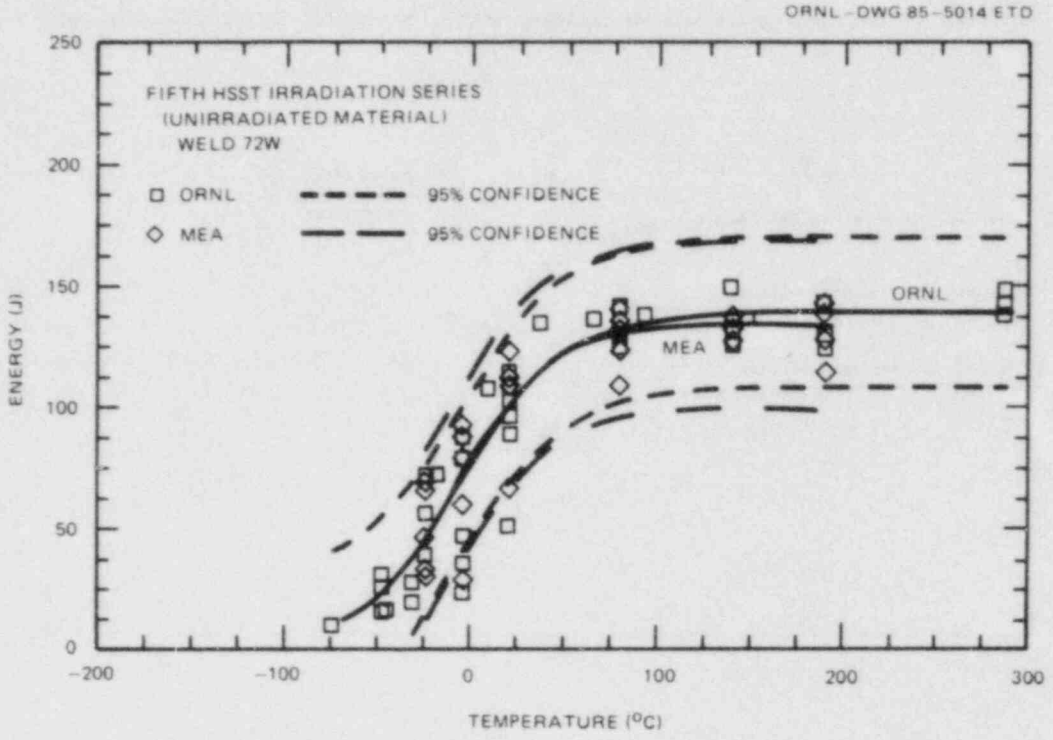

Fig. 6.1. CVN energy vs temperature for unirradiated weld 72W.

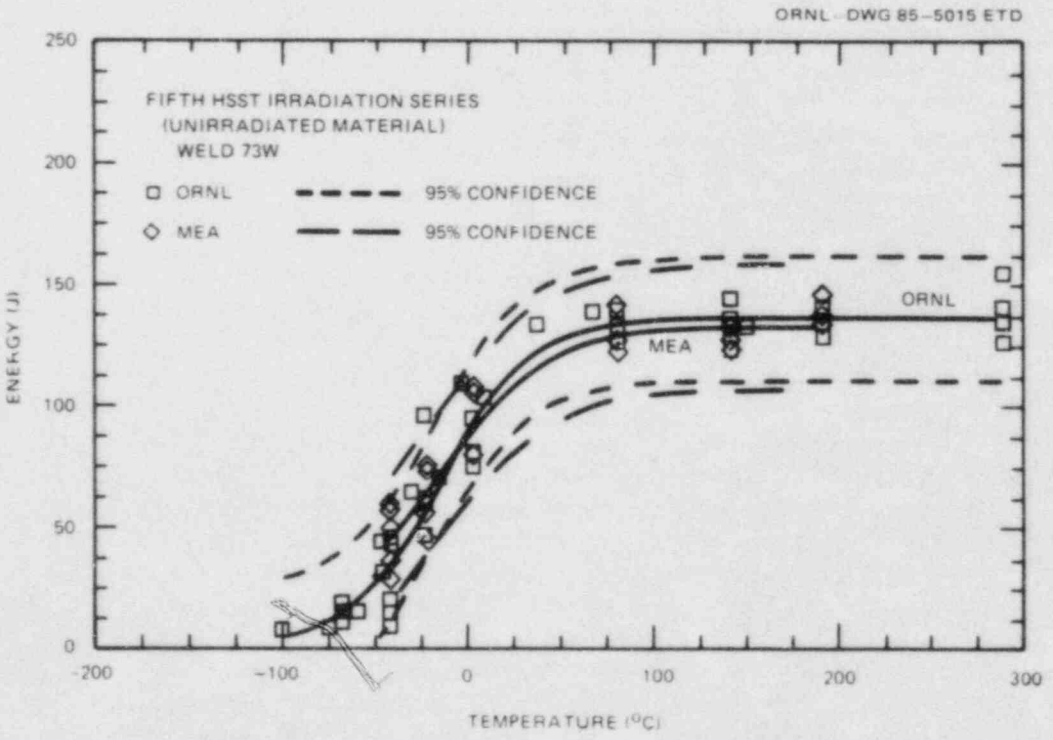

Fig. 6.2. CVN energy vs temperature for unirradiated weld 73W.

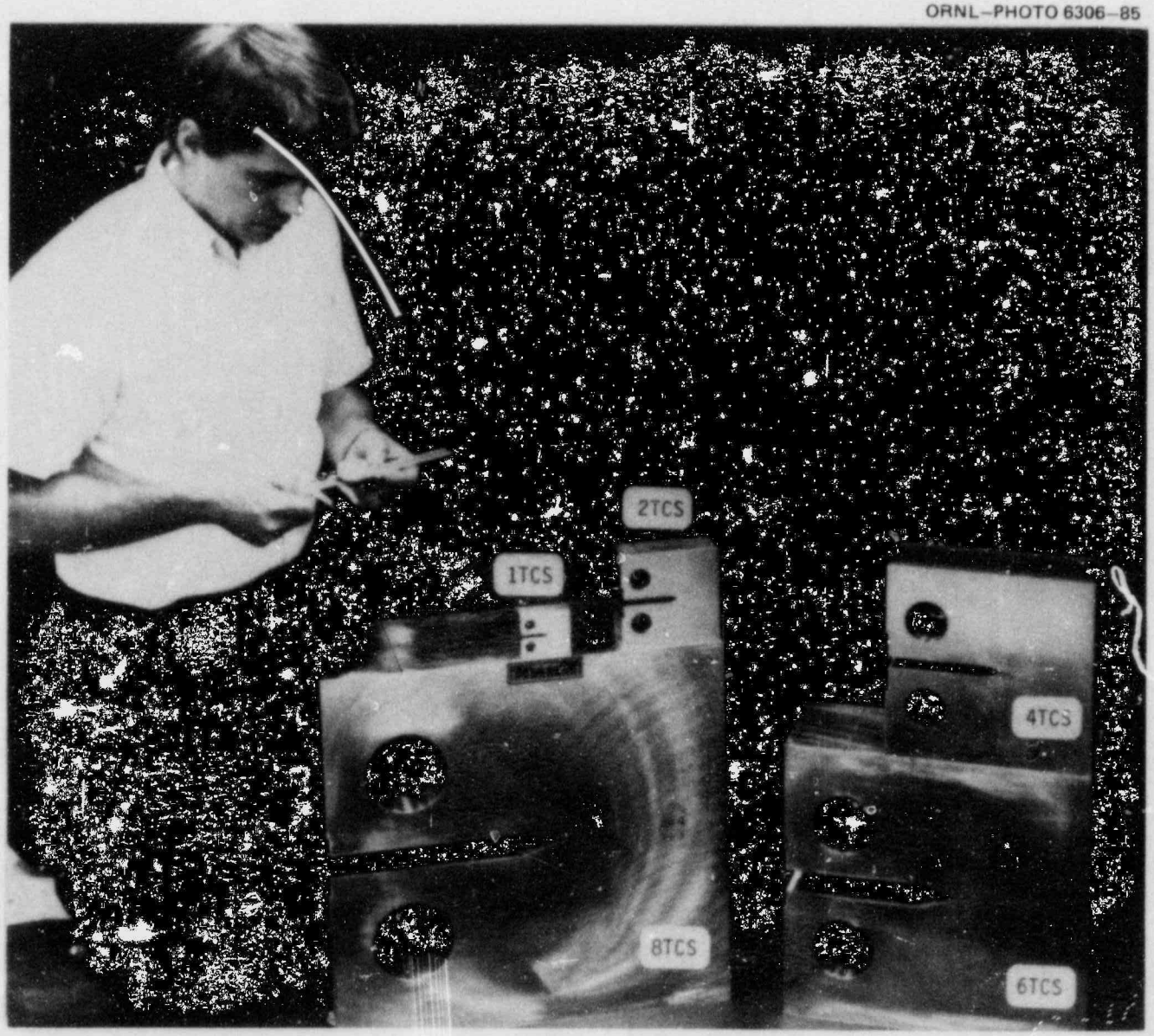

Fig. 6.3. Comparison of fracture mechanics specimens used in Fifth HSST Irradiation Program.

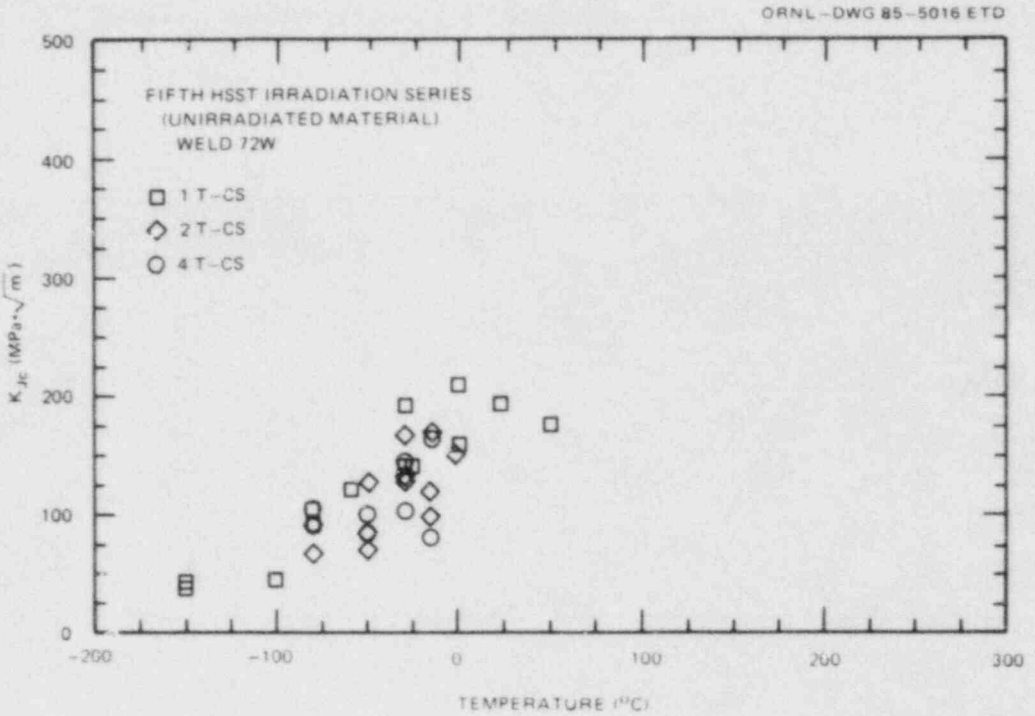

Fig. 6.4. Fracture toughness (K_{Jc}) vs temperature for unirradiated weld 72W.

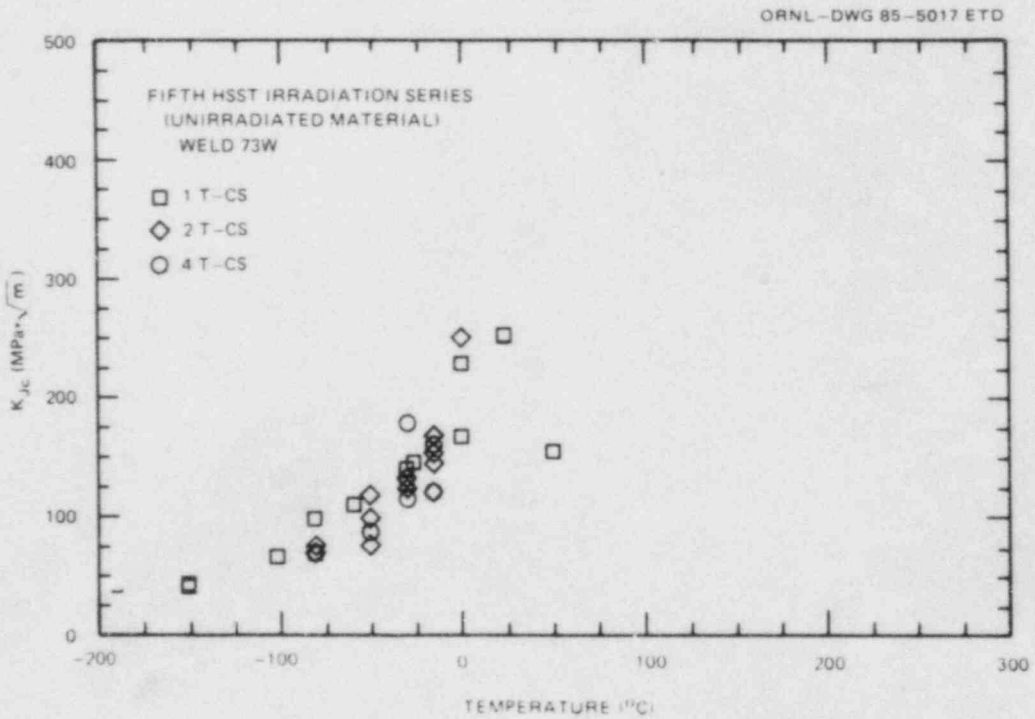

Fig. 6.5. Fracture toughness (K_{Jc}) vs temperature for unirradiated weld 73W.

welds 72W and 73W, respectively. (Only data from ORNL are available at this time.)

Irradiation of the specimens is continuing. Capsules 1—10 have been irradiated, with irradiation of the final two capsules (11 and 12) to begin shortly. Capsule 5 has been disassembled, and capsule 6 is currently being disassembled to provide specimens for drop-weight, CVN, tensile, and 1T-CS testing. Irradiated specimens from capsules 5 and 6 are being packaged for shipment to the Nuclear Science and Technology Facility in Buffalo, New York, for testing by MEA.

6.3 Sixth HSST Irradiation Series: Crack Arrest

W. R. Corwin B. H. Montgomery

The primary objective of this irradiation series is to establish the amount of radiation-induced temperature shift that occurs in the K_{Ia} curve of two high-copper weldments typical of those in older light-water reactor pressure vessels. The results of this experiment in conjunction with those of the Fifth Series, which will determine the shifts in the K_{Ic} curve, Charpy impact curve, and nil-ductility drop-weight temperature, will allow an assessment of the currently used correlation of K_{IR} curve shift being equated to the shift in RT_{NDT}. Toward this aim the high-copper weldments and irradiation conditions of the Sixth Series will be identical to those of the Fifth Series.

The final specimen complement and engineering design of the capsule was completed during this report period. One capsule will be utilized for each weldment. The capsules will be irradiated simultaneously, side by side, and will be rotated about their vertical axes halfway through their irradiation for fluence balancing. The three rows of specimens in each capsule will be oriented so that the crack plane is perpendicular to the primary direction of flux, resulting in a very uniform fluence along the crack plane of each specimen (Fig. 6.6). Each capsule will contain 30 crack-arrest specimens of three different sizes. The largest size will be primarily duplex specimens with the remainder being of the weld-embrittled type (Table 6.1), which will allow the maximum range of K_{Ia} to be investigated using a manageably small irradiation volume. Additionally, CVN specimens will be contained within the crack-arrest specimen notches. These will allow a direct comparison of the radiation-induced material embrittlement between Series 5 and 6.

Calculations of the temperature and fluence gradients within the capsules were performed. The maximum expected temperature variation among the crack planes of all specimens is $<\pm 10°C$. The mean fluence level for all specimen crack planes will be 1.75×10^{23} neutrons/m^2 (>1 MeV), identical to that of the Fifth Series, with an expected standard deviation of 0.29×10^{23} neutrons/m^2 (>1 MeV). A full complement of dosimeters and thermocouples will be utilized in each capsule as they are being used in the Fifth Series.

Fabrication of the testing fixtures, capsules, dosimeters, and capsule support equipment is under way. It is currently anticipated that

ORNL-DWG 85-11540

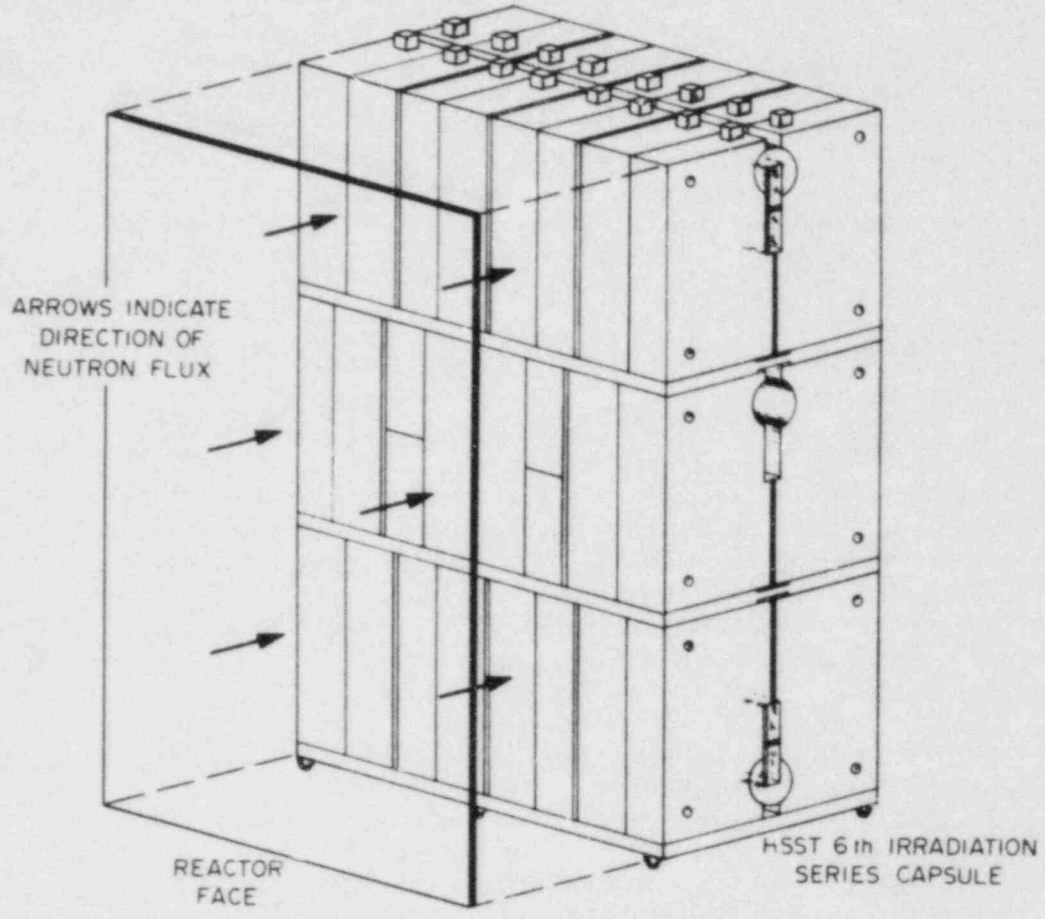

Fig. 6.6. Schematic arrangement of compact crack-arrest specimens with respect to the primary flux direction for the Sixth HSST Irradiation Series.

Table 6.1. Compact crack-arrest specimen complement for each weldment to be irradiated in the Sixth HSST Irradiation Program

Specimen type	Specimen dimensions (mm)	Specimen quantity
Weld embrittled	25.4 × 76.2 × 76.2	8
Weld embrittled	25.4 × 152.4 × 152.4	7
Weld embrittled	33.0 × 152.4 × 152.4	3
Duplex	33.0 × 152.4 × 152.4	12

the irradiation will be performed in the Oak Ridge Research Reactor immediately following the completion of the Fifth Series. Considering the installation of the new capsule supports required by the larger Sixth Series capsules, irradiation should begin around January 1986. The irradiation period will be about 3 months, contingent on the results of the dosimeters that will be pulled from the capsule supports prior to completion of the irradiation. Testing of the control specimens has begun and should be completed by the end of the capsule irradiation. This will allow testing of the irradiated specimens to be completed early in FY 1987.

6.4 Seventh HSST Irradiation Series: Stainless Steel Cladding

W. R. Corwin

The primary objective of the Seventh HSST Irradiation Series is to examine the radiation-induced degradation of fracture properties of stainless steel weld overlay cladding. In the first series (now complete) good quality cladding typical of what would be expected in a reactor pressure vessel showed only slight embrittlement, whereas cladding highly diluted by the ferritic base plate exhibited generally poorer properties and enhanced radiation sensitivity.[2]

To further examine irradiated cladding behavior, the second phase of the Seventh Series is being conducted to examine commercially produced cladding, fluences greater than phase 1, and fracture toughness K_J utilizing compact specimens. The commercial cladding's microstructure and properties have been previously described.[3,4]

Three capsules are being irradiated. Two capsules (D and H) each contain 20 CVN and 6 tensile specimens of the commercial cladding. Capsule D will reach a fluence of 2×10^{23} neutrons/m^2 (>1 MeV), whereas capsule H will reach 5×10^{23} neutrons/m^2 (>1 MeV). The remaining capsule (C) will contain 24 0.5T compact specimens, 12 from the commercial cladding and 12 of good quality cladding examined in phase 1. Capsule C will reach a fluence of 2×10^{23} neutrons/m^2 (>1 MeV).

All irradiations are being conducted at 288°C. The irradiations began September 8, 1985, at the University of Buffalo reactor and should be completed by the end of December 1985.

References

1. D. Marquardt, "An Algorithm for Least Squares Estimation of Nonlinear Parameters," *J. Soc. Indust. and Appl. Math.* 11(2), 431–41 (1963).

2. W. R. Corwin et al., "Fracture Behavior of a Neutron Irradiated Stainless Steel Submerged-Arc Weld Cladding Overlay," paper accepted for publication by *Nuclear Engineering and Design*.

3. W. R. Corwin, "Seventh HSST Irradiation Series: Stainless Steel Cladding," pp. 127-33 in *Heavy-Section Steel Technology Program Semiann. Prog. Rep. October 1984–March 1985*, NUREG/CR-4219, Vol. 1 (ORNL/TM-9593/V1), Martin Marietta Energy Systems, Inc., Oak Ridge Natl. Lab.

4. W. R. Corwin, "Stainless Steel Cladding Investigations," pp. 34-37 in *Heavy-Section Steel Technology Program Semiann. Prog. Rep. October 1984–March 1985*, NUREG/CR-4219, Vol. 1 (ORNL/TM-9593/V1), Martin Marietta Energy Systems, Inc., Oak Ridge Natl. Lab.

7. CLADDING EVALUATIONS

7.1 Flaw-Characterization Studies of Clad BWR Vessel Material

K. V. Cook R. W. McClung

7.1.1 Introduction

As reported previously,[1] nondestructive examination is being conducted to determine flaw density of a segment of a boiling-water reactor (BWR) pressure vessel. The material section was obtained from the salvaged Hope Creek Unit 2 reactor vessel and contained both longitudinal and transverse (girth) seam welds. It was originally purchased by ORNL as one piece (~0.7 by 3 m).

Figure 7.1 shows the three sections that were delivered to the Nondestructive Testing Laboratory in early January 1985. The three vessel pieces were identified from left to right as blocks 2, 3, and 1. The narrow block at the upper-left position (behind block 2` is the one patterned after the *ASME Code* (described in the previous semiannual[1] as Fig. 7.1). The ultrasonic flaw detector used for volumetric inspection on the three vessel specimens is sitting on block 3. Three ultrasonic transducers used in the examinations are also shown on top of block 3. Note the double line on the clad surfaces that locates the approximate weld positions for all three pieces.

An outline of the planned activities to evaluate the pressure vessel section to determine the as-fabricated status of flaw density was presented in the previous semiannual.[1] This plan listed three primary objectives: (1) to evaluate longitudinal and girth welds for flaws with manual ultrasonics, (2) to evaluate the zone under the nominal 6.3-mm clad for cracking (again with manual ultrasonics), and (3) to evaluate the cladding for cracks with a high-sensitivity fluorescent penetrant method. All three objectives have been completed, and a letter report documenting the results is being prepared.

7.1.2 Results of examinations

A fluorescent liquid penetrant inspection was performed on 2.2 m^2 of clad surface for surface-breaking flaws. No significant indications were detected.

The 70° longitudinal angle-beam inspections (i.e., with dual 70° elements in a common search unit design) were performed on the 2.2 m^2 of clad surface also. This inspection is primarily applied to detect cracking in the zone at the clad-to-base metal interface. Again, no significant indications of flaws were detected.

Volumetric flaw detection inspections were also performed on ~3.2 m of weld using procedures patterned after the *ASME Code*, considering both standard and enhanced sensitivities. Inspections were performed from both the clad and unclad surfaces using 45 and 60° shear-wave angle beams. The 60° angle-beam tests were limited because of the relatively

ORNL–PHOTO 5168–85

Fig. 7.1. Section of pressure vessel from Hope Creek Unit 2 reactor with ultrasonic equipment.

small size of our specimens. Again, no significant indications were found when inspecting from the outer surface; however, a few Code-recordable indications were detected (>50% DAC) along with additional indications with amplitudes >20% DAC while inspecting with the 45° shear wave from the clad side.

Examinations were made using tandem probe shear-wave angle-beam transducers with no recordable indications being detected. These tandem inspections were performed only from the clad side, using both through-transmission and pulse-echo methods in both the circumferential and the longitudinal axis directions. We had originally planned to perform the tandem probe evaluations only from the outer surface; however, because of technical, convenience, and monetary reasons we switched to the clad-side tandem evaluation scheme.

Supplementary normal beam evaluations were also applied from the clad surface in zones where the 12 (20% DAC or larger) indications were detected. Only one indication zone (i.e., the 30% DAC) provided a high signal-to-noise reflection.

7.1.3 Results and conclusions

A number of nondestructive tests have been performed on ~3.2 m of pressure vessel longitudinal and girth seam welds and 2.2 m^2 of cladding contained in three samples taken from the Hope Creek Unit 2 BWR vessel. The only indications of possible significant reflectors, when inspecting to the more stringent requirements of recording 20% DAC indications (*ASME Code* requires 50% DAC recordings), were subsurface and were detected during clad-side angle-beam examinations. Twelve such 20% DAC indications were recorded with five being Code-recordable (i.e., 50% DAC or more in amplitude response). Complete sizing analysis was not prepared; however, code sizing techniques indicate lengths and through-wall depths of 25 by 25 mm or less. Consideration of other evaluation criteria (e.g., beam spread, tandem search unit, and normal beam search unit data) suggests that the size of these subsurface indications would be somewhat smaller. Further size analyses before and during destructive sectioning of these samples would be necessary to provide final answers.

7.2. Stainless Steel Cladding Investigations

W. R. Corwin

The principal purpose of this program is to examine the structural effect a layer of tough stainless steel cladding can have on the composite fracture properties of an engineering structure. This will provide insight into what, if any, benefit a flawed reactor pressure vessel would gain from the layer of weld overlay cladding on its inner surface in the event of a severe transient.

Phase 1 of this program examined the effect of cladding on the crack-arrest behavior of flawed steel beams in bending. The results indicated that cladding of moderate toughness may slightly enhance the total structural resistance of the beams to failure, but that they would still fail

under extreme conditions. A topical report on the results of the phase 1 study was issued during this reporting period.[2]

In phase 2, the structural effects of a much tougher commercial cladding will be examined.[3] Beam specimens with enhanced experimental capability and ease of analysis will permit a definitive assessment to be made of the increase in the structural crack initiation and arrest toughness caused by the cladding. Eight beam specimens (six clad and two unclad) as well as material characterization specimens were fabricated during this report period. Testing of the clad beams is planned for early FY 1986.

References

1. K. V. Cook, J. H. Smith, and R. W. McClung, "Flaw Characterization Studies of Clad BWR Vessel Material," pp. 136–38 in *Heavy-Section Steel Technology Program Semiann. Prog. Rep. October 1984–March 1985*, NUREG/CR-4219, Vol. 1 (ORNL/TM-9593/V1), Martin Marietta Energy Systems, Inc., Oak Ridge Natl. Lab.

2. W. R. Corwin et al., *Effect of Stainless Steel Weld Overlay Cladding on the Structural Integrity of Flawed Steel Plates in Bending*, NUREG/CR-4015 (ORNL/TM-9390), Martin Marietta Energy Systems, Inc., Oak Ridge Natl. Lab., April 1985.

3. W. R. Corwin, "Stainless Steel Cladding Investigations," pp. 34–37 in *Heavy-Section Steel Technology Program Semiann. Prog. Rep. October 1984–March 1985*, NUREG/CR-4219, Vol. 1 (ORNL/TM-9593/V1), Martin Marietta Energy Systems, Inc., Oak Ridge Natl. Lab.

8. INTERMEDIATE VESSEL TESTS AND ANALYSIS

J. G. Merkle R. H. Bryan

During this report period, preparation of a topical report on the V-8A test was continued. This test investigated the tearing behavior of a weld with low toughness at upper-shelf temperatures. A summary of the results of posttest tearing instability analyses and evaluations is given here, in advance of a more complete presentation in the final report.[1]

Posttest analyses of vessel V-8A by the J-T diagram procedure were developed by both Oak Ridge National Laboratory (ORNL) and by a group of cooperating organizations in the United Kingdom.[2] The ORNL analyses were of the simplest type, assuming a linear J-T applied line. Although it was possible to obtain an accurate estimate of the tearing instability pressure by using the measured lower bound R-curve, the corresponding estimate of crack extension at instability was not accurate, because this factor was neglected in the basic method. Some of the U.K. calculations[2] also used straight J-T applied lines, but others deliberately omitted this assumption, thereby developing excellent examples of the nonlinearity that occurs in J-T applied curves when the applied load approaches a crack-size-dependent fully plastic load. It was pointed out in the discussion accompanying the U.K. calculations that there are methods other than the J-T diagram procedure by which it is easy to consider both the increase in crack size caused by stable tearing and crack-size-dependent limit loads.

Motivated by the nonlinear J-T applied curves developed numerically in the U.K. calculations, for both power law stress-strain curve and R-6 estimates of J applied, a mathematical expression for the J/T ratio for the R-6 method was developed. This solution confirms the general nonlinearity of J-T applied curves, when the variables of load and crack size are not arbitrarily separated, and eliminates the need for potentially inaccurate numerical differentiation to obtain the values of T applied for the R-6 method.

A posttest analysis of V-8A by the Deformation Plasticity Failure Assessment Diagram (DPFAD) procedure was performed by the Babcock and Wilcox (B&W) Company,[3] the fabricator of the V-8A test weld. This analysis utilizes approximate solution curves based on elastic-plastic J estimates for a through crack in a flat plate. In these calculations, an improvement in accuracy was obtained by changing from a J_D (deformation J) to a J_M (modified J) resistance curve. A straightforward explanation of the DPFAD curve, as a graphical device for solving the nonlinear equation that determines the load satisfying the equation $J_{mat} = J_{appl}$ for a given current crack size, has been developed. An explanation of the physical and mathematical bases for the deformation and modified J parameters has also been developed (see Sect. 2.3 of this report). Because the DPFAD analysis is the only analysis of V-8A that used a modified J resistance curve for the actual test material and its analytical model was an indirect approximation (a through crack in a flat plate), conclusions cannot yet be drawn concerning the relative merits of using J_M vs J_D resistance curves for tearing instability calculations. An evaluation of this

matter would require both a repetition of the other calculations for vessel V-8A, using J_M resistance curves, and a comparison of the analytical assumptions underlying the calculation of J for the flawed vessel and the toughness specimen.

Table 8.1 summarizes all the posttest calculations made for vessel V-8A. The Tangent Modulus calculations are pretest estimates based on an R-curve for weld V8102, the characterization weld known from posttest data to best represent the vessel test material. The range of estimated instability pressures shown in Table 8.1 is less than the range for the pretest calculations,[4] as expected. Also noteworthy are the overestimates of Δa at instability made by the J-T method, because of the neglect of this factor in the calculation of J. In addition, there is a scarcity of strain estimates, with one accurate, but the other inaccurate because of the excess strain near yielding estimated by the Ramberg-Osgood equation. In fact, the only analyses of vessel V-8A that included accurate

Table 8.1. Vessel V-8A posttest calculations and experimental results for ductile flaw instability

Organization	Method	Pressure (MPa)	Outside circumferential strain (%)	Δa (mm)
IWM, Freiburg[a]	R-6	145		9.0
ORNL	Tangent Modulus ($2b_o$ = 279.4 mm)	145		13.3
ORNL	Tangent Modulus ($2b_o$ = 304.8 mm)	144	0.12	12.7
ORNL	J-T	140	0.26	28.2
RNL[b]	J-T	140		15.0
ORNL	Experimental results	140	0.12	5.0
B&W	DPFAD; J_M	139		7.6
CERL[c]	J-T and R-6; $a = a_o$	136		5.0
B&W	DPFAD; J_D	132		5.1
CERL[c]	J-T and R-6; $a = a_o + 6$ mm	130		5.0

[a]Fraunhofer-Institut für Werkstoff Mechanik.

[b]Risley Nuclear Power Development Laboratories.

[c]Central Electricity Research Laboratories.

strain estimates were the Simplified Line Spring and Tangent Modulus estimates. The Tangent Modulus method also produced accurate posttest estimates of both load and strain at instability for vessels V-1, -3, and -6. J-T calculations also produced accurate values of instability load and strain for vessels V-1, -3, and -6, but the same method did not produce an accurate strain estimate for vessel V-8A.

Six different methods of analysis were used for pretest or posttest analyses of V-8A, and it is instructive to compare these methods of analysis with regard to some of their basic features. Five basic features directly related to the completeness, accuracy, and ease of execution of the analytical procedures follow:

1. Plastic instability is considered.
2. Effects of increasing crack size on calculated value of J are considered.
3. The load corresponding to specified values of crack size and toughness can be directly calculated.
4. Load is related to nominal strain by using a numerically or analytically exact elastic-plastic stress and strain analysis solution.
5. Exact solution for J is given.

A comparison of the six methods of analysis used for vessel V-8A with regard to these five analytical features is shown in Table 8.2. Except for load-strain considerations, there is an almost steadily increasing progression of factors considered by the different analytical methods. However, as shown by the last line in Table 8.2., nonlinear numerical methods for calculating J cannot solve for unknown loads. The asterisk (*) in Table 8.2 indicates that the J analysis is based on a fixed relationship between a nominal stress and the load. Nominal strain at the flaw location is not calculated directly, but it can be determined from a separate stress analysis of the uncracked structure. However, the stress calculated at the flaw location by the stress analysis may not be the same as the nominal stress used to calculate J, because of either stress gradients or yielding or both.

Table 8.2. Comparison of features included in analytical methods used to make tearing instability estimates for vessel V-8A

Method	Plastic instability	Crack extension	Load calculation	Load vs strain	Exact J
J-T					
R-6	x			*	
Line Spring	x			*	
DPFAD	x	x	x		
Tangent Modulus	x	x	x	x	
ORVIRT	x	x		x	x

References

1. R. H. Bryan et al., *Test of 6-in.-Thick Pressure Vessels. Series 3: Intermediate Test Vessel V-8A Tearing Behavior of Low Upper-Shelf Material*, ORNL-6187, Martin Marietta Energy Systems, Inc., Oak Ridge Natl. Lab. (in preparation).

2. L. M. Davies, ed., "UK Light Water Reactor Study Group Response to NRC Report NUREG-0744" (for Comment Draft); correspondence between UKAEA and the USNRC dated January 28, 1983, subsequently forwarded by the NRC to the ASME Working Group on Flaw Evaluation for Review.

3. J. M. Bloom and K. K. Yoon, *Analysis of HSST Intermediate Vessel V-8A Test by the Deformation Plasticity Failure Assessment Method*, B&W-1814, Babcock and Wilcox Company, Lynchburg, Va., November 1983.

4. J. G. Merkle, "Preliminary Results of International Round Robin on ITV-8A," pp. 301–6 in *Proceedings of the USNRC Tenth Water Reactor Safety Research Information Meeting*, NUREG/CR-0041, Vol. 4, U.S. Nuclear Regulatory Commission, Washington, D.C., January 1983.

9. THERMAL-SHOCK TECHNOLOGY

R. D. Cheverton

9.1 Summary

A major effort was involved in the completion of three HSST reports pertaining to HSST thermal-shock experiments (TSE-5, TSE-5A, TSE-6, and TSE-7) and the inclusion of three-dimensional (3-D) flaws in the pressurized-water reactor (PWR) pressurized-thermal-shock (PTS) vessel-integrity studies. In addition, OCA-P, the Oak Ridge National Laboratory probabilistic fracture-mechanics code, was adapted to a personal computer (PC), and studies were continued regarding subclad and through-clad flaws.

9.2 Adaptation of OCA-P to a Personal Computer

D. G. Ball R. D. Cheverton

OCA-P,[1] which is a probabilistic fracture-mechanics code, was developed for the Nuclear Regulatory Commission to help in the evaluation of PWR pressure-vessel integrity during PTS transients. The code was originally written for a main-frame computer but because of the popularity of PCs, OCA-P has now been adapted to a PC. The adaptation requires 512 kilobytes of memory and a math coprocessor. These requirements were met with an IBM PC-XT and PC-AT, using the IBM Professional 1.0 compiler.[2]

The OCA-P code consists of two subcodes: a one-dimensional heat transfer code (1-R) and a probabilistic fracture-mechanics code (PFM). The 1-R code will run on a PC without a hard disk; however, because a larger memory (413 kilobytes) is required for PFM, this latter code must be run with a hard disk.

Typical running times for 1-R and PFM on the PC and the IBM 3033 are given in Table 9.1. Although the run times for the PC are much greater than those for the IBM 3033, they do not appear to be unreasonable.

Several additions have been made to OCA-P since Ref. 1 was issued, and these additions are included in the PC version of OCA-P. Two of the additions are discussed in Ref. 3, and a topical report pertaining to the adaptation of OCA-P to a PC, including a discussion of additions to OCA-P, will be published soon.

The opportunity is taken here to point out an error in Ref. 3. The error is in Eq. (6) (page 143), which should be written as

$$\sigma_j \simeq \frac{1}{F_{1j}F_{2j}F_{3j}} \left[\frac{\hat{P}_j(1-\hat{P}_j)}{N'_{vj}} \right]^{1/2} N_j V_j \int_0^w f(a)B(a)da \ .$$

Table 9.1. Typical run times for 1-R and PFM on the PC and IBM-3033

Code	Computer	Run time (min)
1-R	PC	62
	PC-XT (hard disk)	61
	PC-AT	52
	IBM-3033	0.75
PFM	PC-XT (hard disk)	19
	PC-AT	17
	IBM-3033	0.31

9.3 Completion of Reports Relating to Thermal-Shock Studies

R. D. Cheverton

Three topical reports pertaining to the HSST thermal-shock studies were completed and issued. The first of these reports[4] covers thermal-shock experiments TSE-5, TSE-5A, and TSE-6, which investigated the behavior of long axial inner-surface flaws in large (991-mm OD × 1220-mm length) thick-walled (76- and 152-mm wall) steel (A 508 with class-2 chemistry) test cylinders. The second report[5] covers thermal-shock experiment TSE-7, which investigated the behavior of an initially short and shallow (38- × 15-mm) inner-surface flaw in a similar test cylinder with a 152-mm wall. The third report[6] covers an analytical study of the effect of including certain 3-D flaws in the deterministic evaluation of the integrity of PWR vessels when subjected to both pressure and thermal-shock loading conditions.

9.4 Studies Pertaining to the Behavior of Subclad and Through-Clad Flaws

R. D. Cheverton J. W. Bryson

A thermal-shock experiment with a clad test cylinder is being considered that may include both through-clad surface flaws and subclad flaws.[7] Proposed test conditions are similar to those for previous HSST thermal-shock experiments[4] and are included in Table 9.2.

Calculations have been made to investigate the interaction between multiple flaws and to determine an acceptable means for detecting propagation of the subclad flaw into the base material. These studies are discussed below.

Table 9.2. Proposed test conditions for thermal-shock experiment with clad cylinder

Parameter	Value/description
Test facility	TSTF
Quench medium	
Type	LN_2
Application technique	Submersion/natural convection
Sink temperature, °C	−197
Test cylinder initial temperature, °C	100
Pressure differential	0
Test cylinder dimensions, mm	
Inside diameter	686
Outside diameter	991
Length	1220
Clad thickness	5
Test cylinder material	
Type	
Base	A 508 class-2 chemistry
Cladding	308/309 weld deposit
Heat treatment	
Preclad	Water quench from ~870°C
Postclad	Stress relief at ~620°C
Flaws	
Geometry/orientation	6/1 semiellipse/axial
Depth, mm	~25
Generation technique	Electron-beam weld plus hydrogen charging

9.4.1 Interaction of multiple flaws

The particular flaws of interest are 6/1 semielliptical subclad and surface flaws with an axial orientation (see Fig. 9.1 and Ref. 7). It is desired that the test cylinder include several subclad and surface flaws for the thermal-shock experiment, and the flaws are to be located at mid-length of the cylinder. The number of flaws permissible depends on the amount of interaction between the flaws; that is, how much K_I is reduced by having more than one flaw.

Preliminary flaw interaction calculations were made with a 2-D fracture-mechanics model that included either two, six, or twelve 38-mm-deep equally spaced subclad or surface flaws. The K_I values (deepest point for subclad flaws) at 7 min into the proposed thermal transient (time of warm prestressing with $\dot{K}_I = 0$) are given in Table 9.3. It is

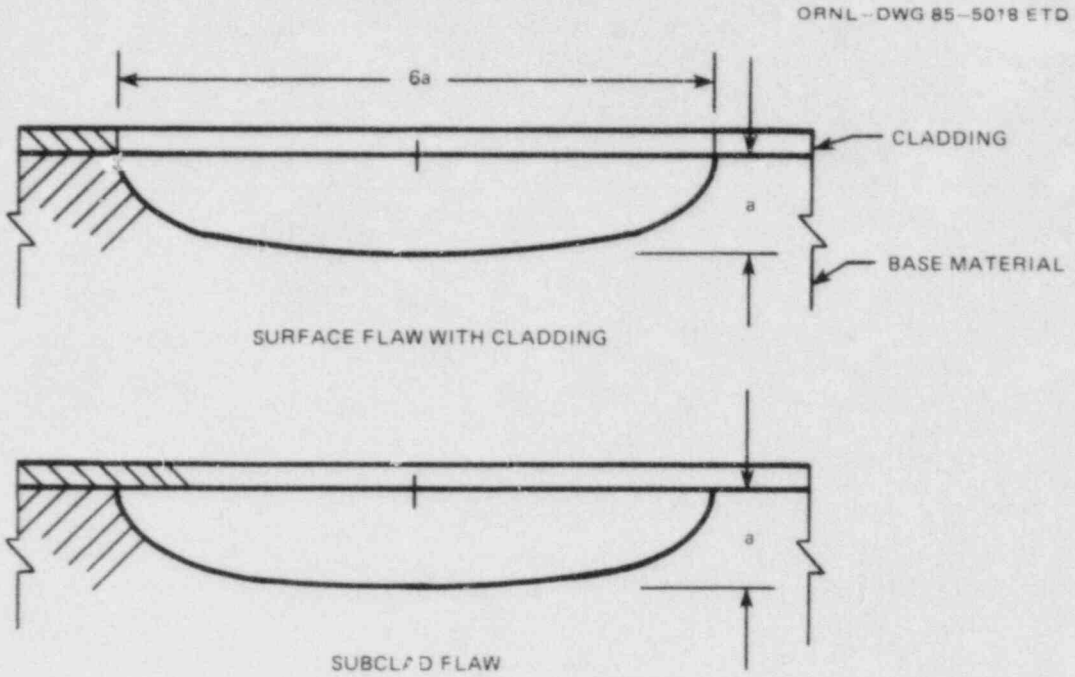

Fig. 9.1. 6/1 semielliptical surface and subclad flaws.

Table 9.3. Results of flaw interaction calculations with 38-mm-deep subclad and surface flaws (t = 7 min)

Type flaw	Number and spacing of flaw	Flaw depth (mm)	K_I at deepest point (t = 7 min)	Reduction in K_I relative to 2-flaw case (%)
Subclad	2 @ 180°	38	48	0
Surface	2 @ 180°	38	138	0
Subclad	6 @ 60°	38	46	4
Surface	6 @ 60°	38	110	20
Subclad	12 @ 30°	38	43	10
Surface	12 @ 30°	38	87	37

apparent that there is little interaction between the subclad flaws (<10%) and substantial interaction for the surface flaws (>10%).

Additional 2-D calculations were conducted using the model shown in Fig. 9.2. One of these models included either two surface or two subclad flaws at 180°, and the effect of introducing these flaws on the tangential stresses 60° from the flaws was evaluated. Figure 9.2 indicates that, compared with no flaw at all, a 76-mm-deep surface flaw reduces the

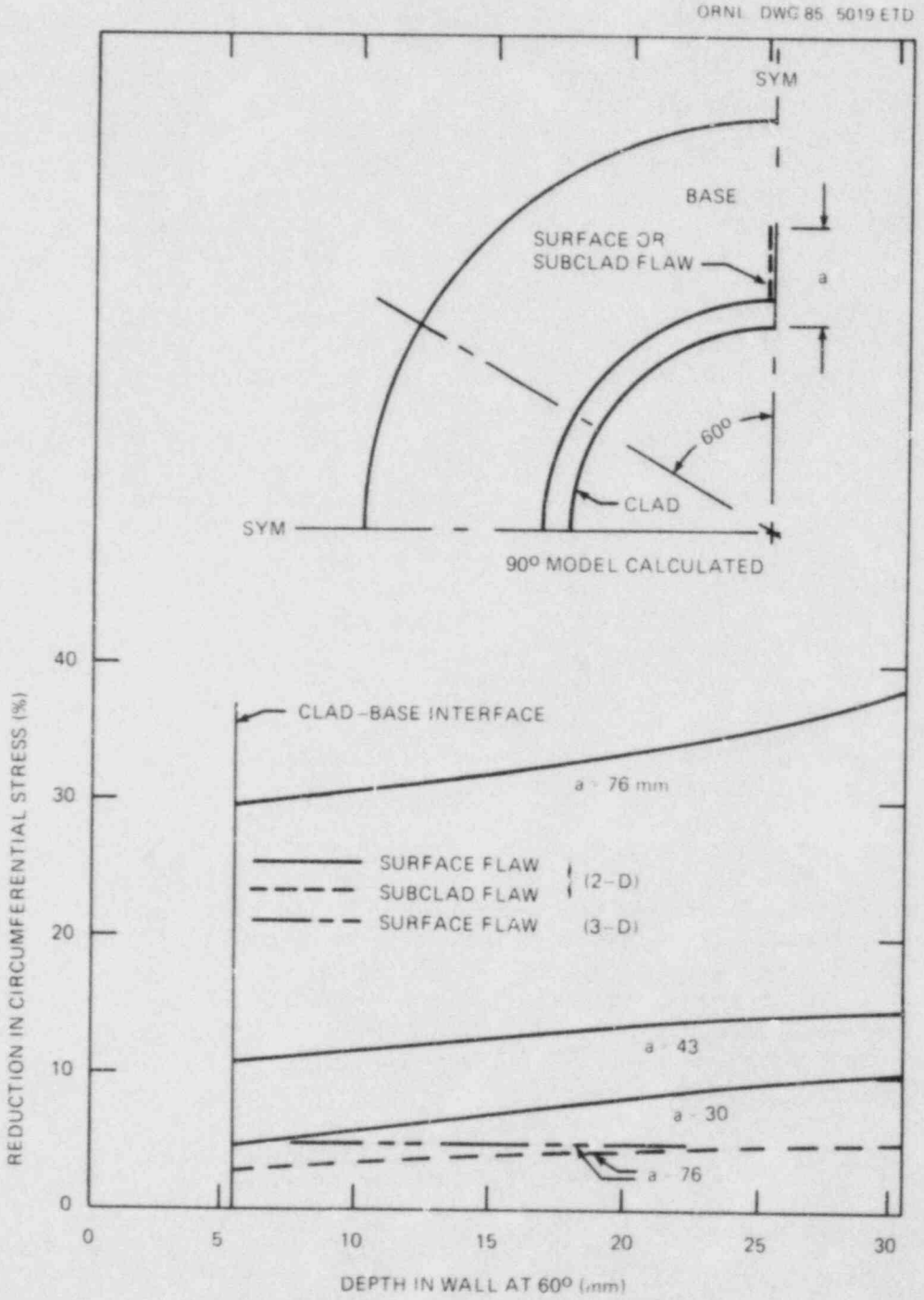

Fig. 9.2. Reduction in circumferential stresses due to introduction of 2-D or 3-D surface or subclad flaw 60° from plane of stress comparison (t = 7 min).

stresses and, thus, the stress-intensity factor ~35%. For shallower surface flaws the reduction in stress is less, and the introduction of a 76-mm-deep subclad flaw reduces the stress by only 4%. These results indicated once again that the interaction between six equally spaced subclad flaws would be negligible, but the effect of two surface flaws on four subclad flaws might not be.

If the surface length of the surface flaws could be limited by some means, the effect of the surface flaw would be less than that estimated with the 2-D analysis. To evaluate 3-D effects, a 3-D analysis was performed with the 90° model shown in Fig. 9.2, and the flaw was assumed to be a 6/1 semielliptical surface flaw. As illustrated in Fig. 9.2, the reduction in stress associated with the introduction of a 76-mm-deep flaw was only 5%. Thus, on the basis of these stress calculations, it appears that the interaction between six equally spaced 6/1 semielliptical flaws (two 76-mm-deep surface flaws spaced 180° and four 25-mm-deep subclad flaws) would be acceptable (<10%).

A direct comparison of K_I values was obtained using the 2-D model shown in Fig. 9.3. This model includes two 25-mm-deep subclad flaws spaced 180° and four surface flaws spaced 60°, or six equally spaced subclad flaws, two of which are 25 mm deep (180° apart) and the others 100 mm deep. The results of the analysis (Fig. 9.3) indicate that introduction of 76-mm-deep surface flaws reduces K_I for the subclad flaws by ~44%, and introduction of 76-mm-deep subclad flaws reduces K_I by ~4%. These results are consistent with those in Fig. 9.2, considering that the model in Fig. 9.3 represents a somewhat more severe situation with regard to flaw interaction.

9.4.2 COD analysis for subclad flaws

In previous HSST thermal-shock experiments[4] the initial flaws extended to the inner surface of the test cylinder, and propagation of the flaw was detected with surface-mounted COD gages that indicated a step change in COD when propagation occurred. It is possible that surface COD gages could also be used for subclad flaws, but the sensitivity (surface strain) would be much less. Thus, the possibility of embedding a COD gage that could measure COD directly for a subclad flaw is being considered. Both of these possibilities are discussed below.

9.4.2.1 Calculated strain at the inner surface. Two-dimensional finite-element calculations were made for a subclad flaw (Fig. 9.4) to determine the change in strain on the inner surface associated with a change in flaw depth. Results are reported in Fig. 9.5 for the earliest time in the transient (3 min) at which propagation would be expected. As indicated, the circumferential displacement on the surface is maximum at a point 15 mm from the flaw plane, and the corresponding displacement per unit of crack extension is $\sim 6 \times 10^{-4}$. If it is assumed that a strain gage mounted on the surface must be sensitive enough to detect a crack extension of 6 mm and if the active length of the gage (weldable strain gage) is 51 mm and the unbonded length is ~30 mm (the gage would straddle the flaw plane), the necessary detectable change in gage strain would be 150 με, which is considered to be marginal.

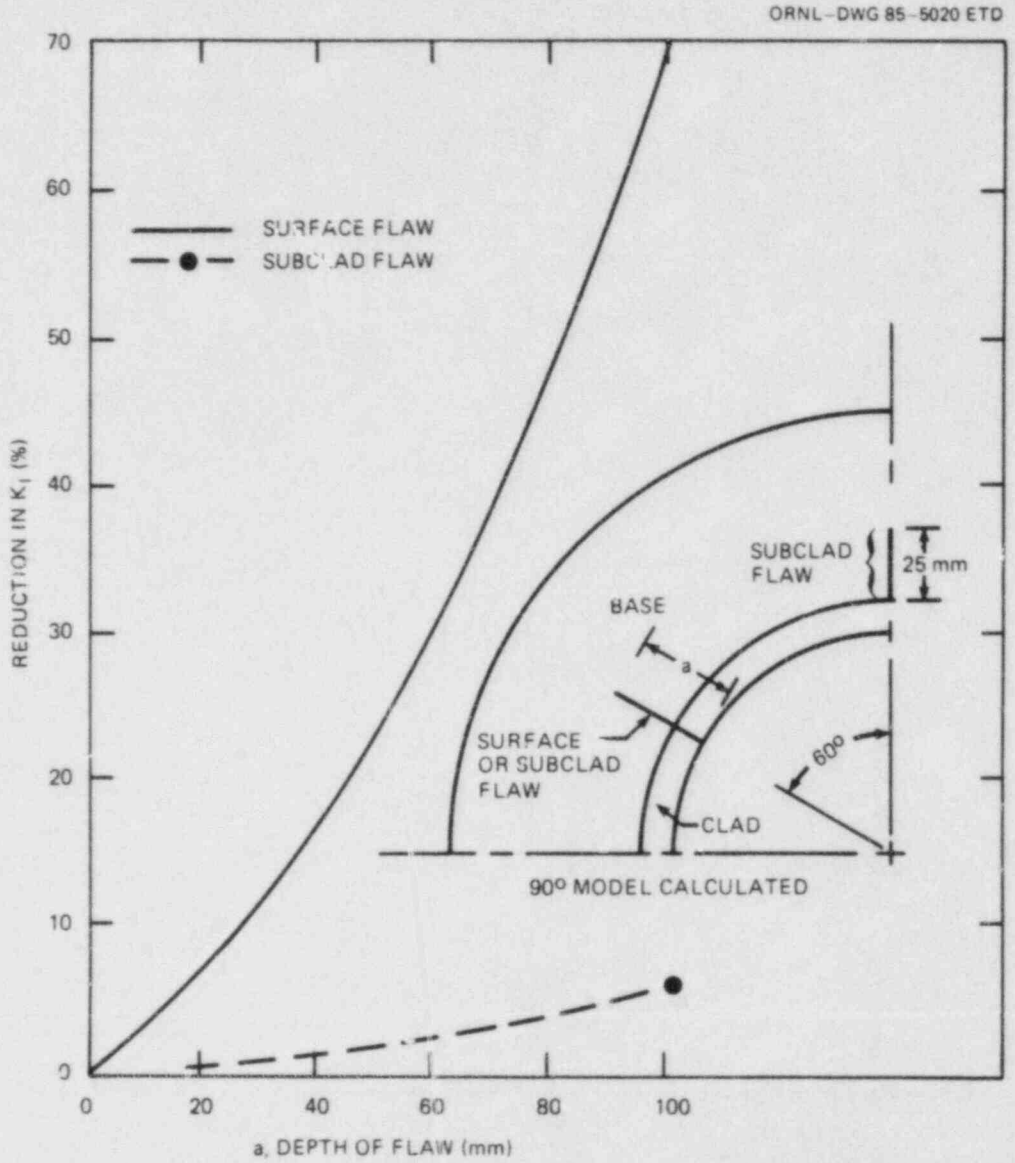

Fig. 9.3. Reduction in K_I for 25-mm-deep, 2-D subclad flaw as a result of introducing 2-D surface or subclad flaw 60° away (t = 7 min).

9.4.2.2 An embedded COD gage. The sensitivity of crack-propagation-detection instrumentation can be improved if the COD of the subclad flaw is measured directly. In principle this can be done with an embedded strain gage as indicated in Fig. 9.6.

Both 2-D and 3-D calculations were made for the subclad flaw to determine the COD for several crack depths at a time of 3 min in the transient. The results, shown in Fig. 9.7, indicate that the largest change in gage output associated with a change in crack depth would be achieved by placing the gage at a depth equal to the depth of the initial flaw. If this were done, a 6-mm extension of the flaw would result in an increase in gage output of ~1500 με, which is considered to be acceptable.

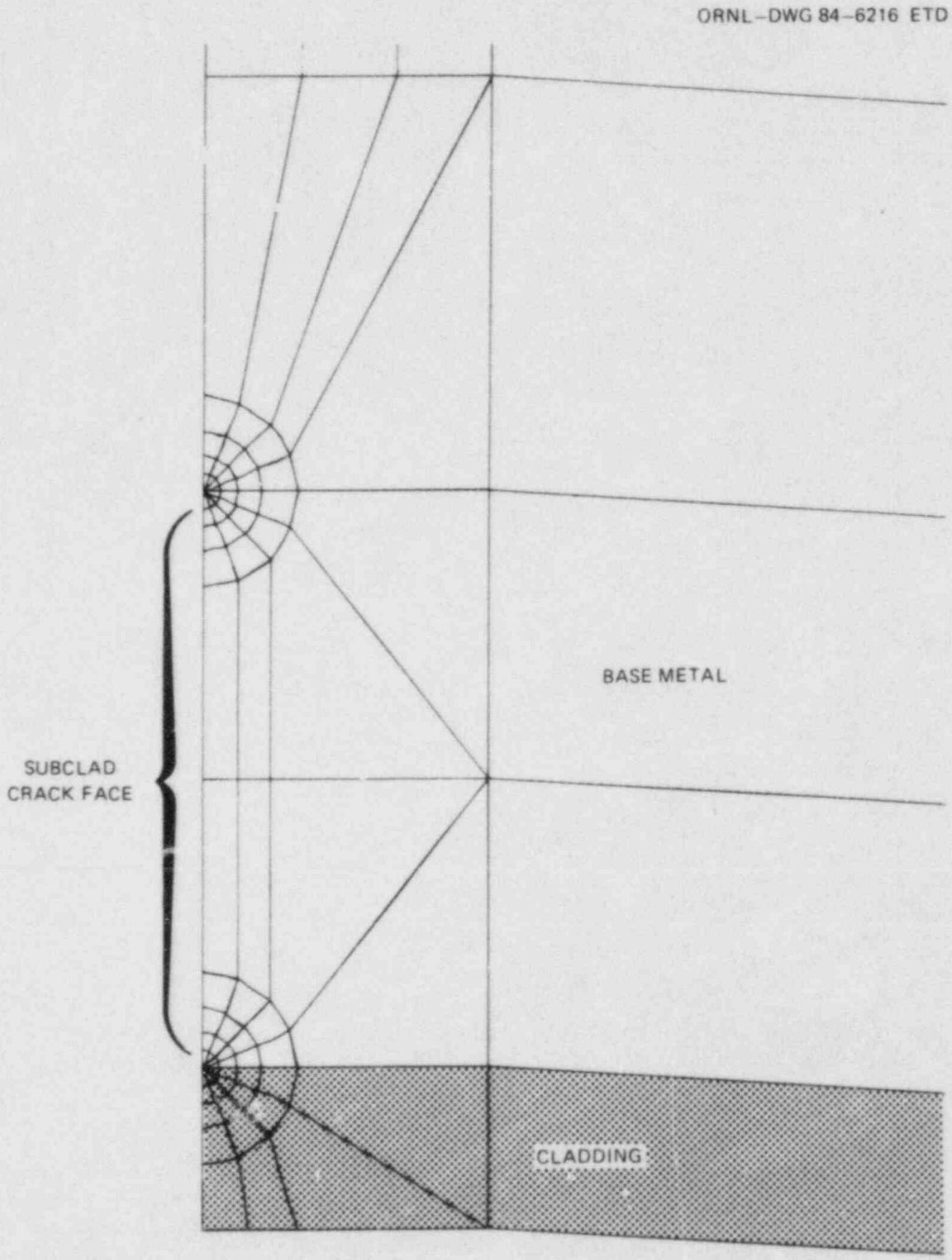

Fig. 9.4. Enlarged view of crack-tip region for 2-D finite-element analysis of subclad flaw in TSE test cylinder.

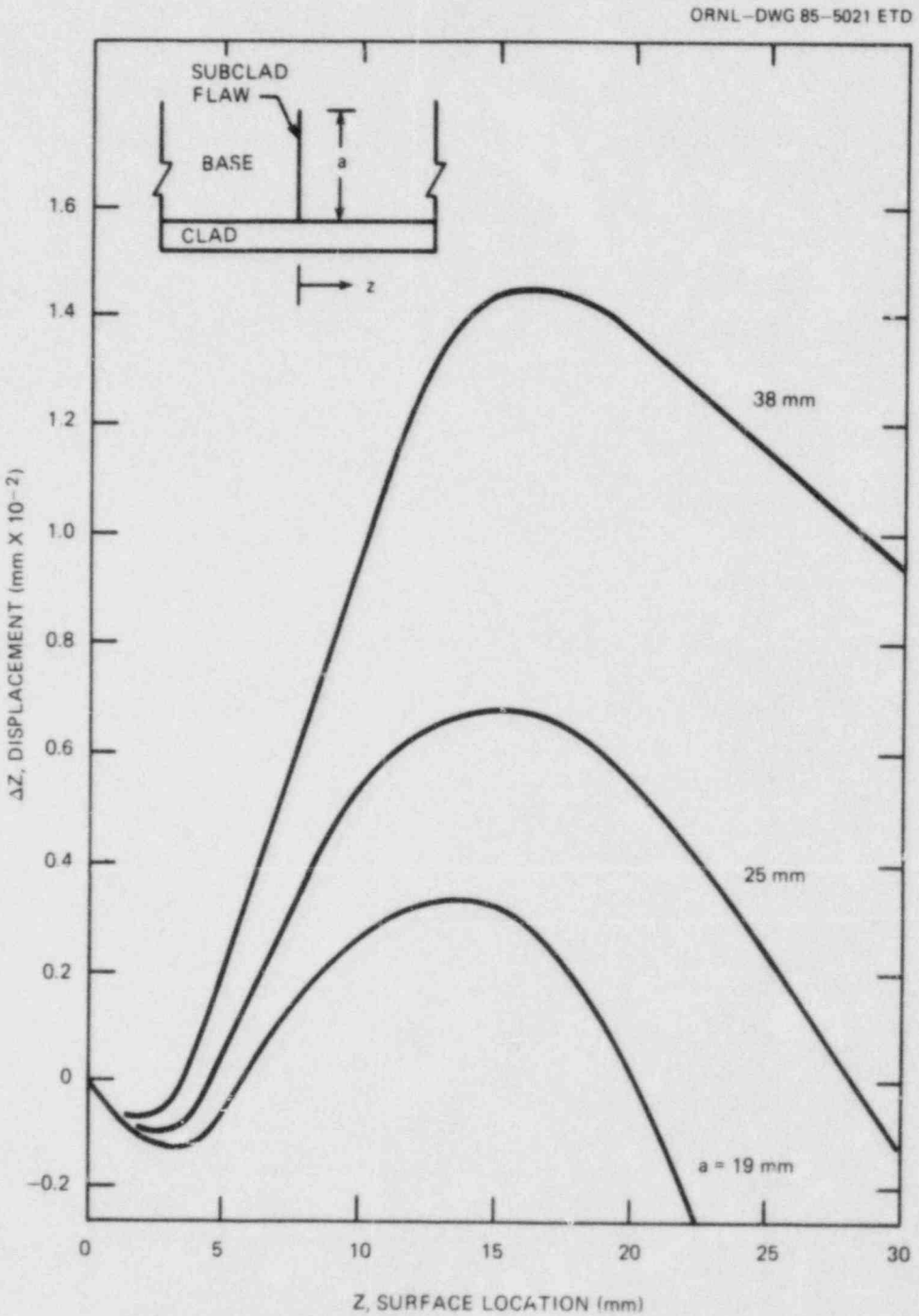

Fig. 9.5. Circumferential displacement of points on inner surface of test cylinder at 3 min into TSE transient.

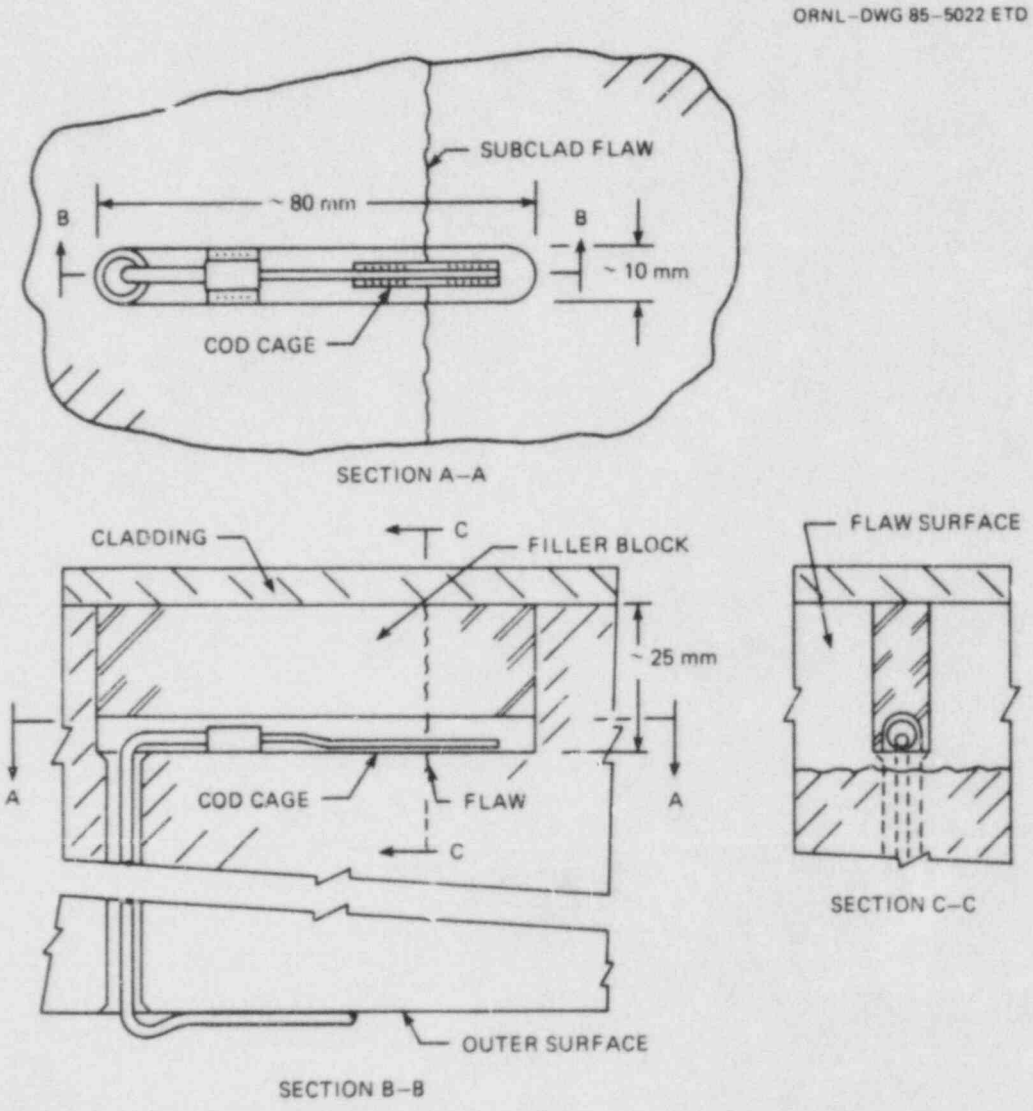

Fig. 9.6. Embedded COD gage for subclad flaw.

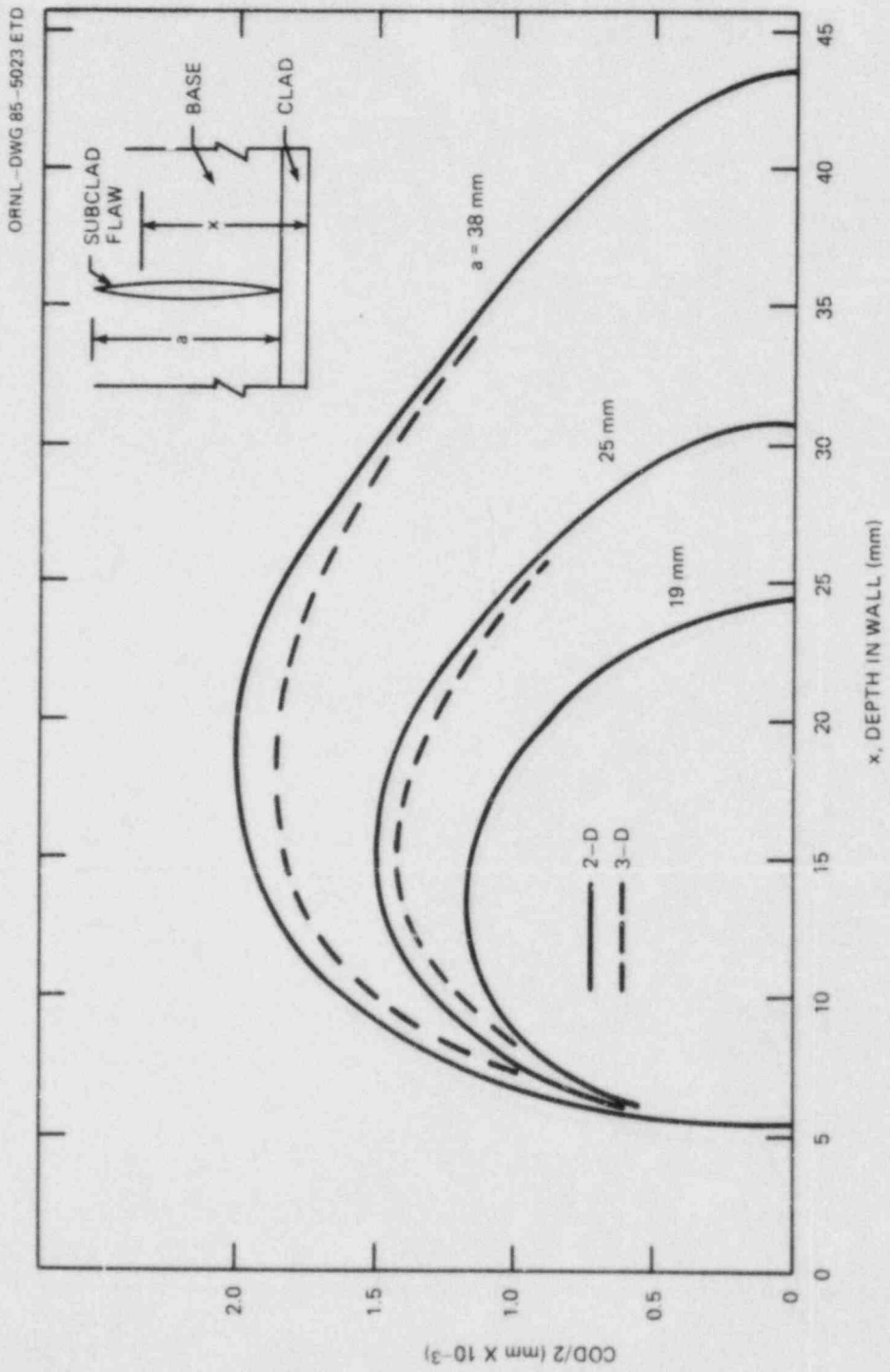

Fig. 9.7. COD for subclad flaw at 3 min into TSE transient.

References

1. R. D. Cheverton and D. G. Ball, *OCA-P, A Deterministic and Probabilistic Fracture-Mechanics Code for Application to Pressure Vessels*, NUREG/CR-3618 (ORNL-5991), Martin Marietta Energy Systems, Inc., Oak Ridge Natl. Lab., May 1984.

2. Professional FORTRAN, IBM Personal Computer Software, by Ryan-Farland Corporation, November 1984.

3. R. D. Cheverton et al., "Thermal-Shock Technology," pp. 140–? in *Heavy-Section Steel Technology Program Semiann. Prog. Rep. October 1984–March 1985*, NUREG/CR-4219, Vol. 1 (ORNL/TM-9593/V1), Martin Marietta Energy Systems, Inc., Oak Ridge Natl. Lab.

4. R. D. Cheverton et al., *Pressure Vessel Fracture Studies Pertaining to the PWR Thermal-Shock Issue: Experiments TSE-5, TSE-5A, and TSE-6*, NUREG/CR-4249 (ORNL-6163), Martin Marietta Energy Systems, Inc., Oak Ridge Natl. Lab., June 1985.

5. R. D. Cheverton et al., *Pressure Vessel Fracture Studies Pertaining to the PWR Thermal-Shock Issue: Experiment TSE-7*, NUREG/CR-4304 (ORNL-6177), Martin Marietta Energy Systems, Inc., Oak Ridge Natl. Lab., August 1985.

6. R. D. Cheverton and D. G. Ball, *A Parametric Study of PWR Pressure Vessel Integrity During Overcooling Accidents, Considering Both 2-D and 3-D Flaws*, NUREG/CR-4325 (ORNL/TM-9682), Martin Marietta Energy Systems, Inc., Oak Ridge Natl. Lab., August 1985.

7. R. D. Cheverton et al., "Thermal-Shock Technology," pp. 154–62 in *Heavy-Section Steel Technology Program Semiann. Prog. Rep. October 1984–March 1985*, NUREG/CR-4219, Vol. 1 (ORNL/TM-9593/V1), Martin Marietta Energy Systems, Inc., Oak Ridge Natl. Lab.

10. PRESSURIZED-THERMAL-SHOCK TECHNOLOGY

10.1 Preparation of Vessel for the Second Pressurized-Thermal-Shock (PTSE-2) Experiment

G. C. Robinson R. H. Bryan

As noted in the previous progress report,[1] following legal negotiations, a subcontract was let to the Babcock & Wilcox Company (B&W) to perform a two-phase activity leading to production of the PTSE-2 vessel and associated material for characterization and wide-plate specimens. In the first phase of the subcontract, B&W purchased a 15.9-cm-thick (6 1/4-in.) 2 1/4 Cr-1 Mo steel plate meeting SA 387 Grade 22 from Lukens Steel Company large enough to provide for the material allocations of both phases of the subcontract. Figure 10.1 shows the approved cutting plan for the plate. Under Phase 1 of the subcontract, B&W determined the response of the plate to heat treatments to obtain specified tensile, Charpy, and tearing resistance requirements. Table 10.1 shows the specified impact and tensile requirements for a low-upper-shelf material for welding into the PTSE-1 vessel and for incorporation into the associated wide-plate specimens. It was anticipated that the desired properties could be achieved only in the transverse orientation relative to the rolling direction; consequently, the layout of Fig. 10.1 has been premised on this consideration. Preliminary Charpy and tensile data have been obtained by B&W in which the variation of response has been obtained by varying the stress-relieving temperature for a hold time of 7 h. Figure 10.2 shows the results from transversely oriented Charpy V-notch tests in low-upper-shelf material as a function of stress-relieving temperature, and Fig. 10.3 shows the data from tensile tests located both in the longitudinal and transverse directions.

Although these data indicate that the transversely oriented upper-shelf values are quite sensitive to the stress-relieving temperature, the transition temperature and Charpy energy curve shape in the transition region are well suited to the requirements for the PTSE-2 test. Figure 10.4 shows that the test behavior for longitudinally oriented Charpy specimens is similar with virtually the same transition behavior but higher upper-shelf energy than for transversely oriented Charpy specimens. The yield strength values shown on Fig. 10.3 fall considerably below the specified values of Table 10.1; however, these requirements have been reviewed and waived. B&W is proceeding with further Phase 1 tests based on a stress-relieving temperature of 551.7 ± 13.9°C.

In the PTSE-2 test it will be necessary to pass several 1.59-mm-OD and 3.18-mm-OD stainless-sheathed instrument leads through the pressure boundary of the PTSE-2 vessel with the requirement for leaktight integrity for pressures to 137.9 MPa and temperatures to 288°C. In the PTSE-1 test this requirement was accomplished by using a packing gland type design, using solid soapstone gland parts for single- and three-hole penetration configurations. Assembly of the packing into the instrument lead through fittings was difficult for the PTSE-1 test because of the attendant close tolerance requirements for parts. An attempt has been made in the PTSE-2

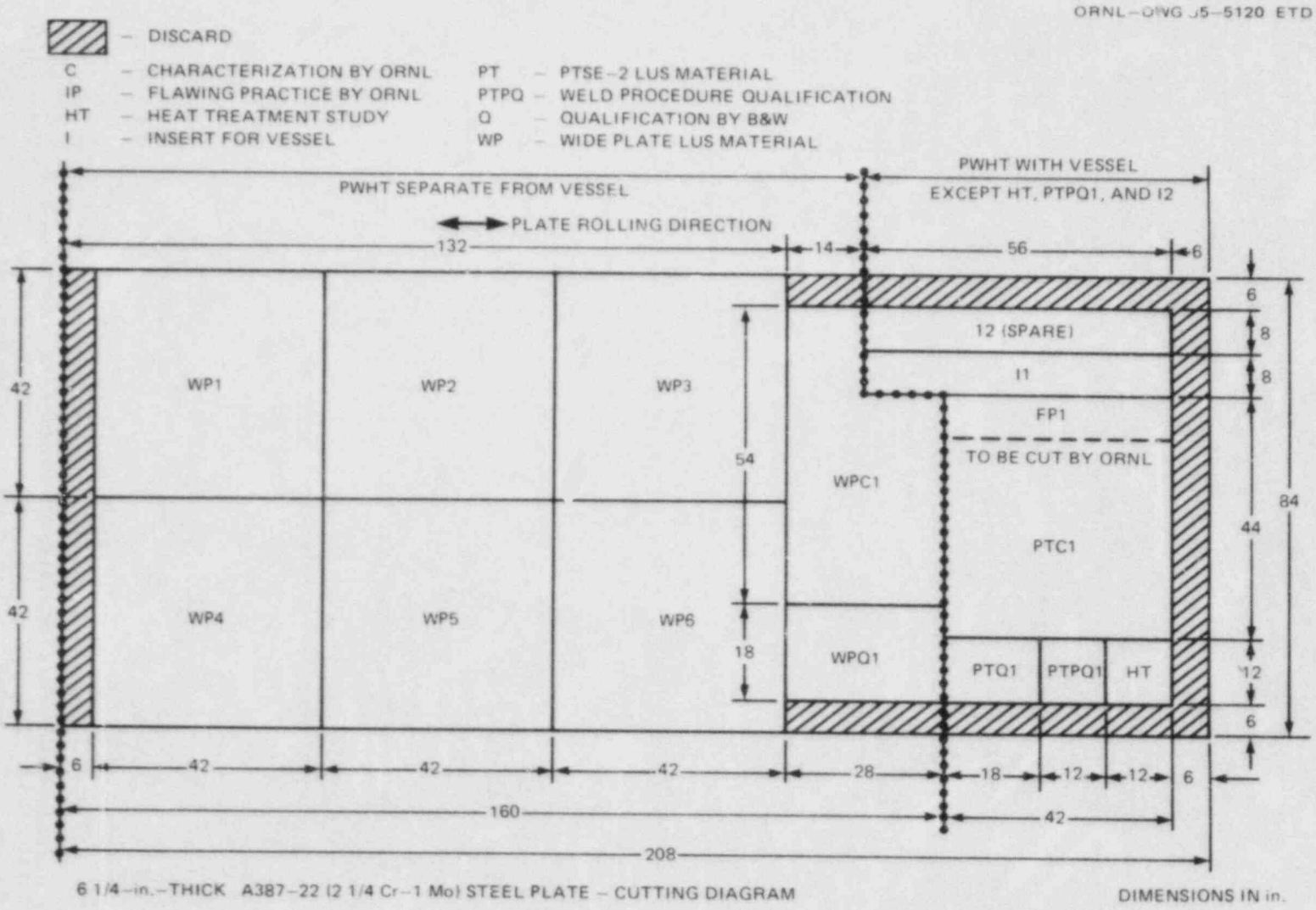

Fig. 10.1. Cutting diagram for 2 1/4 Cr-1 Mo steel plate purchased by B&W for development of low-upper-shelf material to be used in the PTSE-2 vessel.

Table 10.1. Impact and tensile property requirements

Property	Desired value	Acceptable values	
		Minimum	Maximum
Yield strength, MPa	517.1	448.2	620.5
Charpy-V upper-shelf energy,[a] J	61.0	54.2	67.8
Temperature at which Charpy-V energy is at the midpoint of the transition, °C[b]	65.5	51.7	90.6
Maximum temperature at which 100% shear first occurs, °C	121.1		176.7

[a]To be determined at a temperature where the specimen exhibits 100% shear.

[b]Midpoint energy shall be determined by adding 5 ft-lb to the average of the values obtained with 100% shear and dividing the result by 2.

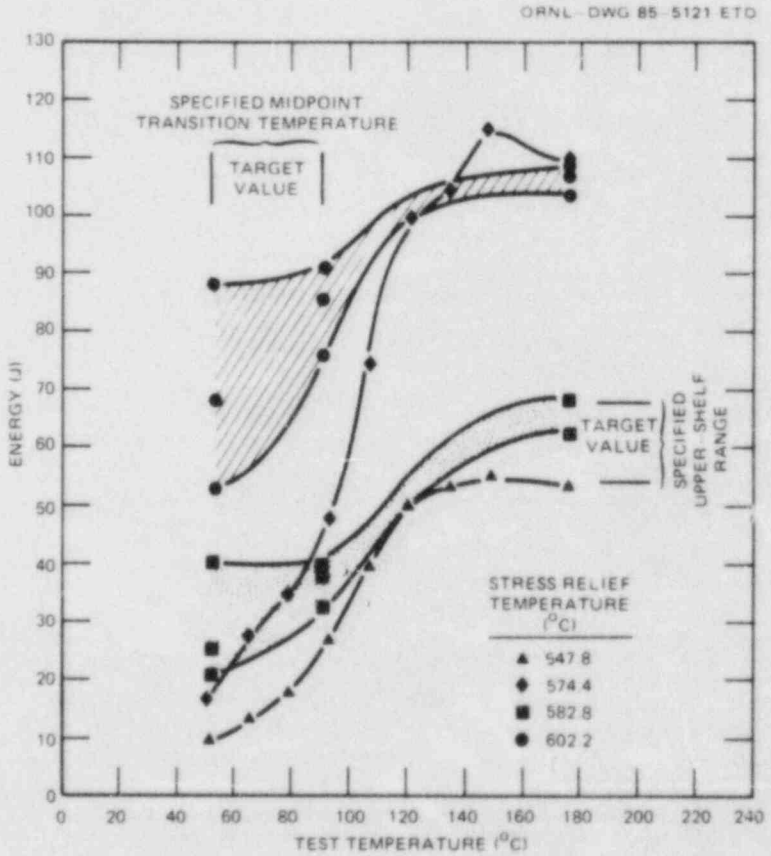

Fig. 10.2. Results of tests of transversely oriented Charpy V-notch specimens of low-upper-shelf material as a function of stress-relieving temperature.

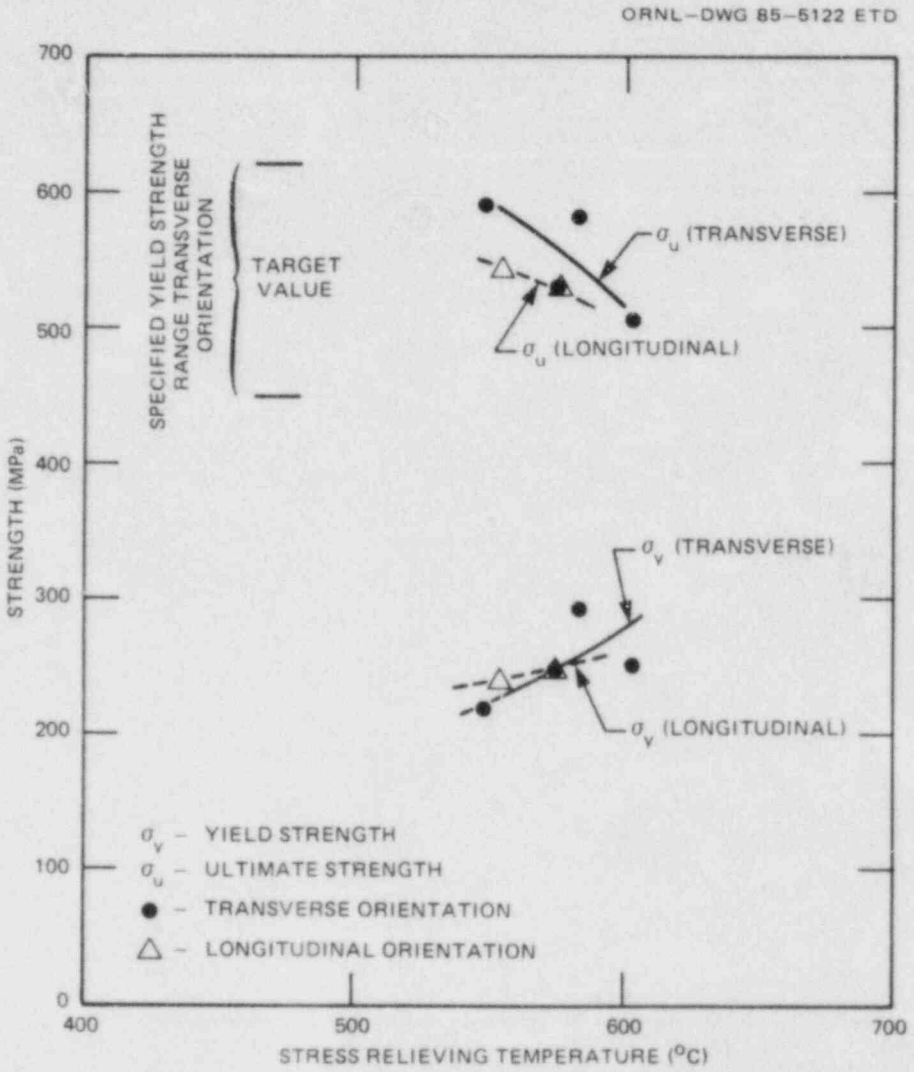

Fig. 10.3. Results of tensile tests of low-upper-shelf material as a function of stress-relieving temperature.

test to relieve this assembly difficulty by designing the soapstone glands as split two-piece configurations. Leak tests with cyclic loading, prolonged hold periods, and pressures and temperatures at maximum anticipated conditions were successfully conducted on the modified seal designs with two sources of native soapstone. The fragility of the designs for either the solid or split-gland configuration is such that considerable care is required at assembly. It is as yet unclear which design will be preferable at final assembly, so provisions are being made to accommodate either design.

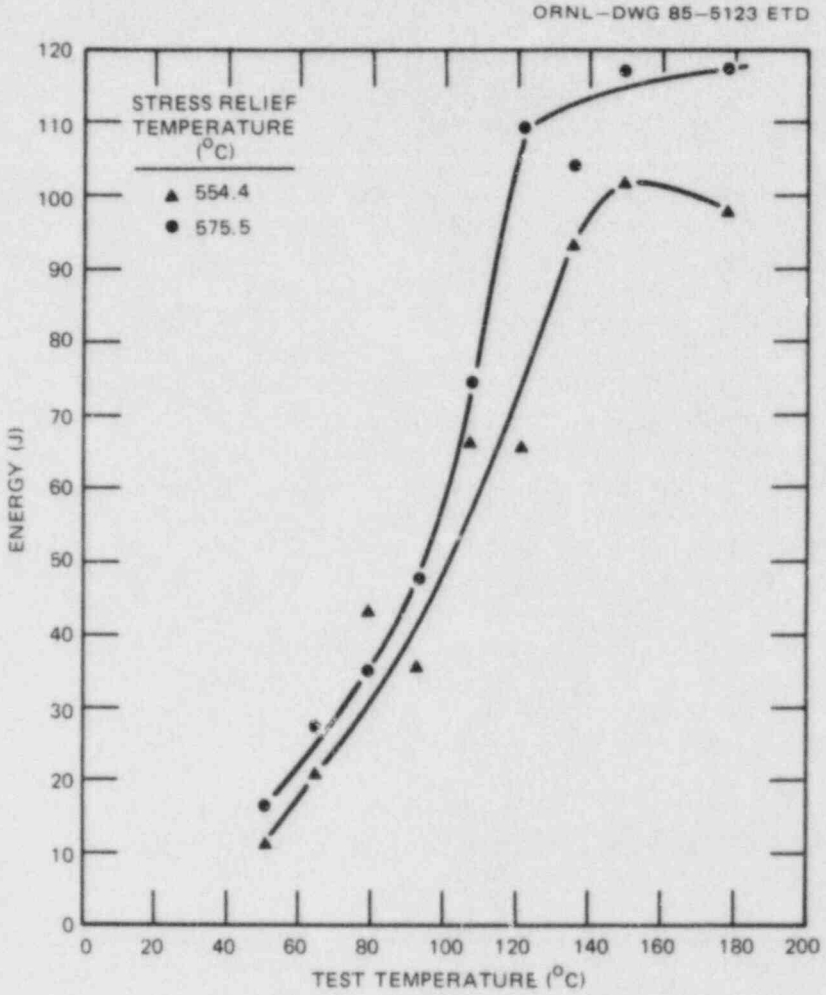

Fig. 10.4. Results of tests of longitudinally oriented Charpy V-notch specimens of low-upper-shelf material as a function of stress-relieving temperature.

10.2 Preliminary Fracture Analysis of the Second Pressurized-Thermal-Shock Experiment

R. H. Bryan

10.2.1 Background

The primary objective of the second pressurized-thermal-shock experiment, PTSE-2, is to investigate the influence of low tearing resistance on crack propagation and growth. Vulnerability of reactor pressure vessels to damage in overcooling accidents is a potential problem only in instances of vessel materials that have low Charpy impact energies at upper-shelf temperatures. While conclusions of overcooling accident analysis are principally determined by transition temperature and

its effect on crack initiation, in some hypothetical transients, crack arrest is the controlling phenomenon. Crack arrest toughness in low-upper-shelf steels is presumed to have the same dependence on temperature T and the reference temperature for the nil ductility transition RT_{NDT} as do steels with more respectable upper-shelf toughness. Even though this may be a valid assumption, it may be found in a fracture evaluation that the arrested cleavage crack is unstable relative to ductile tearing.

PTSE-2 is being designed to produce and investigate a cleavage arrest followed by unstable tearing. The PTSE-1 experiment might have approached this condition because analysis indicated that ~10 mm of ductile tearing should have ensued after the final crack arrest. If the PTSE-1 flaw had been in low-upper-shelf material, the extent of tearing would have exceeded 100 mm, according to a tearing resistance analysis.

In addition to modeling an important fracture condition, PTSE-2 is expected to elucidate the fracture transition from a rapidly propagating crack in a cleavage mode to a slowly propagating ductile fracture. One would like to know whether there is an intrinsic temperature threshold T_D above which only ductile fracture is possible or whether the transition to ductile behavior depends also on the stress-intensity factor K_I of the propagating cleavage crack (see K_{Ia} alternatives A and B, respectively, in Fig. 10.5). Resolution of the question may be impractical economically and unnecessary because tearing instability is likely to ensue in low-upper-shelf material for moderately high K_I values at the time of a cleavage arrest.

The PTSE-2 experiment is also being designed to continue the investigation of warm prestressing started in PTSE-1. The first experiment clearly demonstrated the inhibiting effect of warm prestressing for both positive and negative values of $\dot{K}_I$ when K_I is less than a previous relative maximum. Initiation and reinitiation after periods of warm prestressing were also experienced in PTSE-1, but only after intervening periods of complete unloading. The first phase of the PTSE-2 experiment will be designed to (1) induce simple warm prestressing ($\dot{K}_I < 0$) prior to the time $K_I = K_{Ic}$, (2) induce simple antiwarm prestressing ($\dot{K}_I > 0$) while $K_I > K_{Ic}$, and (3) during antiwarm prestressing increase K_I to levels substantially above the prior maximum value.

10.2.2 Parameter studies

Early indications of the material properties of the material in which the PTSE-2 flaw will reside are at variance with the specified and desired tensile and transition temperature properties, as discussed in Sect. 10.1. OCA/USA analyses were performed to evaluate the impact of these variances and of an enhanced pressurization rate planned for the test facility. Results of some of these analyses are shown here to demonstrate the feasibility of the PTSE-2 objectives and to illustrate limitations and uncertainties. The very low yield strength shown in Fig. 10.3 influences the values of the yield stress σ_Y and flow stress σ_o used in OCA/USA for plastic zone size adjustments and ligament stability calculations. The Charpy energy transition data in Fig. 10.2 suggest that RT_{NDT} might be in the temperature range 90 to 110°C. The higher-than-expected RT_{NDT} could make the transient easier to define.

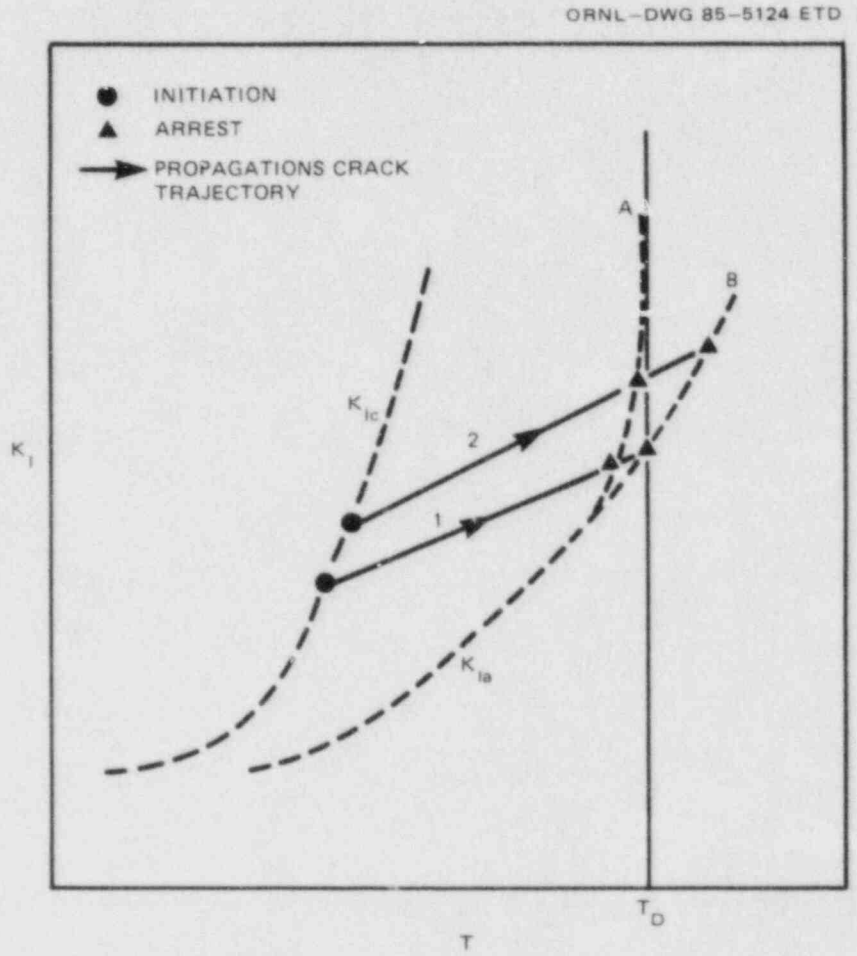

Fig. 10.5. Initiation-arrest trajectories for two alternative K_{Ia} hypotheses. Branch A is asymptotic to a ductile threshold temperature T_D. Branch B indicates that cleavage arrest temperature continues to increase with increasing K_I.

A transient of interest is illustrated by Fig. 10.6, which shows crack-tip temperature for a crack of feasible initial depth, the concurrent pressure transient, and the induced K_I and K_{Ic} variations with time. This transient induces simple warm prestressing between points A and B and simple antiwarm prestressing between B and D. K_I becomes greater than K_{Ic} in the period A-B. K_I is substantially greater than K_{Ic} during much of the antiwarm prestressing phase. From point C to point D K_I is greater than its previous relative maximum value (point A). It is in this phase of the experiment (C-D) that crack initiation is expected to take place.

Figure 10.7 shows the importance of uncertainty in K_{Ic} on the success of the warm prestressing phase of the experiment. In addition to a nominal K_{Ic} curve (for RT_{NDT} = 100°C), the figure shows curves for values of RT_{NDT} 10 K higher and lower. It is imperative that the intersection of

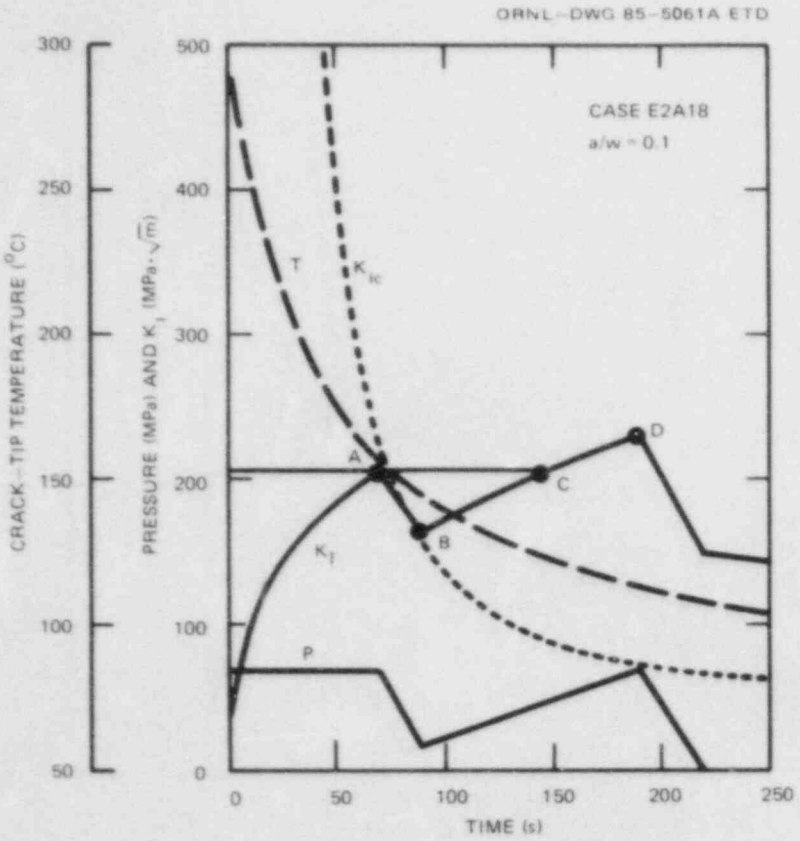

Fig. 10.6. Illustration of a PTSE-2 transient based on speculative material properties.

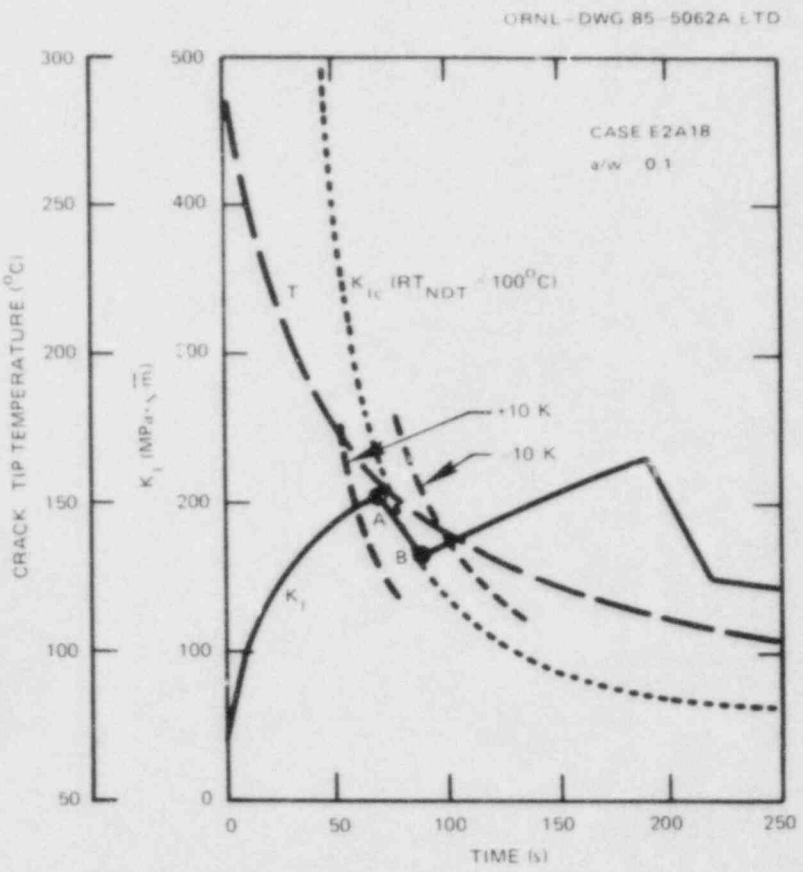

Fig. 10.7. Illustration of effects of uncertainty in K_{Ic} on the warm prestressing phase of PTSE-2. The higher RT_{NDT} (+10 K curve) would cause a crack initiation prematurely, while the lower RT_{NDT} would lead to ambiguous results.

the K_{Ic} and K_I curves be in the warm prestressing phase A-B. An uncertainty of ±10 K would probably preclude conclusive experimental results. However, it is evident that a modified depressurization transient would expand the admissible uncertainty in RT_{NDT} to ±10 K without degrading other aspects of the transient significantly. The window for the K_{Ic} intersection is also quite sensitive to the uncertainty in initial crack depth. Unlike crack depth, which will be measured precisely after the experiment, the location of the K_{Ic} curve will not be revealed by this transient experiment unless subsequent transients are run without warm prestressing.

The success of the arrest and tearing instability phase of the experiment depends on the success of the test strategy in avoiding initiation and arrest at low K_I values. Figures 10.8 and 10.9 illustrate the course of a marginally acceptable transient with respect to arrest and

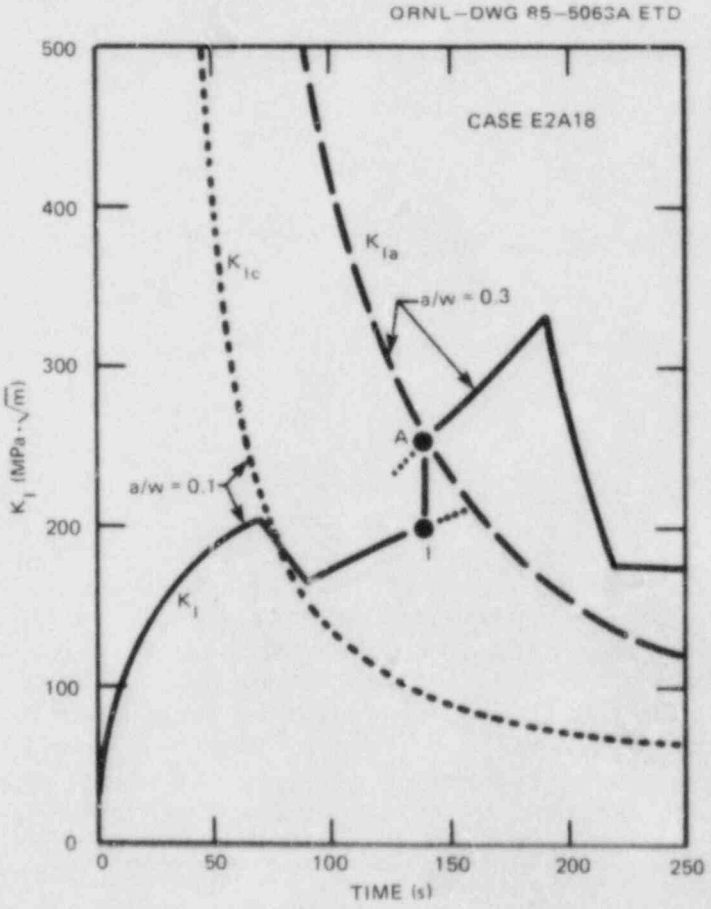

Fig. 10.8. K_I, K_{Ic}, and K_{Ia} vs time for illustrative PTSE-2 transient. In this illustration it is presumed that the initial crack will propagate when K_I increases, during antiwarm prestressing, to a value marginally exceeding its previous maximum value. In this case the ratio of crack depth to wall thickness a/w increases from 0.1 to 0.3 during the crack jump.

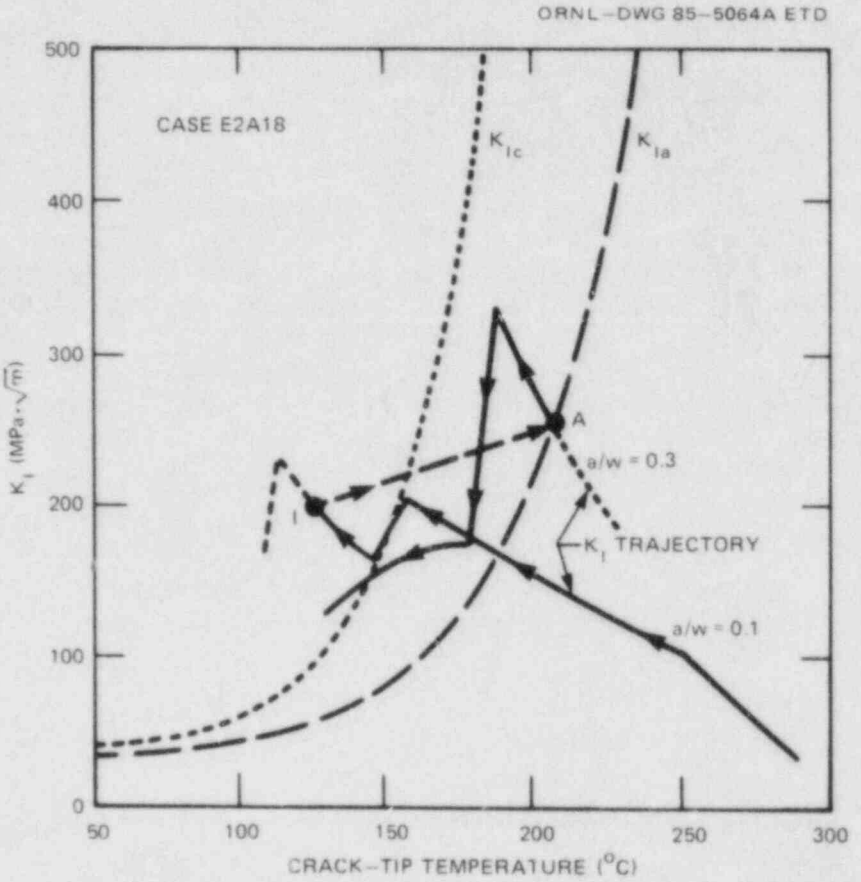

Fig. 10.9. K_I trajectory for the PTSE-2 case presented in Fig. 10.8.

instability. If crack initiation is inhibited by warm prestressing until K_I becomes greater than the previous maximum (point I), the crack jump induces a K_I of ~250 MPa·$\sqrt{m}$ (at point A). This value of K_I is equivalent to a J_I value of ~0.28 MJ/m^2, which, for low toughness material, may be high enough to generate a tearing instability. A detailed evaluation of this point must be made after tearing resistance data become available.

If crack initiation were delayed beyond point I (Fig. 10.8), the crack jump would be deeper, the K_I and J_I at arrest higher, and the likelihood of a tearing instability greater. This would be a more desirable situation because the prediction of a marginally unstable crack is uncertain. If the crack were to initiate earlier than point I, the crack jump would be small, and an instability condition would be doubtful. In this case a second pressurized-thermal-shock transient would be run to complete the experiment. This turn of events could be advantageous because the second initiation would provide a valid measurement of K_{Ic} at a value high enough to resolve the ambiguity mentioned earlier relative to the warm prestressing phase of the experiment. A final isothermal pressure loading may be useful in confirming tearing instability conditions. Many alternatives must be analyzed and evaluated on the basis of better data before a suitable set of transients can be defined.

Reference

1. R. H. Bryan and G. C. Robinson, "Preparation of Vessel for the PTSE-2 Experiment," pp. 186–8 in *Heavy-Section Steel Technology Program Semiann. Prog. Rep. October 1984–March 1985*, NUREG/CR-4219, Vol. 1 (ORNL/TM-9593/V1), Martin Marietta Energy Systems, Inc., Oak Ridge Natl. Lab.

CONVERSION FACTORS[a]

SI unit	English unit	Factor
mm	in.	0.0393701
cm	in.	0.393701
m	ft	3.28084
m/s	ft/s	3.28084
kN	lb_f	224.809
kPa	psi	0.145038
MPa	ksi	0.145038
$MPa \cdot \sqrt{m}$	$ksi \cdot \sqrt{in.}$	0.910048
J	ft·lb	0.737562
K	°F or °R	1.8
kJ/m^2	$in.-lb/in.^2$	5.71015
$W \cdot m^{-2} \cdot K^{-1}$	$Btu/h-ft^2-°F$	0.176110
kg	lb	2.20462
kg/m^3	$lb/in.^3$	3.61273×10^{-5}
mm/N	$in./lb_f$	0.175127
$T(°F) = 1.8\ T(°C) + 32$		

[a]Multiply SI quantity by given factor to obtain English quantity.

NUREG/CR-4219
Volume 2
ORNL/TM-9593/V2
Dist. Category RF

Internal Distribution

1. B. R. Bass
2. S. E. Bolt
3. R. H. Bryan
4. J. W. Bryson
5. R. D. Cheverton
6. J. M. Corum
7. W. R. Corwin
8. D. M. Eissenberg
9. J. A. Getsi
10. R. C. Gwaltney
11. S. K. Iskander
12. A. P. Malinauskas
13. S. S. Manson
14. J. J. McGowan
15. J. G. Merkle
16-17. R. K. Nanstad
18. D. J. Naus
19-23. C. E. Pugh
24. G. C. Robinson
25. G. M. Slaughter
26. J. E. Smith
27. R. W. Swindeman
28. K. R. Thoms
29. H. E. Trammell
30. C. D. West
31-34. G. D. Whitman
35. G. T. Yahr
36. ORNL Patent Office
37. Central Research Library
38. Document Reference Section
39-40. Laboratory Records Department
41. Laboratory Records (RC)

External Distribution

42. C. Z. Serpan, Division of Engineering Technology, Nuclear Regulatory Commission, Washington, DC 20555
43. M. Vagins, Division of Engineering Technology, Nuclear Regulatory Commission, Washington, DC 20555
44. W. H. Bamford, Plant Engineering Division, Westinghouse Electric Corporation, Pittsburgh, PA 15230
45. R. A. Fields, Fracture and Deformation Division, National Bureau of Standards, Gaithersburg, MD 20899
46. W. L. Fourney, Department of Mechanical Engineering, University of Maryland, College Park, MD 20742
47. M. F. Kanninen, Engineering and Material Science Division, Southwest Research Institute, San Antonio TX 78284
48. J. W. Hutchinson, Division of Applied Science, Pierce Hall, Harvard University, Cambridge, MA 02138
49. E. T. Wessel, 3570 Meadowgate Drive, Murrysville, PA 15668
50. Office of Assistant Manager for Energy Research and Development, DOE, ORO, Oak Ridge, TN 37831
51-52. Technical Information Center, DOE, Oak Ridge, TN 37831
53-327. Given distribution as shown in category RF (NTIS – 10)

NRC FORM 335 (2-84) NRCM 1102, 3201, 3202

U.S. NUCLEAR REGULATORY COMMISSION

BIBLIOGRAPHIC DATA SHEET

SEE INSTRUCTIONS ON THE REVERSE

1 REPORT NUMBER (Assigned by TIDC, add Vol. No., if any)

NUREG/CR-4219, Volume 2
ORNL/TM-9593/V2

2 TITLE AND SUBTITLE

Heavy-Section Steel Technology Program Semiannual Progress Report for April–September 1985

3 LEAVE BLANK

4 DATE REPORT COMPLETED

MONTH	YEAR
December	1985

5 AUTHOR(S)

C. E. Pugh

6 DATE REPORT ISSUED

MONTH	YEAR
January	1986

7 PERFORMING ORGANIZATION NAME AND MAILING ADDRESS (Include Zip Code)

Oak Ridge National Laboratory
P.O. Box X
Oak Ridge, TN 37831

8 PROJECT/TASK/WORK UNIT NUMBER

9 FIN OR GRANT NUMBER

B0119

10 SPONSORING ORGANIZATION NAME AND MAILING ADDRESS (Include Zip Code)

Division of Engineering Technology
Office of Nuclear Regulatory Research
U.S. Nuclear Regulatory Commission
Washington, DC 20555

11a TYPE OF REPORT

Semiannual

b PERIOD COVERED (Inclusive dates)

April–September 1985

12 SUPPLEMENTARY NOTES

13 ABSTRACT (200 words or less)

The Heavy-Section Steel Technology (HSST) Program is an engineering research activity conducted by the Oak Ridge National Laboratory for the Nuclear Regulatory Commission. The program comprises studies related to all areas of the technology of materials fabricated into thick-section primary-coolant containment systems of light-water-cooled nuclear power reactors. The investigation focuses on the behavior and structural integrity of steel pressure vessels containing cracklike flaws. Current work is organized into ten tasks: (1) program management, (2) fracture-methodology and analysis, (3) material characterization and properties, (4) environmentally assisted crack growth studies, (5) crack arrest technology, (6) irradiation effects studies, (7) cladding evaluations, (8) intermediate vessel tests and analysis, (9) thermal-shock technology, and (10) pressurized thermal-shock technology.

14 DOCUMENT ANALYSIS – a KEYWORDS/DESCRIPTORS

Pressure vessels
Ferritic steels
Weldments
Irradiation
Cladding
Flaws
Thermal shock
Fracture mechanics
Crack arrest
Crack growth

b IDENTIFIERS/OPEN-ENDED TERMS

15 AVAILABILITY STATEMENT

Unlimited

16 SECURITY CLASSIFICATION

(This page) Unclassified

(This report) Unclassified

17 NUMBER OF PAGES

18 PRICE